

The Pennsylvania State University
The Graduate School
College of Earth and Mineral Sciences

**MOCVD GROWTH AND CHARACTERIZATION OF GALLIUM NITRIDE
AND GALLIUM ANTIMONIDE NANOWIRES**

A Dissertation in
Materials Science and Engineering

by

Robert Alan Burke

© 2008 Robert Alan Burke

Submitted in Partial Fulfillment
of the Requirements
for the Degree of

Doctor of Philosophy

December 2008

The dissertation of Robert Alan Burke was reviewed and approved* by the following:

Joan M. Redwing
Professor of Materials Science and Engineering and Electrical Engineering
Chair, Intercollege Graduate Degree Program
Department of Materials Science and Engineering
Dissertation Advisor
Chair of Committee

Elizabeth C. Dickey
Professor of Materials Science and Engineering

Suzanne Mohny
Professor of Materials Science and Engineering

Jian Xu
Assistant Professor of Engineering Science and Mechanics

*Signatures are on file in the Graduate School

ABSTRACT

Group-III nitride and group-III antimonide thin films have been used for years in optoelectronic, high-speed applications, and high power/high temperature applications such as light emitting diodes (LEDs), microwave power devices, and thermovoltaics. In recent years, nanowires have gained interest due to the ability to take advantage of their geometry for increased light absorption and the synthesis of radial heterostructures. Several growth techniques have been explored for the growth of GaN and GaSb nanowires. Metal-organic chemical vapor deposition (MOCVD) is of particular interest due to its use in the commercial growth and fabrication of GaN-based and GaSb-based devices.

The first part of this thesis focused on addressing several key issues related to the growth of GaN nanowires by MOCVD. Preliminary studies investigated the effect of growth conditions on GaN nanowire formation in a hot wall MOCVD reactor. A computational fluid dynamics-based model was developed to predict the gas phase velocity, temperature and concentration profiles in the reactor. The results demonstrate a strong dependence of GaN nanowire growth on substrate position within the reactor which is due to the rapid reaction and depletion of precursors near the gas inlet of the reactor. Ni-catalyzed GaN nanowire growth was observed to occur over the temperature range of 800-900°C, which is significantly lower than typical GaN thin film temperatures. The nanowires, however, exhibited a tapered diameter due to thin film deposition which occurred simultaneously with nanowire growth. Based on the low growth temperatures, TEM characterization was carried out to investigate the nature of the catalyst. Through

these studies, the catalyst was found to consist of Ni_3Ga , indicating the presence of a vapor-solid-solid growth mechanism.

In an attempt to improve the nanowire growth selectivity, GeCl_4 was added during growth resulting in a drastic increase in nanowire density and a reduction in the tapering of the nanowires. Upon further inspection with TEM, the nanowires were found to consist of two morphologies: smooth nanowires and serrated nanowires. The smooth nanowires were found to consist of the wurtzite crystal structure, while the serrated nanowires were determined to have a wurtzite core with zinc blende faceted islands protruding from the wurtzite core.

The second half of this thesis focused on the growth and characterization of GaSb nanowires. An extensive amount of work has been carried out on GaSb thin films, however only a few reports exist on GaSb nanowire growth. As a result, it was necessary to complete a systematic study to determine a growth window for GaSb nanowires. A narrow range of growth conditions were found for Au-catalyzed GaSb nanowire growth. Vertically oriented nanowires were observed over a pressure range of 150-300 Torr depending on the substrate.

Based on these findings, additional characterization was carried out to investigate the structural properties of the nanowires along with chemical analysis of the catalyst to determine the nature of the catalyst as a function of the growth conditions. The catalyst was found to consist of Ga, Sb, and Au consistent with that expected for vapor-liquid-solid growth, however the concentrations varied depending on the growth conditions and nanowire sample. For one set of nanowires, the seed particle contained a Au-Sb solid

solution (1-15 at.% Sb). For the other set of nanowires, the particle consisted of an AuSb₂ grain and an AuGa or Au₂Ga grain that resulted in the formation of a bicrystalline nanowire. Photoluminescence measurements were also obtained on these samples and compared to the thin film literature. Samples grown on Si (111) were found to possess good optical properties, while samples grown on sapphire substrates were dominated by native defect transitions. The optical quality of the nanowire sample was also found to have a significant dependence on the V/III ratio.

TABLE OF CONTENTS

LIST OF FIGURES	ix
LIST OF TABLES	xxi
ACKNOWLEDGEMENTS	xxii
Chapter 1 Introduction	1
1.1 Motivation.....	1
1.2 Research Objectives.....	7
1.3 Thesis Outline.....	9
1.4 References.....	12
Chapter 2 GaN Nanowire Literature Review.....	15
2.1 Introduction.....	15
2.2 Decomposition Kinetics of GaN Growth by MOCVD.....	15
2.3 Vapor Transport.....	17
2.4 MBE.....	22
2.5 MOCVD	27
2.6 References.....	35
Chapter 3 GaSb Nanowire Literature Review	39
3.1 Introduction.....	39
3.2 Decomposition Kinetics of GaSb Growth by MOCVD	39
3.3 GaSb Thin Film Growth	44
3.4 Synthesis of GaSb Nanowires	49
3.5 References.....	56
Chapter 4 Experimental Techniques.....	58
4.1 Introduction.....	58
4.2 Nanowire Chemical Vapor Deposition System.....	59
4.2.1 Gas Delivery System	60
4.2.2 Metalorganic Delivery System	62
4.2.3 Reactor Configurations.....	63
4.3 Metalorganic Sources	67
4.4 Substrate Preparation	68
4.5 Nanowire Growth	70
4.6 Characterization.....	72
4.7 Computational Modeling.....	73

4.8	References.....	75
Chapter 5 Synthesis of GaN Nanowires		
5.1	Introduction.....	76
5.2	Initial Studies in Constant Temperature Region.....	77
5.3	Effect of Growth Conditions on GaN Nanowire Growth.....	81
5.3.1	Effect of Position.....	81
5.3.2	Effect of Temperature.....	88
5.3.3	Effect of V/III Ratio	91
5.3.4	Effect of Carrier Gas	96
5.4	Characterization.....	97
5.4.1	VLS Growth Mechanism versus VSS Growth Mechanism	97
5.4.2	Transmission Electron Microscopy.....	105
5.4.3	Photoluminescence	119
5.5	Growth of GaN Nanowires with the Addition of GeCl ₄	124
5.5.1	Preliminary Results	127
5.5.2	Transmission Electron Microscopy.....	131
5.5.3	Photoluminescence	138
5.6	Conclusions.....	140
5.7	References.....	142
Chapter 6 Synthesis of GaSb Nanowires		
6.1	Introduction.....	147
6.2	Growth of GaSb Nanowires on Sapphire Substrates.....	149
6.2.1	Effect of Temperature.....	149
6.2.2	Effect of Pressure	159
6.2.3	Effect of the V/III Ratio	163
6.2.4	Effect of Position.....	172
6.3	Growth of GaSb Nanowires with Au Thin Films	175
6.4	Transmission Electron Microscopy	183
6.4.1	Structural Properties and Catalyst Composition Analysis.....	183
6.4.2	Analysis of GaSb Nanowires Grown At Various Pressures.....	202
6.5	Growth of GaSb Nanowires on Si (111) Substrates	213
6.6	Photoluminescence Measurements.....	219
6.7	Conclusions.....	240
6.8	References.....	244
Chapter 7 Thesis Summary and Future Work.....		
7.1	Summary.....	248
7.2	Future Work.....	254
7.2.1	GaN Nanowires	254
7.2.2	GaSb Nanowires.....	259

7.3 References.....	261
Appendix Nanowire Chemical Vapor Deposition System	263
A.1 System Gas Manifold.....	263
A.2 Exhaust Set-Up	266
A.3 Control Panel	268

LIST OF FIGURES

Figure 1.1 : Band gap energy diagrams for group III (a) nitrides and (b) antimonides. ¹¹	2
Figure 1.2 : Schematic of vapor-liquid-solid growth. (a) Gas precursors flow to reaction site and react with nanoparticles. (b) Liquid alloy forms. (c) Liquid alloy becomes supersaturated and precipitates crystal.	3
Figure 1.3 : Diagram of (a) GaN-based core/multishell nanowire heterostructure for light-emitting diode ³² and (b) thermoelectric device consisting of array of nanowires. ³³	5
Figure 2.1 : (a) Diagram for system set-up for vapor transport with Mg ₃ N ₂ located upstream of the Ga metal source and c-plane sapphire substrate located downstream of Ga metal (b) FESEM image of p-type GaN nanowires grown on c-plane sapphire, 10 μm scale bar. ²¹	19
Figure 2.2 : SEM images of GaN nanowires grown on (a) roughened GaN template at 900°C, (b) a-axis ELO stripes, and (c) m-axis ELO stripes. ²⁸	21
Figure 2.3 : FESEM images of (a) top view and (b) cross-section view of irregular matrix layer and protruding GaN nanowires on silicon using MBE. ³⁷	23
Figure 2.4 : FESEM cross-sections of GaN nanorods grown in (a) Ga-rich and (b) N-rich conditions. ³⁹	26
Figure 2.5 : GaN nanowires grown by (a) hot-wall and (b) cold-wall MOCVD on Au-coated c-plane sapphire and alumina substrates, respectively. ^{24,52}	28
Figure 2.6 : (a) Sapphire planes used in epitaxy of GaN and (b) wurtzite crystal structure: Ga atoms are black and N atoms are white. ^{55,56}	30
Figure 2.7 : (a) FESEM image of GaN nanorods displaying the faceting of the cap. (b) SEM image of GaN nanowire array using a silicon nitride template. ^{59,60}	32
Figure 3.1 : (a) Graph of % decomposition vs. temperature of TMG for various carrier gases including H ₂ , D ₂ , N ₂ , He, toluene, and a He/toluene mixture. (b) Graph of % decomposition vs. temperature of TMSb for carrier gases of D ₂ , H ₂ , and He. A flow tube reactor connected to a mass spectrometer was used for both studies. ^{3,4}	40
Figure 3.2 : (a) Pyrolysis of TMG in H ₂ and H ₂ using a tube reactor attached to a molecular beam sampling mass spectrometer. (b) Decomposition of TMG and TMSb measured by ultraviolet spectroscopy in a MOVPE reactor. ^{1,5}	41

Figure 3.3: Low magnification SEM image displaying crater formed by FIB hole and the surrounding network of GaSb nanowires. The inset is a higher magnification SEM image of the porous nanowire network indicating the location of the nanowires and the pure Ga precipitates. ²⁶	51
Figure 3.4: SEM images of GaSb nanowires grown by (a) direct antimodization using SbCl ₃ and (b) reactive vapor transport. ²⁷	52
Figure 3.5: (a) SEM and (b) TEM images of GaSb/GaAs nanowire heterostructures synthesized by Guo <i>et al.</i> ²⁸ (c) SEM image of GaSb/GaAs nanowire heterostructures grown by Jeppsson <i>et al.</i> ³⁰	54
Figure 4.1: (a) Front view of the nanowire system including the (1) precursor delivery systems, (2) system gas manifold, (3) reactor, (4) exhaust, (5) computer with LabView set-up, and (6) control/safety features panel. (b) Backside view of reactor and gas cabinet for gas cylinder storage.	59
Figure 4.2: (a) Photo of the NH ₃ gas tank manifold showing the regulator, N ₂ purge line, leak testing port, and NH ₃ inlet. (b) Photo of the NH ₃ purifier and bypass.	62
Figure 4.3: Photo of metalorganic delivery system for TMG (left) and TMSb/GeCl ₄ (right).	63
Figure 4.4: Temperature calibration profile of Lindberg controller between 300°C and 800°C.	64
Figure 4.5: Picture of hot-wall tube reactor for nanowire growth from (a) gas inlet side and (b) sample loading/exhaust side.	65
Figure 4.6: Reactor configurations for (a) GaN and (b) GaSb nanowire growth.	66
Figure 5.1: Schematic of tube furnace and temperature profile with quartz boat 4 inches from TMG inlet.	78
Figure 5.2: SEM images of GaN nanowires grown with (a) 5% 50 nm Au catalysts and (b) 5 nm Ni Film.	79
Figure 5.3: SEM images of 5% 50 nm Au nanoparticles (a) with no treatment, (b) 5 min TMG pre-flow, and (c) heat up and cool down (no growth).	81
Figure 5.4: Schematic of tube furnace and temperature profile with quartz boat 2 inches away from TMG inlet.	82
Figure 5.5: SEM images of GaN nanowire growth on 5 nm Ni thin films at (a) 8.5 inches, (b) 9 inches, and (c) 9.5 inches into the furnace. 20 μm scale bars for	

all images. Growth conditions: 900°C, 100 Torr, 4 sccm TMG, 200 sccm NH ₃ , 250 sccm H ₂	83
Figure 5.6: (a) Geometry of nanowire system showing location of quartz boat and sapphire substrates. Gas (b) temperature, (c) velocity, and (d) adduct concentration profiles for the thin film experiment. Growth conditions: 900°C, 100 Torr, 200 sccm NH ₃ , 250 sccm H ₂	85
Figure 5.7: Experimental and modeling predictions for GaN thin film growth rate as a function of distance from the TMG inlet. Growth conditions: 900°C, 100 Torr, 4 sccm TMG, 200 sccm NH ₃ , 250 sccm H ₂	86
Figure 5.8: Mass fraction of adducts and thin film growth rate with respect to position. Quartz boat is located at 8 inches. Growth conditions: 900°C, 100 Torr, 4 sccm TMG, 200 sccm NH ₃ , 250 sccm H ₂	88
Figure 5.9: Surface morphology of GaN nanowire growth at a position 2 inches from the group III inlet for furnace temperatures of (a) 750°C (T _s = 675°C), (b) 800°C (T _s = 725°C), (c) 850°C (T _s = 775°C), (d) 900°C (T _s = 825°C), (e) 950°C (T _s = 875°C), and (f) 1000°C (T _s = 925°C). Growth conditions: 100 Torr, 3 sccm TMG, 100 NH ₃ , 250 sccm H ₂	89
Figure 5.10: Model predictions of GaN thin film growth rate at the quartz tube wall for furnace temperatures of 750°C, 800°C, 900°C, and 1000°C. Red dotted line indicates 2 inches from TMG inlet. Growth conditions: 100 Torr, 3 sccm TMG, 100 sccm NH ₃ , 250 sccm H ₂	91
Figure 5.11: SEM images of GaN nanowire growth at (a) 1 sccm, (b) 2 sccm, (c) 3 sccm, and (d) 4 sccm TMG. Growth conditions: 900°C (T _s = 825°C), 100 Torr, 100 sccm NH ₃ , 250 sccm H ₂	92
Figure 5.12: SEM images of GaN nanowire growth at (a) 50 sccm, (b) 100 sccm, (c) 150 sccm, and (d) 200 sccm NH ₃ . Growth conditions: 900°C (T _s = 825°C), 100 Torr, 3 sccm TMG, 250 sccm H ₂	93
Figure 5.13: Radial gas velocity profile at growth front.....	94
Figure 5.14: CFD model predictions for GaN thin film growth rate at quartz tube wall for NH ₃ flowrates of 50, 100, and 200 sccm. Red dotted line indicates 2 inches from TMG inlet. Growth conditions: 900°C, 100 Torr, 3 sccm TMG, 250 sccm H ₂	95
Figure 5.15: Gas phase temperature profile for (a) H ₂ and (b) N ₂ as the carrier gas. Gray rectangle is representative of location of quart boat in tube furnace reactor.	96

- Figure 5.16: SEM image of GaN growth with N₂ as the carrier gas instead of H₂..... 97
- Figure 5.17: Ni-Ga binary phase diagram. The red dotted lines represent the upper (1000°C) and lower (750°C) limits of the temperature range used for GaN nanowire growth.⁵ 99
- Figure 5.20: (a) SAD pattern collected from a region consisting of the NW and the catalyst particle. As shown in Figure 5.18, the main part of the catalyst particle contains two Ni₃Ga grains A and B. Extra diffraction spots not associated with the Ni₃Ga structure are indicated by the arrows. (b) Indices of the diffraction spots from the catalyst particle shown in (a). Two sets of diffraction spots were identified corresponding to grains A and B in Figure 5.18. The crystallographic correlations between the NW and the catalyst particle are $110_A // 110_B // 11\bar{2}0_{NW}$, $002_A // \bar{1}1\bar{2}_B // 1\bar{1}00_{NW}$, and $1\bar{1}0_A // \bar{1}\bar{1}1_B // 0002_{NW}$ 102
- Figure 5.21: Ni-Ga binary phase diagram over range of 21 at.% to 39 at.% Ga. Eutectic melting point is located at 1207°C.⁵ 105
- Figure 5.22: TEM images of GaN nanowires. Inset of SEM image showing triangular cross-section of nanowire. Additional insets are selected area diffraction patterns of the nanowires. Growth conditions: 900°C (T_s = 825°C), 100 Torr, 3 sccm TMG, 100 sccm NH₃. 106
- Figure 5.23: Schematic of the competition between vapor-solid-solid (VSS) growth of the nanowire and the vapor-solid (VS) deposition on the sidewalls of the nanowire. 107
- Figure 5.24: (a) High-angle annular dark-field (HAADF) STEM image of a GaN nanowire grown by MOCVD using a Ni catalyst. The image was collected along the GaN 1100 zone axis. Composition line profiles along (b) A-A and (c) B-B. Ni peak count to Ga peak count ratio for composition line profile for (d) A-A and (e) B-B. Growth conditions: 900°C (T_s = 825°C), 100 Torr, 3 sccm TMG, 100 sccm NH₃. 109
- Figure 5.25: (a) Bright-field image of a GaN nanowire grown by MOCVD using Ni catalyst. The image was collected along the GaN 0002 zone axis. (b) HRTEM image of overlapping between particle and nanowire. Moiré fringes can be seen on the right side of the particle due to the overlapping. (c) Higher magnification image of the particle showing {200} lattice fringes of Ni₃Ga. Growth conditions: 850°C (T_s = 775°C), 100 Torr, 3 sccm TMG, 100 sccm NH₃. 112
- Figure 5.26: (a) Bright-field image of a GaN nanowire grown using Ni as the catalyst.. The image was collected along the GaN 0002 zone axis. (b)

- HRTEM image collected near the particle. Moiré fringes that resulted from the overlapping of the particle and the nanowire are evident in the left half of the particle. (c) Higher magnification image of the particle showing $\{111\}$ lattice fringes of Ni_3Ga . Growth conditions: 900°C ($T_s = 825^\circ\text{C}$), 100 Torr, 4 sccm TMG, 100 sccm NH_3 113
- Figure 5.27: Lattice parameter of the (Ni) and α' (Ni_3Ga) phases as a function of Ga composition.⁵ Data is presented for the (Ni) phase from 0-23 at.% Ga. Data is presented for the α' (Ni_3Ga) phase from ~23-32 at.% Ga. 115
- Figure 5.28: TEM images of various GaN nanowire samples grown at 200 sccm NH_3 . The nanowires were found to possess three growth directions: (a) $11\bar{2}0$ growth direction, (b) $1\bar{1}00$ growth direction, and (c) $1\bar{2}1\bar{1}$ growth direction. Growth conditions: 900°C ($T_s = 825^\circ\text{C}$), 100 Torr, 3 sccm TMG, 200 sccm NH_3 117
- Figure 5.29: Fast Fourier Transformation (FFT) of 35 x 35 nm field of catalyst and nanowire in Figure 5.21 (b). The nanoparticle spots are circled on the image. Splitting of the spots indicates the presence of two phases. 118
- Figure 5.30: Effect of growth temperature on photoluminescence measurements. Growth conditions: 100 Torr, 3 sccm TMG, 100 sccm NH_3 , 250 sccm H_2 121
- Figure 5.31: Effect of TMG flowrate on photoluminescence measurements. Growth conditions: 900°C ($T_s = 825^\circ\text{C}$), 100 Torr, 100 sccm NH_3 122
- Figure 5.32: Effect of NH_3 flowrate on photoluminescence measurements. Growth conditions: 900°C ($T_s = 825^\circ\text{C}$), 100 Torr, 3 sccm TMG. 124
- Figure 5.33: SEM images of GaN nanowire growth with GeCl_4 at a position (a) 2.75 inches (b) 4 inches, and (c) and 4.75 inches from the TMG inlet. Inset of a triangular cross-section of a GaN nanowire. Growth conditions: 900°C , 100 Torr, 3 sccm TMG, 100 sccm NH_3 , 150 sccm H_2 , 0.15 sccm GeCl_4 , and 5 minute growth. 128
- Figure 5.34: X-ray diffraction scan of GaN nanowire sample grown with the addition of GeCl_4 . Growth conditions: 900°C , 100 Torr, 3 sccm TMG, 100 sccm NH_3 , 150 sccm H_2 , 0.15 sccm GeCl_4 , and 10 minute growth. 129
- Figure 5.35: SEM images of GaN nanowire growth after introducing GeCl_4 flowrates of (a) 0.15 sccm, (b) 0.30 sccm, and (c) 0.40 sccm to the growth. Growth conditions: 900°C , 100 Torr, 3 sccm TMG, 100 sccm NH_3 , 150 sccm H_2 , and 10 minute growth. 130

- Figure 5.36: Low magnification TEM image. Two types of nanowires were observed: smooth surface (indicated by blue arrow) and rough surface (indicated by red arrow). Growth conditions: 900°C, 100 Torr, 3 sccm TMG, 100 sccm NH₃, 150 sccm H₂, 0.15 sccm GeCl₄..... 132
- Figure 5.37: (a) Bright-field TEM image of a nanowire with faceted islands on the surface. (b) The corresponding SAD pattern. The wire contains both wurtzite (WZ) and zinc blende (ZB) GaN phases with a high density of twins and stacking faults. The crystallographic relationship between the WZ and ZB GaN is $\langle 1\bar{1}00 \rangle_{\text{WZ}} // \langle 112 \rangle_{\text{ZB}}$, $\langle 11\bar{2}0 \rangle_{\text{WZ}} // \langle 1\bar{1}0 \rangle_{\text{ZB}}$, and $\langle 0001 \rangle_{\text{WZ}} // \langle 111 \rangle_{\text{ZB}}$. The growth direction of the nanowire is $\sim 4^\circ$ away from $\langle 1\bar{1}00 \rangle_{\text{WZ}}$ and $\langle 112 \rangle_{\text{ZB}}$. Growth conditions: 900°C, 100 Torr, 3 sccm TMG, 100 sccm NH₃, 150 sccm H₂, 0.15 sccm GeCl₄..... 133
- Figure 5.38: HRTEM image collected near the surface of the nanowire. The nanowire core is wurtzite GaN with stacking faults while the islands are twinned zinc blende GaN. The twinning occurs at the interface between the nanowire core and the faceted islands. 134
- Figure 5.39: Low magnification image of a GaN nanowire growth with GeCl₄ (left) along with HRTEM images of different segments of the nanowire beginning at the tip and traveling towards the base of the nanowire (right). 136
- Figure 5.40: (a) Bright-field TEM image of a nanowire with smooth surface. (b) SAD pattern of nanowire indicating the presence of the wurtzite GaN structure with (0001) planar defects. (c) HRTEM image of GaN nanowire. 138
- Figure 5.41: Photoluminescence spectra of GaN nanowire samples grown with addition of GeCl₄ for 5 min and 10 min. Growth conditions: 900°C, 100 Torr, 3 sccm TMG, 100 sccm NH₃, 150 sccm H₂, 0.15 sccm GeCl₄. 139
- Figure 6.1: Binary phase diagrams for (a) Au-Ga and (b) Au-Sb. A line is drawn at 500°C to indicate the temperature at which GaSb nanowire growth resulted.¹¹ 151
- Figure 6.2: SEM images of GaSb growth at temperatures of (a) 450°C, (b) 475°C, (c) 500°C, (d) 525°C, and (e) 550°C. Growth conditions: 100 Torr, 1 sccm TMG, 1 sccm TMSb, 100 sccm H₂, and 5 minutes. 152
- Figure 6.3: Graph of temperature vs. length for GaSb nanowires grown at 475°C, 487°C, 500°C, 512°C, and 525°C. Growth conditions: 100 Torr, 1 sccm TMG, 1 sccm TMSb, 100 sccm H₂, and 5 minutes. 155

- Figure 6.4: Arrhenius plot of GaSb nanowire growth at temperatures ranging from 475°C to 525°C. Growth conditions: 100 Torr, 1 sccm TMG, 1 sccm TMSb, and 5 minute growth. 156
- Figure 6.5: Plot of length vs. time for various GaSb nanowire samples grown at 500°C. The growth rate was calculated from the slope of the line as $2.24 \pm 0.23 \mu\text{m}/\text{min}$. Growth conditions: 100 Torr, 1 sccm TMG, 1 sccm TMSb, and 100 sccm H_2 157
- Figure 6.6: SEM image of GaSb nanowire growth at 500°C, 100 Torr, 1 sccm TMG, 1 sccm TMSb, and 100 sccm H_2 . The sample was grown for 5 minutes. The red dotted circles indicate locations where GaSb nanowire growth nucleated from other wires or growths on the surface. 159
- Figure 6.7: SEM images of GaSb growth at pressures of (a) 13 Torr, (b) 100 Torr, (c) 200 Torr, (d) 300 Torr, and (e) 400 Torr. Inset in (d) is a high magnification image of a GaSb nanowire. Inset in (e) shows the thin film/nanowire matrix that forms at 400 Torr. Growth conditions: 500°C, 1 sccm TMG, 1 sccm TMSb, 100 sccm H_2 , and 5 minute growth time. 161
- Figure 6.8: SEM images of GaSb nanowire growth at V/III ratios of (a) 0.5, (b) 1, (c) 1.5, and (d) 2. Inset in (a) shows higher degree of nanowires growing with a preferred orientation. Growth conditions: 500°C, 100 Torr, 100 sccm H_2 , and 5 minute growth. 164
- Figure 6.9: SEM images of GaSb nanowires grown at V/III ratios of (a) 0.5 and (b) 2. The total MO flowrate for these experiments was increased to 3 sccm. (c) and (d) are higher magnification images of GaSb nanowires grown at a V/III ratio of 2 with a total metalorganic flowrate of 2 sccm and 3 sccm respectively. The blue and red arrows in the images are located near the seed particle. 166
- Figure 6.10: Schematic of “reverse tapering.” (a) Gas precursors flown to reaction site and react with nanoparticles. (b) Precipitation of GaSb crystal from catalyst. (c) Catalyst continues to grow in size as the nanowire grows until it reaches equilibrium and then levels out. 170
- Figure 6.11: Schematic of growth in Ga-rich condition. (a) Gas precursors flown to reaction site and react with nanoparticles. (b) Particle continues to grow until they reach their supersaturation point. (c) Precipitation of GaSb crystal from catalyst leading to nanowire growth. 171
- Figure 6.12: SEM images of GaSb nanowire growth with 5% 50 nm Au nanoparticles. The boat is located in the center of the hot zone. (a) is located ~1.5 inches upstream from the center of the hot zone. (b) is located ~0.5

- inches upstream of the center of the hot zone (~1 inch further back than (a)). Growth conditions: 500°C, 300 Torr, 1 sccm TMG, 1 sccm TMSb, 100 sccm H₂, and 5 minute growth time..... 174
- Figure **6.13**: SEM images of GaSb nanowire growth using 2.5 nm Au thin films at pressures of (a) 100 Torr, (b) 200 Torr, (c) 300 Torr, and (d) 400 Torr. Inset in (b) is a higher magnification image of the nanowire growth. Inset in (c) shows the epitaxial nature of the GaSb nanowire growth. Growth conditions: 500°C, 1 sccm TMG, 1 sccm TMSb, 100 sccm H₂, and 5 minute growth..... 177
- Figure **6.14**: SEM images of GaSb growth on 2 nm Au thin films at multiple positions on the quartz boat. (a) was placed at the front of the boat or 1.25 inches upstream of the center of the hot zone. (b) was placed 1.5 inches away from (a). (c) was placed 2.75 inches away from (a). Growth conditions: 500°C, 200 Torr, 1 sccm TMG, 1 sccm TMSb, 100 sccm H₂, and 5 minute growth time..... 179
- Figure **6.15**: SEM images of GaSb nanowire growth using (a) 10 nm, (b) 20 nm, (c) 40 nm, (d) 50 nm, (e) 80 nm, and (f) 100 nm Au nanoparticles. Growth conditions: 500°C, 100 Torr, 1 sccm TMG, 1 sccm TMSb, 100 sccm H₂, and 5 minute growth time..... 181
- Figure **6.16**: (a) Low magnification and (b) high resolution TEM images of GaSb nanowires. Inset in (a) is an electron diffraction pattern. The sharp interface between the nanowire and seed particle can be seen in (b). Growth conditions: 500C, 100 Torr, 1 sccm TMG, and 1 sccm TMSb. 185
- Figure **6.17**: (a) High-angle annular dark-field (HAADF) STEM image of a GaSb nanowire. (b) Typical EDS spectrum of the body of the GaSb nanowire. The Cu peak is due to the lacey carbon grid. (c) and (d) are XEDS line profiles along the axis and cross section of the nanowire..... 186
- Figure **6.18**: High magnification image of a bicrystalline GaSb nanowire with a catalyst particle containing two grains. Inset is a selected area diffraction pattern displaying a growth direction of [220] for the top part of the nanowire. Growth conditions: 475°C, 100 Torr, and V/III ratio of 1. The image was collected along the $\bar{1}12$ zone axis. 190
- Figure **6.19**: (a) High-angle annular dark-field (HAADF) STEM image of a GaSb nanowire. Compositional line profiles of (b) A-A', (c) B-B', (d) C-C', and (e) D-D'. The image was collected along the $1\bar{1}0$ zone axis. 191
- Figure **6.20**: (a) Low magnification TEM image of GaSb nanowire grown at 475°C. High resolution images of (b) interface between left side of nanowire and particle, c) top of seed particle exhibiting grains A and B, and (d) right

side of nanowire. The nanowire appears to be bicrystalline. The left side of the nanowire is a few degrees away from the [111] growth direction. The image was taken along the $1\bar{1}0$ zone axis.	192
Figure 6.21: (a) High-angle annular dark-field (HAADF) STEM image of a GaSb nanowire. Compositional line profiles of (b) A-A' and B-B'. The image was collected along the $1\bar{1}0$ zone axis.	193
Figure 6.22: Composition (at.%) line profiles of D-D' in Figure 6.19 and B-B' in Figure 6.21.	195
Figure 6.23: Schematic representation of Au-Sb phase diagram for Au-Sb alloys on the nanometer scale. ³³	196
Figure 6.24: HRTEM images of catalyst/nanowire interface (a) before and (b) after exposure to electron beam. Blue arrows indicate the location of the original interface. Red arrow indicates the location of the planar defect present before exposure to the electron beam. Growth conditions: 500C, 100 Torr, 1.33 sccm TMG, and 0.67 sccm TMSb.	198
Figure 6.25: (a) TEM image of GaSb nanowire after exposure to an electron beam. The arrows indicate the original interface between the nanowire and the particle. A secondary phase is present in the nanowire (red arrow). (b) High-angle annular dark-field STEM image of the GaSb nanowire. The image was collected along the $1\bar{1}0$ zone axis. (c) Composition line profiles of A-A' and B-B'. Growth direction of the nanowire was determined to be [111].	199
Figure 6.26: (a) High-angle annular dark-field STEM image of a GaSb nanowire. The image was collected along the $1\bar{1}0$ zone axis. Red arrows indicate the necking region of the nanowire. (c) Composition line profiles of A-A' and B-B'. Growth direction of the nanowire was determined to be [111]. Growth conditions: 500°C, 100 Torr, and V/III ratio of 2.	201
Figure 6.27: (a) Low magnification and (b) HRTEM images of GaSb nanowire grown at 200 Torr with Au catalyst. Inset is an selected area diffraction pattern. The growth direction was determined to be [111]. The image was collected along the $1\bar{1}0$ zone axis. Growth conditions: 500°C, 200 Torr, 1 sccm TMG, and 1 sccm TMSb.	203
Figure 6.28: (a) Low magnification and (b) high-resolution TEM images of a GaSb nanowire grown at a pressure of 300 Torr. Inset is a SAD pattern showing the [111] growth direction. Red arrows indicate a secondary phase present on the surface of the nanowire. The image was collected along the	

110 zone axis. Growth conditions: 500°C, 300 Torr, 1 sccm TMG, and 1 sccm TMSb.....	204
Figure 6.29: High-angle annular dark-field STEM images and XEDS axial line scans for GaSb nanowires samples grown at pressures of (a) 100 Torr, (b) 200 Torr, and (c) 300 Torr. The red arrows demonstrate the contact angle observed in each case.....	206
Figure 6.30: Binary phase diagram for Ga-Sb system. The blue line indicates the point at which GaSb would precipitate out of the catalyst at a growth temperature of 500°C. ⁴²	208
Figure 6.31: Diagram of a nanowire demonstrating the contact angle, Θ , for a catalyst consisting of (a) Au, Ga, and Sb versus a catalyst consisting of (b) Au and Ga. γ_{SL} , γ_{LV} , and γ_{SV} are representative of the surface energies for the solid-liquid, liquid-vapor, and solid-vapor interfaces, respectively. Adapted from Nebol'sin <i>et al.</i> ⁴³	211
Figure 6.32: (a) Low magnification image of GaSb nanowire. (b) High-angle annular dark-field STEM image of the GaSb nanowire. (c) Composition line scans through the catalyst along the x-axis (A-A') and y-axis (B-B') of the particle. The growth direction was determined to be [111]. The images were collected along the 110 zone axis.	212
Figure 6.33: SEM images of GaSb nanowire grown on Si (111) coated with 50 nm Au. The samples were grown for (a) 3 minutes and (b) 10 minutes. Scale bars are 10 μm and 20 μm , respectively. Growth conditions: 500°C, 100 Torr, 1 sccm TMG, 1 sccm TMSb, and 100 sccm H ₂	214
Figure 6.34: Plot of length vs. time for various GaSb nanowire samples grown at 500°C. The growth rate was calculated from the slope of the line as 2.38 $\mu\text{m}/\text{min}$. Growth conditions: 100 Torr, 1 sccm TMG, 1 sccm TMSb, and 100 sccm H ₂	215
Figure 6.35: SEM images of GaSb nanowire growth on Si (111) using 50 nm Au nanoparticles. Samples were grown at pressures of (a) 100 Torr, (b) 150 Torr, (c) 200 Torr, (d) 250 Torr, and (e) 300 Torr. Insets in (c) and (d) show presence of epitaxial growth. Inset in (e) shows disparity in nanowire diameter. These samples were located 1.5 inches upstream of the center of the hot zone. Growth conditions: 500°C, 1 sccm TMG, 1 sccm TMSb, and 100 sccm H ₂	217
Figure 6.36: SEM images (tilted 15°) of GaSb nanowire growth on Si (111) using 2 nm Au thin film. Samples were grown at pressures of (a) 150 Torr and (b) 200 Torr. (c) and (d) show cross sections of (a) and (b). These samples were	

located in the center of the hot zone. Growth conditions: 500°C, 1 sccm TMG, 1 sccm TMSb, and 100 sccm H ₂	219
Figure 6.37: SEM images of GaSb nanowires grown at 300 Torr on (a) Si (111) and (b) sapphire using Au thin films. The silicon sample was placed directly in front of the sapphire sample on the quartz boat. Growth conditions: 500°C, 1 sccm TMG, 1 sccm TMSb, and 5 minute growth time.	223
Figure 6.38: Temperature-dependent photoluminescence spectrums of a GaSb nanowire sample grown on Si (111) at a pressure of 300 Torr. Inset shows shoulder on high energy side of peak at 4K.	224
Figure 6.39: Photoluminescence spectrum of GaSb nanowire sample grown on silicon at 7K. The dotted peaks are peak fits for the various transitions and are offset from the axis. The blue peak is the overall fit for the spectrum. The red underlying spectrum is the original curve based on the PL data.....	225
Figure 6.40: Graph of intensity of 777 meV (A) transition with respect to % Power. The intensity saturates at high power output indicating a donor-acceptor pair transition.	227
Figure 6.41: (a) Graph of intensities of 710 meV (first ionized state of native acceptor) and 777 meV (native acceptor) with respect to temperature. (b) Energy band diagram of native acceptor (A) and its first ionized state (A ⁻). E _C , E _D , E _F , and E _V stand for the conduction band, donor level, Fermi level, and valence band, respectively. Adapted from Nicholas <i>et al.</i> ⁵⁹	229
Figure 6.42: Temperature-dependent photoluminescence spectrums of a GaSb nanowire sample grown on sapphire at a pressure of 300 Torr.....	230
Figure 6.43: Photoluminescence spectrum of GaSb nanowire sample at 3.6K. The dotted peaks are peak fits for the various transitions and are offset from the axis. The blue peak is the overall fit for the spectrum. The red underlying spectrum is the original curve based on the PL data.	232
Figure 6.44: Photoluminescence measurements of GaSb nanowire samples grown on sapphire using 50 nm Au nanoparticles at V/III ratios of 0.5, 1, 1.5, and 2. The sample grown at a V/III ratio of 1 was completed with a laser power of 15 mW and a temperature of 3.5K. The other samples were analyzed at a laser power of 12 mW and a temperature of 5K. The intensities of the photoluminescence for samples grown at V/III ratios of 1, 1.5, and 2 were multiplied by 8 for comparison purposes. Growth conditions: 500°C, 100 Torr, and 5 minute growth time.....	236

- Figure 6.45: Photoluminescence spectrum at 5K of GaSb nanowire sample with a V/III ratio of 2. The dotted peaks are peak fits for the various transitions and are offset from the axis. The blue peak is the overall fit for the spectrum. The red underlying spectrum is the original curve based on the PL data.....240
- Figure 7.1: SEM images of GaN growth on r-plane sapphire (a) without and (b) with the addition of GeCl₄ to the gas phase mixture. Growth conditions: 900°C, 100 Torr, 3 sccm TMG, 100 sccm NH₃, and 10 minute growth time. For the growth with GeCl₄, the GeCl₄ flowrate was 0.15 sccm.258
- Figure 1.1: LabView set-up for controlling the mass flow controllers and pneumatic valves on the system gas manifold.....264
- Figure 1.2: Exhaust set-up for nanowire CVD system including throttle valve, nitrogen vent line, nitrogen dilution line, scrubber, pump bypass valve (37), and pump valve (36).268
- Figure 1.3: Photo of the control panel for the nanowire CVD system which includes: 1) safety interlock power witch, 2) alarm reset, 3) alarm speaker, 4) emergency stop, 5) LifeLine II toxic gas monitors, 6) throttle valve pressure controller, 7) MOCVD pressure controller power supply, 8) MOCVD pressure controllers, and 9) MFC power supply. The pirani pressure gauge display is located below the MFC power supply.....270

LIST OF TABLES

Table 4.1: Chemistry model for MOCVD growth of GaN nanowires.	74
Table 5.1: Lattice parameter data of various Ni-Ga intermetallic compounds. ⁵	103
Table 6.1: Diameter and length measurements of GaSb nanowires at various reactor pressures.	162
Table 6.2: Length measurements of GaSb nanowires at various V/III ratios. For certain growths, the total metalorganic flowrate was increased and is noted in the table.....	167
Table 6.3: GaSb nanowire diameter and length ranges for various Au nanoparticle diameters.....	182
Table 6.4: Composition of GaSb nanowire seed particle.	188
Table 6.5: Photoluminescence transitions for bulk GaSb at 4.2K. Adapted from Dutta <i>et al.</i> ⁵⁴	221

ACKNOWLEDGEMENTS

I would like to begin by thanking my advisor, Joan Redwing, for her support and guidance during my time at Penn State. For the most part, she allowed me to explore my own ideas for my research project. Eventually, she had to put her foot down though and ban me from the lab, so I would be forced to write the dissertation you are about to read. I would also like to thank my committee for their input through this process and of course letting me graduate.

I would also like to acknowledge the National Science Foundation and the Penn State MRSEC Center for Nanoscale Science for funding my research project. I would like to extend a special thanks to Dr. Xiaojun Wang for the amazing TEM that went into my dissertation. Without him, this document would not have turned out as well as it did. I would also like to thank Roger Reeve's research group at the University of Canterbury in New Zealand for the PL measurements on the GaSb nanowires.

I would like to sincerely thank my research group who helped me survive this process. In particular, I would like to thank Sarah and Pramod for their input on my project and their friendship. I would like to thank Sharis for being my swing dance partner when I was in the mood, and I would like to thank Jeff for keeping me on my toes. I would like to thank the MOCVD group (Ian, Dongjin, Jeremy, and AJ) for putting up with all the toxic gas tanks changes. I would also like to thank Ian for putting up with me talking to myself (and him) while in the office.

I would like to thank my family and friends who helped me get through some difficult times. I would like to thank my parents, Scott and Joyce Burke, for their support

and love throughout this process. I would also like to thank my brothers (Mike, Dan, and William) for being there when I needed them. I would also like to thank my bowling buddies (Chad, Dave, Pat, and Mike) for the good times on Sunday nights. I would also like to extend a special thanks to Mike and his wife, Trish, for their support when I went through a difficult time in March.

Last but not least, I would like to thank Caroline, my significant other, for helping pick up the pieces when she didn't even know what she was doing. I would like to thank her for her support and love throughout this whole process, and, of course, for feeding me so I could work on my dissertation. She has filled me with happiness, and I hope it continues through my experience in New Zealand and beyond.

Chapter 1

Introduction

1.1 Motivation

Group-III nitrides are direct-gap semiconductors with band gap energies spanning from the infrared into the ultraviolet. The group-III nitrides consist of aluminum nitride (AlN), gallium nitride (GaN), and indium nitride (InN) which have band gap energies of 0.7 eV, 3.4 eV, and 6.2 eV, respectively (Figure 1.1 (a)).^{1,2} Alloying InN and AlN with GaN permits the tuning of band gaps and emission wavelengths over a wide range, with a particular interest in the blue-green region of the visible spectrum. This capability makes GaN-based thin film devices optimal for use in optoelectronic device applications.³⁻⁶ The main commercial application for GaN-based devices are as light emitting diodes (LEDs) which are commonly used in full color displays, numerical readouts, indicator lamps, and traffic lights. LEDs have gained commercial interest for general lighting applications over other technologies such as incandescent light bulbs due to lower costs associated with lower power consumption.³ In addition to its wide band gap, GaN possesses a good chemical stability, high breakdown field and relatively high thermal conductivity. These properties make GaN useful for high power/high temperature applications such as microwave power transistors.^{7,8}

Group-III antimonides are also direct-gap semiconductors, however their band gaps are smaller with energies spanning from 0.17 eV (InSb) to 1.6 eV (AlSb).^{9,10} As

was also the case for group-III nitrides, InSb and AlSb can be alloyed with GaSb to create optoelectronic devices in the near- to mid-infrared region of the electromagnetic spectrum (Figure 1.1 (b)). Group-III antimonides also possess high carrier mobilities which make them ideal for high-speed applications. The electron and hole mobilities for GaSb are on the order of $3,700 \text{ cm}^2/\text{V}\cdot\text{s}$ and $850 \text{ cm}^2/\text{V}\cdot\text{s}$, whereas the electron and hole mobilities of InSb are $80,000 \text{ cm}^2/\text{V}\cdot\text{s}$ and $1250 \text{ cm}^2/\text{V}\cdot\text{s}$, respectively.¹¹⁻¹³ Group-III antimonides have been implemented in devices such as infrared sensors and lasers,¹⁴⁻¹⁷ photodetectors,¹⁸ magnetic field sensors,⁹ and thermovoltaics.^{19,20}

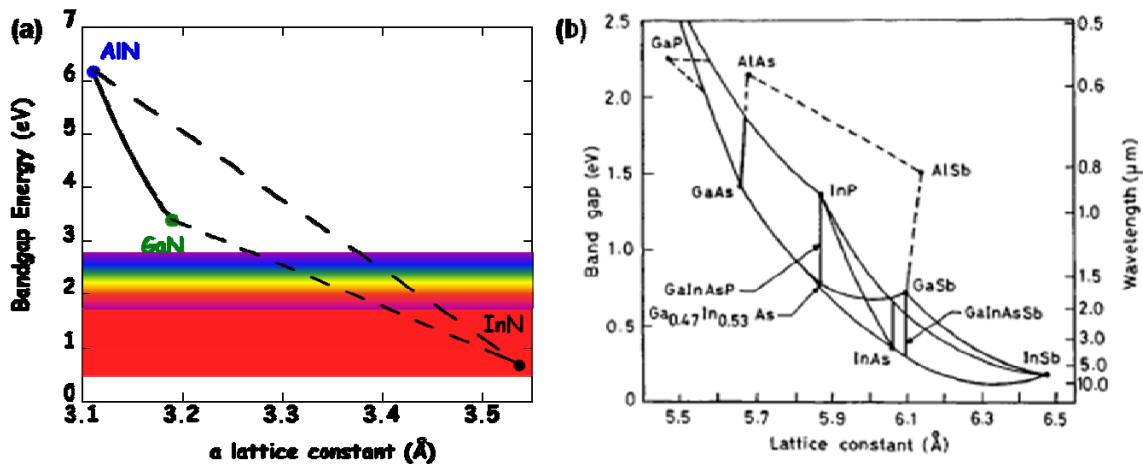


Figure 1.1: Band gap energy diagrams for group III (a) nitrides and (b) antimonides.¹¹

The demand for smaller devices with better performance has led to the investigation of nanoscale structures such as nanowires and nanorods. The feature size of thin film devices is primarily limited by processing techniques such as optical and e-beam lithography. Nanowires, on the other hand, are typically synthesized using the vapor-liquid-solid (VLS) mechanism.²¹ In VLS growth, a metal nanoparticle catalyst becomes a preferred site for deposition. The precursor(s) are flown into a reactor and

decompose into their constituents (Figure 1.2 (a)). The constituents in their atomic form absorb onto the surface of the nanoparticles and diffuse into the metal nanoparticles due to the solubility between the elements and the metal catalyst. Ultimately, this leads to the formation of a liquid alloy when the mixture of the components reduces the melting temperature (eutectic melting point) below that of the growth temperature (Figure 1.2 (b)). Eventually, the liquid alloy becomes supersaturated and crystal growth occurs by precipitation at the solid-liquid interface. This leads to the formation of a nanowire (Figure 1.2 (c)) with a high aspect ratio due to the diameter of the nanowire being determined by the metal nanoparticle size which can be as low 10 nm.

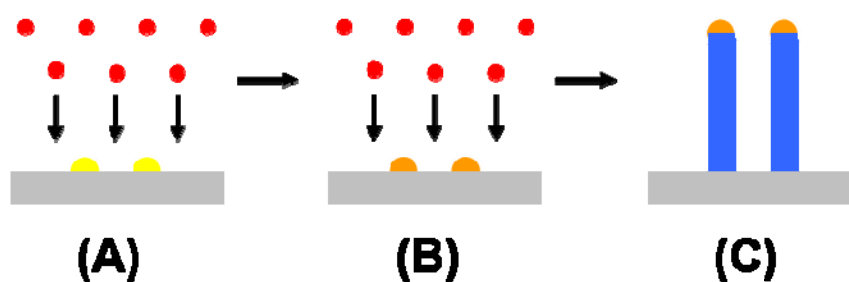


Figure 1.2: Schematic of vapor-liquid-solid growth. (a) Gas precursors flow to reaction site and react with nanoparticles. (b) Liquid alloy forms. (c) Liquid alloy becomes supersaturated and precipitates crystal.

There still remains some uncertainty, however, as to the mechanism responsible for III-V nanowire growth. A condition which is critical to VLS growth is that the seed particle should be in the liquid phase at the growth temperature. The state of the particle can be predicted by examining the binary phase diagram for the metal-vapor system. Typical growth temperatures for III-V nanowire growth, however, are significantly lower than the eutectic melting point for the metal-vapor alloy. As a result, another mechanism has been proposed for the growth of III-V nanowires known as vapor-solid-solid (VSS)

growth.²² This mechanism is a solid-phase diffusion mechanism which was first proposed to explain the synthesis of GaAs nanowires using Au nanoparticles.²³ In VSS growth, the particle remains soluble with its constituents, however a liquid alloy never forms. In some cases, the group-V constituent is not soluble with the seed particle and incorporates into the nanowire at the particle/nanowire interface. Overall, the mechanism responsible for nanowire growth is highly dependent on the choice of catalyst, nanowire material involved, and the growth conditions utilized for synthesis.

A change in properties has also been observed in nanoscale structures, which adds to the interest in studying these structures. For example, a reduction in the melting point of a material has been observed on the nanoscale.²⁴ This fact can lead to a decrease in annealing temperature necessary to remove defects from crystalline materials. A change in the electrical properties with decreasing nanowire diameter has also been reported for the case of Bi nanowires where a transition to a semiconducting behavior was observed at a critical radius due to two-dimensional quantum confinement of the quasi-one-dimensional electron gas.²⁵ Nanowires have also gained interest in thermoelectric cooling and power generation applications. Due to boundary scattering, a decrease in thermal conductivity was observed as the diameter of the nanowire approached the mean free path of phonons.²⁶ Nanowires have also been studied for biological and chemical sensing applications due to the increased surface to volume ratio which enhances the change in the electrical response of nanowires when species adsorb on their surfaces.²⁷

Several prototype GaN-based nanowire devices have been fabricated in recent years that attempt to take advantage of the nanoscale properties. Field-effect transistors have been fabricated using n-type GaN nanowires which exhibit gate-dependent

conductance variation.²⁸ Optically pumped lasing has been observed in n-type GaN nanowires and GaN/AlGaN core/shell nanowire heterostructures.²⁹⁻³¹ These devices take advantage of the strong emission intensity at the nanowire ends due to sharp cleaved end facets.²⁹ In addition, the heterostructure nanowire laser exhibits photon and carrier confinement due to the AlGaN shell acting as a cladding layer.³¹ Nanowire light-emitting diodes³² have also been produced using a combination of nanowire growth and thin film deposition to form radial core-shell heterostructures (Figure 1.3 (a)).

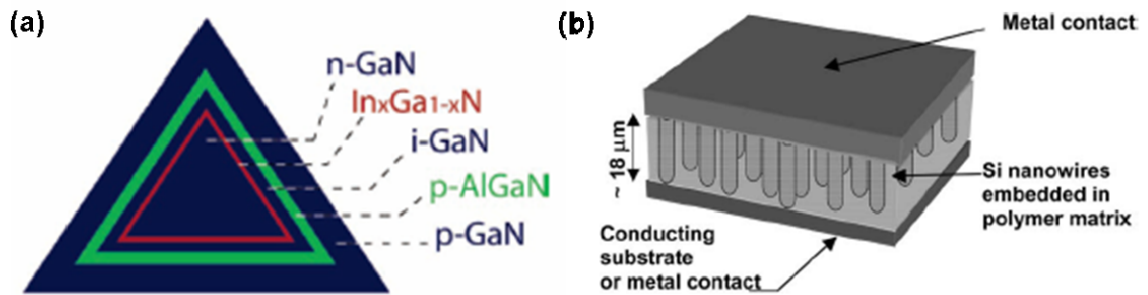


Figure 1.3: Diagram of (a) GaN-based core/multishell nanowire heterostructure for light-emitting diode³² and (b) thermoelectric device consisting of array of nanowires.³³

In contrast to GaN, there have only been a few reports of GaSb nanowire growth and characterization. Back-gated GaSb nanowire transistors were fabricated to determine the polarity and conductivity of the nanowires,¹² and optically pumped near-infrared (NIR) lasing of GaSb nanowires has also been demonstrated.³⁴ GaSb nanowires are also of interest for thermoelectrics. The quality of a thermoelectric is based on its figure of merit: $ZT = S^2\sigma T/k$. In order to increase the figure of merit, it is necessary to either increase the electrical conductivity (σ) or decrease the thermal conductivity (k) of a material.³⁵ This proves to be difficult in thin films due to the fact that increasing the electrical conductivity tends to lead to an increase in the thermal conductivity and vice

versa. Theoretical studies³⁶⁻³⁸ have shown that it may be possible to reduce the thermal conductivity in a nanowire due to phonon scattering while maintaining or increasing the electrical conductivity of the material. A potential thermoelectric device involving the use of nanowires is shown in Figure 1.3 (b). For this device, n- or p-type Si nanowires were grown epitaxially on a complementary-doped Si (111) substrate (p-type if the nanowires are n-type and vice versa).³³ After growth, the Si nanowires were embedded in parylene and a chromium/gold contact layer was deposited as a top contact layer, creating the thermoelectric device. Another potential device would consist of alternating n-type and p-type nanowire arrays connected electrically in series and thermally in parallel. This design could also be applied to an array of GaSb nanowires. GaSb nanowires could potentially be grown epitaxially on GaAs or GaSb substrates.

There are a variety of techniques currently used for the synthesis of GaN and GaSb nanowires, however metal-organic chemical vapor deposition (MOCVD) is of particular interest since it is the epitaxial growth technique currently used to fabricate commercial optoelectronic devices. MOCVD growth of GaN involves the deposition of group-III nitride materials from metalorganic precursors such as trimethylgallium (TMG, Ga(CH₃)₃), trimethylindium (TMIn, In(CH₃)₃), and trimethylaluminum (TMAl, Al(CH₃)₃) and ammonia (NH₃). Initial reports have shown the capability to utilize MOCVD for GaN nanowire growth^{32,39-42} as well as the ability to control the growth orientation of the nanowires via the choice of substrate.⁴³⁻⁴⁵ Further studies are needed, however, to identify the window of growth conditions necessary for nanowire growth and better understand the effect of growth conditions on the structural properties of the nanowires. Through these studies, it will also be worthwhile to examine the mechanism

(VLS or VSS) responsible for GaN nanowire growth since typical growth temperatures are significantly lower than the eutectic melting temperature for the group III-metal alloy systems. Tapering of the nanowire diameter has been reported^{40,45} which arises due to the competition between thin film and nanowire growth. Consequently, it is necessary to gain a better understanding of the growth of GaN nanowires using MOCVD in order to identify a growth window that optimizes the selectivity of nanowire growth over thin film deposition.

In contrast to GaN nanowire growth, the synthesis of GaSb nanowires has received much less attention.^{10,46-48} Recently, the MOCVD growth of GaSb nanowires was reported,^{47,48} although there is limited information available on the effect of the growth conditions on the growth rate and properties (structural, optical, and electrical) of the material. Therefore, it is not only necessary to determine a window of growth conditions that leads to the synthesis of GaSb nanowires, but also investigate the effect of the growth conditions on the nanowire properties and the nature of GaSb nanowire growth.

1.2 Research Objectives

The overall focus of this thesis is to examine the effects of growth conditions on the structural and optical properties of GaN and GaSb nanowires grown by MOCVD. As was previously noted, the window of growth conditions necessary for GaN nanowire growth using MOCVD is not well understood and is different from that used for thin film deposition. This is in part due to the complex chemical reactions involved in MOCVD

growth. MOCVD growth of GaN typically involves high temperatures in the range of 800-1000°C due to the low efficiency in the decomposition of NH_3 . At the same time, TMG begins to decompose at a relatively low temperature of 410°C.⁴⁹ This fact in combination with TMG and NH_3 being highly reactive in the gas phase at room temperature complicates MOCVD growth of GaN nanowires in a hot-wall tube reactor. As a result, these factors play an intricate role in determining the nanowire growth regime for GaN in MOCVD. To complicate matters further, vapor-solid growth can occur along with nanowire growth which results in the growth of tapered GaN nanowires.^{40,45}

As a result, an extensive study was completed examining the effect of the growth conditions on the growth and structural properties of GaN nanowires. Computational reactor modeling was utilized in combination with experiments in order to gain a better understanding of the growth conditions required for nanowire synthesis. The mechanism of GaN nanowire growth via metal catalysts is poorly understood. As a result, detailed TEM studies were carried out to investigate the nature of the catalyst particle and evaluate if a VLS or VSS growth mechanism was operative during growth. Photoluminescence measurements were also carried out in order to examine the effect of the growth conditions on the optical properties of the GaN nanowires. Finally, a Cl-based precursor was introduced to the gas phase mixture in an attempt to enhance the selectivity of GaN nanowire growth over vapor-solid deposition in order to reduce the tapering of the GaN nanowires.

The second half of the study investigated the effect of the growth conditions on GaSb nanowire growth. As was previously mentioned, there are only a few reports of GaSb nanowire growth. Therefore, a comprehensive study examining the effect of

temperature, pressure, and V/III ratio on GaSb nanowire growth was carried out. TEM was employed not only to look at the structural properties of the resulting GaSb nanowires but also to investigate the nature of the catalyst particle similar to that done for GaN nanowire growth. Photoluminescence measurements were also completed in order to determine the effect of the growth conditions on the optical properties of the GaSb nanowires.

1.3 Thesis Outline

This work presents a thorough study investigating the synthesis and characterization of GaN and GaSb nanowires fabricated by MOCVD. In particular, growth conditions including temperature, pressure, and V/III ratio that lead to nanowire growth for each system were determined. The effect of the growth conditions on the structural and optical properties was examined to determine optimal growth conditions for high quality nanowire growth. Additional characterization was also carried out in order to investigate if nanowire growth for each system proceeds via the VLS or VSS mechanism.

Chapters 2 and 3 provide background information concerning the synthesis of GaN and GaSb nanowires, respectively. Chapter 2 begins by addressing the complex reactions that result due to the interactions between TMG and NH_3 during GaN growth. This chapter continues with a review of the various techniques for the growth of GaN nanowires with an emphasis on MOCVD. The chapter not only addresses the variety of

techniques which can be utilized for GaN growth, but also outlines the pros and cons of each technique.

As was previously noted, Chapter 3 focuses on areas of interest for the synthesis of GaSb nanowires. Chapter 3 begins with a discussion of the pyrolysis kinetics pertaining to the precursors (TMG and TMSb). This chapter progresses to a brief review of MOCVD-grown GaSb thin films due to the lack of GaSb nanowire literature and ends with a discussion of the limited number of studies concerning GaSb nanowire growth. Details regarding the structural and optical properties of the material systems are also woven throughout both literature review chapters.

In Chapter 4, a description of the nanowire chemical vapor deposition (CVD) reactor utilized for the studies is included. Additional details about some aspects of the reactor can also be found in the Appendix. This chapter contains an overview of the MOCVD set-up along with a compilation of the equations and variables used in calculating the flowrates of the metalorganic precursors. After the overview of the metalorganic set-up, the reactor configurations for GaN and GaSb nanowire growth are provided. The chapter concludes with a discussion of the sample preparation and growth procedure along with details concerning the modeling studies and characterization methods.

Chapter 5 presents the results for the experimental and modeling studies relating to the synthesis of GaN nanowires. The chapter begins by addressing the effect of the growth conditions on the density and diameter of the GaN nanowires along with a comparison to process modeling results for GaN thin film deposition which are used to explain the experimental results. The growth conditions which are examined are the

position of the substrate with respect to the TMG inlet, temperature, V/III ratio (TMG and NH_3 flowrates), and carrier gas. The mechanism of growth (VLS vs. VSS) is then discussed based on chemical analysis and electron diffraction data of the nanowire catalyst particles carried out using transmission electron microscopy. Photoluminescence (PL) results are included which explain the effect of the growth conditions on the optical properties of the GaN nanowires. Finally, preliminary results are included on the effect of GeCl_4 on the structural and optical properties of the nanowires.

In Chapter 6, the results pertaining to MOCVD growth of GaSb nanowires on c-plane sapphire and Si (111) using Au nanoparticles and thin films are presented. This chapter begins by providing a window of growth conditions that led to GaSb nanowire growth. The growth conditions which were examined are temperature, pressure, V/III ratio, and position. The chapter also includes an extensive TEM analysis of various samples investigating the structural properties of the nanowires. XEDS was employed to perform a chemical analysis of the seed particles to determine if growth proceeded via a VLS or VSS mechanism. The TEM analysis also evaluated the effect of the catalyst composition on the contact angle between the nanowire and seed particle. The chapter ends by analyzing PL data of various samples and comparing the data to previous results for GaSb thin films. The transitions which are responsible for the peaks observed are identified.

Chapter 7 provides a summary of the major findings from the GaN and GaSb studies. In particular, an emphasis is placed on the effect of the growth conditions on the structural and optical properties of the nanowires. This chapter also contains suggestions

for future work that could be carried out based on the results that are discussed throughout the thesis.

1.4 References

- 1 S. C. Jain, M. Willander, J. Narayan, and R. Van Overstraeten, *Journal of Applied Physics* **87**, 965-1006 (2000).
- 2 J. Wu, W. Walukiewicz, K. M. Yu, J. W. Ager, E. E. Haller, H. Lu, W. J. Schaff, Y. Saito, and Y. Nanishi, *Applied Physics Letters* **80**, 3967-3969 (2002).
- 3 S. N. Mohammad and H. Morkoc, *Progress in Quantum Electronics* **20**, 361-525 (1996).
- 4 K. Sugimoto, E. Shinichi, A. Masatoshi, and T. Honda, *Physica Status Solidi (c)* **4**, 53-56 (2007).
- 5 M. Umeno, T. Egawa, and H. Ishikawa, *Materials Science in Semiconductor Processing* **4**, 459-466 (2001).
- 6 D. Starikov, I. Berishev, J.-W. Um, N. Badi, N. Medelci, A. Tempez, and A. Bensaoula, *Journal of Vacuum Science and Technology B* **18**, 2620-2623 (2000).
- 7 S. Rajan, H. L. Xing, S. DenBaars, U. K. Mishra, and D. Jena, *Applied Physics Letters* **84**, 1591-1593 (2004).
- 8 C. E. Weitzel and K. E. Moore, *Journal of Electronic Materials* **27**, 365-369 (1998).
- 9 R. M. Biefeld, *Materials Science & Engineering R-Reports* **36**, 105-142 (2002).
- 10 S. Vaddiraju, M. Sunkara, A. Chin, C. Ning, and G. Dholakia, *Journal of Physical Chemistry C* **111**, 7339-7347 (2007).
- 11 P. S. Dutta, H. L. Bhat, and V. Kumar, *Journal of Applied Physics* **81**, 5821-5870 (1997).
- 12 M. Jeppsson, K. Dick, H. Nilsson, N. Skold, J. Wagner, P. Caroff, and L.-E. Wernersson, *Journal of Crystal Growth* (2008).
- 13 Q. Ye, T. Yamada, H. Liu, R. Scheffler, N. Mingo, and R. Leverenz, in *Single Crystal InSb Nanowires: Synthesis, Characterization, Properties, and Applications*, San Francisco, CA, 2006 (Materials Research Society).
- 14 X. Marcadet, C. Becker, M. Garcia, I. Prevot, C. Renard, and C. Sirtori, *Journal of Crystal Growth* **251**, 723-728 (2003).
- 15 R. M. Biefeld, A. A. Allerman, and S. R. Kurtz, *Materials Science and Engineering B-Solid State Materials for Advanced Technology* **51**, 1-8 (1998).
- 16 R. M. Biefeld, A. A. Allerman, S. R. Kurtz, and K. C. Baucom, *Journal of Crystal Growth* **195**, 356-362 (1998).
- 17 S. Kurtz, A. Allerman, R. Biefeld, and K. Baucom, *Applied Physics Letters* **72**, 2093-2095 (1998).
- 18 T. Ashley, A. B. Dean, C. T. Elliott, C. F. Mcconville, G. J. Pryce, and C. R. Whitehouse, *Applied Physics Letters* **59**, 1761-1763 (1991).

- 19 C. A. Wang, H. K. Choi, S. L. Ransom, G. W. Charache, L. R. Danielson, and D.
M. Depoy, *Applied Physics Letters* **75**, 1305-1307 (1999).
- 20 H. K. Choi, C. A. Wang, G. W. Turner, M. J. Manfra, D. L. Spears, G. W.
Charache, L. R. Danielson, and D. M. Depoy, *Applied Physics Letters* **71**, 3758-
3760 (1997).
- 21 R. S. Wagner, in *Whisker Technology*, edited by A. P. Levitt (John Wiley & Sons,
Inc., New York, 1970), p. 47-69.
- 22 A. I. Persson, M. W. Larsson, S. Stenstrom, B. J. Ohlsson, L. Samuelson, and L.
R. Wallenberg, *Nature Materials* **3**, 677-681 (2004).
- 23 A. I. Persson, B. J. Ohlsson, S. Jeppsson, and L. Samuelson, *Journal of Crystal
Growth* **272**, 167-174 (2004).
- 24 Y. N. Xia, P. D. Yang, Y. G. Sun, Y. Y. Wu, B. Mayers, B. Gates, Y. D. Yin, F.
Kim, and Y. Q. Yan, *Advanced Materials* **15**, 353-389 (2003).
- 25 Z. B. Zhang, X. Z. Sun, M. S. Dresselhaus, J. Y. Ying, and J. P. Heremans,
Applied Physics Letters **73**, 1589-1591 (1998).
- 26 G. Chen, A. Narayanaswamy, and C. Dames, *Superlattices and Microstructures*
35, 161-172 (2004).
- 27 F. Patolsky and C. M. Lieber, in *Materials Today; Vol. 8* (2005), p. 20-28.
- 28 Y. Huang, X. F. Duan, Y. Cui, and C. M. Lieber, *Nano Letters* **2**, 101-104 (2002).
- 29 S. Gradecak, F. Qian, Y. Li, H. G. Park, and C. M. Lieber, *Applied Physics
Letters* **87**, 1731111-3 (2005).
- 30 J. C. Johnson, H. J. Choi, K. P. Knutsen, R. D. Schaller, P. D. Yang, and R. J.
Saykally, *Nature Materials* **1**, 106-110 (2002).
- 31 H. J. Choi, J. C. Johnson, R. R. He, S. K. Lee, F. Kim, P. Pauzauskie, J.
Goldberger, R. J. Saykally, and P. D. Yang, *Journal of Physical Chemistry B* **107**,
8721-8725 (2003).
- 32 F. Qian, S. Gradecak, Y. Li, C. Y. Wen, and C. M. Lieber, *Nano Letters* **5**, 2287-
2291 (2005).
- 33 A. R. Abramson, W. C. Kim, S. T. Huxtable, H. Q. Yan, Y. Y. Wu, A. Majumdar,
C. L. Tien, and P. D. Yang, *Journal of Microelectromechanical Systems* **13**, 505-
513 (2004).
- 34 A. H. Chin, S. Vaddiraju, A. V. Maslov, C. Z. Ning, M. K. Sunkara, and M.
Meyyappan, *Applied Physics Letters* **88**, - (2006).
- 35 A. Majumdar, *Science* **303**, 777-778 (2004).
- 36 D. Cahill, W. Ford, K. Goodson, G. Mahan, A. Majumdar, H. Maris, R. Merlin,
and S. Phillpot, *Applied Physics Reviews* **93**, 793-818 (2003).
- 37 N. Mingo and D. A. Broido, *Physical Review Letters* **93**, - (2004).
- 38 N. Mingo, *Applied Physics Letters* **84**, 2652-2654 (2004).
- 39 F. Qian, Y. Li, S. Gradecak, D. L. Wang, C. J. Barrelet, and C. M. Lieber, *Nano
Letters* **4**, 1975-1979 (2004).
- 40 J. Su, G. Cui, M. Gherasimova, H. Tsukamoto, J. Han, D. Ciuparu, S. Lim, L.
Pfefferle, Y. He, A. V. Nurmikko, C. Broadbridge, and A. Lehman, *Applied
Physics Letters* **86**, 013105 (2005).
- 41 T. Kuykendall, P. Pauzauskie, S. K. Lee, Y. F. Zhang, J. Goldberger, and P. D.
Yang, *Nano Letters* **3**, 1063-1066 (2003).

- 42 G. Kipshidze, B. Yavich, A. Chandolu, J. Yun, V. Kuryatkov, I. Ahmad, D.
Aurongzeb, M. Holtz, and H. Temkin, *Applied Physics Letters* **86**, 033104
(2005).
- 43 T. Kuykendall, P. J. Pauzauskie, Y. F. Zhang, J. Goldberger, D. Sirbuly, J.
Denlinger, and P. D. Yang, *Nature Materials* **3**, 524-528 (2004).
- 44 J. Han, K. Kim, J. Su, M. Gherasimova, A. V. Nurmikko, S. F. Chichibu, and C.
Broadbridge, in *MOCVD Growth and Characterization of AlGaInN Nanowires
and Nanostructures*, Boston, MA, 2006 (Materials Research Society), p. 0892-
FF31-01.1-10.
- 45 G. T. Wang, A. A. Talin, D. J. Werder, J. R. Creighton, E. Lai, R. J. Anderson,
and I. Arslan, *Nanotechnology* **17**, 5773-5780 (2006).
- 46 A. Lugstein, J. Bernardi, C. Tomastik, and E. Bertagnolli, *Applied Physics Letters*
88, - (2006).
- 47 M. Jeppsson, K. Dick, J. Wagner, P. Caroff, K. Deppert, L. Samuelson, and L.-E.
Wernersson, *Journal of Crystal Growth* (2008).
- 48 Y. N. Guo, J. Zou, M. Paladugu, H. Wang, Q. Gao, H. H. Tan, and C. Jagadish,
Applied Physics Letters **89**, - (2006).
- 49 T. Mihopoulos, Doctor of Philosophy Thesis, Massachusetts Institute of
Technology, 1999.

Chapter 2

GaN Nanowire Literature Review

2.1 Introduction

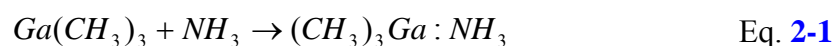
GaN thin film growth has been extensively studied over the last two decades. Over the last few years, there has been a significant interest in the synthesis of GaN nanowires. The most popular (and first) technique used for the synthesis of GaN nanowires is vapor transport. In vapor transport, a Ga-based powder is heated to a vapor phase and reacts with NH_3 at a substrate placed downstream of the Ga precursor to form GaN nanowires. Other techniques which have become popular for GaN nanowire growth are molecular beam epitaxy (MBE) and metal-organic chemical vapor deposition (MOCVD). These techniques will be discussed in more detail in the following sections in order to give a better overview of the research that has been carried out in the GaN nanowire field. Before these techniques are discussed, however, a section concerning the gas phase chemistry for MOCVD growth of GaN will be covered.

2.2 Decomposition Kinetics of GaN Growth by MOCVD

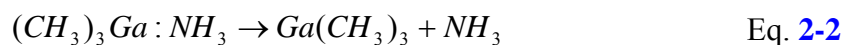
As was discussed in the introduction, MOCVD is typically the technique of choice for the growth of GaN and other group-III nitrides due to its commercial applications. As is the case with any technique, there are usually drawbacks that must be

overcome. One of the common problems with MOCVD growth of GaN is the parasitic pre-reactions between trimethylgallium (TMG) and ammonia (NH₃). This leads to the formation of stable Lewis acid-base adducts and oligomers that inhibit the growth of GaN. To complicate matters, high growth temperatures (800-1050°C) are necessary for sufficient decomposition of NH₃ and to enhance the mobility of nitrogen within the GaN lattice. TMG, on the other hand, decomposes at a relatively low temperature of 410°C.¹ Due to these conditions, the GaN growth chemistry proves to be quite complex.

Based on experimental results and modeling studies, a series of reactions for the synthesis of GaN have been devised. The initial reaction which occurs at room temperature is the formation of the Lewis acid-base adduct:²



The Ga-N bond for this adduct is fairly weak and as a result decomposes at 31°C back into its constituents:³

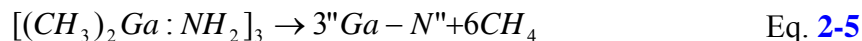


The Lewis acid-base adduct has also been shown to form a cyclic compound at ~90°C with the release of one methane group per Ga atom. This reaction is believed to proceed in a two step process:^{4,5}



The formation of the cyclic compound or trimer has been proposed as the mechanism responsible for GaN growth.⁶ In general, a reduction in growth rate has been linked to the

formation of the cyclic trimer, which supports the belief that it is responsible for GaN growth.⁴ The final reaction which has been discussed is the decomposition of the trimer into “Ga-N,” which is considered to be low molecular weight products with similar physical properties of GaN:⁷



Recently, it has been suggested that the cyclic trimer is not actually present at elevated temperatures in the gas phase chemistry.⁸ In one study, FTIR measurements were utilized to investigate the presence of methane which is a byproduct of the trimer formation.⁹ There was no measurable methane production, which indicates that the trimer does not form. Instead, it has been suggested that GaN growth involves the homogeneous pyrolysis of TMG and the formation of radical fragments. These radical fragments recombine into clusters or nuclei that do not reach the surface of the substrate, effectively decreasing the material in the gas stream for growth.¹⁰

Overall, these studies display the complexity of the gas phase chemistry for GaN growth by MOCVD. As a result, there still remains some uncertainty as to the true chemistry involved for GaN growth. In any case, these reactions will be utilized in modeling studies in Chapter 5 in an attempt to explain the GaN nanowire growth.

2.3 Vapor Transport

Vapor transport is the most popular technique used for the synthesis of GaN nanowires. Typically, a powder consisting of Ga or GaN is placed in a quartz boat and loaded into a tube furnace. A substrate is placed downstream of this boat. The furnace

heats the quartz boat and substrate to their respective temperatures for growth. NH_3 is added to the system, mixes with the Ga vapor, and transports to the substrate where GaN nanowire growth results. A tremendous amount of research has been carried out in this area from catalyst selection^{11,12} to doping¹³⁻¹⁶ and substrate choice.¹⁷⁻¹⁹ As a result, a few studies have been selected for this literature review in order to give an overview of the field and its progress.

A representation of the basic approach to GaN nanowire growth using vapor transport is provided by Bae *et al.*²⁰ In this study, a Ga/GaN powder mixture was placed in a quartz boat roughly 10 cm upstream from another quartz boat containing alumina substrates. The alumina substrates were coated with a 0.01M ethanol solution containing $\text{HAuCl}_4 \cdot 3\text{H}_2\text{O}$. The tube furnace had multiple heating zones in order to heat the Ga source to 1100°C and the substrate to approximately 950°C . NH_3 was flown into the reactor as the N source for GaN nanowire growth. After growth, SEM and TEM were employed to characterize the samples. The nanowires were found to possess a triangular cross-section with an average diameter of 50 nm and an average length of 20 μm . SAD showed that the nanowires consisted of the wurtzite crystal structure with a primary growth direction of $[\bar{1}2\bar{1}0]$. XRD measurements further supported these findings. Photoluminescence measurements were also carried out, and the PL spectra were found to have a broad peak at 3.45 eV at room temperature. For a PL spectra obtained at a temperature of 8K, peaks were resolved at 3.478, 3.30, 3.22, and 3.14 eV.

Zhong *et al.*²¹ expanded upon the basic approach to synthesize GaN nanowires doped with Mg (Figure 2.1). GaN nanowires are unintentionally doped n-type through the growth process, therefore it is somewhat difficult to dope the nanowires p-type. This

was the first successful attempt to accomplish this feat. A boat containing magnesium nitride (Mg_3N_2) was placed upstream of a boat containing Ga metal in order to dope the nanowires p-type. The distance between these two boats was varied in order to control the dopant incorporation. A c-plane substrate coated with Ni as a catalyst was placed downstream of the boats containing the Ga and Mg sources. Two terminal resistance measurements found the resistance to increase as the separation, d , between the two boats decreased. When the boat containing magnesium nitride was placed 1-4 inches from the Ga boat, the wires were p-type; however, when the boat was placed further away, the nanowires were n-type. This was attributed to the presence of nitrogen vacancies and oxygen impurities.

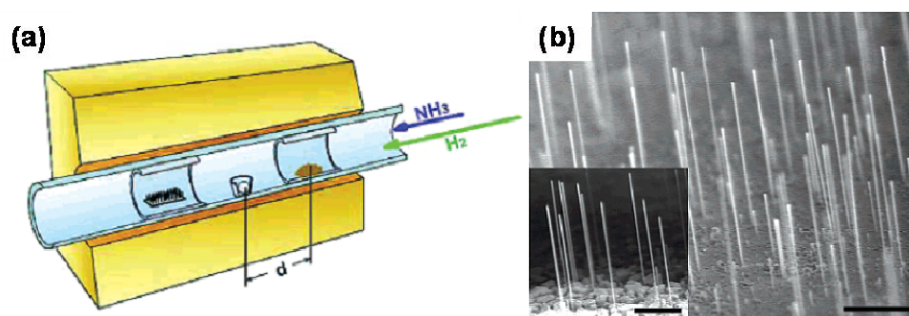


Figure 2.1: (a) Diagram for system set-up for vapor transport with Mg_3N_2 located upstream of the Ga metal source and c-plane sapphire substrate located downstream of Ga metal (b) FESEM image of p-type GaN nanowires grown on c-plane sapphire, 10 μm scale bar.²¹

In the next study, He *et al.*²² were able to eliminate the need for a catalyst through the direct reaction of Ga metal and NH_3 . Pure Ga metal was placed in a boron nitride boat and was placed at the bottom of a quartz liner. Growth was carried out at a pressure of 15 Torr without a carrier gas over a temperature range of 800-1000°C. The initial growth consisted of an amorphous GaN matrix and thin platelets. Eventually, nanowires

and nanorods began to grow from the sides of the platelets. The diameter of these nanowires could be controlled by the temperature and NH_3 flowrate. Higher temperatures and NH_3 flowrates led to thicker platelets, and the nanowire diameter was determined by the thickness of these platelets. Therefore, increasing the temperature and NH_3 flowrate produced nanowires with larger diameters. The nanowires were determined to primarily grow along the $[2\bar{1}\bar{1}0]$ direction.

Zhang *et al.*²³ extended the scope of the vapor transport studies by investigating the use of a variety of catalysts for the growth of GaN nanowires. Attempts were made to grow nanowires with In, Fe, Ni, and Au. GaN growth occurred using In, Fe, and Ni, however GaN growth with Au as the catalyst was unsuccessful. There are conflicting reports in the literature as to the ability to grow GaN nanowires using Au.²³⁻²⁶ Nitrogen is known to have a low solubility in Au.²⁷ As a result, N atoms may not be transported efficiently to the liquid/solid interface of the nanowires. This study displayed the ability to grow GaN nanowires using multiple catalysts as long as a liquid alloy could form between Ga and the respective metal.

The final study which will be discussed involved the ability to grow GaN nanowires epitaxially on various surfaces. Kim *et al.*²⁸ carried out a study involving the growth of GaN nanowires on “spontaneously roughened” GaN templates and epitaxial lateral overgrowth (ELO) stripes. In both cases, the GaN templates and ELO stripes were grown in a commercial horizontal MOCVD reactor. The roughened GaN templates were created by growing GaN films at non-optimum conditions or by terminating the growth before the films could fully coalesce. The ELO stripes, on the other hand, were selectively grown using a SiO_2 mask. After the samples were prepared, a Ni layer was

deposited on these structures using e-beam evaporation. The samples were then transported to a hot-wall tube furnace reactor where growth proceeded with Ga metal and NH_3 as the sources over a temperature range of 850-950°C. When the samples were grown on the roughened GaN templates, nanowires were observed to grow in the $[10\bar{1}0]$ direction from m-plane facets and c-plane mesa surfaces (Figure 2.2 (a)). The density of nanowire growth was found to increase with increasing temperature. The nanowires were believed to grow on the m-plane facets as it is the low energy planes for this system. At higher temperatures, the nanowires are able to grow on c-plane surfaces as the increased temperature allows the growth to overcome the higher surface energy of the c-plane surfaces. In a separate experiment, an attempt was made to grow GaN nanowires on a-axis and c-axis ELO stripes. In this case, the nanowires were found to grow perpendicular to the surface in the a-axis stripes (Figure 2.2 (b)) and at angles of 60° and 120° on m-axis stripes (Figure 2.2 (c)).

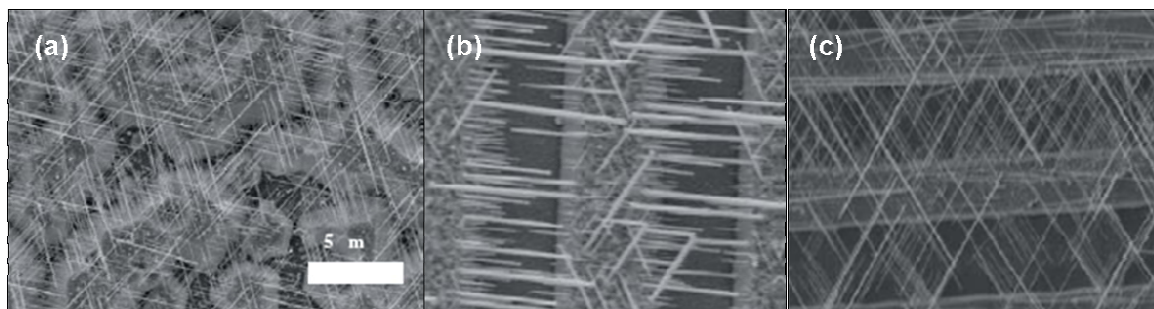


Figure 2.2: SEM images of GaN nanowires grown on (a) roughened GaN template at 900°C, (b) a-axis ELO stripes, and (c) m-axis ELO stripes.²⁸

Vapor transport is a popular approach for the synthesis of GaN nanowires due to its simplicity. Small diameter nanowires have been grown using this technique. Vapor transport has been useful in studying the properties of GaN nanowires and understanding

the VLS growth mechanism. A multitude of metal catalysts have been investigated due to the success of VLS growth in this field. At the same time, strides have been made to eliminate the need for a catalyst, since it can potentially incorporate into the nanowire during growth. Over time, better control of the growth direction and doping has been achieved, however issues still remain. In particular, there still remains a limited ability to control the gas phase precursor concentrations which is critical to doping of the material for device applications.

2.4 MBE

Molecular beam epitaxy (MBE) is a technique that has primarily been used for the deposition of high quality thin films. However, it has gained interest in the nanowire field because of the ability to grow nanowires without the use of a catalyst or lithography. Being able to eliminate the use of a catalyst could prove beneficial, since the catalyst has been shown to incorporate into the nanowire during growth for various systems.²⁹⁻³¹ This, in turn, leads to termination of growth and the addition of impurities to the crystalline nanowire structure. Research in the area of MBE growth of GaN nanowires and nanorods has focused on the growth of GaN on silicon and sapphire substrates with and without the use of an AlN buffer layer.^{32,33}

Due to difficulties involved in the growth of GaN nanowires on sapphire and silicon, early studies focused at the use of an AlN buffer layer for MBE growth of GaN nanowires. In particular, early attempts to grow directly on the substrate led to either the formation of an amorphous layer on the surface of the substrate³⁴ or nanowire growth that

was not perpendicular to the substrate.³⁵ AlN buffer layers are typically employed for the growth of GaN thin films when using substrates with large lattice mismatches to reduce the formation of dislocations and other defects. This same technique was utilized by Sanford *et al.*³⁶ in order to grow GaN nanorods and nanowires using plasma-assisted molecular beam epitaxy (PAMBE). In preliminary studies, a thin AlN buffer layer was deposited directly on c-plane sapphire or Si (111) substrates to reduce the lattice mismatch in order to minimize the presence of defects at the base of the GaN nanorods and nanowires. In later studies, a layer of pure Al was deposited before the deposition of the AlN buffer layer.³⁷ The Ga and atomic nitrogen were found to react at the substrate at a temperature of 810-830°C to form an irregular matrix layer and GaN nanorod/nanowire growth. The irregular matrix layer was observed to have deep holes with faceted sides. The wires protrude from the matrix layer along the c-axis with a hexagonal cross-section and appear to inhibit growth of the matrix in the surrounding area of the wire. An example of the resulting growth is shown in Figure 2.3.

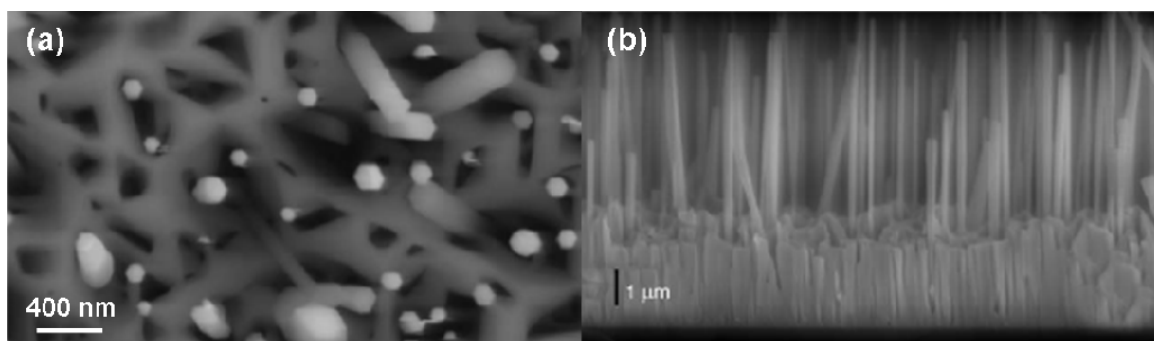


Figure 2.3: FESEM images of (a) top view and (b) cross-section view of irregular matrix layer and protruding GaN nanowires on silicon using MBE.³⁷

Additional studies were completed by Bertness *et al.* in order to gain a better understanding of the mechanism responsible for the nucleation and growth of GaN nanowires.^{34,38} For these experiments, the GaN nanowires were synthesized over a temperature range of 800-840°C on Si (111) and Si (100) substrates. From these studies, the matrix layer was found to consist of small, dense hexagonal pits that are formed by intersecting {1012} planes. The nanowires were observed to nucleate from the center of these hexagonal pits after the formation of a seed crystal. The nanowire growth was believed to proceed due to a difference in sticking coefficients for Ga atoms on the nanowire tip (c-axis) compared to the m-plane sidewalls. As a result, atoms that absorb on the tip or within a surface diffusion length of the tip incorporate into the nanowire, whereas atoms that are further away tend to desorb due to the high growth temperatures.

The other possibility is that the nanowire growth proceeded by a self-catalytic process where the tip consisted of Ga droplets. This hypothesis was tested by altering the procedure for cooling down after growth.³⁸ When a Ga flux was maintained while cooling down to 300°C, the continued growth was found to overcoat the sidewalls of the nanowires. When the sample was cooled down under a Ga flux without the addition of an N₂ plasma, a slight bulge at the tips was observed due to decomposition of the crystal. In both cases, Ga was not the dominant factor contributing to the growth of GaN nanowires. Atomic nitrogen was actually found to have a greater affect on the successful synthesis of GaN nanowires using MBE. Increasing the V/III ratio or power of the plasma led to an increase in the nucleation density of nanowires.³⁴ The importance of atomic nitrogen was confirmed when the N₂ plasma was replaced with NH₃. This action led to a high density of hexagonal pits but a lack of nanowire growth. Finally, the

importance of the AlN buffer layer as a template for growth was reinforced by MBE growth of GaN nanowires on Si (100) substrates. Even though the orientation of the substrate changed, the nanowires were still found to grow along the c-axis.

Park *et al.*, on the other hand, was able to overcome the issues with growing GaN nanowires/nanorods directly on Si (111) substrates using PAMBE.³⁹ In the study, Park *et al.* looked at the evolution of nanorod formation. The samples were grown at a temperature of 800°C, and the V/III ratio was varied by adjusting the Ga flux. Initiating the growth in N-rich conditions led to the formation of epitaxial columnar morphologies with an average diameter of 30 nm. The columns continued to grow until they reached approximately 400 nm in diameter. At this point, hexagonal nanorods were observed to grow from the columnar structures (Figure 2.4 (a)). A high density of stacking faults and dislocations were observed in the columnar bases, however the defects did not extend to the hexagonal nanorods. When the initial layer was grown at a V/III ratio of 1 or in Ga-rich conditions, the columnar structure became more compact (Figure 2.4 (b)). It was believed that by going to Ga-rich conditions, nitrogen had less of an effect on the surface diffusion of Ga adatoms. Photoluminescence spectra were obtained for these nanorods, a strong emission was observed at 3.47 eV. There was also a broad emission at 3.41 eV.

Meijers *et al.* also investigated the growth of GaN nanowires without the use of a AlN buffer layer.⁴⁰⁻⁴³ The nanowires were grown over a temperature range of 770-810°C at various V/III ratios using Si (111) and thermally oxidized Si (100) substrates. During the initial stages, growth proceeds in N-rich conditions in order to form an amorphous silicon nitride (SiN_x) layer by nitridation of the Si substrate.⁴⁰ After the SiN_x layer forms, a thin GaN “wetting” layer was observed to deposit on top of the amorphous silicon

nitride. GaN clusters grow on the “wetting” layer which led to nanowire formation that grew primarily along the c-axis. GaN nanowires also grew tilted with respect to the substrate, and this was attributed to step bunches on the surface and the non-uniform amorphous layer. The nanowires were found to be typically in the range of 10-15 nm in diameter. The tapering and coalescence of the nanowires could be varied based on the V/III ratio.⁴¹ When a high Ga flux was utilized, the nanowires were found to broaden and coalesce. As the Ga flux was lowered, the tapering and enlargement of the nanowires were eliminated.

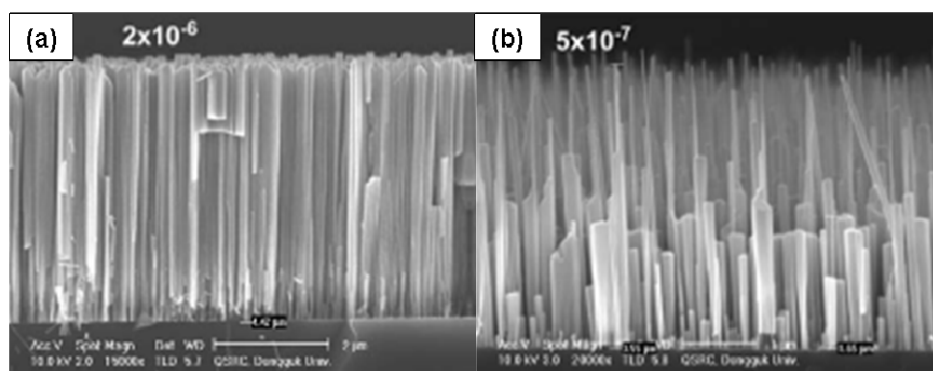


Figure 2.4: FESEM cross-sections of GaN nanorods grown in (a) Ga-rich and (b) N-rich conditions.³⁹

Molecular beam epitaxy has been utilized to grow high quality GaN nanorods without the use of a catalyst. As a result, issues concerning the possible incorporation of the metal catalyst in nanowire growth are eliminated. Even without the use of a catalyst, the ability to grow GaN nanorods with specific diameters and lengths using MBE was demonstrated by varying the growth conditions. Low throughput and high costs, however, still remain as issues associated with MBE growth of GaN.

2.5 MOCVD

Metal organic chemical vapor deposition (MOCVD) is one of the more modern techniques that have been utilized for the growth of GaN nanowires. MOCVD is well-known for its ability to grow high quality GaN thin films. It is commercially used because of the ability to grow thin films on large substrates, its high throughput, and the ability to grow AlGaN/GaN and InGaN/GaN heterostructures using TMAI and TMIIn. As a result, MOCVD is an ideal growth technique for the synthesis of GaN nanowires. The first successful attempt at growing GaN nanowires using metalorganic precursors was completed in 2003.²⁴ Since then, a number of studies have been performed in the area of MOCVD of GaN nanowires.⁴⁴⁻⁵¹ This section will step through the advancements in this field from the first study involving the use of a hot-wall reactor to epitaxial growth of GaN nanowires and the formation of radial heterostructures.

Kuykendall *et al.*²⁴ were responsible for the first successful attempt at growing GaN nanowires using MOCVD. A hot-wall reactor with a coaxial tube set-up was used for growth, and TMG and NH₃ were the Ga and N sources. Ni, Au, and Fe thin films were deposited on Si, c-plane sapphire, and a-plane sapphire. Growth occurred over a temperature range of 800-1000°C at atmospheric pressure. N₂ was the carrier gas for TMG, whereas H₂ was the carrier gas for NH₃. Nanowires grown on c-plane sapphire possessed triangular cross-sections with a spherical metal droplet at their tips (Figure 2.5 (a)). X-ray diffraction (XRD) confirmed that the nanowires were of the wurtzite crystal structure. One interesting observation from the study was that the nanowires possessed a $[10\bar{1}0]$ growth direction when Au or Ni was used as the catalyst, however the growth

direction changed to $[11\bar{2}0]$ when Fe was employed as the catalyst. No real explanation was given for this occurrence. Photoluminescence studies were also performed on these nanowires at various temperatures. The peak position at 5K was located at 370 nm (3.35 eV), while the peak position shifted to 380 nm (3.26 eV) at 285K.

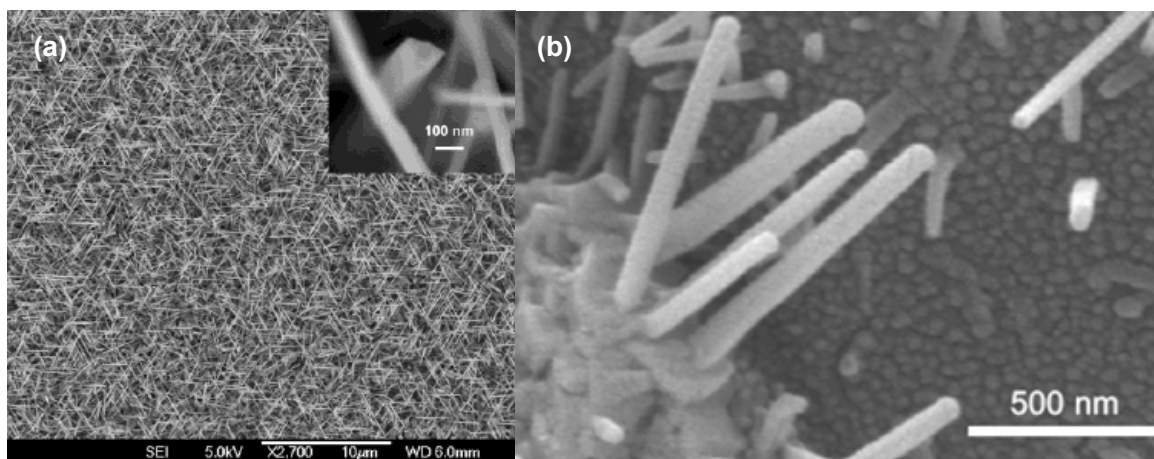


Figure 2.5: GaN nanowires grown by (a) hot-wall and (b) cold-wall MOCVD on Au-coated c-plane sapphire and alumina substrates, respectively.^{24,52}

Su *et al.*,^{52,53} on the other hand, utilized a conventional cold-wall reactor for synthesis of GaN nanowires. Sapphire, alumina, and SiO₂ dipped in 0.01M Ni(NO₃)₂ were utilized for these experiments. In this study, Su *et al.* investigated the effect of NH₃ flowrate on the growth of GaN nanowires. Utilizing a flowrate of 10 sccm NH₃ resulted in large Ga droplets with conical-shaped GaN tails due to an insufficient supply of nitrogen. At an intermediate flowrate, the resulting morphology was GaN nanorods that were 0.5 μm in length and 100 nm in diameter. The nanowires were found to taper as growth proceeded, and this action was attributed to a gradual solidification and shrinkage of the Ga droplets as growth proceeded. Under high NH₃ flowrates, faceted GaN crystallites formed and nanowire growth ceased. Based on these experiments, the ideal

NH_3 flowrate was determined to be 20 sccm. In an attempt to expand the range of V/III ratios applicable for GaN nanowire growth and resolve the tapering issue, In was introduced into the system in the form of TMIIn. In acted as a surfactant and promoted GaN nanowire growth over a wider range of V/III ratios. An example of GaN nanowire grown on alumina substrates with the addition of TMIIn is shown in Figure 2.5 (b). The nanowires in this case were on average 90 nm in diameter and 1-2 μm in length.

A typical problem with GaN nanowire growth is the presence of multiple growth directions for a given sample. The optical and electrical properties have been shown to vary depending on the growth direction. As a result, there has been a drive to control the orientation of the nanowire growth. This can be achieved through epitaxial growth of the GaN nanowires. In any attempt to grow GaN nanowires epitaxially, it is important to choose a substrate that is a close match in symmetry and lattice constant to that of GaN. GaN consists of the hexagonal close-packed crystal structure (HCP). In this structure, the upper and lower surfaces are hexagons, and the side faces are rectangles. Figure 2.6 (a) shows some of the common crystallographic planes that are relevant to growth of GaN nanowires, whereas Figure 2.6 (b) shows the wurtzite crystal structure for GaN.

Typically for growth of GaN nanowires on c-plane sapphire, multiple growth directions are observed and epitaxial growth has not been achieved; however, the possibility does exist to grow GaN nanowires epitaxially on r-plane sapphire due to the commonly observed $[11\bar{2}0]$ growth direction for GaN nanowires. Wang *et al.* was able to take advantage of this growth direction and grow GaN nanowires epitaxially on r-plane sapphire using a nickel nitrate solution ($\text{Ni}(\text{NO}_3)_2 \cdot 6\text{H}_2\text{O}$) to apply the catalyst.⁵⁴ Epitaxial growth of GaN nanowires was observed at low nickel nitrate concentrations and

approximately 85% of the nanowires surveyed by TEM were found to grow in the $[11\bar{2}0]$ direction while the remainder grew along the $[10\bar{1}0]$ growth direction. The nanowires were tapered with triangular cross-sections due to competing thin film deposition on the sidewalls of the wires. It was determined that Ni was important to the growth of GaN nanowires as no growth was observed in sections where the nickel nitrate solution was not applied.

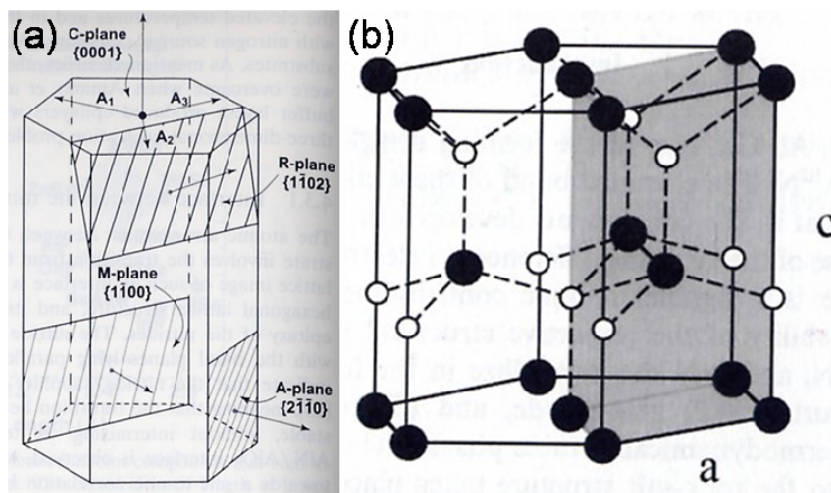


Figure 2.6: (a) Sapphire planes used in epitaxy of GaN and (b) wurtzite crystal structure: Ga atoms are black and N atoms are white.^{55,56}

Kuykendall *et al.*, on the other hand, were able to control the growth direction by using an alternative to the typical sapphire substrate.⁵⁷ In this case, Au-coated (100) γ -LiAlO₂ and (111) MgO single crystal substrates were utilized for epitaxial growth. GaN nanowire growth on (100) γ -LiAlO₂ resulted in epitaxial growth of GaN with a triangular cross-section and a $[1\bar{1}00]$ growth orientation. For growth on (111) MgO, a hexagonal cross-section was observed with a $[0001]$ growth direction. Kuykendall *et al.* was also able to show the effect that growth direction has on the optical properties of GaN

nanowires. A significant blue-shifted emission in photoluminescence measurements was observed for epitaxial wires grown along the $[1\bar{1}00]$ direction with respect to wires grown along the $[0001]$. The blue-shifted photoluminescence was believed to be due to either polarity effects (polar vs. non-polar), differences in tensile stress, or defects associated with each growth direction.

Han *et al.*⁵⁸ investigated the use of AlN as a suitable substrate for epitaxial growth. Initial growth studies involving the use of alumina, sapphire, and silicon dioxide substrates indicated that a majority of the nanowires grew along the $[10\bar{1}0]$ (m-axis) growth direction and a small fraction grew along the $[11\bar{2}0]$ (a-axis) growth direction. As a result of these studies, Han *et al.* used a-, c-, and m-plane AlN substrates for epitaxial growth of GaN nanowires. Growth on c-plane AlN resulted in growth along the surface. Growth on a-plane AlN produced nanowires growing along both the a- and m-axis. Growth on m-plane AlN resulted in approximately 90% of the growth being epitaxial. The high degree of epitaxial growth on the m-plane AlN substrate was expected based on the initial results on alumina, sapphire, and silicon dioxide.

Another issue concerning the growth of GaN nanowires is the use of a metal catalyst. As was discussed in the MBE section, catalysts can potentially contaminate the nanowires due to incorporation during growth. As a result, attempts have been made to eliminate the catalyst. Deb *et al.* was able to successfully grow GaN nanorods without a catalyst by using a silicon dioxide (SiO_x) template.⁵⁹ An Al film was anodized to create a porous template for the GaN nanorod growth. The pattern was transferred to the SiO_x layer via reactive ion etching, and the porous aluminum oxide template was removed by

wet etching. The diameter of the pores was tunable in the range of 50-200 nm. A silicon dioxide template was utilized, since GaN does not have a tendency to nucleate on it, therefore allowing selective growth only in the exposed regions of the GaN film. The GaN nanorods were grown at a V/III ratio of 1500 and a temperature of 1020°C for 5 minutes. After the growth, the SiO_x template was removed with a buffered oxide etch. FESEM analysis showed that the nanorods possessed a pyramidal cap, and growth proceeded in a lateral direction when the nanorods emerged from the template (Figure 2.7 (a)). TEM analysis, on the other hand, showed that the nanorods were free of dislocations. In this study, the nanorod length was limited by the thickness of the silicon dioxide layer in order to prevent the lateral growth as the nanorods emerged from the template.

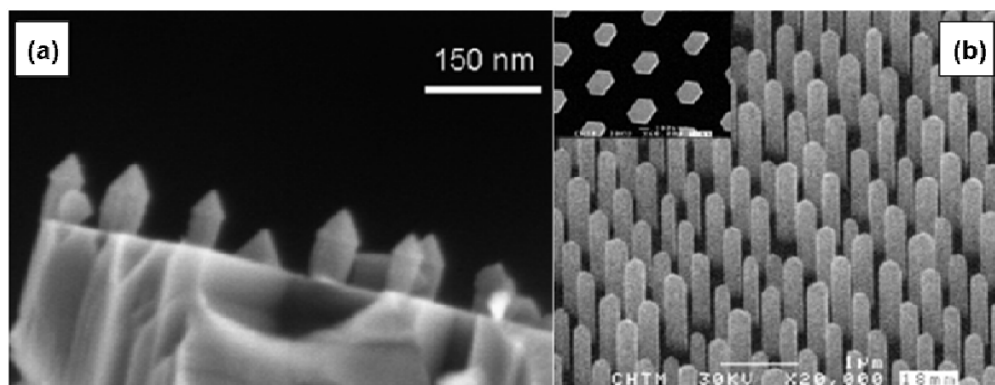


Figure 2.7: (a) FESEM image of GaN nanorods displaying the faceting of the cap. (b) SEM image of GaN nanowire array using a silicon nitride template.^{59,60}

Hersee *et al.*⁶⁰ were able to overcome this issue by using a pulsed MOCVD technique. This technique was first applied by Kipshidze *et al.* for the synthesis of GaN nanowires using Ni as a catalyst.⁶¹ When using this technique, TMG and NH₃ are introduced alternately in a sequence in order to suppress the gas phase reactions and limit

lateral growth. Hersee *et al.* employed pulsed MOCVD to grow GaN nanowires from a silicon nitride (SiN_x) template. During the first growth stage, a high V/III ratio of 1500 was employed to ensure nucleation in all of the apertures. After this was achieved, the precursors were flown into the reactor alternately in a certain sequence. After growth, the silicon nitride layer was removed, and the samples were analyzed by SEM (Figure 2.7 (b)). During TEM analysis, the growth direction was found to be along the c-axis, and the top of the nanowire was observed to have a small, central (0001) facet which was bound by inclined $\{1102\}$ facets. The nanowires did not have any threading dislocations, and the diameter remained constant as the nanowire emerged from the SiN_x template. The author believed that the lower V/III ratio utilized for the pulsed portion of growth promoted axial growth over lateral growth.

The previous study showed how the MOCVD process could be manipulated to successfully grow GaN nanowires without the use of a catalyst. One of the main reasons why MOCVD is of immense interest is its versatility. Qian *et al.*⁶² exemplified this versatility through the growth of radial heterostructures. A core/shell/shell (CSS) nanowire heterostructure was synthesized consisting of n-GaN/InGaN/p-GaN. Qian *et al.* were able to alter the conditions to favor shell growth versus axial growth. The n-type GaN core was grown using TMG, NH_3 , and silane as the n-type dopant. The conditions were then altered to grow an InGaN shell with TMG, TMIIn, and NH_3 . Finally, the outer shell was grown using biscyclopentadienylmagnesium as the p-type dopant. The nanowire growth resulted in a triangular cross-section and the catalytic particle determined the size of the n-GaN core. PL measurements of an n-GaN wire displayed a sharp peak at 367 nm corresponding to band-edge emission. The CSS heterostructure

produced a sharp peak at 448 nm corresponding to the band-edge emission of InGaN. A band-edge emission for GaN was also observed, however it was roughly 20 times smaller than the band-edge emission for InGaN. Qian *et al.* was also able to extend this procedure for the synthesis of core/multishell nanowires consisting of an n-GaN core with an $\text{In}_x\text{Ga}_{1-x}\text{N}/\text{GaN}/\text{p-AlGaN}/\text{p-GaN}$ shell⁶³ and a dopant free GaN/AlN/AlGaN radial nanowire heterostructure.⁶⁴

MOCVD has been investigated extensively for the growth of GaN thin films, however it is still a relatively new technique for the synthesis of GaN nanowires. GaN nanowires have been successfully grown in hot-wall and cold-wall reactors using various substrates and metal catalysts. GaN nanowires have also been grown epitaxially by choosing a proper substrate. Epitaxial growth is of great importance for device applications. In recent years, it has been shown that GaN nanowires can be grown epitaxially without the use of a catalyst by implementing a patterned substrate. Core/shell nanowire heterostructures have been synthesized, demonstrating the ability to integrate thin film and nanowire MOCVD technologies. While progress has been made in the MOCVD field towards the fabrication of GaN nanowire devices, there still remains a lot to be learned. Outside Wang *et al.*⁵⁴ extensive studies determining the window of growth conditions necessary for nanowire growth and the effect of growth conditions on nanowire properties has yet to be carried out. There also remains uncertainty as to the mechanism responsible for catalyst-assisted GaN nanowire growth.

2.6 References

- 1 T. Mihopoulos, Doctor of Philosophy Thesis, Massachusetts Institute of
Technology, 1999.
- 2 T. G. Mihopoulos, V. Gupta, and K. F. Jensen, *Journal of Crystal Growth* **195**,
733-739 (1998).
- 3 A. Thon and T. F. Kuech, *Applied Physics Letters* **69**, 55-57 (1996).
- 4 J. Sun, J. M. Redwing, and T. F. Kuech, *Physica Status Solidi B* **176**, 693-698
(1999).
- 5 S. A. Safvi, J. M. Redwing, M. A. Tischler, and T. F. Kuech, *Journal of the
Electrochemical Society* **144**, 1789-1796 (1997).
- 6 M. J. Almond, M. G. B. Drew, C. E. Jenkins, and D. A. Rice, *Journal of Chemical
Society - Dalton Transactions*, 5-9 (1992).
- 7 J. Sun, J. M. Redwing, and T. F. Kuech, *Journal of Electronic Materials* **29**, 2-9
(2000).
- 8 D. Sengupta, *Journal of Physical Chemistry B* **107**, 291-297 (2003).
- 9 J. R. Creighton, G. T. Wang, W. G. Breiland, and M. E. Coltrin, *Journal of
Crystal Growth* **261**, 204-213 (2004).
- 10 J. R. Creighton and G. T. Wang, *Journal of Physical Chemistry A* **109**, 10554-
10562 (2005).
- 11 X. M. Cai, A. B. Djuricic, and M. H. Xie, *Thin Solid Films* **515**, 984-989 (2006).
- 12 C.-C. Chen, C.-C. Yeh, C.-H. Chen, M.-Y. Yu, H.-L. Liu, J.-J. Wu, K.-H. Chen,
L.-C. Chen, J.-Y. Peng, and Y.-F. Chen, *Journal of the American Chemical
Society* **123**, 2791-2798 (2001).
- 13 P. V. Radovanovic, C. J. Barrelet, S. Gradecak, F. Qian, and C. M. Lieber, *Nano
Letters* **5**, 1407-1411 (2005).
- 14 X. Chen, S. J. Lee, and M. Moskovits, *Applied Physics Letters* **91**, 082109-1-3
(2007).
- 15 J. Liu, X.-M. Meng, C.-S. Lee, I. Bello, and S.-T. Lee, *Applied Physics Letters*
83, 4241-4243 (2003).
- 16 E. Cimpoiasu, E. Stern, R. Klie, R. A. Munden, G. Cheng, and M. A. Reed,
Nanotechnology **17**, 5735-5739 (2006).
- 17 S. Y. Bae, H. W. Seo, D. S. Han, M. S. Park, W. S. Jang, C. W. Na, J. Park, and
C. S. Park, *Journal of Crystal Growth* **258**, 296-301 (2003).
- 18 Y. N. Xia, P. D. Yang, Y. G. Sun, Y. Y. Wu, B. Mayers, B. Gates, Y. D. Yin, F.
Kim, and Y. Q. Yan, *Advanced Materials* **15**, 353-389 (2003).
- 19 T. Y. Kim, C.-S. Lee, Y. H. Mo, H. W. Shim, K. S. Nahm, E.-K. Suh, J. W. Yang,
K. Y. Lim, and C. S. Park, *Journal of Crystal Growth* **257**, 97-103 (2004).
- 20 S. Y. Bae, H. W. Seo, J. Park, H. N. Yang, H. Kim, and S. Kim, *Applied Physics
Letters* **82**, 4564-4566 (2003).
- 21 Z. H. Zhong, F. Qian, D. L. Wang, and C. M. Lieber, *Nano Letters* **3**, 343-346
(2003).

- 22 M. Q. He, P. Z. Zhou, S. N. Mohammad, G. L. Harris, J. B. Halpern, R. Jacobs,
W. L. Sarney, and L. Salamanca-Riba, *Journal of Crystal Growth* **231**, 357-365
(2001).
- 23 J. Zhang and L. D. Zhang, *Journal of Vacuum Science & Technology B* **21**, 2415-
2419 (2003).
- 24 T. Kuykendall, P. Pauzauskie, S. K. Lee, Y. F. Zhang, J. Goldberger, and P. D.
Yang, *Nano Letters* **3**, 1063-1066 (2003).
- 25 D. K. T. Ng, L. S. Tan, and M. H. Hong, *Current Applied Physics* **6**, 403-406
(2006).
- 26 C.-C. Chen and C.-C. Yeh, *Advanced Materials* **12**, 738-741 (2000).
- 27 *Phase Diagrams of Binary Nickel Alloys; Vol. 6*, edited by P. Nash (ASM
International, Materials Park, 1991).
- 28 K. Kim, T. Henry, G. Cui, J. Han, Y.-K. Song, A. V. Nurmikko, and H. Tang,
Physica Status Solidi (b) **244**, 1810-1814 (2007).
- 29 J. B. Hannon, S. Kodambaka, F. M. Ross, and R. M. Tromp, *Nature* **440**, 69-71
(2006).
- 30 J. E. Allen, E. R. Hemesath, D. E. Perea, J. L. Lensch-Falk, Z. Y. Li, F. Yin, M.
H. Gass, P. Wang, A. L. Bleloch, R. E. Palmer, and L. J. Lauhon, *Nature* **3**, 168-
173 (2008).
- 31 M. I. den Hertog, J.-L. Rouviere, F. Dhalluin, J. Desre, P. Gentile, P. Ferret, F.
Oehler, and T. Baron, *Nano Letters* **8**, 1544-1550 (2008).
- 32 L. H. Robins, K. A. Bertness, J. M. Barker, N. A. Sanford, and J. B. Schlager,
Journal of Applied Physics **101**, 113505-1-8 (2007).
- 33 R. Calarco and M. Marso, *Applied Physics A* **87**, 499-503 (2007).
- 34 K. A. Bertness, A. Roshko, L. M. Mansfield, T. E. Harvey, and N. A. Sanford,
Journal of Crystal Growth **300**, 94-99 (2007).
- 35 R. Songmuang, O. Landre, and B. Daudin, *Applied Physics Letters* **91**, 251902-1-
3 (2007).
- 36 N. A. Sanford, L. H. Robins, M. H. Gray, J. E. Van Nostrand, C. Stutz, R. Cortez,
A. V. Davydov, A. Shapiro, I. Levin, and A. Roshko, *Physica Status Solidi C* **7**,
2357-60 (2003).
- 37 K. A. Bertness, A. Roshko, N. A. Sanford, J. M. Barker, and A. Davydov, *Journal*
of Crystal Growth **287**, 522-527 (2006).
- 38 K. A. Bertness, A. Roshko, L. M. Mansfield, T. E. Harvey, and N. A. Sanford,
Journal of Crystal Growth **310**, 3154-3158 (2008).
- 39 Y. S. Park, S. H. Lee, J. E. Oh, C. M. Park, and T. W. Kang, *Journal of Crystal*
Growth **282**, 313-319 (2005).
- 40 T. Stoica, E. Sutter, R. J. Meijers, R. K. Debnath, R. Calarco, H. Luth, and D.
Grutzmacher, *Small* **4**, 751-754 (2008).
- 41 R. J. Meijers, T. Richter, R. Calarco, T. Stoica, H.-P. Bochem, M. Marso, and H.
Luth, *Journal of Crystal Growth* **289**, 381-386 (2006).
- 42 R. Calarco, R. J. Meijers, R. K. Debnath, T. Stoica, E. Sutter, and H. Luth, *Nano*
Letters **7**, 2248-2251 (2007).
- 43 R. K. Debnath, R. J. Meijers, T. Richter, T. Stoica, R. Calarco, and H. Luth,
Applied Physics Letters **90**, 123117-1-3 (2007).

- 44 J. Su, M. Gherasimova, G. Cui, H. Tsukamoto, J. Han, T. Onuma, M. Kurimoto,
S. F. Chichibu, C. Broadbridge, Y. He, and A. V. Numikko, *Applied Physics
Letters* **87**, 183108 (2005).
- 45 S. Gradecak, F. Qian, Y. Li, H.-G. Park, and C. M. Lieber, *Applied Physics
Letters* **87**, 173111 (2005).
- 46 H. S. Jung, Y. J. Hong, Y. Li, J. Cho, Y.-J. Kim, and G.-C. Yi, *ACS Nano* **2**, 637-
642 (2008).
- 47 J. Yoo, Y. J. Hong, S. J. An, G.-C. Yi, B. Chon, T. Joo, J.-W. Kim, and J.-S. Lee,
Applied Physics Letters **89**, 043124 (2006).
- 48 J. Khanderi, A. Wohlfart, H. Parala, A. Devi, J. Hambrock, A. Birkner, and R. A.
Fishcer, *Journal of Materials Chemistry* **13**, 1438-1446 (2003).
- 49 Y. Inoue, A. Tajima, A. Ishida, and H. Mimura, *Physica Status Solidi C* **5**, 3001-
3003 (2008).
- 50 Y. Inoue, A. Tajima, S. Takeda, A. Ishida, H. Mimura, and S. Sakakibara, *Physica
Status Solidi C* **4**, 2366-2370 (2007).
- 51 S.-K. Lee, H.-J. Choi, P. Pauzauskie, P. Yang, N.-K. Cho, H.-D. park, E.-K. Suh,
K. Y. Lim, and H.-J. Lee, *Physica Status Solidi B* **241**, 2775-2778 (2004).
- 52 M. Gherasimova, J. Su, G. Cui, Z.-Y. Ren, S.-R. Jeon, J. Han, Y. He, Y.-K. Song,
A. V. Nurmikko, D. Ciuparu, and L. Pfefferle, *Physica Status Solidi C* **2**, 2361-
2364 (2005).
- 53 J. Su, G. Cui, M. Gherasimova, H. Tsukamoto, J. Han, D. Ciuparu, S. Lim, L.
Pfefferle, Y. He, A. V. Nurmikko, C. Broadbridge, and A. Lehman, *Applied
Physics Letters* **86**, 013105 (2005).
- 54 G. T. Wang, A. A. Talin, D. J. Werder, J. R. Creighton, E. Lai, R. J. Anderson,
and I. Arslan, *Nanotechnology* **17**, 5773-5780 (2006).
- 55 *Group III Nitride Semiconductor Compounds: Physics and Applications; Vol.*,
edited by B. Gil (Oxford University Press, New York, 1998).
- 56 *Gallium Nitride (GaN) I; Vol. 50*, edited by J. I. Pankove and T. D. Moustakas
(Academic Press, New York, 1998).
- 57 T. Kuykendall, P. J. Pauzauskie, Y. F. Zhang, J. Goldberger, D. Sirbuly, J.
Denlinger, and P. D. Yang, *Nature Materials* **3**, 524-528 (2004).
- 58 J. Han, K. Kim, J. Su, M. Gherasimova, A. V. Nurmikko, S. F. Chichibu, and C.
Broadbridge, in *MOCVD Growth and Characterization of AlGaInN Nanowires
and Nanostructures*, Boston, MA, 2006 (Materials Research Society), p. 0892-
FF31-01.1-10.
- 59 P. Deb, H. Kim, V. Rawat, M. Oliver, S. Kim, M. Marshall, E. Stach, and T.
Sands, *Nano Letters* **5**, 1847-1851 (2005).
- 60 S. D. Hersee, X. Sun, and X. Wang, *Nano Letters* **6**, 1808-1811 (2006).
- 61 G. Kipshidze, B. Yavich, A. Chandolu, J. Yun, V. Kuryatkov, I. Ahmad, D.
Aurongzeb, M. Holtz, and H. Temkin, *Applied Physics Letters* **86**, 033104
(2005).
- 62 F. Qian, Y. Li, S. Gradecak, D. L. Wang, C. J. Barrelet, and C. M. Lieber, *Nano
Letters* **4**, 1975-1979 (2004).
- 63 F. Qian, S. Gradecak, Y. Li, C. Y. Wen, and C. M. Lieber, *Nano Letters* **5**, 2287-
2291 (2005).

- ⁶⁴ Y. Li, J. Xiang, F. Qian, S. Gradecak, Y. Wu, H. Yan, D. A. Blom, and C. M. Lieber, *Nano Letters* **6**, 1468-1473 (2006).

Chapter 3

GaSb Nanowire Literature Review

3.1 Introduction

This chapter is focused on presenting a comprehensive review of the GaSb literature. The chapter begins by discussing the decomposition kinetics of GaSb growth using TMG and TMSb as precursors. This information will be applied in a later chapter. The chapter will progress to a discussion of the GaSb thin film literature, since there are only a limited number of studies concerning GaSb nanowire growth. The chapter will end with a discussion of the few literature reports that exist concerning GaSb nanowire growth.

3.2 Decomposition Kinetics of GaSb Growth by MOCVD

Due to the low temperatures necessary for GaSb growth, the assortment of precursors available to successfully grow GaSb is limited. Typically, trimethylgallium (TMG) and trimethylantimony (TMSb) have been employed for the synthesis of GaSb, nevertheless alternative precursors such as triethylgallium (TEG), triethylantimony (TESb), and tertiarybutyldimethylantimony (TBDMSb) have been investigated as these precursors possess lower pyrolysis temperatures.^{1,2} However, TMG and TMSb remain the popular choice of precursors for the synthesis of GaSb due to their availability and multitude of studies involving these materials.

Detailed studies of decomposition kinetics of TMG and TMSb have been performed in order to obtain a better understanding of the pyrolysis mechanisms.³⁻⁵ In a series of studies by Larsen *et al.*,^{3,4} a flow tube apparatus with a time-of-flight mass spectrometer was employed to investigate the effect of various carrier gases on the decomposition of TMG and TMSb at atmospheric pressure. The results of this study are shown in Figure 3.1. It is evident from the graphs that the choice of carrier gas has a significant effect on the decomposition of both TMG and TMSb. For the case of TMG, complete pyrolysis occurs at roughly 475°C for H₂ and at 525°C for He. Examining the graph for the pyrolysis of TMSb, complete decomposition occurs at roughly 460°C using H₂ and 550°C when using He as the carrier gas.

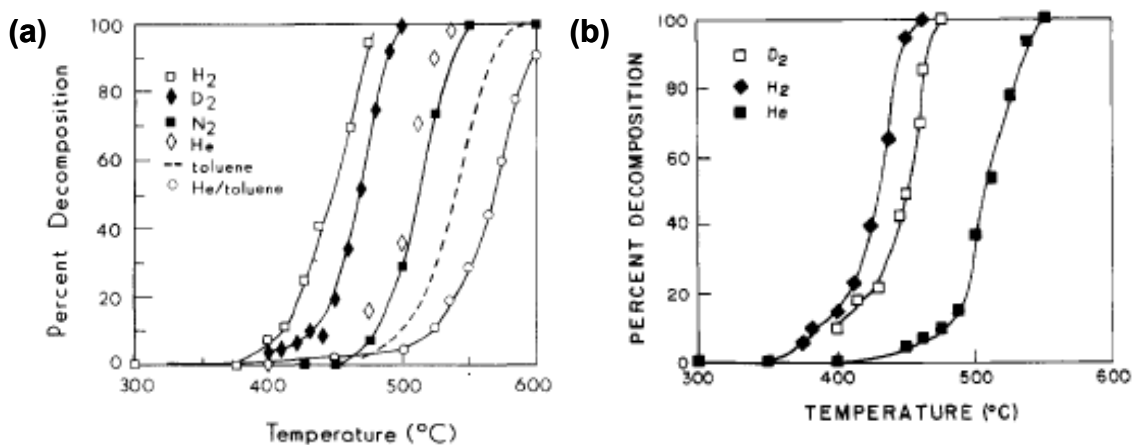


Figure 3.1: (a) Graph of % decomposition vs. temperature of TMG for various carrier gases including H₂, D₂, N₂, He, toluene, and a He/toluene mixture. (b) Graph of % decomposition vs. temperature of TMSb for carrier gases of D₂, H₂, and He. A flow tube reactor connected to a mass spectrometer was used for both studies.^{3,4}

In another study by Q. Chen *et al.*,⁵ the thermal decomposition of TMG was examined in H₂ and N₂ in a low pressure quartz tube reactor. The reactor was connected to a molecular beam sampling mass spectrometer set-up. At low pressures, TMG was

determined to be 50% pyrolysed at approximately 475°C and does not go to completion until 550°C in H₂ (Figure 3.2 (a)). The decrease in the decomposition rate can be attributed to a decrease in the frequency of collisions present at reduced pressures.⁵ H₂ has been observed to be a factor in the decomposition rate of TMG; therefore, H₂ will play a larger role at elevated pressures as more collisions will occur between TMG and H₂.

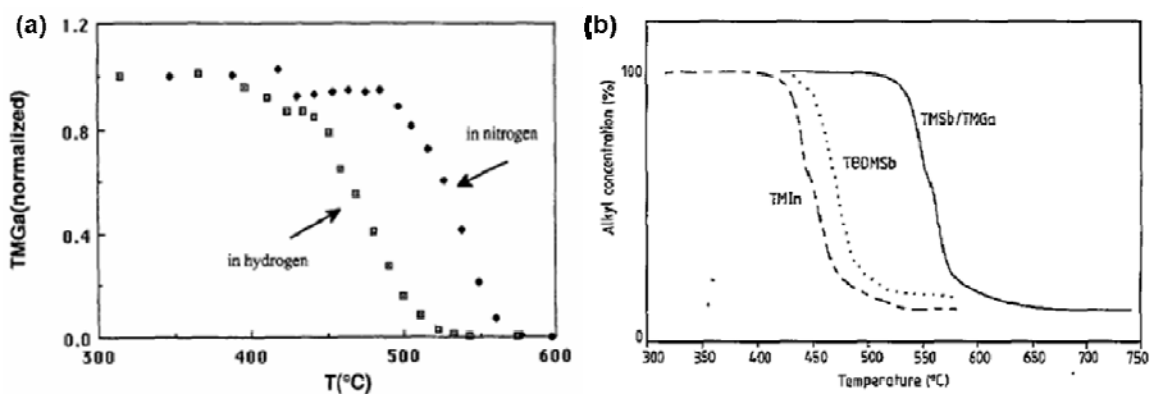


Figure 3.2: (a) Pyrolysis of TMG in H₂ and N₂ using a tube reactor attached to a molecular beam sampling mass spectrometer. (b) Decomposition of TMG and TMSb measured by ultraviolet spectroscopy in a MOVPE reactor.^{1,5}

Pressure is one factor that can play a role in altering the pyrolysis of the metalorganic precursors, nevertheless the reactor design can also contribute to changes in the decomposition characteristics. Graham *et al.* looked at the decomposition of TMG and TMSb in a resistance-heated MOCVD reactor using ultraviolet spectroscopy.¹ A resistance heater consisting of thin graphite elements encased in boron nitride was placed within the growth cell. This set-up allowed for rapid temperature changes unlike a tube furnace. In this study, TMSb was found to be 50% pyrolysed at 560°C (Figure 3.2 (b)), whereas in previous studies TMSb was found to be completely decomposed at 460°C

(Figure 3.1 (b)). The differences demonstrate how the heating mechanism and differences in the gas temperature profile can affect the decomposition rate. As a result, there are a variety of factors that can contribute to the reported values for the decomposition of TMG and TMSb. Therefore, it is necessary to account for these factors when comparing them to the GaSb nanowire results.

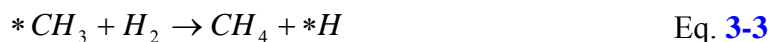
As was previously noted, a disparity in the pyrolysis kinetics has been observed based on the carrier gas of choice. Studies have been performed to investigate this effect and determine the mechanisms that are responsible for this disparity.^{6,7} The difference in the decomposition rate between N₂ and H₂ for the pyrolysis of TMG and TMSb was ascribed to a change in the primary reactions.⁶ For both N₂ and H₂, the initial reaction was found to be the homolytic fission of the first methyl group:⁸



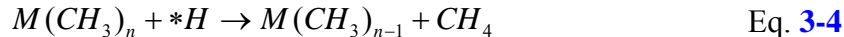
where M is representative of Ga or Sb. CH₃ radicals that were produced in Equation 3-1 contribute to the decomposition of the precursors via the following reaction:⁹



When H₂ was utilized, additional reactions were found to contribute to the pyrolysis of TMG and TMSb. CH₃ radicals react with H₂ to form H radicals:⁷



The H radicals that are produced in Equation 3-3 contribute to the eventual decomposition of TMG and TMSb into monomethyl gallium and antimony via the following reaction:⁸



Based on this reaction scheme, hydrogen is capable of accelerating the pyrolysis of TMG and TMSb unlike N₂ or He. The effectiveness of the carrier gas will also depend on the conditions that are utilized for the experiments. In particular, pressure will play an important role. As was previously mentioned, H₂ will have more interaction with the precursors at elevated pressures due to an increase in collisions between the molecules. This was observed in the decomposition studies as the precursors completely decomposed at lower temperatures at atmospheric pressure (Figure 3.1 (a)) compared to low pressure (Figure 3.2 (a)).

The choice of carrier gas is not the only factor that has been found to contribute to the decomposition of the precursors. The selection of precursors has also been found to alter the rate of pyrolysis. For the MOCVD growth of InSb, TMIn pyrolysis has been found to lead to an increase in the TMSb pyrolysis rate, however TMSb actually retards the pyrolysis of TMIn.³ TMSb and TMIn compete with one another for H radicals (Equation 3-4). The rate of reaction of H radicals with TMSb at lower temperatures is higher than TMIn, therefore decomposition of TMSb is accelerated. A similar effect is observed for the TMG/TMSb chemistry. The production of H radicals by TMG leads to an acceleration of the decomposition of TMSb, however the TMG pyrolysis rate is not affected.⁷

These findings will be utilized in Chapter 6 to gain a better understanding of the growth conditions necessary for the synthesis of GaSb nanowires. In addition, comparisons will be made to the GaSb thin film literature as some similarities will be

observed. As was previously mentioned, a variety of factors such as carrier gas, reactor design, and pressure contribute to decomposition of TMG and TMSb. This fact will be taken into consideration when discussing the nanowire results in Chapter 6.

3.3 GaSb Thin Film Growth

Due to the lack of literature concerning MOCVD growth of GaSb nanowires, a small section on GaSb thin film growth using MOCVD is included. This section will highlight the importance of the growth conditions on the structural, optical, and electrical properties of the GaSb thin films. In particular, the growth temperature and V/III ratio are critical factors in the quality of the GaSb thin films. In addition, a study will be provided that looks at the effect of alternative metalorganic precursors on the growth of GaSb.

Due to the extensive number of studies, there is a good understanding of the growth conditions that lead to high quality GaSb thin films. In general, GaSb thin films with the best morphology are grown at temperatures lower than 600°C and a V/III ratio close to unity due to the low equilibrium vapor pressure of antimony.¹⁰ When growth is carried out at V/III ratios significantly higher than unity, excess antimony that is not incorporated into the growing thin film accumulates on the surface of the thin film, leading to the formation of a secondary phase on the surface (Sb hillocks).¹¹ At the same time, for growth at V/III ratios less than unity, Ga droplets have been observed to form on the surface.¹² It should be noted, however, that the optimal range of V/III ratios is dependent on the reactor design, growth conditions, and precursors utilized. As was

shown in the previous section, these details will affect the decomposition kinetics for GaSb growth which, in turn, affects the actual V/III ratio. In a study carried out by Subeki *et al.* at atmospheric pressure and a temperature of 540°C, a V/III ratio less than 0.72 was found to lead to the formation of Ga droplets on the surface, while a V/III ratio greater than 2 resulted in microcrystalline Sb hillocks.¹¹ These values were found to shift for Koljonen *et al.* where a V/III ratio less than 1 led to Ga droplet formation and a V/III ratio greater than 1.5 led to the formation of Sb hillocks.¹³ In this case, a higher growth temperature of 600°C was utilized which led to the shift in the window of V/III ratios. In another study by Su *et al.*, the optimal V/III ratio was found to be significantly higher at 6.64 for a growth temperature of 550°C, reactor pressure of 100 Torr, and using triethylgallium (TEGa) as the Ga source instead of TMG. V/III ratios as high as 45 have been found to yield the best GaSb thin films depending on the growth conditions.¹⁰

The V/III ratio has also been found to have a significant effect on the electrical properties of MOCVD-grown GaSb thin films. GaSb is observed to be unintentionally-doped p-type due to the presence of a native defect. The native defect is believed to be a $V_{Ga}Ga_{Sb}$ centre which is caused by a deficiency of Sb in the growing thin film.^{14,15} Typical hole concentrations and mobilities for GaSb thin films are $1 \times 10^{16} \text{ cm}^{-3}$ and 800-900 $\text{cm}^2/\text{V}\cdot\text{s}$, respectively, at room temperature.¹⁰ As a result of this deficiency, slight changes in the V/III ratio can lead to a dramatic change in the electrical quality of a GaSb thin film. Typically, samples grown in Ga-rich conditions and at higher temperatures lead to the degradation of the electrical properties due to the presence of excess Ga_{Sb} antisite defects, while the mobility loss and increase in carrier concentration are not

nearly as severe in Sb-rich conditions. This is attributed to the low solubility of Sb in GaSb, since Sb tends to deposit on the surface of the thin film as crystalline hillocks.

An example of these trends is provided by Subeki *et al.* who investigated the growth of GaSb thin films by atmospheric pressure MOCVD.¹¹ This study was carried out in a 2 inch horizontal reactor using semi-insulating GaAs (100) substrates. In these experiments, the best electrical properties were observed at a V/III ratio near unity which produced a hole mobility of $500 \text{ cm}^2/\text{V}\cdot\text{s}$ and a hole carrier concentration of $5 \times 10^{16} \text{ cm}^{-3}$. When the V/III ratio was decreased to a V/III ratio of 0.1 (Ga-rich), the mobility dropped to $20 \text{ cm}^2/\text{V}\cdot\text{s}$, while the hole concentration increased significantly to $2 \times 10^{19} \text{ cm}^{-3}$. At a higher V/III ratio of 10 (Sb-rich), the mobility dropped to roughly $150 \text{ cm}^2/\text{V}\cdot\text{s}$. The hole carrier concentration increased but not as dramatically to $2 \times 10^{17} \text{ cm}^{-3}$.

The electrical characteristics were found to not only be dependent on the V/III ratio but also the growth temperature.¹² The hole mobility and carrier concentration remained nearly constant at values of $500 \text{ cm}^2/\text{V}\cdot\text{s}$ and $3 \times 10^{16} \text{ cm}^{-3}$, respectively, up to a growth temperature of 525°C . At higher growth temperatures, the mobility was found to decrease and the carrier concentration increased. At a temperature of 600°C , the mobility and hole carrier concentration were $50 \text{ cm}^2/\text{V}\cdot\text{s}$ and $8 \times 10^{17} \text{ cm}^{-3}$, respectively. In general, the mobility and carrier concentration were found to be highly dependent on the V/III ratio, however the growth temperature was also found to have an affect on the actual V/III ratio, which also affected the electrical properties.

In the thin film literature, the electrical quality of a GaSb sample is typically a good indicator of the optical quality of the sample. This is in large part due to the contributions from the native defect to the optical properties of the sample. The optical

quality of a GaSb sample is normally determined by the ratio of the BE peaks to the A peak. The BE peaks, BE1-BE4, are attributed to excitons bound to the native acceptor (native defect). BE1 and BE2 peaks are typically observed in GaSb thin films grown near a V/III ratio of unity or in Ga-rich conditions,^{16,17} while the BE3 and BE4 peaks are typically stronger in GaSb thin films grown in Sb-rich conditions.¹⁷⁻¹⁹ The A peak, on the other hand, is normally a transition between a donor located 2-3 meV below the conduction band and the native acceptor.¹⁹ This peak is usually found to dominate in Ga-rich conditions due to the formation of $V_{Ga}Ga_{Sb}$ centres.

An example of the effect of the V/III ratio on the optical properties of GaSb thin films is provided by Chidley *et al.*¹⁷ The GaSb thin films were grown over a temperature range of 500-650°C and V/III ratios between 0.45 and 1.56.^{20,21} After growth, photoluminescence (PL) measurements were carried out at a temperature of 4.2K. Two prominent peaks were resolved in the photoluminescence spectra centered at 793 meV and 773 meV. The peak at 793 meV corresponds to a bound exciton transition, BE4, whereas the peak at 773 meV is attributed to a transition from the conduction band to the native acceptor, A. At low V/III ratios (Ga-rich conditions), the intensity of the A line compared to the BE4 line increased. This was attributed to the formation of more native acceptors which are linked to the Ga_{Sb} antisite defect. When the V/III ratio was around a value of unity, the PL spectra were dominated by the BE4 transition and acceptor A disappears. For samples grown in Sb-rich conditions, however, the A line increased again in intensity compared to the BE4 line. In this study, it became clear that the optical quality of the sample was sensitive to the V/III ratio.

The final study which will be discussed was carried out by Wang *et al.*² In this study, the effect of various metalorganic precursors on the growth of GaSb were examined. TMG and TEG were used as the Ga precursor, and TMSb, TESb, and TDMASb were used as the Sb precursor. It should be noted that these experiments were performed at a lower pressure of 150 Torr. The first set of experiments centered around the effect of temperature on the growth rate of GaSb using either TMG or TEG with TMSb. For TMG, the growth rate increased with temperature over the range of 560-640°C. On the other hand, the growth rate remained almost constant when TEGa was introduced into the system over a temperature range of 525-640°C. This trend is due to the higher decomposition temperature for TMG than TEG. As a result, the growth rate for TEGa was not affected by temperature over the range investigated.

The next set of experiments focused on the effect of the V/III ratio on the morphology. A minimum V/III ratio was determined for various precursor combinations as a function of growth temperature. Below this minimum V/III ratio, Ga droplets formed on the surface of the substrate. As a result, it remained pertinent to remain above this minimum value. For a combination of TMG and TMSb, the minimum V/III ratio increased over the temperature range of 580-640°C due to the decomposition of TMG. When TEG and TMSb were used, the V/III ratio necessary for high quality growth was constant at 0.9 above 600°C and increased with decreasing temperature below 600°C. When TMSb was replaced by TESb, the V/III ratio became constant at 550°C. This was the case because TESb has a lower decomposition temperature than TMSb. Using TDMASb caused the V/III ratio to become constant at 500°C. Below 500°C, the V/III ratio decreased due to incomplete pyrolysis of TEG. For TEG and TMSb, a temperature

range of 550-625°C resulted in a superb morphology. The same outcome was observed for TEG and TMSb for a temperature range of 580-640°C. When TEG and TESb or TDMASb were used, surface defects were observed for all growth conditions. This was due to pre-reactions between the precursors. Overall, this study displayed the importance the choice of precursors is to the growth of GaSb. At the same time, the connection between growth temperature and V/III ratio was realized. Until a specific temperature was reached, the V/III ratio must be adjusted to compensate for the temperature change.

The GaSb thin film literature can be utilized to gain a better understanding of the growth conditions necessary for GaSb nanowire growth. In particular, a strong dependence on the growth temperature and V/III ratio was realized. If growth proceeds too far away from unity, Ga droplets or Sb hillocks will form. At the same time, V/III ratios around 1 have been found to be optimal for the optical and electrical properties of the GaSb thin films. GaSb thin films were grown at low and atmospheric pressure, but low pressures would be expected to be necessary for nanowire growth in order to inhibit competing thin film deposition. Overall, the GaSb thin film literature provides a good starting point to determine optimal GaSb nanowire growth conditions.

3.4 Synthesis of GaSb Nanowires

Unlike the GaN nanowire field, only a limited number of studies have been reported concerning the synthesis of GaSb nanowires. Primarily, research in the area of GaSb has focused on the deposition of thin films. Recently, however, interest in GaSb nanowires for near- and mid-infrared optoelectronic devices²² and thermoelectrics^{23,24} has

gained momentum. As a result, a concerted effort to grow GaSb nanowires has been observed over the last two years. To the author's knowledge, only four groups have been successful in the growth of GaSb nanowires to date. GaSb nanowires have been grown by three techniques: 1) focused ion beam approach,^{25,26} 2) direct antimodization/reactive vapor transport,²⁷ and 3) cold-wall MOCVD.²⁸⁻³¹ These techniques will be discussed in detail in the subsequent paragraphs.

The first successful attempt to grow GaSb nanowires occurred in 2006 by Lugstein *et al.* using the focused ion beam (FIB) approach.^{25,26} By exposing a GaSb substrate to a 50 keV Ga⁺ ion beam, a porous network of nanowires is found to surround craters formed by the ion beam (Figure 3.3). This process was duplicated on a Sb substrate for the synthesis of Sb nanowires.³² In both cases, the studies were carried out in a high vacuum chamber at room temperature without the addition of a carrier or source gases. Utilizing Auger electron spectroscopy (AES) and high resolution transmission electron microscopy (HRTEM), the GaSb nanowires were found to be primarily amorphous with an average diameter of 25 nm. Some areas up to 5 nm in diameter were found to possess some crystallographic order. Precipitates were also observed on the nanowires and were determined to consist of pure Ga. The beam energy was varied, and GaSb nanowires were not observed if the beam energy was 30 keV or less. Instead, only Ga droplets were found on the substrate surface. Based on these observations, it was suggested that the focused ion beam forms Ga clusters on the surface which absorb material that is decomposed by the beam leading to the supersaturation of the Ga-based clusters and precipitation of GaSb nanowires. This hypothesis was tested by employing a Si ion beam in order to observe if Ga acts as a catalyst for the nanowire growth. When a

60 keV Si ion beam was utilized, the typical crater is formed, however a porous nanowire matrix does not result.

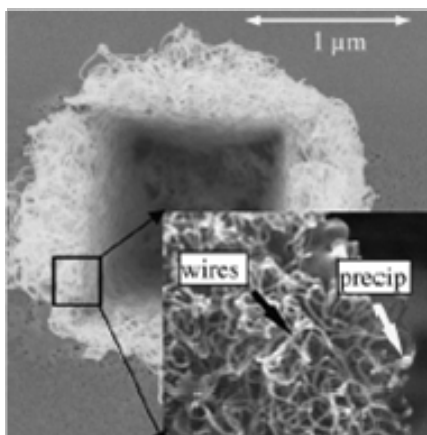


Figure 3.3: Low magnification SEM image displaying crater formed by FIB hole and the surrounding network of GaSb nanowires. The inset is a higher magnification SEM image of the porous nanowire network indicating the location of the nanowires and the pure Ga precipitates.²⁶

Vaddiraju *et al.*,²⁷ on the other hand, was able to successfully grow GaSb nanowires utilizing two techniques: direct antimodization and reactive vapor transport. For direct antimodization, amorphous quartz substrates coated with molten Ga droplets were exposed to a Sb vapor in a hot-wall chemical vapor deposition (CVD) reactor over a temperature range of 800-1050°C. The Sb vapor was supplied by an antimony powder located in a quartz crucible upstream of the reaction site or by antimony chloride (SbCl₃) which was contained in a cylinder at 80°C. The mm-sized Ga droplets became supersaturated and led to spontaneous nucleation of GaSb crystal nuclei on top of the droplets. GaSb nanowires then proceeded to grow out of the droplets in all directions via basal attachment. For the most part, the nanowires were found to possess rectangular cross-sections with [110] growth directions, however some nanowires had a hexagonal

cross-section instead due to the formation of $\{110\}$ and $\{111\}$ facets. By using x-ray diffraction (XRD), the nanowires were confirmed to consist of the diamond cubic crystal structure with a lattice parameter of 6.0959 Å. When a Sb powder was used as the vapor source, the nanowires were found to be 700-900 nm in diameter and up to 1 mm in length. When SbCl_3 was utilized instead, the nanowires were roughly 20-30 nm in diameter and 5 μm in length (Figure 3.4 (a)). It is believed that the significant difference in diameter is due to the presence of chlorine which suppresses the lateral growth and promotes the axial growth of the GaSb nanowires. When chlorine is not present, it is possible for the GaSb nuclei to coalesce forming larger crystals and as a result larger diameter nanowires.²⁷

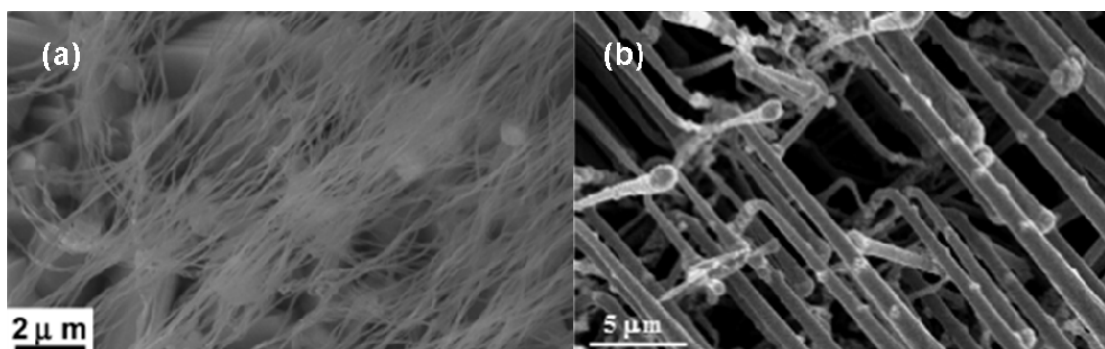


Figure 3.4: SEM images of GaSb nanowires grown by (a) direct antimodization using SbCl_3 and (b) reactive vapor transport.²⁷

For the other technique, reactive vapor transport, both Ga and Sb are supplied to the reaction site in the vapor form. A blank quartz substrate is placed directly above the Ga source, and the furnace is heated to 1000°C for growth. Nanowires were observed to grow on the quartz substrate only on the side facing the Ga source via self-catalytic growth. Initially, GaSb crystals are nucleated on the surface, and GaSb nanowires grow from Ga droplets which are located on top of the crystals. The nanowires were

determined to be roughly 100-200 nm in diameter and in some cases grew in size (Figure 3.4 (b)). The author attributed this to a change in the contact angle between the Ga droplet and underlying crystal.²⁷ Once again, the nanowires were found to grow along the [110] growth direction. Room temperature photoluminescence measurements were carried out on the nanowires, and a peak was observed at 0.72 eV which corresponds to the band gap of GaSb. Some initial experiments were also completed looking at the lasing properties of the nanowires.²²

The final technique to be successfully employed for the synthesis of GaSb nanowires is MOCVD. Guo *et al* was able to utilize MOCVD to grow GaSb/GaAs nanowire heterostructures on GaAs (111)B substrates in a commercial cold-wall horizontal flow reactor at 76 Torr.^{28,29} The growth was aided by Au nanoparticles on the order of 10-50 nm in diameter. The GaAs segment was grown first at a temperature of 450°C for 15 minutes using TMG and AsH₃. Once this segment was complete, the TMG source was turned off and the sample was cooled to 425°C. The AsH₃ source was turned off, and TMG and TMSb were turned on for 120 minutes to grow the GaSb segment of the heterostructure. Using SEM, the nanowires were found to be tapered with a thick column shaped head (Figure 3.5 (a)). The column shaped head was attributed to the GaSb segment being fully relaxing to relieve strain. TEM was utilized to look at the structure of the nanowires, and the GaAs region contained planar defects; however, the GaSb region was defect-free and the interface did not possess any misfit dislocations which would be expected if the segment did not become fully relaxed (Figure 3.5 (b)). The GaSb segment length was measured, and the growth rate was determined to be 50

times slower than the GaAs segment. This was attributed to the GaSb nanowire growth being controlled by thermodynamics.²⁸

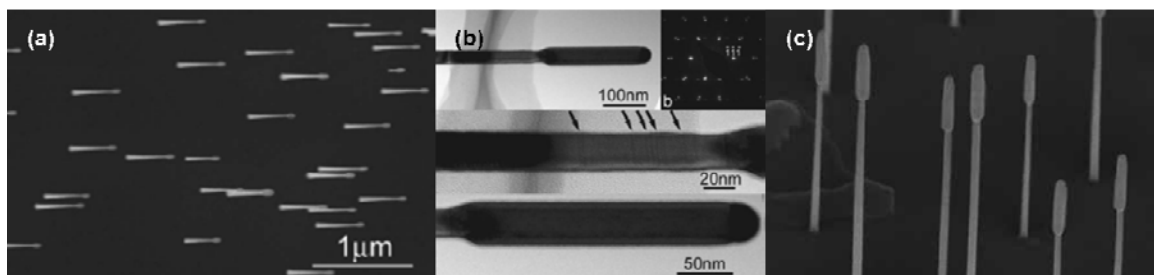


Figure 3.5: (a) SEM and (b) TEM images of GaSb/GaAs nanowire heterostructures synthesized by Guo *et al.*²⁸ (c) SEM image of GaSb/GaAs nanowire heterostructures grown by Jeppsson *et al.*³⁰

Jeppsson *et al.* duplicated and expanded upon the research completed by Guo *et al.* in their studies of GaSb/GaAs nanowire heterostructures.³⁰ A horizontal cold-wall MOCVD system was utilized for these experiments at a pressure of 75 Torr. GaAs (111)B substrates were coated with 40 nm Au nanoparticles via an aerosol technique. The GaAs segment was grown at a V/III ratio of 25 for 1.5-10 minutes, while the GaSb segment was grown at various V/III ratios (0.6-6.2) for 3.5-120 minutes. The TMG flowrate was held constant for ease of switching, and the TMSb flowrate was varied in order to adjust the V/III ratio for the GaSb segment. For this study, the growth temperature for the GaSb region was varied between 410-510°C. After the growths were completed, SEM and TEM were utilized to look at the structural properties of the growths in more detail (Figure 3.5 (c)). The GaAs segment was found to be tapered and roughly 40 nm in diameter. The GaSb segment, however, was not tapered over the entire temperature range and was at least 55 nm in diameter. Radial growth was observed, but it was uniform across the length of the GaSb region and was believed to proceed via

“birth-and-spread” growth. The GaSb nanowires were found to grow at a rate of 3-30 nm/min.

Looking further at the samples with TEM, the GaSb segment was confirmed to consist of the zinc blende crystal structure. Stacking faults were observed in the GaAs region, however no defects were found in the GaSb segment, just as was the case in the previous study. XEDS was employed to look at the composition of the seed particle, and the particle was found to consist of either ~49 at% or ~64 at% Ga with the rest of the particle consisting of Au and residual amounts of Sb. Based on these findings, the nanowires were believed to growth along two pseudo-binary lines of the Au-Ga-Sb ternary phase diagram. The pseudo-binaries were AuGa and AuGa₂. As a result, the increase in diameter for the GaSb segment was attributed to a change in the crystal structure due to the formation of AuGa and AuGa₂. In an additional study, the optical and electrical properties of individual nanowires were investigated.³¹ Photoluminescence measurements of individual nanowires displayed a single peak between 0.785 eV and 0.805 eV with a FWHM of 8 meV. By performing I-V measurements on the nanowires, a resistivity on the order of 0.2-0.4 Ω-cm was calculated.

Overall, a limited number of studies have been carried out on the synthesis of GaSb nanowires. For the most part, only initial studies on the growth have been performed. A minimal amount of data on the structural, optical, and electrical properties of the nanowires has been published. There also are no reports on doping of GaSb nanowires, and the only heterostructure growths reported are GaSb/GaAs nanowires. Once a better understanding is obtained on the growth and how it affects the properties of the material, it will be possible to delve into the growth of complex heterostructures and

doping for the purpose of fabricating devices for optoelectronic and thermoelectric applications.

3.5 References

- 1 R. M. Graham, A. C. Jones, N. J. Mason, S. Rushworth, A. Salesse, T.-Y. Seong, G. Booker, L. Smith, and P. J. Walker, *Semiconductor Science and Technology* **8**, 1797-1802 (1993).
- 2 C. A. Wang, S. Salim, K. F. Jensen, and A. C. Jones, *Journal of Crystal Growth* **170**, 55-60 (1997).
- 3 C. A. Larsen, S. H. Li, and G. B. Stringfellow, *Chemistry of Materials* **3**, 39-44 (1991).
- 4 C. A. Larsen, N. I. Buchan, S. H. Li, and G. B. Stringfellow, *Journal of Crystal Growth* **102**, 103-116 (1990).
- 5 Q. Chen and P. D. Dapkus, *Journal of the Electrochemical Society* **138**, 2821-2826 (1991).
- 6 M. Yoshida, H. Watanabe, and F. Uesugi, *Journal of the Electrochemical Society* **132**, 677-679 (1985).
- 7 M. K. Rathi, B. E. Hawkins, and T. F. Kuech, *Journal of Crystal Growth* **296**, 117-128 (2006).
- 8 G. B. Stringfellow, *Organometallic Vapor-Phase Epitaxy: Theory and Practice*, 2 ed. (Academic Press, Boston, 1999).
- 9 G. B. Stringfellow, *Materials Science and Engineering B* **87**, 97-116 (2001).
- 10 R. M. Biefeld, *Materials Science & Engineering R-Reports* **36**, 105-142 (2002).
- 11 A. Subekti, E. M. Goldys, M. J. Paterson, K. Drozdowicz-Tomsia, and T. L. Tansley, *Journal of Materials Research* **14**, 1238-1245 (1999).
- 12 A. Subekti, E. M. Goldys, and T. L. Tansley, *Journal of Physics and Chemistry of Solids* **61**, 537-544 (2000).
- 13 T. Koljonen, M. Sopanen, H. Lipsanen, and T. Tuomi, *Journal of Electronic Materials* **24**, 1691-1696 (1995).
- 14 Y. J. Van Der Meulen, *Journal of Physics and Chemistry of Solids* **28**, 25-32 (1967).
- 15 W. G. Hu, Z. Wang, B. F. Su, Y. Q. Dai, S. J. Wang, and Y. W. Zhao, *Physics Letters A* **332**, 286-290 (2004).
- 16 Y. K. Su and S. M. Chen, *Journal of Applied Physics* **73**, 8349-8352 (1993).
- 17 E. Chidley, S. K. Haywood, A. B. Henriques, N. J. Mason, R. J. Nicholas, and P. J. Walker, *Semiconductor Science and Technology* **6**, 45-53 (1991).
- 18 C. Agert, P. S. Gladkov, and A. W. Bett, *Semiconductor Science and Technology* **17**, 39-46 (2002).
- 19 M. Lee, D. J. Nicholas, K. E. Singer, and B. Hamilton, *Journal of Applied Physics* **59**, 2895-2900 (1986).

- 20 S. K. Haywood, A. B. Henriques, N. J. Mason, R. J. Nicholas, and P. J. Walker,
Semiconductor Science and Technology **3**, 315-320 (1988).
- 21 S. K. Haywood, N. J. Mason, and P. J. Walker, Journal of Crystal Growth **93**, 56-
61 (1988).
- 22 A. H. Chin, S. Vaddiraju, A. V. Maslov, C. Z. Ning, M. K. Sunkara, and M.
Meyyappan, Applied Physics Letters **88**, - (2006).
- 23 N. Mingo and D. A. Broido, Physical Review Letters **93**, - (2004).
- 24 N. Mingo, Applied Physics Letters **84**, 2652-2654 (2004).
- 25 A. Lugstein, J. Bernardi, C. Tomastik, and E. Bertagnolli, Applied Physics Letters
88, 163114 (2006).
- 26 A. Lugstein, C. Schoendorfer, M. Weil, C. Tomastik, A. Jauss, and E. Bertagnolli,
Nuclear Instruments and Methods in Physics Research B **255**, 309-313 (2007).
- 27 S. Vaddiraju, M. K. Sunkara, A. H. Chin, C. Z. Ning, G. R. Dholakia, and M.
Meyyappan, Journal of Physical Chemistry C **111**, 7339-7347 (2007).
- 28 Y. N. Guo, J. Zou, M. Paladugu, H. Wang, Q. Gao, H. H. Tan, and C. Jagadish,
Applied Physics Letters **89**, 231917 (2006).
- 29 Y. Kim, Q. Gao, H. J. Joyce, H. H. Tan, C. Jagadish, M. Paladugu, and J. Zou, in
III-V nanowires for optoelectronics, 2006 (SPIE), p. 635226.
- 30 M. Jeppsson, K. Dick, J. Wagner, P. Caroff, K. Deppert, L. Samuelson, and L.-E.
Wernersson, Journal of Crystal Growth (2008).
- 31 M. Jeppsson, K. Dick, H. Nilsson, N. Skold, J. Wagner, P. Caroff, and L.-E.
Wernersson, Journal of Crystal Growth (2008).
- 32 C. Schoendorfer, A. Lugstein, Y.-J. Hyun, E. Bertagnolli, L. Bischoff, P. M.
Nellen, V. Callegari, and P. Pongratz, Journal of Applied Physics **102**, 044308
(2007).

Chapter 4

Experimental Techniques

4.1 Introduction

The first part of this chapter will describe the low pressure chemical vapor deposition (LPCVD) system used for the synthesis of group-IV and group III-V nanowires. The nanowire chemical vapor deposition system was built by Dr. Kok-Keong Lew and Ms. Diane Wilson for the synthesis of group-IV nanowires and the potential growth of III-V nanowires. Modifications were performed by the author in order to make the system capable of growing III-V nanowires. Details of the system in its original state can be found in the Appendix and Dr. Kok-Keong Lew's thesis,¹ while modifications to the system will be discussed in this chapter. The second part of this chapter will detail the substrate preparation, growth procedure, and characterization involved in the study of GaN and GaSb nanowires. The characterization techniques include optical microscopy, scanning electron microscopy (SEM), transmission electron microscopy (TEM), photoluminescence spectroscopy (PL), and x-ray diffraction (XRD). In the last part of the chapter, computational modeling concepts carried out by Dr. Daniel Lamborn involving GaN nanowire growth will be presented and discussed.

4.2 Nanowire Chemical Vapor Deposition System

All of the GaN and GaSb nanowire growths described in this thesis were carried out in the nanowire chemical vapor deposition system located in Room 220 of the Electrical Engineering West Building. The system is currently set up for the growth of silicon, germanium, gallium nitride, and gallium antimonide nanowires. The system also includes p-type and n-type dopant gases for silicon nanowire growth. The design of the system is divided into the following sections: (1) precursor delivery systems, (2) system gas manifold, (3) reactor configurations, (4) exhaust set-up, and (5) control panel. The overall system layout is displayed in Figure 4.1. This section will discuss the precursors utilized for GaN and GaSb nanowire growth, the delivery system for these precursors, and the reactor configurations for these experiments. Details concerning the system gas manifold, exhaust set-up, and control panel can be found in the Appendix.

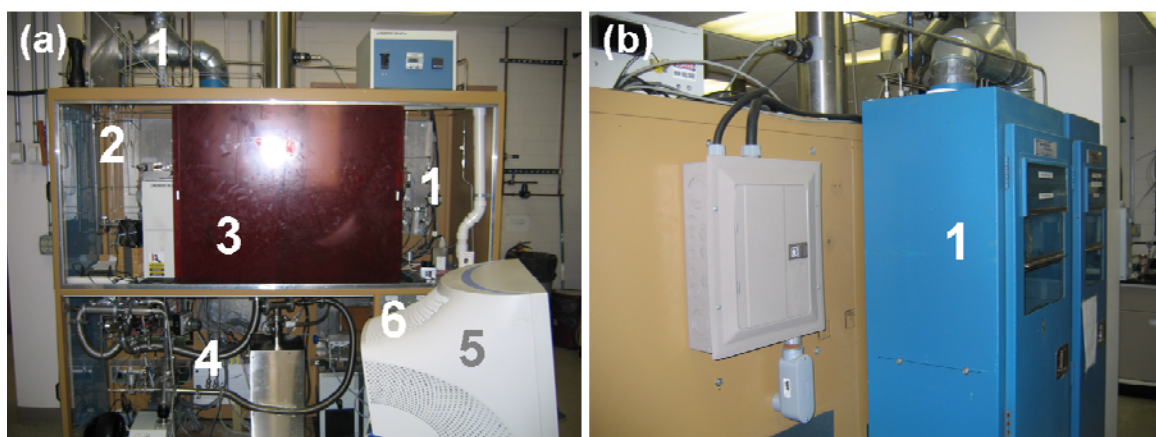


Figure 4.1: (a) Front view of the nanowire system including the (1) precursor delivery systems, (2) system gas manifold, (3) reactor, (4) exhaust, (5) computer with LabView set-up, and (6) control/safety features panel. (b) Backside view of reactor and gas cabinet for gas cylinder storage.

4.2.1 Gas Delivery System

The nanowire chemical vapor deposition (CVD) system was designed for the growth of group-IV and III-V nanowires. As a result, the precursor delivery system can be divided into two main sections: the gas delivery system and the metalorganic delivery system. The gas delivery system includes hydrogen (H_2) and nitrogen (N_2) for carrier gases, the precursors necessary for group-IV nanowire growth, and ammonia (NH_3) for GaN nanowire growth. Nitrogen is supplied through an in-house liquid nitrogen tank (Air Products and Chemicals, Inc.), whereas hydrogen is provided through ultra high purity (UHP) gas tanks (GTS-Welco, Inc.). The carrier gases are flown through in-line purifiers (MicroTorr PS11 Series, SAES and Pure Gas, Inc.) prior to entering the nanowire CVD system. The exception is an additional nitrogen line which is used to dilute hydrogen and the toxic gases as they enter a $KMnO_4$ scrubber. Typically, purified nitrogen is used for purging the system gas manifold and reactor before and after experiments have been performed. N_2 gas was utilized as a carrier gas during growth for one series of GaN nanowire experiments, otherwise H_2 gas was utilized as the carrier gas for the synthesis of GaN and GaSb nanowires.

As was previously mentioned, the gas delivery system includes the precursors for group-IV nanowire growth and ammonia for GaN nanowire growth. There are two gas cabinets for storage of the gas tanks. One of the gas cabinets houses silane (SiH_4 , Air Products and Chemicals, Inc.) and germane (GeH_4 , Voltaix, LLC) gas tanks for silicon and germanium nanowire growth. The other gas cabinet contains lecture bottles for phosphine (PH_3 , Voltaix, LCC) for n-type doping and trimethylboron (TMB, Voltaix,

LLC) or diborane (B_2H_6 , Voltaix, LLC) for p-type doping along with VLSI grade ammonia (NH_3 , Air Products and Chemicals, Inc.) for GaN nanowire growth. Each gas tank is connected to a gas tank manifold which is used to supply the gas at a controlled rate to the system gas manifold. In Figure 4.2, the gas tank manifold for the NH_3 set-up is displayed. The gas tank manifold has a Series AP 1500 SH regulator (Fulcrum Technologies, Inc.) due to the corrosive nature of NH_3 . The regulator is surrounded by two quarter turn valves. A VCR cross is located to the right of the regulator and is the intersection of the N_2 purge line, leak check port, and NH_3 inlet line. The N_2 purge line is utilized to flush the gas tank manifold if NH_3 has not been used for at least a week. The leak check port is used in conjunction with the leak checker if a tank change occurs or a possible leak may be present. A NH_3 purifier (MicroTorr PS11 Series, SAES and Pure Gas, Inc.) was connected to the regulator in order to remove water and oxygen impurities that could be incorporated into the GaN nanowires. A bypass line was installed in order to flush the gas tank manifold or to complete a series of experiments without the use of the purifier. Double-walled stainless steel tubing was plumbed from the gas cabinet to the main cabinet. The double-walled tubing was utilized as a safety measure in case a leak were to occur in the $\frac{1}{4}$ inch tubing that is not located in a ventilated enclosure. If a leak were to occur, it would be contained by $\frac{1}{2}$ inch tubing and drawn to the exhaust through the $\frac{1}{2}$ inch tubing.

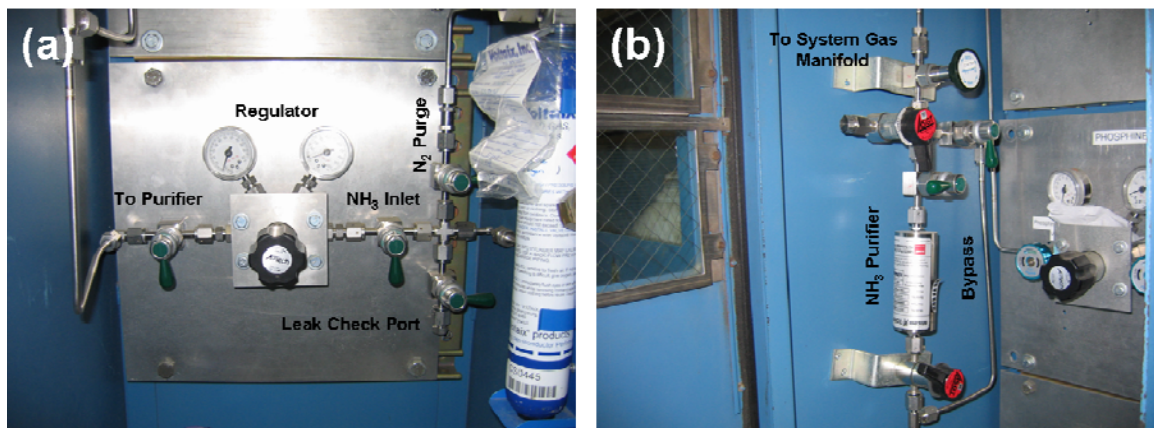


Figure 4.2: (a) Photo of the NH_3 gas tank manifold showing the regulator, N_2 purge line, leak testing port, and NH_3 inlet. (b) Photo of the NH_3 purifier and bypass.

4.2.2 Metalorganic Delivery System

The other portion of the precursor delivery system is the metalorganic delivery system. The metalorganics that have been used for these studies are adduct grade trimethylgallium (TMG), trimethylantimony (TMSb), and germanium tetrachloride (GeCl_4). Currently, there are only two set-ups for metalorganic bubblers. The overall metalorganic set-up can be seen in Figure 4.3. The main components include a mass flow controller (MFC), pressure transducer, and a solenoid valve. The carrier gas, H_2 , flows into the set-up through the MFC. The MFC is utilized to regulate the H_2 flowrate for the purposes of controlling the metalorganic flowrate. This action is represented by the red arrows in Figure 4.3. During an experiment, hydrogen gas is flown into the metalorganic bubbler via the red arrows and exits the bubbler via the blue arrows. The total pressure in the bubbler is controlled by the pressure transducer working in conjunction with the solenoid valve. The pressure transducer and solenoid valve are

connected to a Type 260 MKS pressure controller. The pressure controller is set to a specific pressure, and the solenoid valve adjusts in order to maintain this pressure. If the metalorganic bubbler is not in use, then the bypass pneumatic valve is opened rather than the metalorganic pneumatic valves (orange arrows).

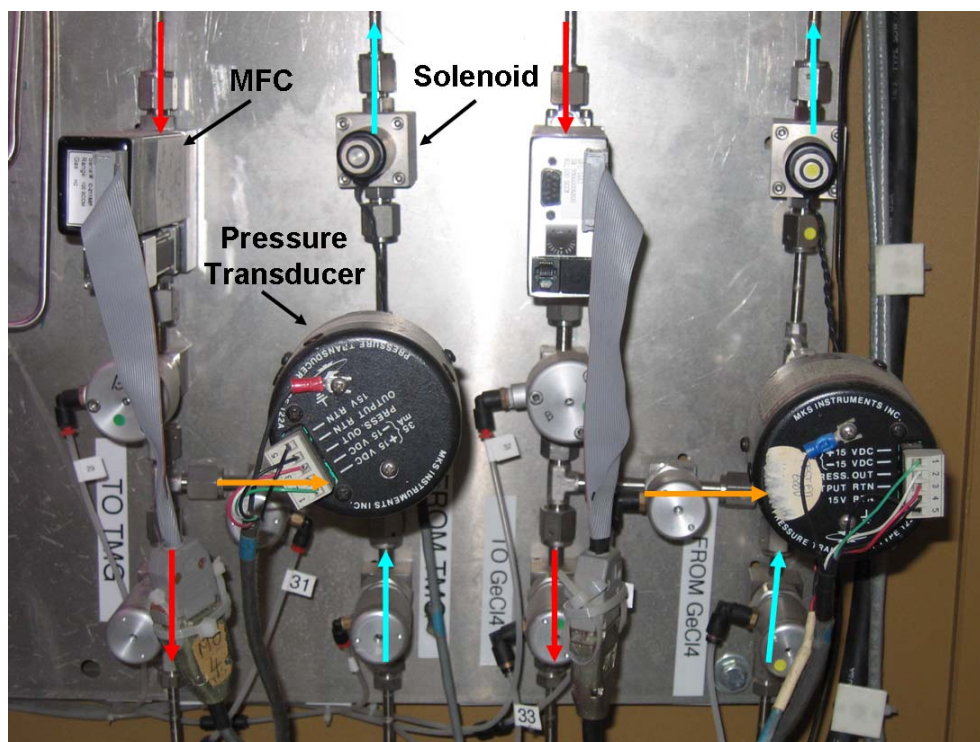


Figure 4.3: Photo of metalorganic delivery system for TMG (left) and TMSb/GeCl₄ (right).

4.2.3 Reactor Configurations

The reactor used for nanowire growth is a horizontal hot-wall reactor with a 1 inch OD quartz tube. The furnace utilized for these experiments is a Lindberg Blue M 1200°C single zone split-hinge tube furnace (HTF55322A) with a 12 inch hot zone.

From calibrating the furnace controller, it was determined that the actual temperature in the reactor is approximately 20°C higher than the setpoint on the furnace controller (Figure 4.4). As a result, the setpoint used during growth is 20°C lower in order to account for the discrepancy. The furnace has been attached to a rail system in order to shift the location of the furnace when performing hydrogen bakes. Typically, the length of the quartz tube is 32 inches long, however due to the need to perform hydrogen bakes for GaN and GaSb nanowire growth, the quartz tube is 37 inches long in order to be able

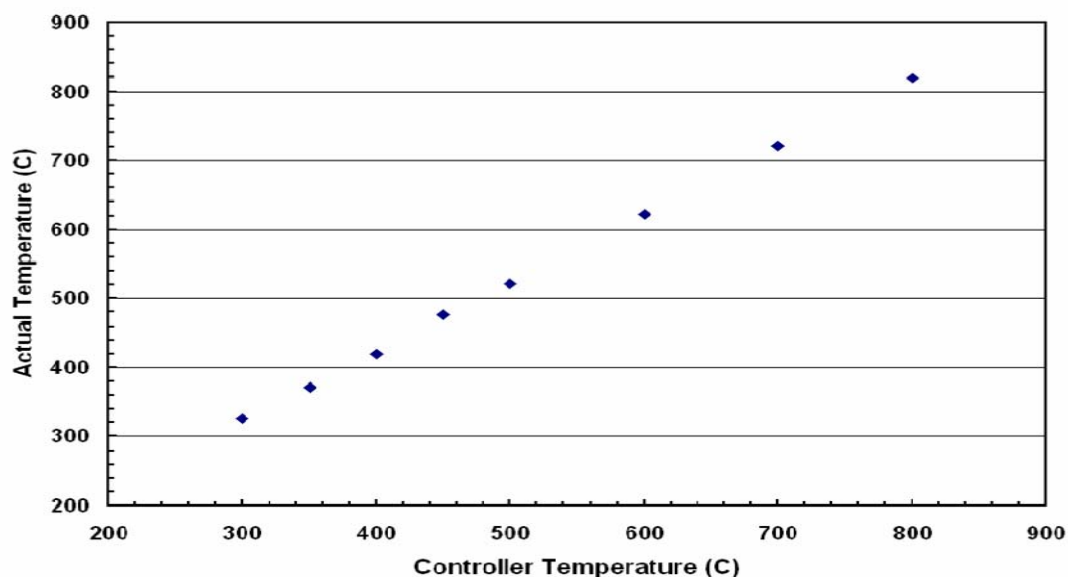


Figure 4.4: Temperature calibration profile of Lindberg controller between 300°C and 800°C.

to move the reactor so the wall deposits are located in the hot zone. A picture of the reactor set-up is provided in Figure 4.5. Figure 4.5 (a) provides the view from the right side of the reactor where the gases enter the reactor. In the background, the system gas manifold is present. The samples for growth are loaded on the left side of the furnace where a viewport is also located (Figure 4.5 (b)). The samples are placed on a quartz

boat which is pushed into the reactor with a glass rod to a predetermined location. The reactor pressure is controlled with a throttle valve (Model 253B, MKS Instruments, Inc.) and a pressure controller (Model 651C, MKS Instruments, Inc.). The pressure is typically regulated between 13-600 Torr for the experiments. There is also a pirani gauge (Model 315, MKS Instruments, Inc.) on the system for leak checking applications. After a sample is loaded into the system for a nanowire growth, the reactor is pumped down to be leak checked.

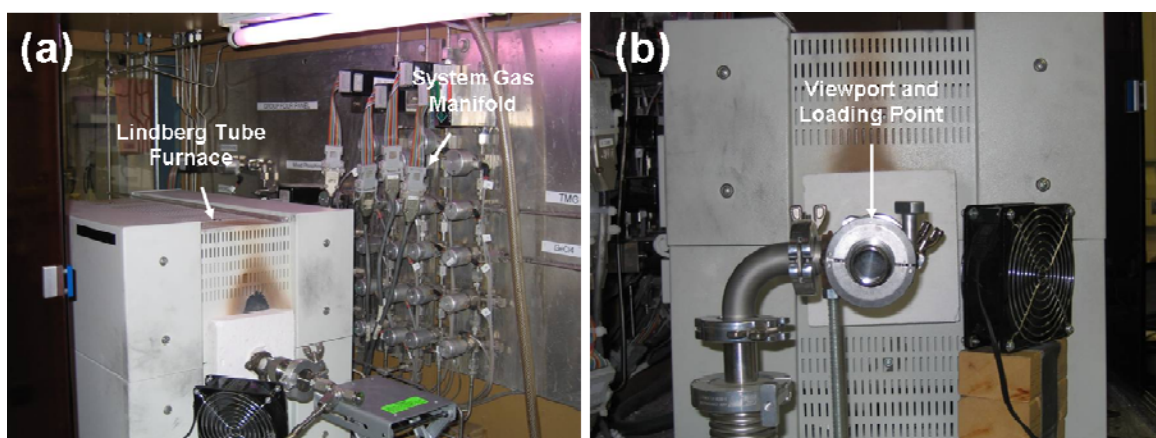


Figure 4.5: Picture of hot-wall tube reactor for nanowire growth from (a) gas inlet side and (b) sample loading/exhaust side.

The leak check includes the tube set-up and the system gas manifold. When pumped down, the system is able to hold a pressure of 3×10^{-4} Torr. A valve is closed to isolate the system from the pump for the leak check. Typically over a five minute span, the final pressure is no more than 7×10^{-4} Torr. If the pressure were to be significantly higher, the run would be aborted and extensive leak checking would be necessary to determine if a leak is present.

Two different reactor configurations were utilized for GaN and GaSb nanowire growth (Figure 4.6). For GaN nanowire growth, a concentric tube inlet geometry was

used in order to prevent pre-reactions between TMG and NH_3 prior to reaching the growth front, since TMG and NH_3 are highly reactive at room temperature. The inlet tube was inserted into the reactor 4 inches from the hot zone. It was not possible to insert it any further, because TMG decomposes at roughly 410°C and coats the interior of the inlet tube if inserted any further. The inlet tube was sealed and centered using an ultra-torr fitting. NH_3 was flown into the reactor through the 1 inch OD quartz tube. For GaSb nanowire growth, a set-up similar to one used for Si nanowire growth was used (Figure 4.6 (b)). In this case, a concentric tube inlet geometry was not necessary, since TMG and TMSb are not highly reactive with one another at room temperature. A tee was connected to the gas inlet side of the reactor, and TMG and TMSb entered the reactor through the sample flex line. Additional H_2 gas was flown into the reactor through a second flex line.

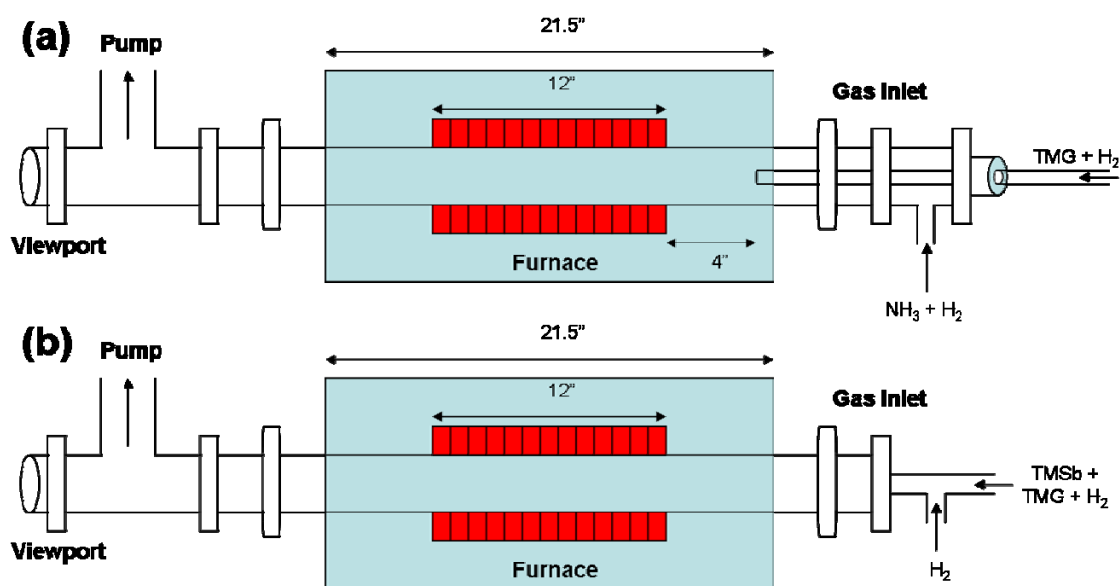


Figure 4.6: Reactor configurations for (a) GaN and (b) GaSb nanowire growth.

4.3 Metalorganic Sources

As was previously mentioned, three metalorganic sources have been used for the synthesis of GaN and GaSb nanowires. The sources are trimethylgallium (TMG), trimethylantimony (TMSb), and germanium tetrachloride (GeCl_4). The metalorganic flowrate of each source is determined based on three variables. These variables are the total pressure of the bubbler, the partial pressure of the metalorganic source, and the carrier gas flowrate. The metalorganic flowrate is determined by the following equation:

$$\text{Flowrate}(M) = \text{Flowrate}(H_2) \times \left(\frac{P_M/P_T}{1 - P_M/P_T} \right) \quad \text{Eq. 4-1}$$

where M stands for metalorganic, P_M stands for the vapor pressure of the metalorganic, and P_T stands for the total pressure within the bubbler. The vapor pressure of the metalorganic is dependent on the temperature of the refrigerating bath that the bubbler is situated in. Equations for determining the vapor pressure of the metalorganics with respect to temperature were provided by SAFC Hitech and are shown below:

$$\text{TMG} : \log_{10} P(\text{Torr}) = 8.07 - 1703/T(K) \quad \text{Eq. 4-2}$$

$$\text{TMSb} : \log_{10} P(\text{Torr}) = 7.73 - 1709/T(K) \quad \text{Eq. 4-3}$$

$$\text{GeCl}_4 : \log_{10} P(\text{Torr}) = 7.325 - 1690/T(K) \quad \text{Eq. 4-4}$$

The TMG bubbler was typically kept at -10°C ($P_M = 39.67$ Torr). The TMSb bubbler was typically kept at 4°C ($P_M = 36.62$ Torr), and the GeCl_4 bubbler was normally

maintained at -12°C ($P_M = 12.55$ Torr). The total pressure (P_T) of the bubbler was maintained by the pressure controller at a value of 760 or 850 Torr. These values were chosen with a range of metalorganic flowrates in mind. The MFCs for the metalorganic set-up had a maximum flowrate of 100 sccm, while the maximum pressure of the pressure controller was 1000 Torr.

4.4 Substrate Preparation

For GaN nanowire growths, $330\ \mu\text{m}$ thick c-plane (0001) and r-plane ($1\bar{1}02$) oriented, one-side polished 2 inch sapphire substrates from Saint-Gobain Crystals were used. For GaSb nanowire growths, c-plane sapphire from Saint-Gobain Crystals was used along with $279\ \mu\text{m}$ thick 2 inch boron-doped (111) silicon substrates from Addison Engineering, Inc. In all cases, the substrates were cleaned in acetone and then isopropyl alcohol for 10 minutes using an ultrasonic bath. After these cleaning steps, the wafers were rinsed in DDI water approximately 10 times and dried using in-house N_2 . Prior to thin film deposition, the oxide was removed from the silicon substrate using a BOE etch. The wafers were loaded into a Denton Explorer™ 14 sputtering system and pumped to a base pressure of 2×10^{-7} Torr. Ni and Au thin films were sputter deposited on the wafers at a 5 mTorr working pressure of Ar by Chad Eichfeld. For GaN nanowire growth, 1-5 nm Au and Ni films were deposited on the sapphire substrates. For GaSb nanowire growth, 2.5 nm Au thin films were deposited on the sapphire and silicon substrates. After deposition, the wafers were scribed into small pieces for growth. For the GaN nanowire growths, the pieces were placed into a 4 inch quartz boat and loaded into the tube

furnace. The samples were annealed at 1000°C and 600 Torr for 30 minutes in H₂. All samples for GaN nanowire growth were annealed prior to growth due to the varying position of the quartz boat during growth. This step was not necessary for GaSb nanowire growth.

Substrates coated with Au nanoparticles were also utilized for the nanowire studies. In this case, the sapphire and silicon substrates were scribed into small pieces prior to the cleaning steps. For nanoparticle application, the sapphire and silicon pieces are placed in individual glass vials. A solution of 30 μL 10% APTMS (3-aminopropyltrimethoxysilane) and 2700 μL ethanol was added to each vial. The vials were capped and placed in a mini orbital shaker (MS1 Minishaker, IKA) for 5 minutes at 600 rpm. After this task was complete, the vials were rinsed with ethanol three times and then DDI water three times. The substrates were transferred to new vials and rinsed three more times with DDI water. It is important to make sure to rinse the vials thoroughly, because the Au colloidal solution will aggregate if any ethanol is present. Once the vials were rinsed thoroughly, the Au colloidal solution (Ted Pella, Inc.) was added to each vial. The volume of solution added will depend on the concentration required for the particular growth. The concentration varied from 0.17-40% depending on the nanoparticle size and density. Nanoparticle size varied between 10-200 nm in this study, however 50 nm Au was the primary choice. DDI water was added to each vial to make the total volume of the solution 3000 μL. For 50 nm Au nanoparticles, a concentration of 5% Au was used for sapphire and 7.5% was used for silicon. This results in 150 μL Au and 2850 μL DDI water for sapphire and 225 μL Au and 2775 μL DDI water for silicon. The vials were placed in the orbital shaker and shaken for 15 minutes at 600 rpm. The vials were rinsed

three times, and then DDI water was added to each vial to immerse the sample until it was used for growth.

4.5 Nanowire Growth

Prior to each experiment, the nanowire CVD reactor was baked out to remove any wall deposits from the previous run. For GaN nanowire growths, the reactor was moved to the right about 6 inches in order to shift the wall deposits into the hot zone. This was not necessary for GaSb nanowire growths, because the deposits were already located in the hot zone. For GaN experiments, the hydrogen bake was performed at 1100°C for one hour under an H₂ gas flow. For GaSb experiments, it was only necessary to heat the reactor to 1000°C for 15 minutes under an H₂ gas flow in order to remove the deposits. The quartz boat was placed in the center of the reactor for both cases. Quartz tube inserts were placed at the end of the tube near the viewport in order to collect the deposits.

Before the silicon samples were loaded into the reactor, a BOE etch was performed to remove the oxide present. The nanoparticle samples were removed from their vials and placed on a Kimwipe to air dry. The samples were placed on a quartz boat and loaded into the reactor. Typically, a blank sapphire or silicon piece was added to the growth as a control. The quartz boat was pushed to a predetermined location using a glass rod. The system was pumped down in order to perform a leak check. Once the system has been pumped down, the pump valve was closed and the pressure was observed over a period of 5 minutes. As long as the leak rate wasn't too high, the experiment would proceed.

Nitrogen gas was reintroduced into the system and the MFCs were ramped up to their maximum values. Nitrogen was flown through the reactor and vent lines for approximately 10 minutes. If NH_3 had not been used in over a week, the NH_3 line was flushed at this time with N_2 . After 10 minutes had elapsed, the N_2 - H_2 interchange valve was closed in order to drain N_2 gas from the run lines. H_2 gas was then introduced into the reactor, and the MFCs were ramped up to their maximum value.

Once the MFCs reached their maximum value, the furnace controller was turned on, and the temperature was set to the growth temperature. The temperature was increased at a rate of $15\text{-}30^\circ\text{C}/\text{min}$ until it reached the growth temperature. At the same time, the MFCs were reduced to the flowrates necessary for the experiment, the throttle valve controller was set to the growth pressure, and the pressure controller(s) for the metalorganic(s) were set to the appropriate pressure. Once the reactor reached the growth temperature, the system stabilized at this temperature for approximately 20 minutes.

When there were 2 minutes left in this step, H_2 was flown into the metalorganic bubbler(s) and then to vent. If a GaN nanowire growth was being done, the NH_3 MFC was set to the appropriate flowrate. After 20 minutes, the precursors were flown to the reactor for 1-30 minutes depending on the growth. After the growth was complete, the precursors were switched back to vent and the system was cooled down. If a GaN nanowire growth was being performed, NH_3 continued to flow into the reactor until approximately 350°C . Once the metalorganics were switched to the vent lines, the bubbler valves were closed and H_2 was flown through the bypass valve(s). Once the temperature reached 350°C , the throttle valve pressure controller was opened, the MFCs were set to their maximum values, and the metalorganic pressure controller(s) were set to

0 Torr. H_2 was drained from the lines along with the precursors. Once the gases were drained, N_2 was flown through the reactor for 5 minutes. Then, the throttle valve was closed, and the reactor was brought up to atmospheric pressure so the samples could be unloaded.

4.6 Characterization

Immediately after growth, a Leitz Ergolux optical microscope was used in order to perform a visual inspection of the surface and determine if nanowire growth resulted. A FEI-Philips XL-20 scanning electron microscope (SEM) was utilized to perform a more detailed analysis of the growth to measure the diameter, length, and density of the nanowires.

A Philips 420 transmission electron microscope (TEM) was used to perform a detailed analysis of the diameter, length, and degree of tapering of GaN nanowires. TEM specimens were prepared by sonicating the samples in isopropanol for approximately 30 seconds to release the wires from the substrate and then dispersing the solution onto lacey carbon films. For more detailed studies of the GaN and GaSb nanowires, a JEOL EM-2010F TEM/STEM (transmission electron microscope/scanning transmission electron microscope) was utilized by Dr. Xiaojun Wang, a research associate at the Materials Research Institute. HRTEM (high resolution transmission electron microscope) images of the nanowires and catalysts were taken along with diffraction patterns of the samples. XEDS point and line scans were performed in order to investigate the composition of the

cross-section and axial direction of nanowire growth and also the composition of the catalyst in each case.

Photoluminescence measurements of the GaN nanowires were performed at room temperature in order to determine the optical quality of the nanowire growth. The PL system utilized for this study consisted of an Instruments SA, Inc. HR-640 Spectrograph Monochromator and an Nd:YAG laser with a 266 nm excitation wavelength. Photoluminescence studies of the GaSb nanowires were carried out using a 0.25M Spex Minimate and the 488 nm line of an argon laser by Professor Roger Reeve's research group at the University of Canterbury.

Finally, a Rigaku Geigerflex x-ray diffractometer was used to determine the crystalline phase of the GaN nanowire growth when GeCl_4 was introduced to the growth.

4.7 Computational Modeling

Computational fluid dynamics (CFD) modeling was utilized in conjunction with the experimental results in order to gain a better understanding of the effect of growth conditions on GaN nanowire growth. Computational modeling has previously been used to study the effects of process conditions on GaN thin film deposition in a thin film cold-wall MOCVD reactor.²⁻⁴

The modeling studies were performed using the commercial software package CFD-ACE+™ (ESI-Group, Huntsville, Al) in collaboration with Dr. Daniel Lamborn, a former chemical engineering graduate student in our group. The software package is based on the finite element method in which the model is divided into a mesh and each

grid box is individually evaluated for the specified conditions and boundaries. In order to reduce the complexity of the system, a 2D axis-symmetric geometry was used where the center line of the reactor is the line of symmetry of the system. The CFD-ACE+™ software package implements a variety of equations for the estimation of gas-phase mixture properties (kinetic theory property estimation) and simultaneously solves the total mass continuity, momentum continuity, and energy balance equations.⁵

MOCVD growth of GaN involves a complex set of chemical reactions which are not yet fully understood. As previously noted in the literature review, TMG and NH₃ are highly reactive at room temperature and will readily form the adduct Ga(CH₃)₃:NH₃.³ As the gas phase reactions progress further, alternative adducts and products can form. A chemistry model for GaN growth using MOCVD developed by Theodoros Mihopoulos⁶ is shown in Table 4.1. This chemistry model is built into the software package and was utilized in the modeling analysis.

Table 4.1: Chemistry model for MOCVD growth of GaN nanowires.

Reactant → Products	k _o (1/s)	E _a (kcal/mol)
Ga(CH ₃) ₃ → GaCH ₃ + 2CH ₃	3.5X10 ¹⁵	59.5
Ga(CH ₃) ₃ + NH ₃ ↔ Ga(CH ₃) ₃ :NH ₃	1.0X10 ¹²	0.0
Ga(CH ₃) ₃ :NH ₃ ↔ Ga(CH ₃) ₃ + NH ₃	9.5X10 ⁹	19.0
Ga(CH ₃) ₃ :NH ₃ → Ga(CH ₃) ₂ NH ₂ + CH ₄	1.0X10 ¹³	32.0
Ga(CH ₃) ₃ :NH ₃ + NH ₃ → Ga(CH ₃) ₂ NH ₂ + CH ₄ + NH ₃	1.0X10 ¹²	15.0
3Ga(CH ₃) ₂ NH ₂ → [Ga(CH ₃) ₂ NH ₂] ₃	1.0X10 ²¹	0.0
[Ga(CH ₃) ₂ NH ₂] ₃ → 3"GaN" + 6CH ₄	4.0X10 ¹⁵	60.0

The CFD modeling was used to predict the gas phase concentrations, temperature profiles, and velocity profiles in the reactor. The software also provides GaN thin film

deposition rates and mass fractions of the adduct reactions with respect to position within the reactor. The thin film deposition rate is determined at the quartz tube wall, while the mass fractions are obtained at the centerline of the reactor. The CFD software package incorporated the specific geometry of the nanowire reactor along with the nanowire growth conditions for pressure, temperature, TMG flowrate, NH₃ flowrate, and carrier gas flowrate.

4.8 References

- ¹ K.-K. Lew, Doctor of Philosophy Thesis, Pennsylvania State University, 2005.
- ² S. A. Safvi, J. M. Redwing, M. A. Tischler, and T. F. Kuech, in *A Modeling Study of GaN Growth by MOVPE*, 1996 (Materials Research Society), p. 255-260.
- ³ C. Theodoropoulos, T. J. Mountziaris, H. K. Moffat, and J. Han, *Journal of Crystal Growth* **217**, 65-81 (2000).
- ⁴ J. X. Sun, J. M. Redwing, and T. F. Kuech, *Journal of Electronic Materials* **29**, 2-9 (2000).
- ⁵ B. E. Poling, J. M. Prausnitz, and J. P. O'Connell, *The Properties of Gases and Liquids*, 5 ed. (McGraw-Hill, New York, 2000).
- ⁶ T. Mihopoulos, Doctor of Philosophy Thesis, Massachusetts Institute of Technology, 1999.

Chapter 5

Synthesis of GaN Nanowires

5.1 Introduction

This chapter is focused on studies investigating the effect of growth conditions on the nanowire growth and properties. GaN nanowires were successfully synthesized in a hot wall tube furnace reactor utilizing metalorganic precursors. Based on the results, the nanowire growth was found to be strongly dependent on position, temperature, and V/III ratio. The chemistry of GaN MOCVD growth has previously been studied and can be used to predict thin film growth rate for a variety of reactor configurations.¹⁻³ In this study, a computational fluid-dynamics (CFD) based model of the GaN nanowire growth was developed for the simple hot wall horizontal reactor geometry. The modeling was used in conjunction with the experimental studies to investigate the effects of the process conditions on GaN nanowire growth.

After completing the experiments, transmission electron microscopy (TEM) and photoluminescence (PL) were utilized to look at the structural and optical properties of nanowires grown at various conditions. In particular, TEM was used to investigate the state of the seed particle due to uncharacteristically low growth temperatures than would be expected for VLS growth. This task was completed in an attempt to determine if nanowire growth proceeded based on the typical VLS mechanism or if another growth mode was responsible.

From the TEM analysis, the diameter of the GaN nanowires was found to taper to varying degrees based on the growth conditions. The tapering was found to be due to a competition between axial (nanowire) growth and radial (thin film) deposition. Studies involving the addition of GeCl_4 to the gas phase mixture were completed in an attempt to change the growth chemistry and thereby alter the rate of radial deposition vs. axial growth. GeCl_4 was used for preliminary studies, since HCl or another Cl-based precursor was not available at the time. Based on the SEM results, TEM and PL were utilized in order to investigate the effect of GeCl_4 on the GaN nanowires.

The author would like to note that the modeling was completed by Dr. Daniel Lamborn, a former graduate student in Professor Joan Redwing's group. Initial TEM analysis of samples grown with and without GeCl_4 was performed by the author. Additional TEM analysis of samples grown with and without GeCl_4 was carried out by Dr. Xiaojun Weng, a research associate at the Materials Research Institute. The PL studies in this chapter were completed by the author.

5.2 Initial Studies in Constant Temperature Region

As was previously discussed in Chapter 4, NH_3 and a carrier gas (H_2 or N_2) are flown into the reactor through a 1 inch outer diameter (OD) quartz tube which is highlighted in blue in Figure 5.1. TMG and a carrier gas (H_2 or N_2) are flown into the reactor through a $\frac{1}{4}$ inch OD quartz tube that has been centered in the 1 inch OD quartz tube. The TMG inlet is highlighted in red in Figure 5.1. The TMG inlet was only placed 6 inches into the quartz tube reactor due to the low decomposition temperature of 410°C

for TMG.⁴ Initial studies for GaN nanowire growth were performed with the quartz boat located 4 inches from the TMG inlet. This placed the quartz boat at the front edge of the hot zone. The hot zone of the furnace was a 12 inch section located in the center of the furnace that was maintained at a constant temperature. As a result of the location of the quartz boat and TMG inlet, gas phase reactions occurred over a distance of 4 inches prior to reaching the boat and the sapphire wafer pieces.

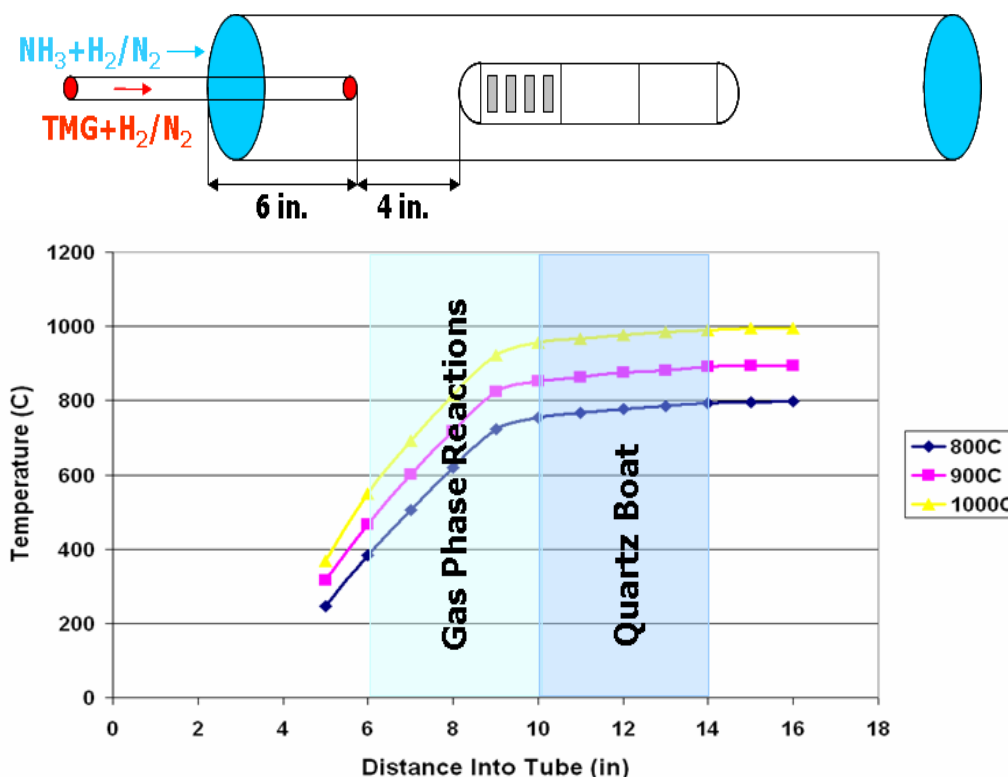


Figure 5.1: Schematic of tube furnace and temperature profile with quartz boat 4 inches from TMG inlet.

In general, limited success resulted for the growth of GaN nanowires with the boat 4 inches from the TMG inlet. Reproducibility of the results proved to be an issue. An example of the most promising growth is shown in Figure 5.2. For the most part, the

primary growth appeared to be vapor-solid deposition. There have been conflicting reports in the GaN nanowire literature as to the effectiveness of Au as a catalyst. The solubility of nitrogen in Au is known to be quite low.⁵ In some cases, literature reports indicate success in the growth of GaN nanowires using Au.⁶⁻⁸ However, other reports did not observe nanowire growth and attributed this to the poor solubility between nitrogen and gold.^{9,10} In general, minimal success was observed for growth of GaN nanowires using Au as the catalyst of choice for this study.

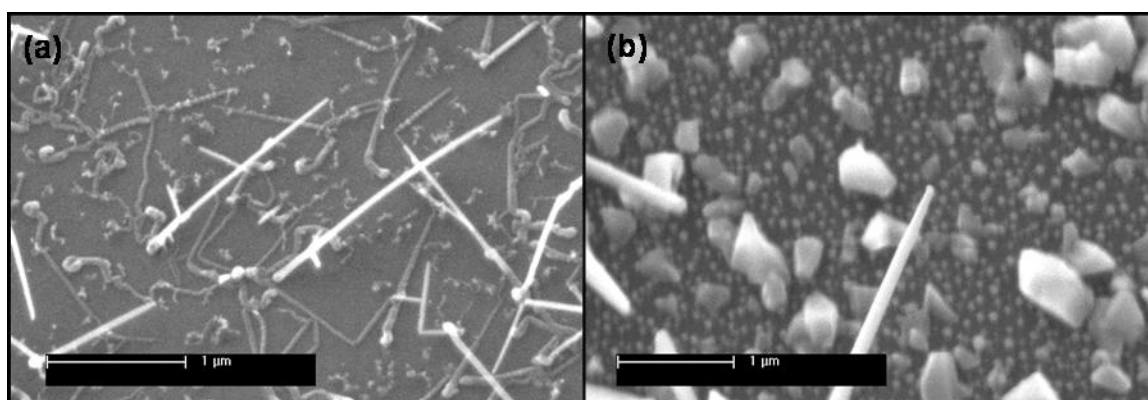


Figure 5.2: SEM images of GaN nanowires grown with (a) 5% 50 nm Au catalysts and (b) 5 nm Ni Film.

After each growth, a significant amount of wall deposits were observed beginning at the exit of the TMG inlet and spanning approximately 2-3 inches indicating the depletion of the gas phase precursors prior to the substrate. Gas phase depletion of the precursors was believed to be responsible for the limited success of growing GaN nanowires in the constant temperature region. Attempts were made to try and overcome this issue. Increasing the flowrates of the precursors and carrier gas did not have a significant effect on the deposited material; however, this action did increase the region in which wall deposits occurred to approximately 4 inches. The TMG inlet was also

inserted 2 inches closer to the constant temperature region of the furnace in an attempt to improve the GaN nanowire growth. This did result in an increase in the density of nanowire growth, however the TMG decomposed inside the inlet tube resulting in the collection of gallium on the inner walls of the inlet until the opening became completely sealed.

In the process of performing these studies, it was discovered that wall deposits from previous growth runs significantly affected subsequent growths. Figure 5.3 (a) is an SEM image of a sapphire sample that was coated with a solution of 5% 50 nm Au nanoparticles. In Figure 5.3 (b), the Au-coated substrate was heated up to a growth temperature of 900°C and TMG was flown through the reactor for 5 minutes before the reactor was cooled down to room temperature. The particles increased in size as they reacted with the TMG. In Figure 5.3 (c), the substrate was heated up to a growth temperature of 900°C and cooled down to room temperature without introducing any precursors. The particles were also found to increase in diameter even though the sample was not exposed to TMG. The sample was placed in the SEM and energy dispersive x-ray spectroscopy (EDS) was performed. EDS detected the presence of Ga even though TMG was not introduced into the system. It was established that as the furnace was heated and reached equilibrium, H₂ etched the wall deposits, and they redeposited on the sapphire substrate prior to growth. It is well known that H₂ will etch GaN at elevated temperatures.¹¹ This issue was resolved by introducing a hydrogen bake after each growth to remove the wall deposits. The furnace was placed on rails in order to shift it after each run so that the wall deposits were located in the constant temperature region.

For each hydrogen bake, the furnace was heated up to 1100°C for 1 hour under H₂ flow to remove the wall deposits.

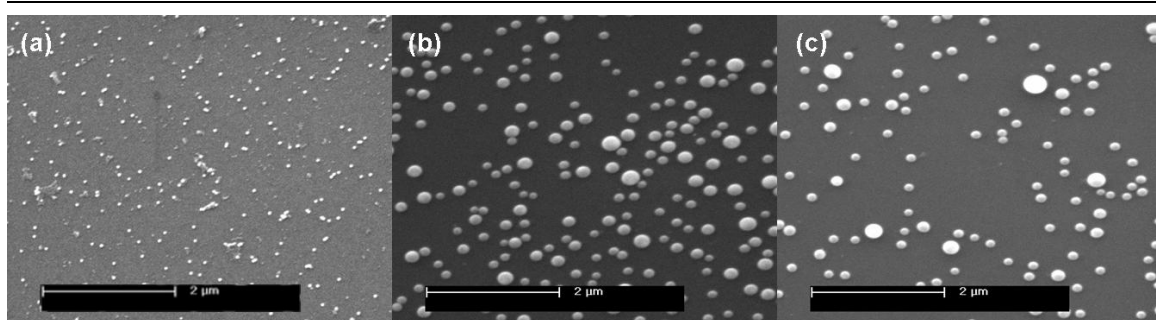


Figure 5.3: SEM images of 5% 50 nm Au nanoparticles (a) with no treatment, (b) 5 min TMG pre-flow, and (c) heat up and cool down (no growth).

As was previously mentioned, reproducibility of the results also proved to be an issue. One matter suspected to be partially responsible for the reproducibility issues was the devitrification of the quartz tube. The wall deposits were resistant to cleaning via wet etching. They adhere to the quartz tube causing the quartz to chip and roughen during the etching process. As a result, the gas phase mixture was exposed to the roughened surface which led to an increase in the amount of wall deposits during growth.

5.3 Effect of Growth Conditions on GaN Nanowire Growth

5.3.1 Effect of Position

After exhausting all possibilities for growth conditions with the quartz boat in the hot zone, the quartz boat was shifted 2 inches closer to the TMG inlet (2 inches from the TMG inlet) in order to observe the effect of position on GaN nanowire growth (Figure 5.4). It should be noted that the front half of the quartz boat was no longer in the

constant temperature region. It was determined using a thermocouple that the front edge of the boat is roughly 100°C lower than the furnace temperature in the constant temperature region. This factor was taken into consideration when analyzing the data. Unless otherwise noted, the reported temperature is the furnace temperature. As a result of the new location of the quartz boat, gas phase reactions occurred over a distance of 2 inches rather than 4 inches prior to reaching the boat and the sapphire wafer pieces.

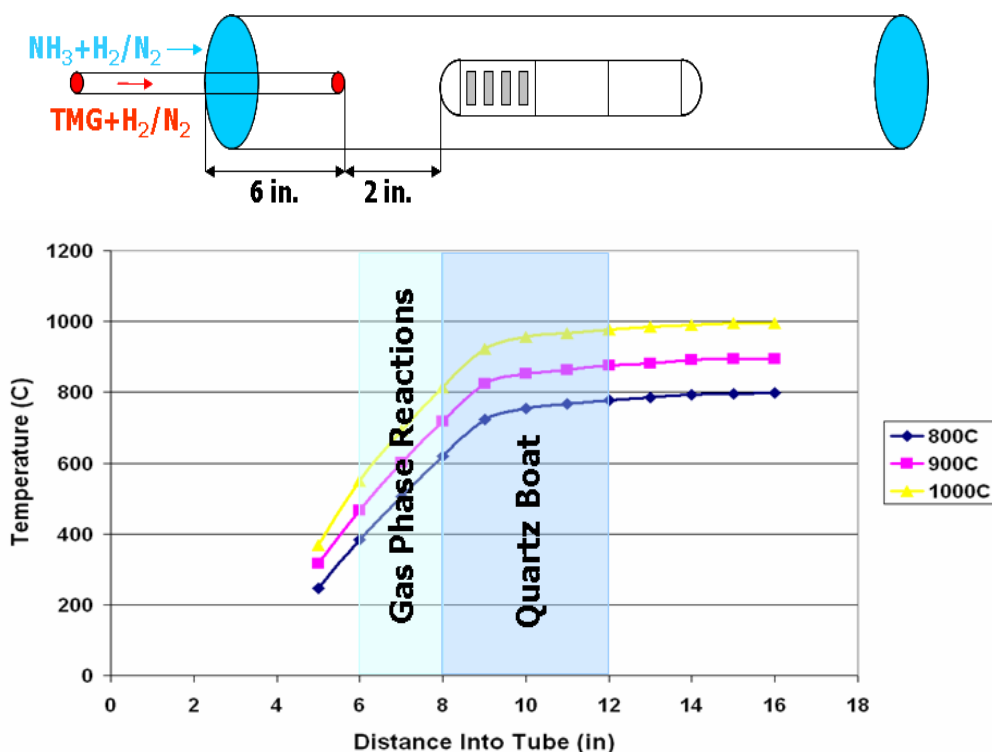


Figure 5.4: Schematic of tube furnace and temperature profile with quartz boat 2 inches away from TMG inlet.

As a result of the position shift, an improvement in nanowire density and reproducibility was observed for samples grown with a Ni thin film. However, it was not possible to grow GaN nanowires using Au thin films or nanoparticles after the position shift. Figure 5.5 is a series of SEM images of GaN nanowire growth using Ni thin films

for growth conditions of 900°C, 100 Torr, 4 sccm TMG, 200 sccm NH₃, and 250 sccm H₂. The SEM images of the sample surface are shown as a function of distance from the TMG inlet tube. A noticeable change in nanowire density, diameter, and length was observed with respect to position. Sapphire samples placed further into the reactor resulted in a reduction in the nanowire density, diameter, and length. The average diameter at the tip of the nanowire for the sample placed 2.5 inches from the TMG inlet (Figure 5.5 (a)) was 185±50 nm, whereas the value decreased to 76±26 nm for the sample located 3 inches from the TMG inlet (Figure 5.5 (b)). Vapor-solid growth became more dominant on substrates placed further into the reactor (Figure 5.5 (c)), and eventually nanowire growth ceased.

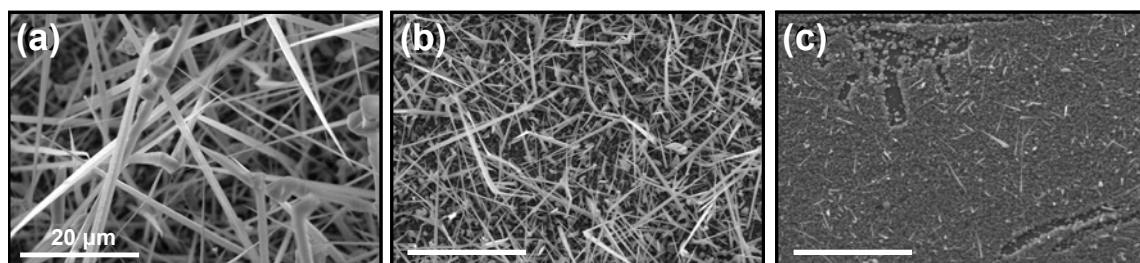


Figure 5.5: SEM images of GaN nanowire growth on 5 nm Ni thin films at (a) 8.5 inches, (b) 9 inches, and (c) 9.5 inches into the furnace. 20 μm scale bars for all images. Growth conditions: 900°C, 100 Torr, 4 sccm TMG, 200 sccm NH₃, 250 sccm H₂.

Modeling studies were performed in order to understand the significance of the location of the quartz boat. Before the modeling software was utilized for the GaN nanowire results, a study was carried out to compare the model predictions to the experimentally measured thin film growth rate of GaN in the reactor. This study was completed to test the validity of the CFD transport and chemistry model for the quartz tube reactor. In this experiment, three long uncoated sapphire substrates were placed

along the length of the quartz boat. The quartz boat was then placed adjacent to the group III inlet as shown in Figure 5.6 (a). The GaN thin film deposition was carried out for 10 minutes using the same growth conditions as the nanowire growth experiment above (900°C, 100 Torr, 4 sccm TMG, 200 sccm NH₃, 250 sccm H₂). The byproduct of this experiment was a polycrystalline GaN thin film spanning the length of the sapphire substrates, since the samples were not coated with a Ni or Au. The thickness of the thin film along the length of the sapphire substrates was determined from SEM images of the sample cross-sections.

The gas phase temperature, velocity, and adduct concentration profiles for the experimental conditions were calculated using the CFD model. Based on the furnace temperature profile (Figure 5.4), the gas phase temperature in the area of the group III inlet was determined to be approximately 470°C for a furnace temperature of 900°C (Figure 5.6 (b)). The gas phase temperature in this region along with a high gas velocity (Figure 5.6 (c)) prevents any premature decomposition of the TMG precursor in the inlet tube. Figure 5.6 (d) is a plot of the mass fraction of the intermediate ring species [Ga(CH₃)₂NH₂]₃ in the gas phase which is considered to be the adduct responsible for GaN thin film growth.^{2,12} The concentration of this species is highest in the region directly adjacent to the TMG inlet demonstrating the instantaneous reaction between TMG and NH₃ that occurs when they combine at the group III tube exit.

The experimentally measured GaN thin film growth rate as a function of distance from the TMG inlet is displayed in Figure 5.7 along with the results from the modeling. Very high GaN thin film growth rates (6-130 μm/hr) were obtained in this hot wall geometry compared to typical growth rates of 1-5 μm/hr obtained in traditional cold-wall

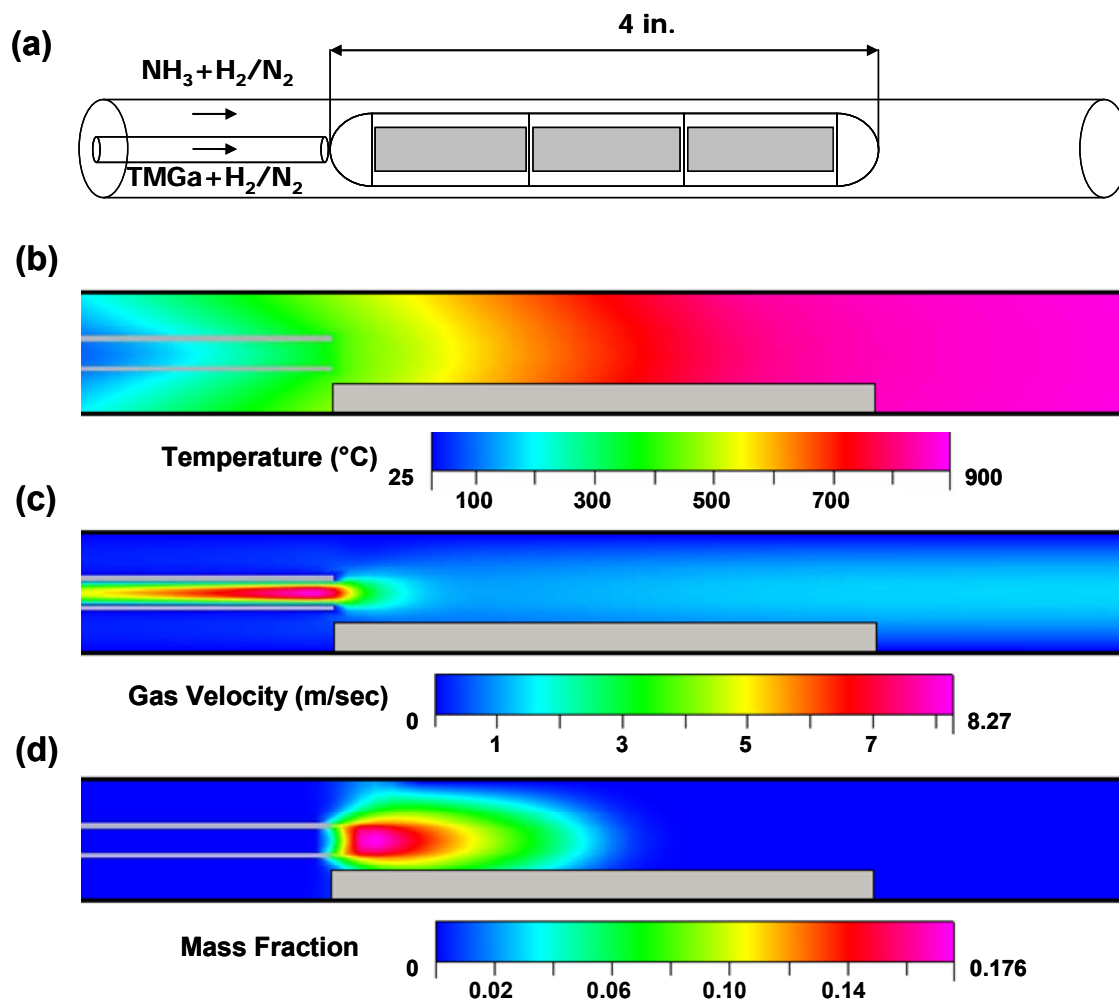


Figure 5.6: (a) Geometry of nanowire system showing location of quartz boat and sapphire substrates. Gas (b) temperature, (c) velocity, and (d) adduct concentration profiles for the thin film experiment. Growth conditions: 900°C, 100 Torr, 200 sccm NH_3 , 250 sccm H_2 .

MOCVD reactors. The simulated GaN thin film growth rate profile compares favorably to that obtained experimentally, indicating a maximum in the growth rate at a position of approximately 0.6 inches (0.8 inches for experimental) from the group III inlet. However, the predicted maximum growth rate ($\sim 1 \mu\text{m}/\text{min}$) is about a factor of two lower than that measured experimentally. This may be attributed to the fact that the model

prediction is based on GaN deposition on the reactor walls, whereas the experimentally measured values were obtained from sapphire substrates on the quartz boat in the reactor which places the substrates at the center line of the reactor tube. In addition, the GaN thin film surface was very rough in the region of high growth rate (0.5-1.0 inches from the group III inlet) which introduced errors into the thickness measurements. Despite the differences in the magnitude of the GaN thin film growth rate, the growth rate profile obtained from the CFD model compares favorably to that measured experimentally providing confidence that the model can be used to accurately simulate gas phase conditions during nanowire growth.

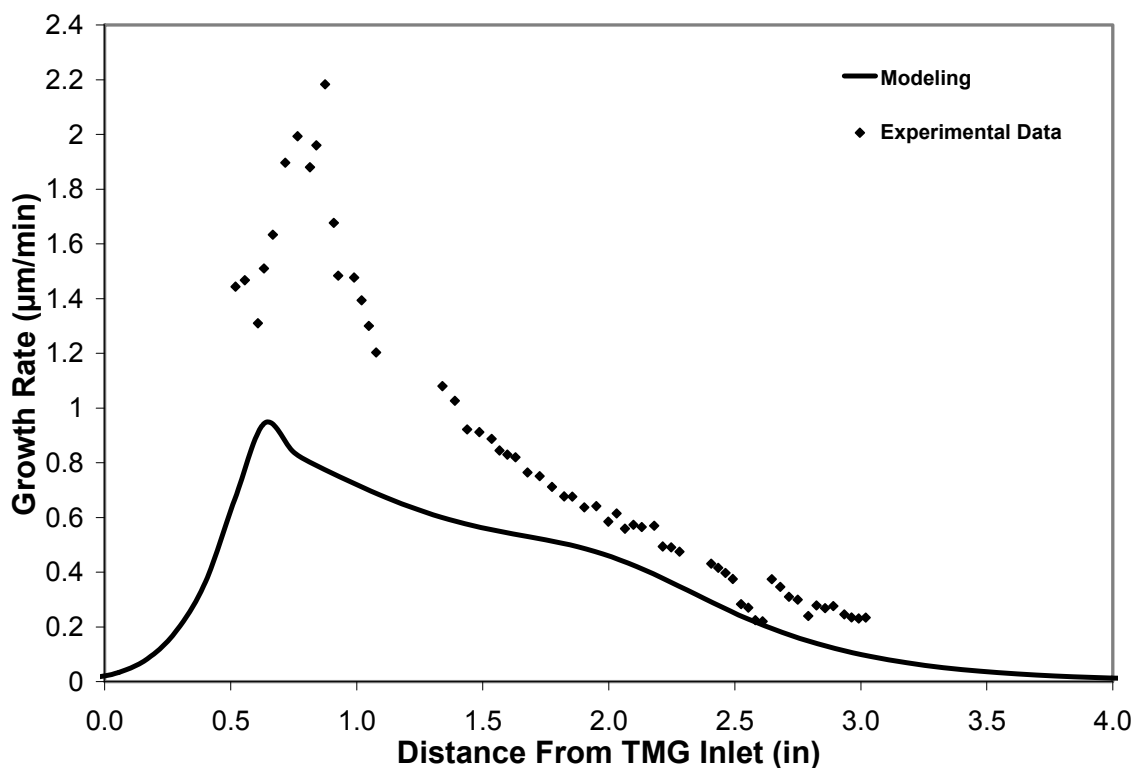


Figure 5.7: Experimental and modeling predictions for GaN thin film growth rate as a function of distance from the TMG inlet. Growth conditions: 900°C, 100 Torr, 4 sccm TMG, 200 sccm NH_3 , 250 sccm H_2 .

Once the CFD transport and chemistry model was validated, a study was carried out using identical processing conditions to those described above for GaN nanowire growth. The particular goal was to understand why nanowire growth resulted when the boat was placed 2 inches from the TMG inlet but not 4 inches from the TMG inlet. Figure 5.8 is a graph of the mass fraction of gas phase reactants and intermediates with respect to position for the growth conditions used to obtain the samples shown in Figure 5.5. The predicted GaN thin film growth rate with respect to position is also included. As was discussed in Chapter 4, the mass fractions are obtained at the centerline of the tube furnace, while the thin film deposition rate is obtained at the quartz tube wall. The gray rectangle is a representation of the location of the quartz boat for the new configuration. When the boat was placed 2 inches from the TMG inlet (8 inch mark on the graph), a small fraction of the intermediate ring species $[\text{Ga}(\text{CH}_3)_2\text{NH}_2]_3$ remains in the gas phase, while a high mass fraction of the “Ga-N” gas phase is present. When the boat was placed 4 inches from the inlet (10 inch mark), all of the gas phase species were essentially non-existent. In an additional experiment, the quartz boat was placed adjacent to the TMG inlet in order to determine if nanowire growth was possible closer to the group III inlet. In this region, only polycrystalline thin film deposition was observed on the Ni-coated sapphire. Thin film deposition dominated in this area as it also coincides with the maximum in the thin film growth rate shown in Figure 5.8. This observation clearly shows that there is a window of growth for GaN nanowires.

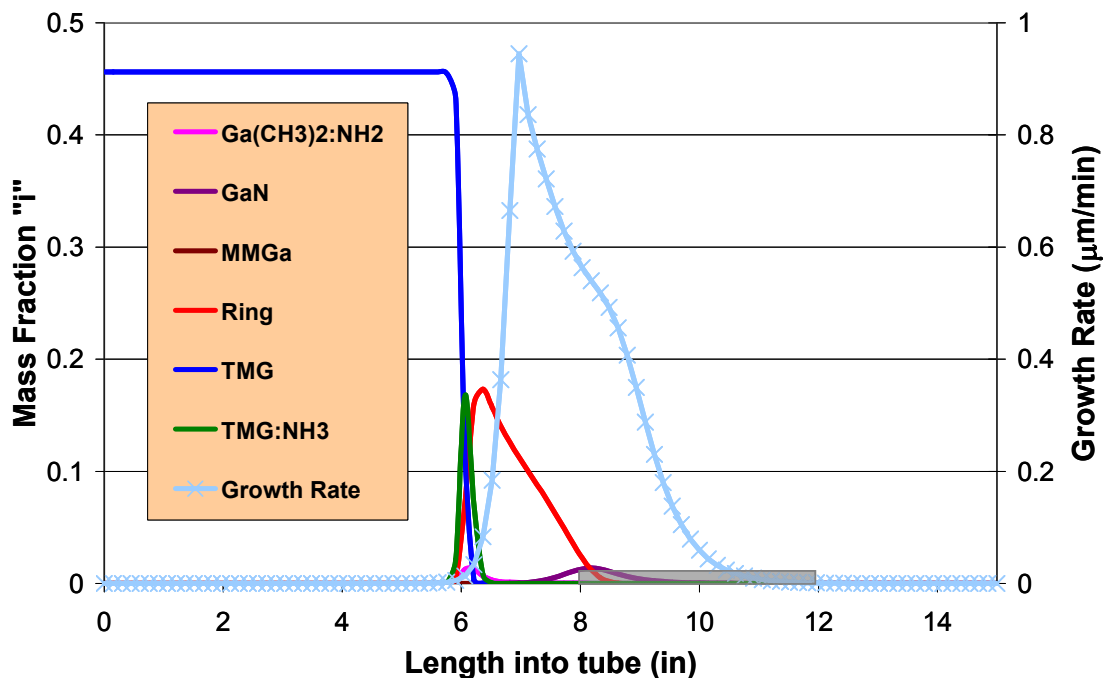


Figure 5.8: Mass fraction of adducts and thin film growth rate with respect to position. Quartz boat is located at 8 inches. Growth conditions: 900°C, 100 Torr, 4 sccm TMG, 200 sccm NH₃, 250 sccm H₂.

5.3.2 Effect of Temperature

In order to investigate the effect of growth temperature, the furnace temperature set-point was varied over the range of 750-1000°C. For the temperature study, the pressure was held constant at 100 Torr, while the TMG and NH₃ flowrates were held constant at 3 sccm and 100 sccm, respectively with a H₂ carrier gas flowrate of 250 sccm. As was previously noted, the samples are no longer located in the constant temperature region, and this must be accounted for in the analysis. The front edge of the boat is

roughly 100°C lower than the furnace temperature, and the Ni-coated sapphire sample is roughly 75°C lower than the furnace temperature. As a result, the temperature will be reported as both the furnace temperature and substrate temperature (T_s). Unless specified, the reported temperature is the furnace temperature.

Nanowire growth was observed over a furnace temperature range of $800\text{-}900^{\circ}\text{C}$ (Figure 5.9 (b)-(d)). Below 800°C (Figure 5.9 (a)) and above 900°C (Figure 5.9 (e)-(f)), vapor-solid growth of faceted crystals was the only morphology present. In this series of experiments, the overall total flowrate is lower compared to the position-based experiments. Consequently, the region of nanowire growth shifts closer to the TMG inlet, and the growth results in smaller diameter nanowires.

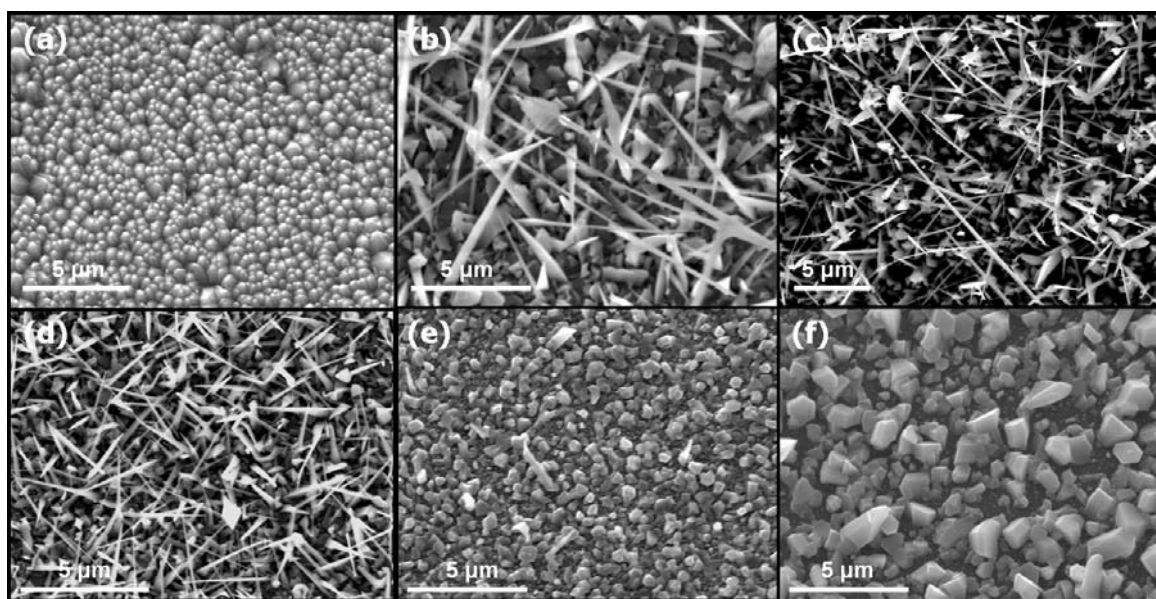


Figure 5.9: Surface morphology of GaN nanowire growth at a position 2 inches from the group III inlet for furnace temperatures of (a) 750°C ($T_s = 675^{\circ}\text{C}$), (b) 800°C ($T_s = 725^{\circ}\text{C}$), (c) 850°C ($T_s = 775^{\circ}\text{C}$), (d) 900°C ($T_s = 825^{\circ}\text{C}$), (e) 950°C ($T_s = 875^{\circ}\text{C}$), and (f) 1000°C ($T_s = 925^{\circ}\text{C}$). Growth conditions: 100 Torr, 3 sccm TMG, 100 NH_3 , 250 sccm H_2 .

These results conflict with those of Kuykendall *et al.* where MOCVD growth of GaN nanowires was observed over a substrate temperature range of 800-1000°C.^{6,13} In the study, nanowire growth was also found to be independent of position. Thick nanowire coverage was found when the substrates were placed 1-10 cm away from the TMG inlet. These differences may be due to variations in reactor design and operating conditions. In the study by Kuykendall *et al.*, the experiments were also carried out in a hot-wall CVD reactor, however nitrogen was utilized as a carrier gas for the TMG source, and the experiments were completed at atmospheric pressure.

The effect of furnace temperature on GaN nanowire growth can be explained using the predicted GaN thin film growth rate profiles obtained from the CFD model (Figure 5.10). The predicted GaN thin film growth rate profiles were obtained at the quartz wall rather than the centerline of the quartz tube. As the furnace temperature is reduced, the maximum in the GaN thin film growth rate shifts farther away from the group III inlet. At 2 inches from the TMG inlet (red dotted line), which corresponds to the SEM images shown in Figure 5.9, the GaN thin film growth rate is close to its maximum value at 750°C but has dropped off considerably at 1000°C. At both of these temperature extremes, vapor-solid deposition was observed to be predominate over nanowire growth (Figure 5.9 (a) and (f)) at 2 inches from the TMG inlet. In the intermediate furnace temperature region from 800-900°C, GaN nanowire growth was observed (Figure 5.9 (b)-(d)). From the furnace temperature profiles (Figure 5.4), the gas phase temperature 2 inches from the group III inlet tube where GaN nanowire growth was observed ranges from ~620-720°C, providing further evidence that lower temperatures promote axial wire growth at these conditions.

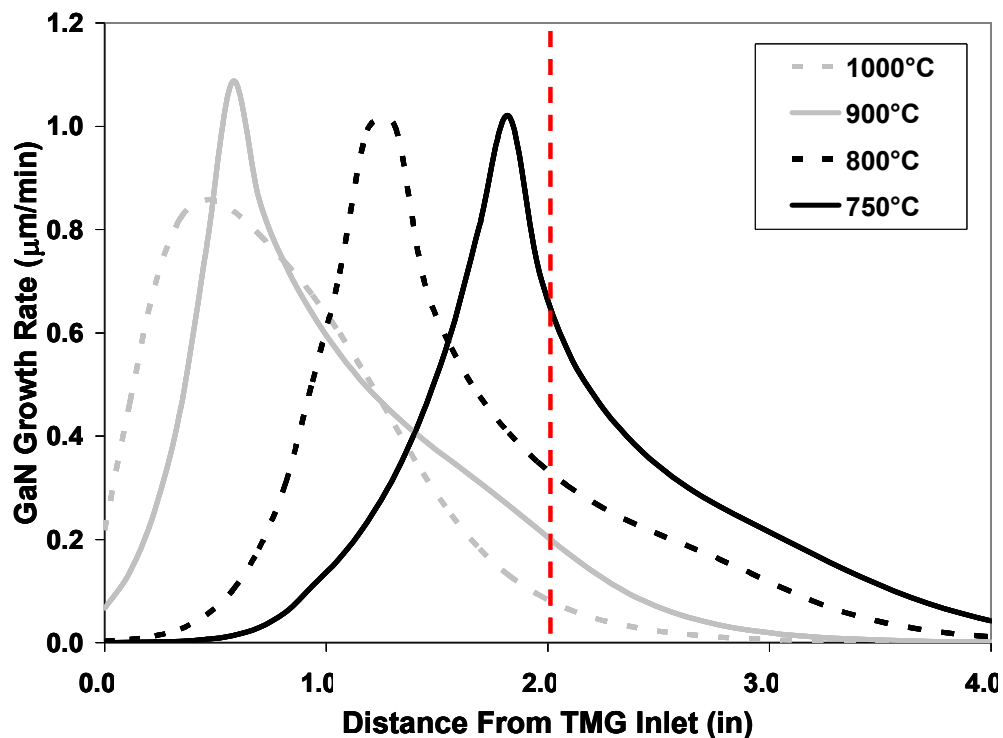


Figure 5.10: Model predictions of GaN thin film growth rate at the quartz tube wall for furnace temperatures of 750°C, 800°C, 900°C, and 1000°C. Red dotted line indicates 2 inches from TMG inlet. Growth conditions: 100 Torr, 3 sccm TMG, 100 sccm NH₃, 250 sccm H₂.

5.3.3 Effect of V/III Ratio

In the first set of experiments, the flowrate for TMG was increased from 1 sccm to 4 sccm while the NH₃ flowrate was maintained at 100 sccm. This resulted in a V/III ratio between 100 (1 sccm TMG) and 25 (4 sccm TMG). The furnace temperature set-point was held constant at 900°C ($T_s = 825^\circ\text{C}$), and the reactor pressure was held constant at 100 Torr with a H₂ carrier flowrate of 250 sccm. Figure 5.11 shows the variation in nanowire growth with respect to TMG flowrate at a position 2 inches from

the group III inlet. As the TMG flowrate increased, the nanowire density, diameter, and length increased. The supply of TMG has been shown to be the rate limiting step in GaN thin film growth by MOCVD.^{14,15} Therefore, by increasing the flux of TMG, the nanowire and thin film growth rates increase. There was a significant change in nanowire diameter and length between 2 sccm (Figure 5.11 (b)) and 3 sccm TMG (Figure 5.11 (c)). The change was not as noticeable between 3 sccm and 4 sccm TMG

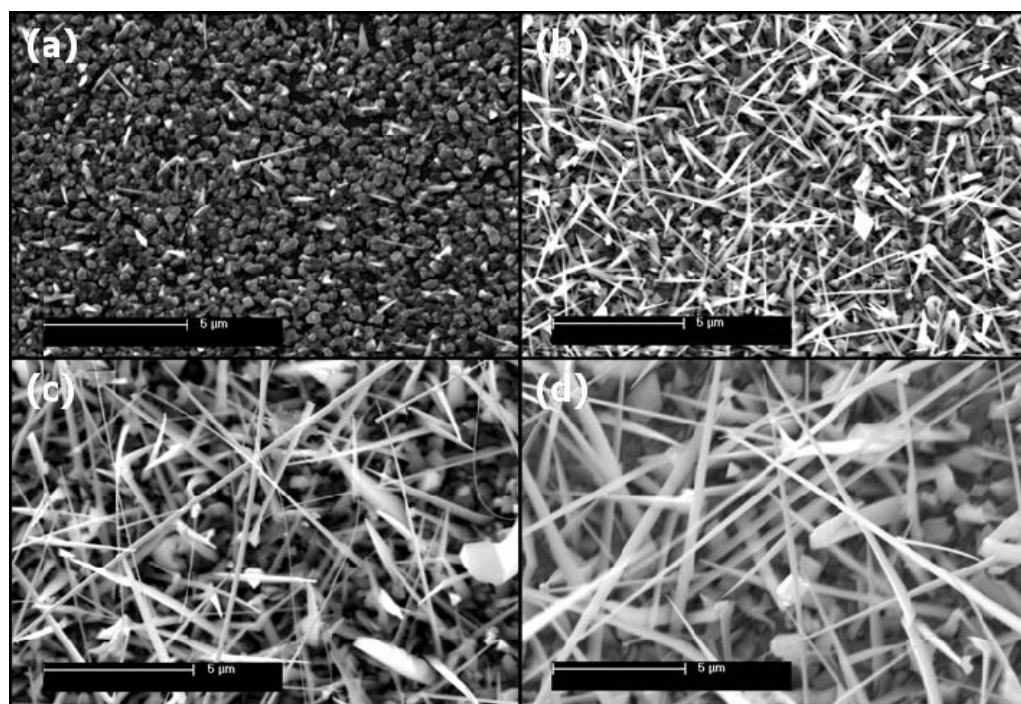


Figure 5.11: SEM images of GaN nanowire growth at (a) 1 sccm, (b) 2 sccm, (c) 3 sccm, and (d) 4 sccm TMG. Growth conditions: 900°C ($T_s = 825^\circ\text{C}$), 100 Torr, 100 sccm NH_3 , 250 sccm H_2 .

(Figure 5.11 (d)). For a TMG flowrate of 3 sccm, the average tip diameter was 63 ± 27 nm, the average base diameter was 210 ± 61 nm, and the average length was $9.5 \mu\text{m}$. For a TMG flowrate of 4 sccm, the average tip diameter was 68 ± 17 nm, the average base diameter was 323 ± 86 nm, and the average length was $12 \mu\text{m}$.

In the second set of experiments, the NH_3 flowrate was increased from 50 sccm to 200 sccm while the TMG flowrate was maintained at 3 sccm to vary the V/III ratio from 17 to 67. The furnace temperature set-point was held constant at 900°C ($T_s = 825^\circ\text{C}$), while the pressure was held constant at 100 Torr with a H_2 flowrate of 250 sccm. SEM images of the sample surface at a position of 2 inches from the TMG inlet are shown in Figure 5.12. Interestingly enough, increasing the NH_3 flowrate (V/III ratio) had the same effect as increasing the TMG flowrate, however the increase in nanowire density, diameter, and length was much more pronounced. This conflicts with the TMG flowrate

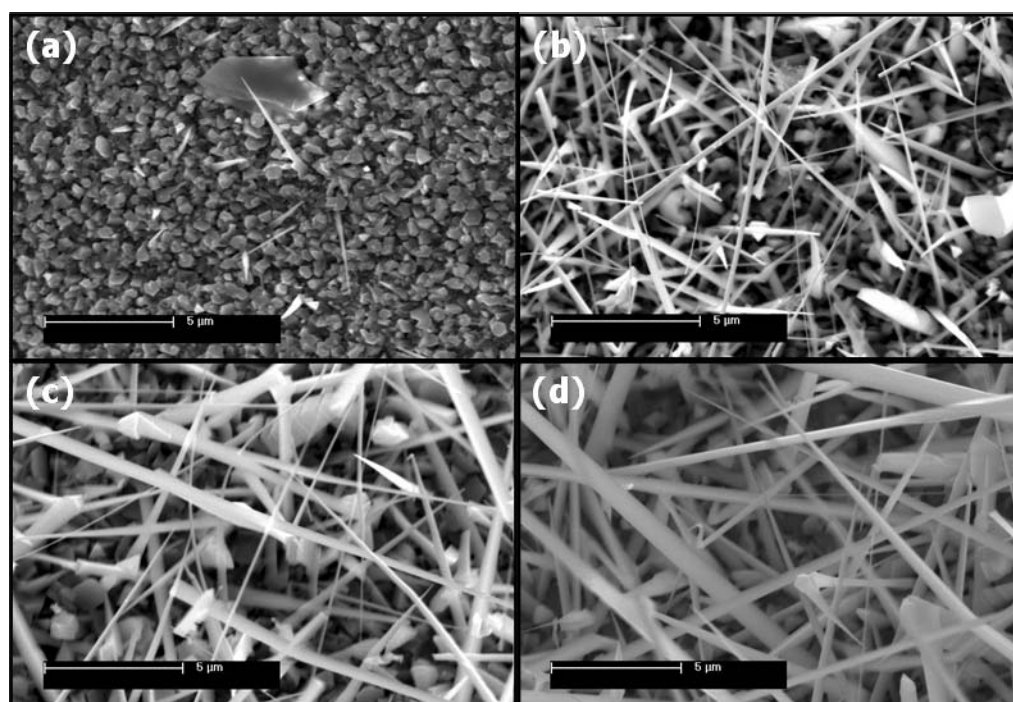


Figure 5.12: SEM images of GaN nanowire growth at (a) 50 sccm, (b) 100 sccm, (c) 150 sccm, and (d) 200 sccm NH_3 . Growth conditions: 900°C ($T_s = 825^\circ\text{C}$), 100 Torr, 3 sccm TMG, 250 sccm H_2 .

results as increasing the TMG flowrate led to a decrease in the V/III ratio. At a V/III ratio of 33 (100 sccm NH_3), the average diameter of the tip and base of the GaN

nanowires were 63 ± 27 nm and 210 ± 61 nm, respectively with an average length of $9\ \mu\text{m}$. When the V/III ratio was increased to 67 (200 sccm NH_3), the average diameter of the tip was 87 ± 22 nm, whereas the average base diameter and length climbed to 840 ± 282 nm and $38\ \mu\text{m}$, respectively.

An increase in the NH_3 flow rate will alter the properties of the gas phase mixture such as thermal conductivity and will also lead to an increase in the gas velocity. Figure 5.13 is a radial gas velocity profile at the growth front for NH_3 flowrates of 50 sccm and 200 sccm. The x-axis represents the centerline of the quartz tube furnace. By increasing the NH_3 flowrate from 50 sccm to 200 sccm, the gas velocity increased from 81 cm/sec to 114 cm/sec at the growth front. This along with a reduction in the gas phase mixture thermal conductivity impacts the extent of gas phase reactions and the GaN thin film growth rate. From the CFD model, it was found that as the V/III ratio is increased

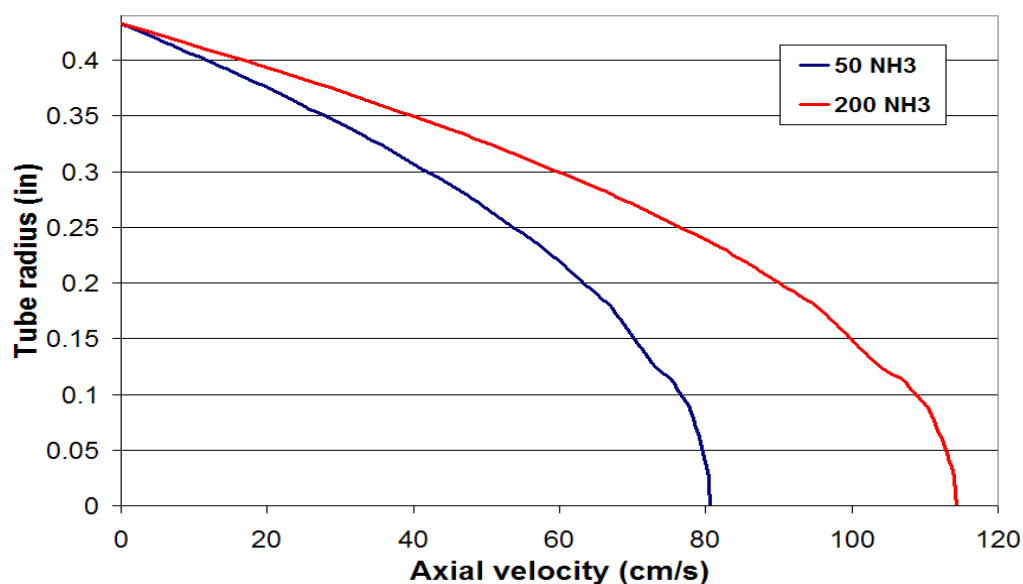


Figure 5.13: Radial gas velocity profile at growth front.

from 17 to 67, the GaN thin film growth rate increases at the location of the samples (Figure 5.14). The GaN thin film growth rate with a V/III ratio of 67 is approximately four times larger than that obtained at a V/III ratio of 17. This, in turn, results in an increase in the growth rate of the GaN nanowires as well as an increase in the degree of tapering of the wire diameter due to an increase in vapor-solid deposition on the nanowire surface during growth. The base diameter increases with NH_3 flowrate, whereas the tip diameter is not affected as it is not exposed to the thin film deposition. These results indicate that in this reactor geometry, lower V/III ratios (NH_3 flowrates) are advantageous for promoting axial nanowire growth over radial thin film deposition.

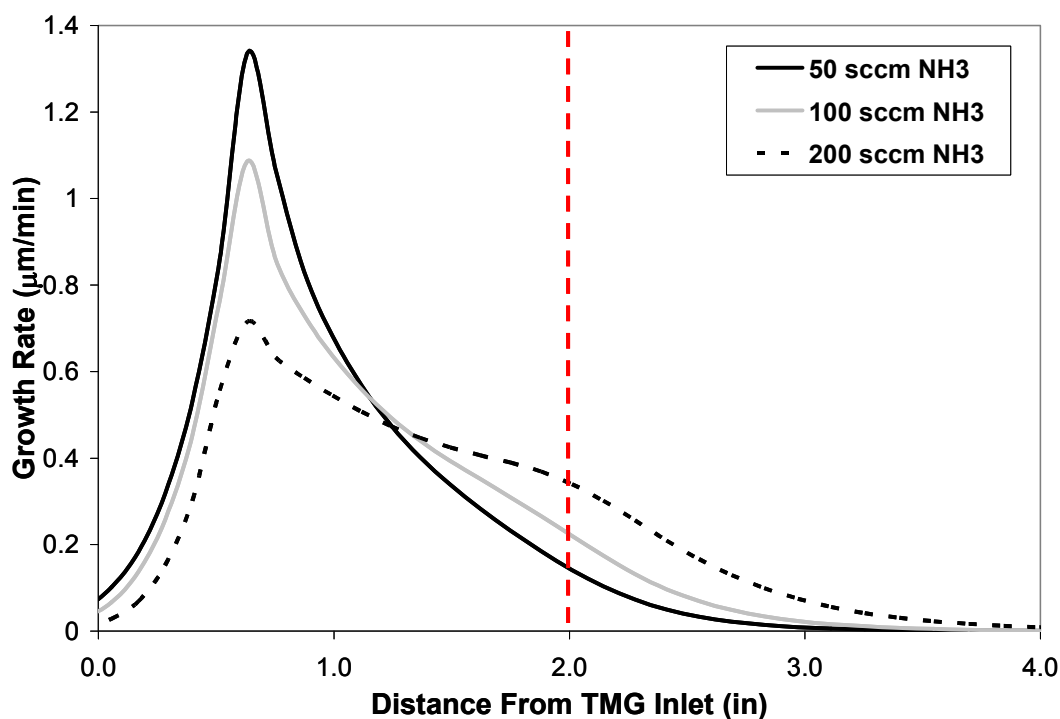


Figure 5.14: CFD model predictions for GaN thin film growth rate at quartz tube wall for NH_3 flowrates of 50, 100, and 200 sccm. Red dotted line indicates 2 inches from TMG inlet. Growth conditions: 900°C , 100 Torr, 3 sccm TMG, 250 sccm H_2 .

5.3.4 Effect of Carrier Gas

N_2 was investigated as a carrier gas instead of H_2 , since it has a low thermal conductivity compared to H_2 .¹⁶ By reducing the gas mixture thermal conductivity, the gas phase temperature would decrease, reducing the extent of gas phase reactions upstream of the substrate. Figure 5.15 shows the gas phase temperature profiles for H_2 as the carrier gas and N_2 as the carrier gas. A “cold finger” exists as shown in Figure 5.15 (b) due to the lower thermal conductivity of N_2 compared to H_2 . This is the case, because H_2 is also no longer present in the system, therefore the gas mixture thermal conductivity is significantly lower. By removing H_2 from the system and replacing it with N_2 , H_2 is no longer present to etch the GaN thin film growth.¹⁷⁻¹⁹ The combination of these two factors results in highly tapered structures that are several microns in diameter (Figure 5.16). As a result, H_2 is the proper choice as the carrier gas in order to achieve nanowire growth.

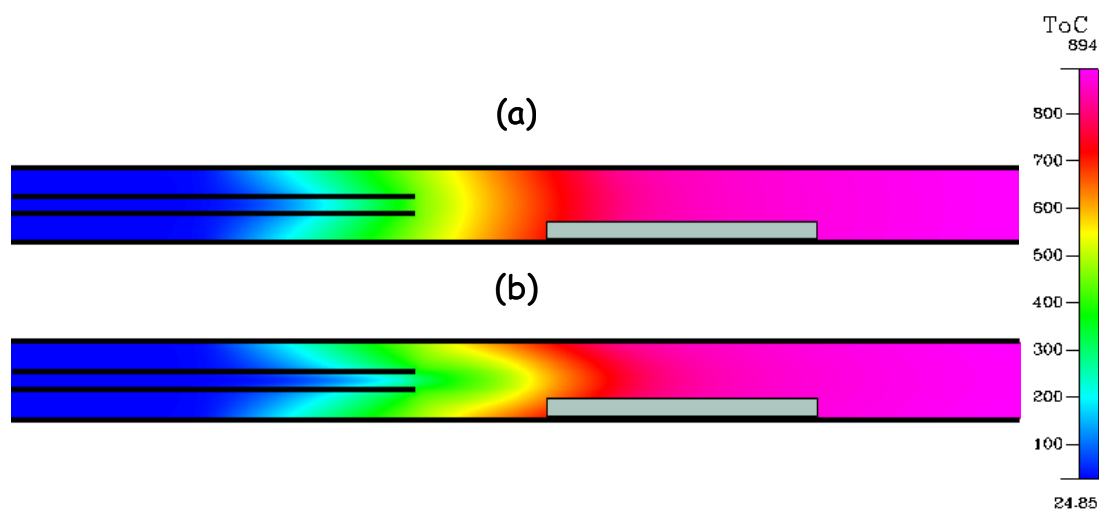


Figure 5.15: Gas phase temperature profile for (a) H_2 and (b) N_2 as the carrier gas. Gray rectangle is representative of location of quartz boat in tube furnace reactor.

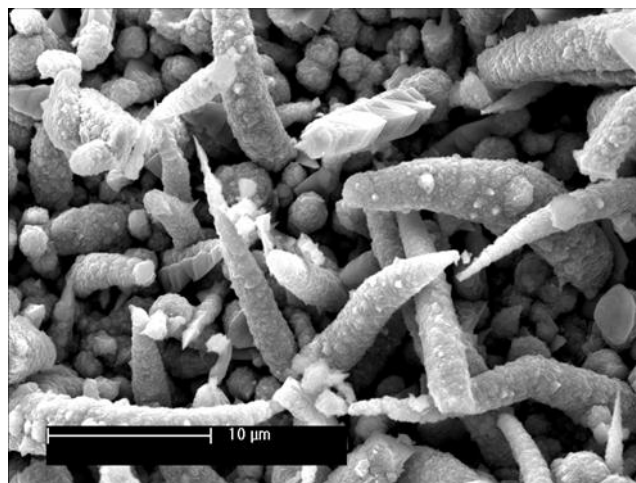


Figure 5.16: SEM image of GaN growth with N₂ as the carrier gas instead of H₂.

5.4 Characterization

5.4.1 VLS Growth Mechanism versus VSS Growth Mechanism

In VLS growth, a metal nanoparticle catalyst becomes a preferred site for deposition. A liquid alloy forms between the metal catalyst and the vapor. The liquid alloy becomes supersaturated, and crystal growth results by precipitation at the solid-liquid interface. The key to this process is the formation of a liquid alloy; therefore, it is pertinent to choose a metal catalyst which will form a liquid alloy with the precursor at the growth temperature. For GaN nanowire growth with Ni as the metal catalyst, literature reports suggest that the VLS mechanism is responsible for nanowire growth even though the growth temperature is significantly lower than the eutectic melting point.^{6,20,21} In general, the literature reports attribute the temperature difference to

melting point depression due to size effects at the nanoscale.^{9,22} The problem with this explanation is the fact that melting point reduction has only had a significant effect on nanoparticles with a diameter less than 10 nm.^{23,24}

In 2004, Persson *et al.*²⁵ suggested that the VLS growth mechanism was not responsible for growth of III-V nanowires under the conditions of their study. Instead, he proposed a solid-phase diffusion mechanism known as vapor-solid-solid (VSS) growth mechanism for the growth of GaAs nanowires with Au nanoparticles. Based on the Au-As phase diagram, one would not expect arsenic to incorporate into the Au catalyst due its limited solubility. Therefore, the formation of a liquid alloy would be dependent on the Au-Ga phase diagram. Persson *et al.* looked at the composition of the catalyst after growth of GaAs nanowires using XEDS point measurements of the seed particle to determine the Ga content. The seed particle was found to contain only 9 at.% Ga. According to the binary phase diagram for Au-Ga at a growth temperature of 540°C, the alloy would remain a solid since the composition is located below the eutectic melting point. As a result, GaAs nanowire growth was attributed to the presence of a solid-phase diffusion mechanism known as vapor-solid-solid growth. In VSS growth, the particle remains soluble with the gas phase constituents, however a liquid alloy never forms. Instead, the seed particle remains a solid alloy of Au and Ga, and As is incorporated into the wire at the interface between the seed particle and the nanowire. Since these findings, Samuelson has extended the VSS mechanism to other III-V nanowires such as InAs, InP, and GaP.^{26,27}

Based on these findings, it was pertinent to look at the Ni-Ga-N system in order to determine if the VLS or VSS mechanism is actually responsible for GaN nanowire

growth. Based on the Ni-N phase diagram and experimental results,⁵ N was found to be minimally soluble with Ni. As a result, N is expected to incorporate into the GaN nanowire at the interface between the seed particle and the nanowire. Therefore, the formation of a liquid alloy would be dependent on the Ni-Ga phase diagram. The Ni-Ga phase diagram is shown in Figure 5.17 along with the temperature range utilized in the GaN nanowire experiments (red dotted lines). According to the binary phase diagram,

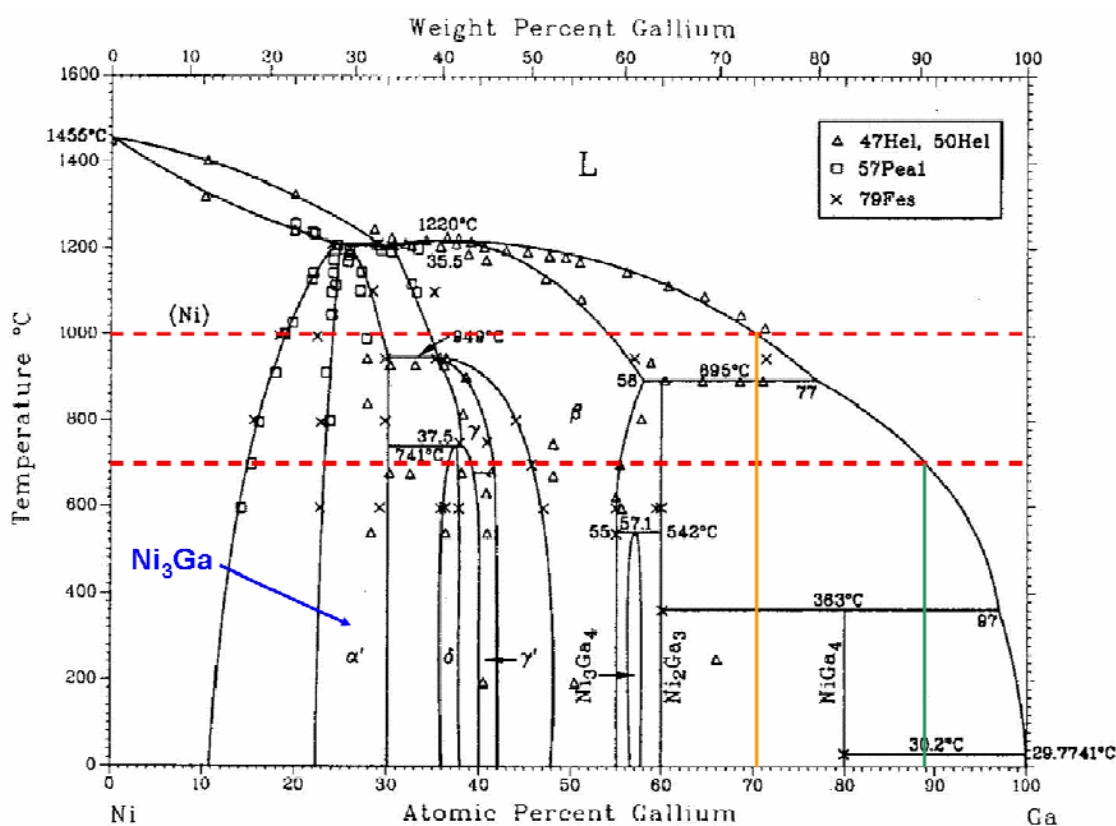


Figure 5.17: Ni-Ga binary phase diagram. The red dotted lines represent the upper (1000°C) and lower (750°C) limits of the temperature range used for GaN nanowire growth.⁵

the seed particle would have to consist of approximately 71 at.% Ga at the upper limit of the temperature range (1000°C) for a liquid alloy to be present (orange line). The

concentration increases to 89 at.% Ga at the lower limit (750°C) of the GaN nanowire temperature range (green line). At the same time, the upper limit for the temperature range is approximately 200°C lower than the eutectic melting point (1207°C). Based on these observations, it appears highly unlikely that a liquid alloy was present. This suggests that the vapor-solid-solid growth mechanism may be responsible for the GaN nanowire growth rather than the vapor-liquid-solid mechanism.

In order to investigate this theory, TEM characterization was performed in order to take an in-depth look at the Ni catalyst. Figure 5.18 is a high-angle annular dark-field (HAADF) image of a typical GaN nanowire with a Ni catalyst. The growth conditions for this sample were 900°C ($T_s = 825^\circ\text{C}$), 100 Torr, 3 sccm TMG, and 100 sccm NH_3 . A selected area diffraction pattern was taken of the nanowire, and the growth direction was determined to be $[11\bar{2}0]$. The contrast in the GaN nanowire most likely is due to the nanowire having a triangular cross-section along with thickness fringes being present due

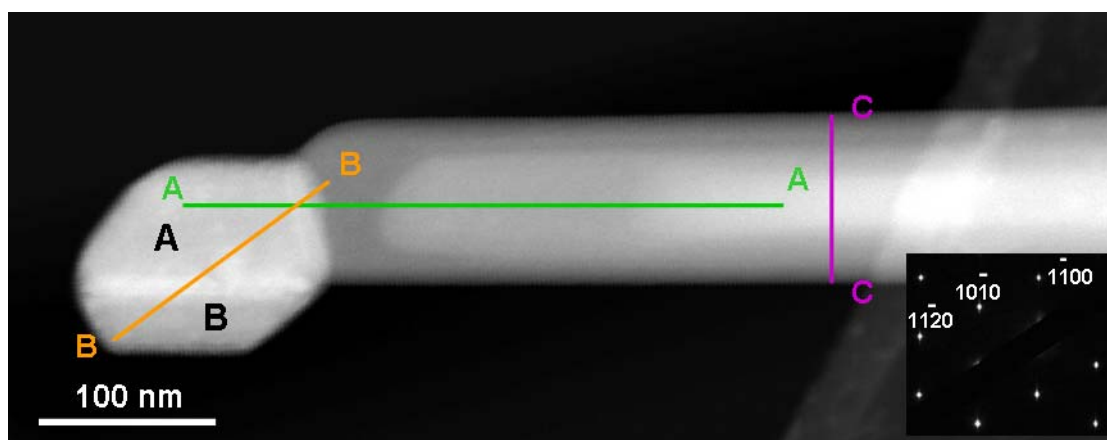


Figure 5.18: High-angle annular dark-field (HAADF) STEM image of a GaN NW with Ni catalyst. The image was collected along the GaN 0002 zone axis. Insert is a selected area diffraction (SAD) pattern of the GaN nanowire. The growth direction of the nanowire is $11\bar{2}0$. Growth conditions: 900°C ($T_s = 825^\circ\text{C}$), 100 Torr, 3 sccm TMG, 100 sccm NH_3 .

to tapering of the GaN nanowire. The Ni seed particle also appears to be faceted which is indicative of the formation of an intermetallic compound.²⁸

In order to observe the composition of the nanowire and catalyst, composition line scans were performed along the axis of the nanowire (A-A) and through the catalyst (B-B). An additional line scan was performed along the cross-section of the nanowire (C-C) in order to determine its homogeneity. The seed particle was found to contain both Ga and Ni with the Ni composition decreasing sharply near the particle/nanowire interface (Figure 5.19 (a) and (b)). The Ga peak intensity changes that occur near 120 nm and 300

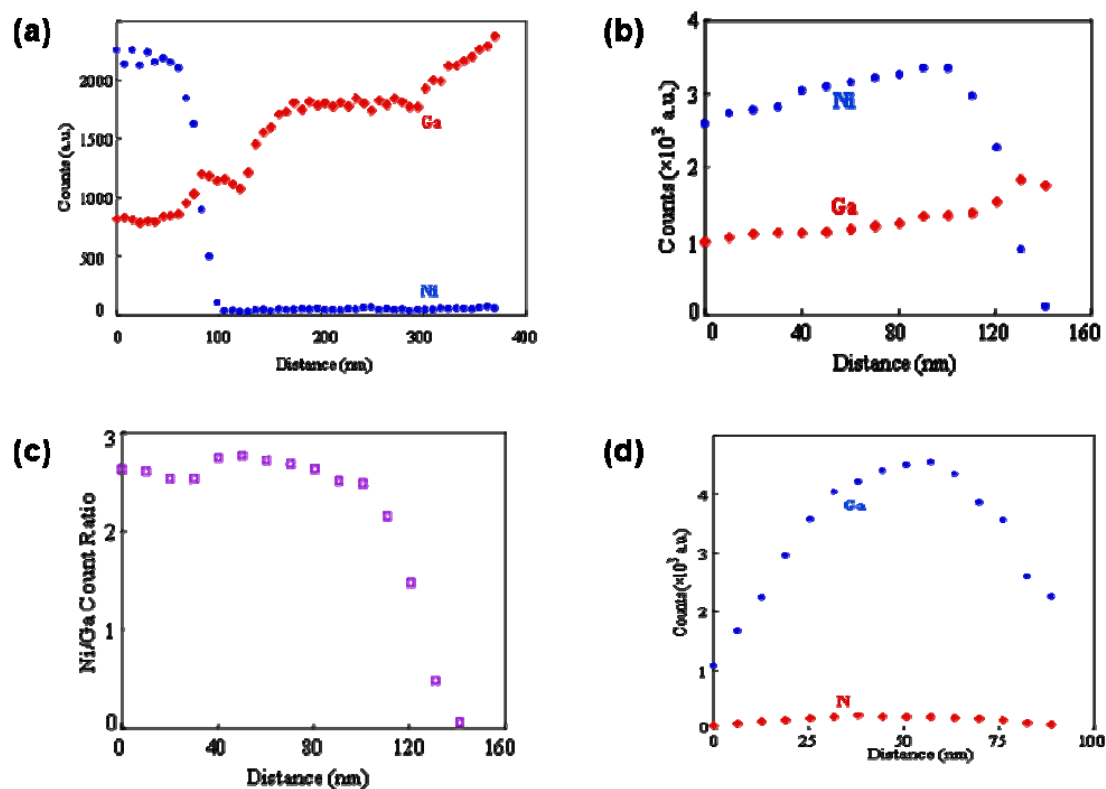


Figure 5.19: (a) Composition line profiles of A-A and (b) B-B in Figure 5.18. (c) Ratio of Ni to Ga peak intensities along B-B. (d) Composition line profile of C-C in Figure 5.18.

nm are mostly likely due to thickness changes of the GaN nanowire. For the cross-section line scan, the Ga and N counts peak at the midpoint due to the nanowire being thickest at this point as a result of the triangular cross-section (Figure 5.19 (d)). The Ni/Ga ratio for the line scan through the catalyst was calculated with respect to position and was found to be 2.79 ± 0.05 (Figure 5.19 (c)).

To determine if there is any significance to the Ni/Ga ratio that was observed, selected area diffraction (SAD) was performed on the Ni catalyst particle (Figure 5.20). Diffraction spots for both the nanowire and catalyst were observed, since SAD was collected from regions containing both the particle and GaN nanowire. The SAD pattern for the seed particle resembles a cubic structure, and the lattice parameter of the particle

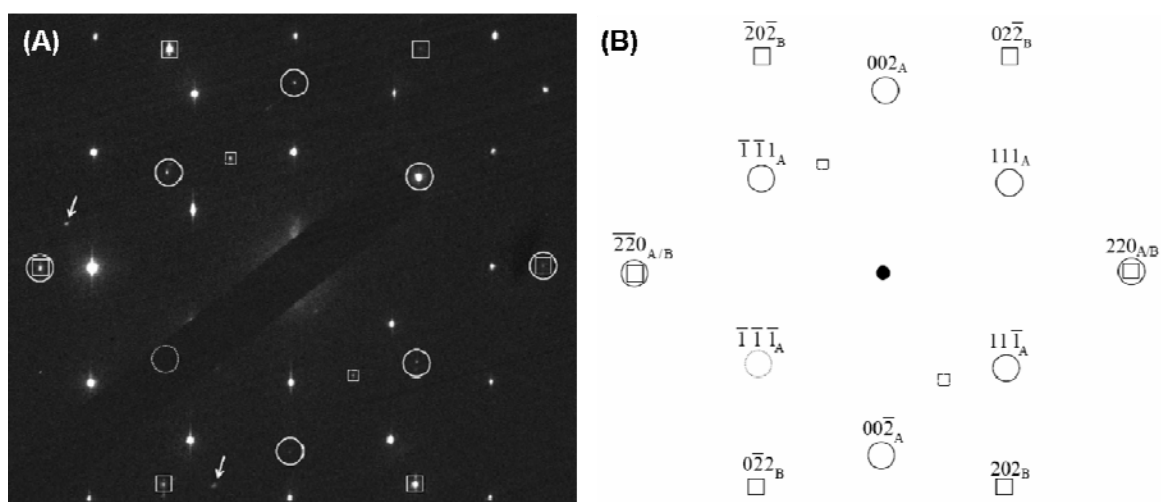


Figure 5.20: (a) SAD pattern collected from a region consisting of the NW and the catalyst particle. As shown in Figure 5.18, the main part of the catalyst particle contains two Ni_3Ga grains A and B. Extra diffraction spots not associated with the Ni_3Ga structure are indicated by the arrows. (b) Indices of the diffraction spots from the catalyst particle shown in (a). Two sets of diffraction spots were identified corresponding to grains A and B in Figure 5.18. The crystallographic correlations between the NW and the catalyst particle are $110_A // 110_B // 11\bar{2}_{\text{NW}}$, $002_A // \bar{1}1\bar{2}_B // 1\bar{1}00_{\text{NW}}$, and $1\bar{1}0_A // \bar{1}\bar{1}1_B // 0002_{\text{NW}}$.

was found to vary between 3.578 Å (0.3578 nm) and 3.597 Å (0.3597 nm) depending on the nanowire sample. The average lattice parameter for this condition was 3.584 Å (0.3584 nm).

Looking at data for various Ni-Ga intermetallic compounds (Table 5.1), the lattice parameter matches well with Ni₃Ga. This also corresponds well with the Ni/Ga ratio observed in Figure 5.19 (c) and previous studies concerning Ni₃Ga.²⁹⁻³¹ Ni₃Ga has also been previously observed for Ni-assisted MBE growth of GaN nanowires.³² The fact

Table 5.1: Lattice parameter data of various Ni-Ga intermetallic compounds.⁵

Phase	Composition (%Ga)	Lattice Parameter (nm)		
		a	b	c
(Ni)	0	0.3524	---	---
(Ni)	28	0.359	---	---
α' (Ni ₃ Ga)	26	0.3585	---	---
β (NiGa)	50	0.2873	---	---
β (NiGa)	51.6	0.288861	---	---
γ (Ni ₃ Ga ₂)	35.5	0.4002	---	0.4988
γ (Ni ₃ Ga ₂)	40	0.3995	---	0.498
δ (Ni ₅ Ga ₃)	36	0.376	---	0.339
γ' (Ni ₃ Ga ₂)	41	1.3785	0.7883	0.8457
Ni ₃ Ga ₄	55.5	1.141	---	---
β' (Ni ₂ Ga ₃)	60	0.405	---	0.489
ε (NiGa ₄)	70	0.842	---	---
ε (NiGa ₄)	80	0.8406	---	---
(Ga)	100	0.451	0.764	0.451

that the ratio is not quite 3:1 could be due to the omission of the k-factor for each constituent associated with the XEDS line scan or the knowledge that Ni₃Ga tends to be non-stoichiometric due to vacancies.³³ The catalyst particle for this nanowire was found to contain two Ni₃Ga grains indicated as A and B (Figure 5.18). The diffraction spots that are representative of each of these grains are shown in Figure 5.20 (a) and are

identified in Figure 5.20 (b). Extra diffraction spots which are indicated by arrows in Figure 5.20 (a) are not associated with the Ni_3Ga structure but rather an unidentified phase in the interface layer between the particle and the nanowire. The small squares in Figure 5.20 which are not identified are weak superlattice reflection spots of the ordered L1_2 structure of Ni_3Ga . These spots help to distinguish Ni_3Ga from the face-centered cubic Ni-Ga solid solution.

Looking back at the Ni-Ga phase diagram (Figure 5.17), Ni_3Ga is only present over a range of 23-30 at.% Ga. As was previously indicated, a liquid alloy wouldn't form until the composition consisted of 71 at.% Ga at 1000°C and 89 at.% Ga at 750°C. Examining a magnified view of the Ni_3Ga region (Figure 5.21), the eutectic melting point is located at 1207°C at 29.5 at.% Ga. This value is roughly 300°C higher than the highest furnace temperature at which GaN nanowire growth was achieved. Based on the presence of Ni_3Ga and the high eutectic melting point, it seems very unlikely that the vapor-liquid-solid mechanism is responsible for the GaN nanowire growth. Instead, it appears as though the vapor-solid-solid mechanism is a more likely candidate and that GaN nanowire growth follows the same route of growth as other III-V nanowires.³⁴ Additional TEM analysis in the next section provides further support for the VSS mechanism rather than the VLS mechanism.

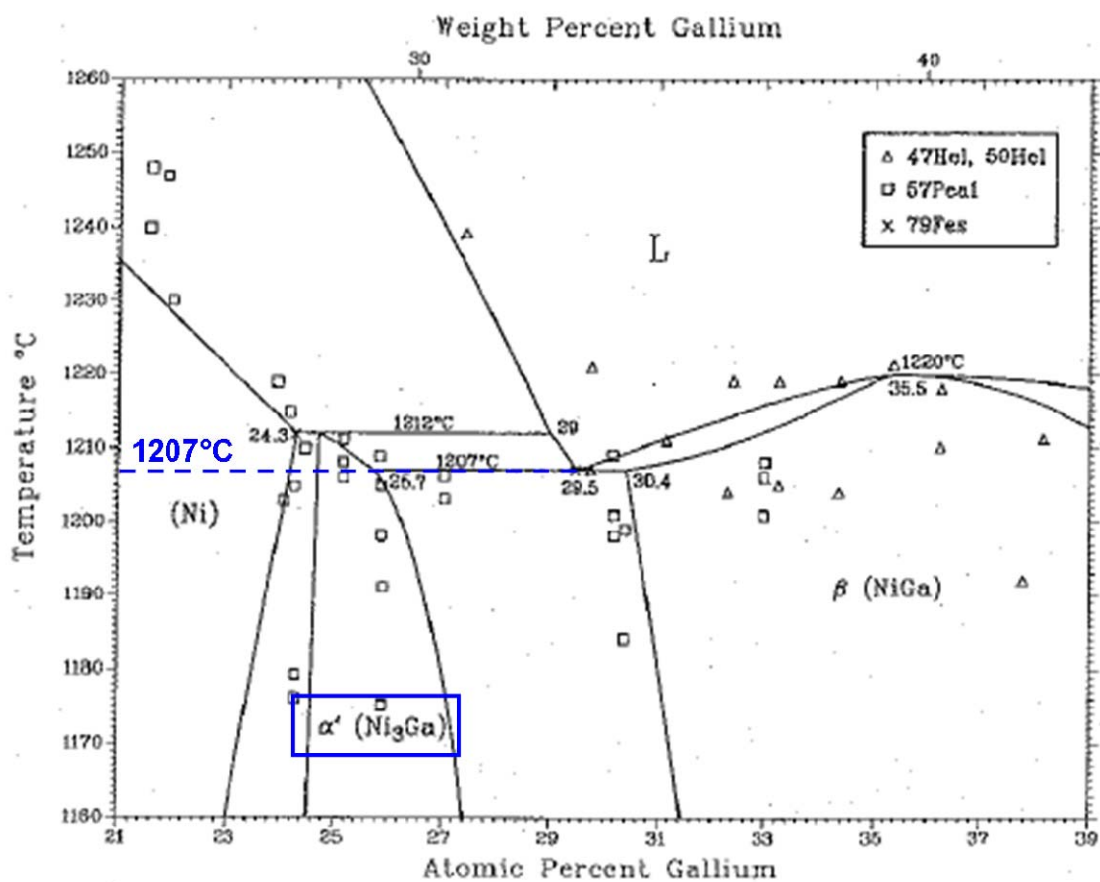


Figure 5.21: Ni-Ga binary phase diagram over range of 21 at.% to 39 at.% Ga. Eutectic melting point is located at 1207°C.⁵

5.4.2 Transmission Electron Microscopy

Based on the SEM results, the highest quality nanowires appeared to be grown with the following conditions: 900°C ($T_s = 825^\circ\text{C}$), 100 Torr, 3 sccm TMG, and 100 sccm NH_3 . As a result, initial TEM characterization was performed on a sample with these conditions. Typical GaN nanowires grown at these these conditions are shown in Figure 5.22. For both nanowires, a faceted catalyst particle was observed at the tip of the

GaN nanowire as was the case in the previous analysis of this sample (Figure 5.18). The SEM inset shows the triangular cross-section of the nanowire which is commonly seen for GaN nanowire growth.^{6,35} Selected area diffraction was also performed on these nanowires, and the nanowires were found to be single crystalline wurtzite GaN with a predominant growth direction of $[11\bar{2}0]$ which is a common growth direction observed in MOCVD-grown GaN nanowires.^{6,36} The secondary growth direction appeared to be $[1\bar{1}00]$ which has also been observed for GaN nanowires.^{37,38} The GaN nanowires exhibited tapering with a tip diameter of 63 ± 28 nm and a base diameter of 210 ± 61 nm. These measurements were done on 21 nanowires that were removed from the substrate

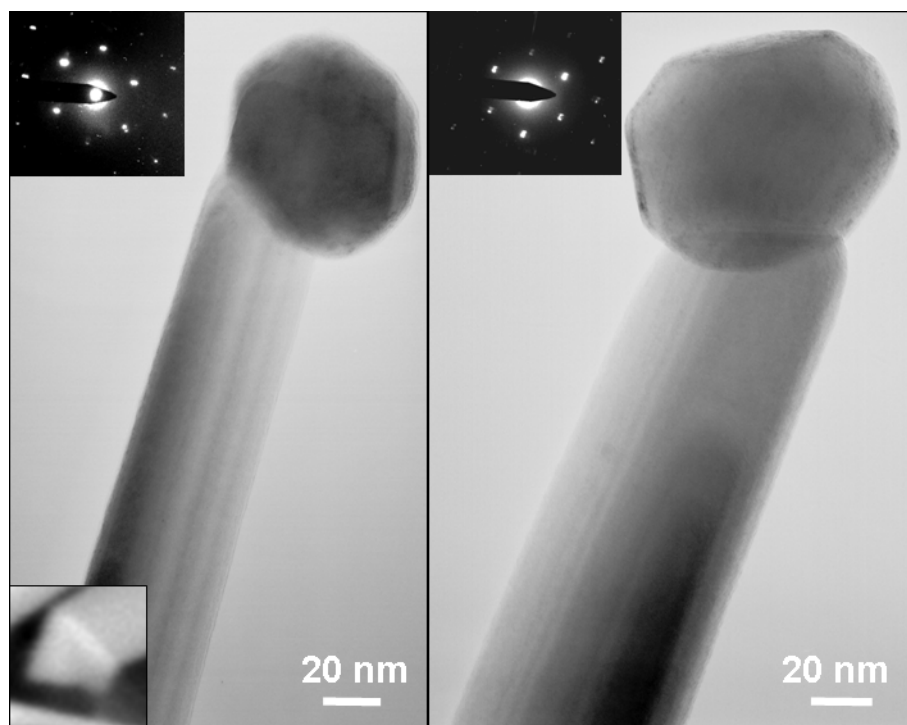


Figure 5.22: TEM images of GaN nanowires. Inset of SEM image showing triangular cross-section of nanowire. Additional insets are selected area diffraction patterns of the nanowires. Growth conditions: 900°C ($T_s = 825^{\circ}\text{C}$), 100 Torr, 3 sccm TMG, 100 sccm NH_3 .

surface by sonication and transferred to a TEM grid. In general, the diameter of the nanowires appeared to be slightly smaller than the diameter of the Ni catalyst. The variation in diameter is due to the polydispersity in Ni nanoparticle diameter after annealing of the Ni film. The base diameter value is less certain due to the fact that the nanowire removal may have caused the wires to break from the substrate at random locations along their length.

As was previously noted, one issue concerning MOCVD growth of GaN nanowires is the presence of a competing thin film (vapor-solid mechanism) growth along with the vapor-solid-solid (VSS) nanowire growth (Figure 5.23). This competition leads to tapering of the GaN nanowire diameter as shown in Figure 5.5 (a). As the nanowire grows, vapor-solid growth occurs on the side walls of the nanowire. The base of the nanowire was exposed to this deposition for the entire length of the growth time. The tip of the nanowire, however, had minimal exposure to the thin film deposition. As a result, the tip's diameter is dependent on the nanoparticle catalyst size, whereas the base diameter of the nanowire is dependent on both the nanoparticle catalyst size and the thin film deposition rate.

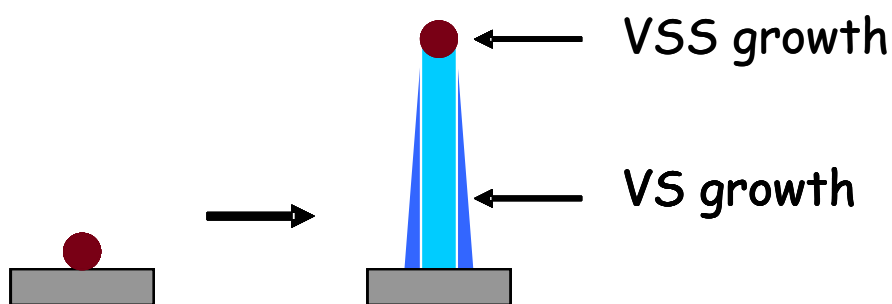


Figure 5.23: Schematic of the competition between vapor-solid-solid (VSS) growth of the nanowire and the vapor-solid (VS) deposition on the sidewalls of the nanowire.

As was previously mentioned, there is uncertainty in the accuracy of the base diameter due to the fact that the nanowires did not necessarily break at the substrate during sonification. This is also valid for nanowire length as the length varied from 2-24 μm . To obtain a better idea of the degree of tapering, a simple equation was used:

$$\text{Tapering} = \frac{R_{\text{Base}} - R_{\text{Tip}}}{\text{Length}} \quad \text{Eq. 5-1}$$

The radius of the tip was subtracted from the radius of the base and divided by the length of the nanowire. The typical degree of tapering was 10 nm/ μm ; however, the degree of tapering varied from 4 to 46 nm/ μm . A possible explanation for the spread in tapering is the variation in the growth direction of the nanowires within the sample. A change in growth direction would lead to a change in the axial growth rate and possibly a change in the radial growth rate as different side wall facets would be present.³⁹

Additional XEDS under STEM mode and SAD (not shown) were carried out on this sample in order to verify the observations and conclusions made in the previous section. A HAADF STEM image of another nanowire from this sample is shown in Figure 5.24 (a). Composition line profiles were obtained of the GaN nanowire in Figure 5.24 (a) through different segments of the seed particle (A-A and B-B). The results, shown in Figure 5.24 (b) and (c), reveal an abrupt change in the Ni intensity at the interface between the nanowire and the catalyst. The Ni/Ga ratios were calculated for the line profiles A-A and B-B, and the count ratio was found to be relatively constant at a value close to 3:1 (Figure 5.24 (d) and (e)) further supporting the previous results.

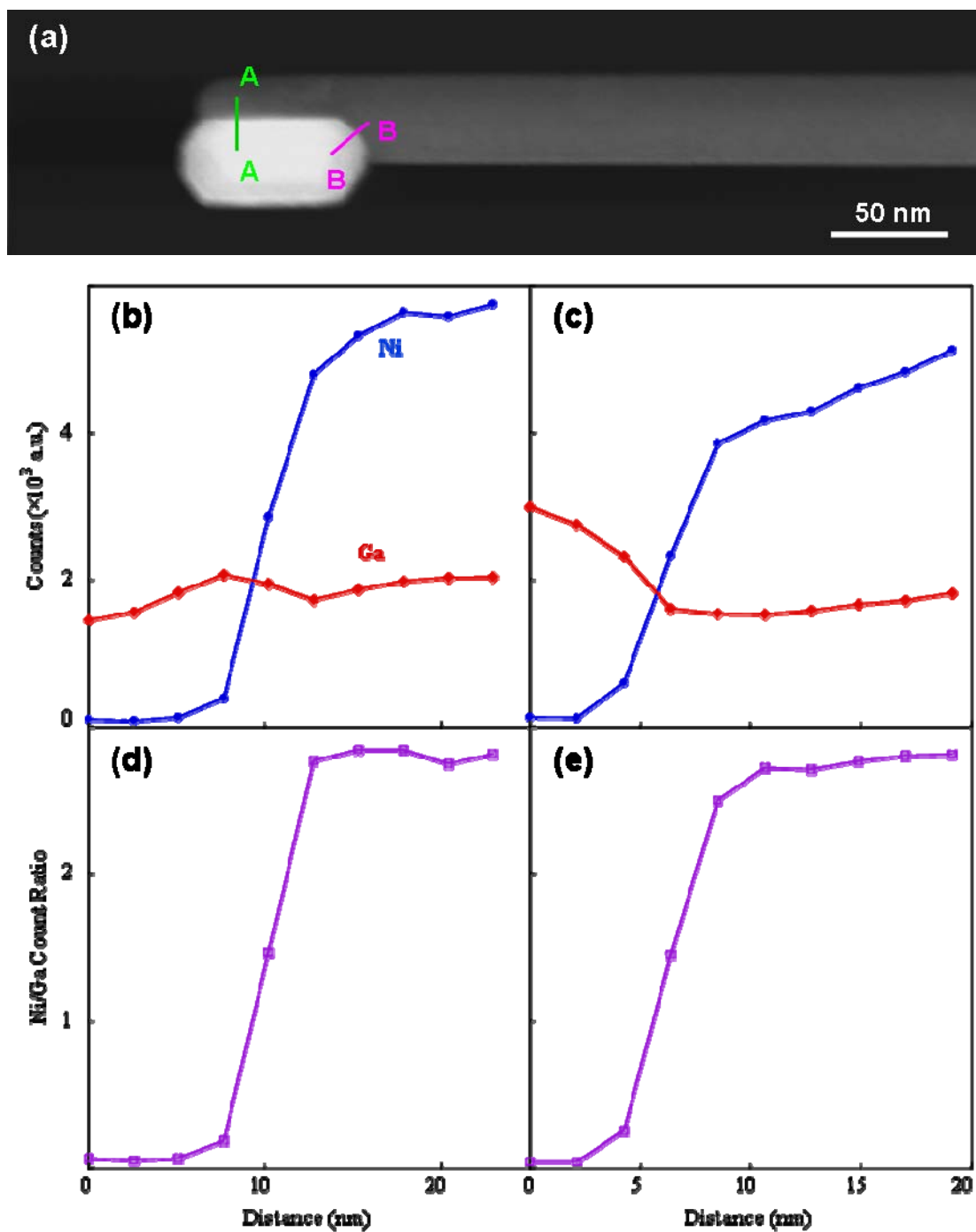


Figure 5.24: (a) High-angle annular dark-field (HAADF) STEM image of a GaN nanowire grown by MOCVD using a Ni catalyst. The image was collected along the GaN 1100 zone axis. Composition line profiles along (b) A-A and (c) B-B. Ni peak count to Ga peak count ratio for composition line profile for (d) A-A and (e) B-B. Growth conditions: 900°C ($T_s = 825^\circ\text{C}$), 100 Torr, 3 sccm TMG, 100 sccm NH_3 .

Emispec ES Vision software (FEI Company) was also employed to obtain an estimate of the Ga concentration within the catalyst. The ES Vision Standardless Quantification method was used to determine the composition ratio of each element present in the particle. The composition ratio of the catalyst is determined by multiplying the intensity ratio by a k-factor which is theoretically determined for each constituent. The k-factor for the alloy is determined by the following equation:

$$k(AB) = \frac{k(B)}{k(A)} \quad \text{Eq. 5-2}$$

where k(A) and k(B) are the k-factors for elements A and B. The theoretical k-factors for Ga and Ni are 2.832 and 3.116, respectively. Once the k-factor for the alloy has been calculated, the composition ratio of the alloy is determined by the following equation:

$$\frac{C(A)}{C(B)} = k(AB) \times \frac{I(A)}{I(B)} \quad \text{Eq. 5-3}$$

where C(A) and C(B) are the compositions of element A and B, and I(A) and I(B) are the intensity values for element A and B which are obtained from the XEDS line scans. Based on the k-factors for Ga and Ni, the Ga content was found to vary between ~24.4 at.% and ~26.8 at.% for the seed particle. Based on the Ni-Ga phase diagram (Figure 5.21), this places the Ga content within the range observed for Ni₃Ga. SAD analysis (not shown) performed on the catalyst particle confirmed that the particle was single crystalline Ni₃Ga with a lattice parameter of approximately 0.36 nm.

Once the initial characterization was complete, TEM analysis was carried out on GaN nanowire samples at lower growth temperatures (850°C), higher TMG flowrates (4 sccm), and higher NH₃ flowrates (200 sccm) in order to observe how the growth

conditions affected the structural properties of the nanowires. Figure 5.25 is an example of a nanowire grown at a temperature of 850°C ($T_s = 775^\circ\text{C}$). For this sample, the catalyst is faceted just as was the case for the sample at 900°C ($T_s = 825^\circ\text{C}$), and there appears to be the presence of an oxide surrounding the catalyst and nanowire, which most likely formed after exposure to the atmosphere. In Figure 5.25 (a), the seed particle and nanowire appear to overlap based on the contrast seen within the particle. This fact becomes more evident in the high resolution TEM (HRTEM) image in Figure 5.25 (b). On the right side of the particle, moiré fringes are present due to the overlapping of the particle and the nanowire. The oxide surrounding the catalyst and nanowire can also be seen clearly in this image as well as in Figure 5.25 (c). The oxide appears to be roughly 4-5 nm thick for this sample. In the HRTEM image in Figure 5.25 (c), the $\{200\}$ lattice fringes of the Ni_3Ga grain can be seen.

Selected area diffraction (not shown) was collected from a region consisting of the nanowire and Ni particle. Double diffraction spots were observed due to the overlapping of the nanowire and particle. The diffraction spots from the particle were indexed as being Ni_3Ga . The particle was found to be single crystalline with an average lattice parameter of 0.3566 nm. XEDS line scan (not shown) was taken through the catalyst, and the Ni/Ga count ratio was found to be approximately 2.52 ± 0.16 . This value is contradicting, because a lower Ga content would be expected since the lattice parameter was found to be smaller than in the samples grown at 900°C (0.3578-0.3597 nm).⁵ This observation could be explained by error associated with the XEDS measurements due to the overlap that occurs between the nanowire and the particle. SAD was also captured from three nanowires in order to look at the growth direction. Two of

the nanowires were found to have a growth direction of $[11\bar{2}0]$, while the other nanowire had a growth direction of $[1\bar{1}00]$.

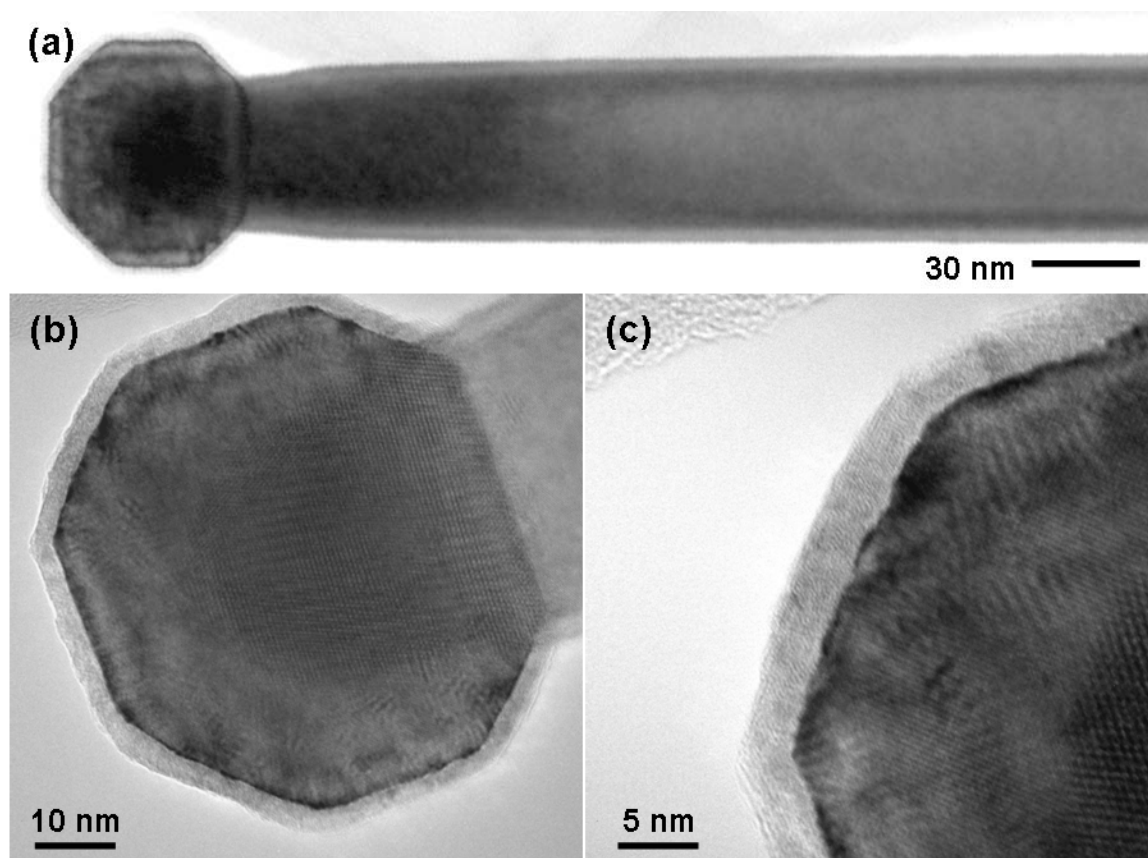


Figure 5.25: (a) Bright-field image of a GaN nanowire grown by MOCVD using Ni catalyst. The image was collected along the GaN 0002 zone axis. (b) HRTEM image of overlapping between particle and nanowire. Moiré fringes can be seen on the right side of the particle due to the overlapping. (c) Higher magnification image of the particle showing $\{200\}$ lattice fringes of Ni_3Ga . Growth conditions: 850°C ($T_s = 775^\circ\text{C}$), 100 Torr, 3 sccm TMG, 100 sccm NH_3 .

As was mentioned above, a higher Ga content is expected to lead to a larger lattice parameter for the Ni_3Ga phase along with a lower Ni/Ga ratio. In order to investigate this effect, TEM characterization was completed on a sample grown at a higher TMG flowrate (4 sccm) as shown in Figure 5.26 (a). One difference between this

sample and the previous samples is the fact that the catalyst particle isn't nearly as faceted. The particle and nanowire, however, are found to overlap with one another based on the viewing plane. This can clearly be seen in Figure 5.26 (b) where moiré fringes are present in the area where the overlapping occurs. Arrows on the image indicate where the interface between the particle and nanowire begins. A higher magnification image of the particle is displayed in Figure 5.26 (c). The markings on the image indicate the $\{111\}$ lattice fringes of Ni_3Ga .

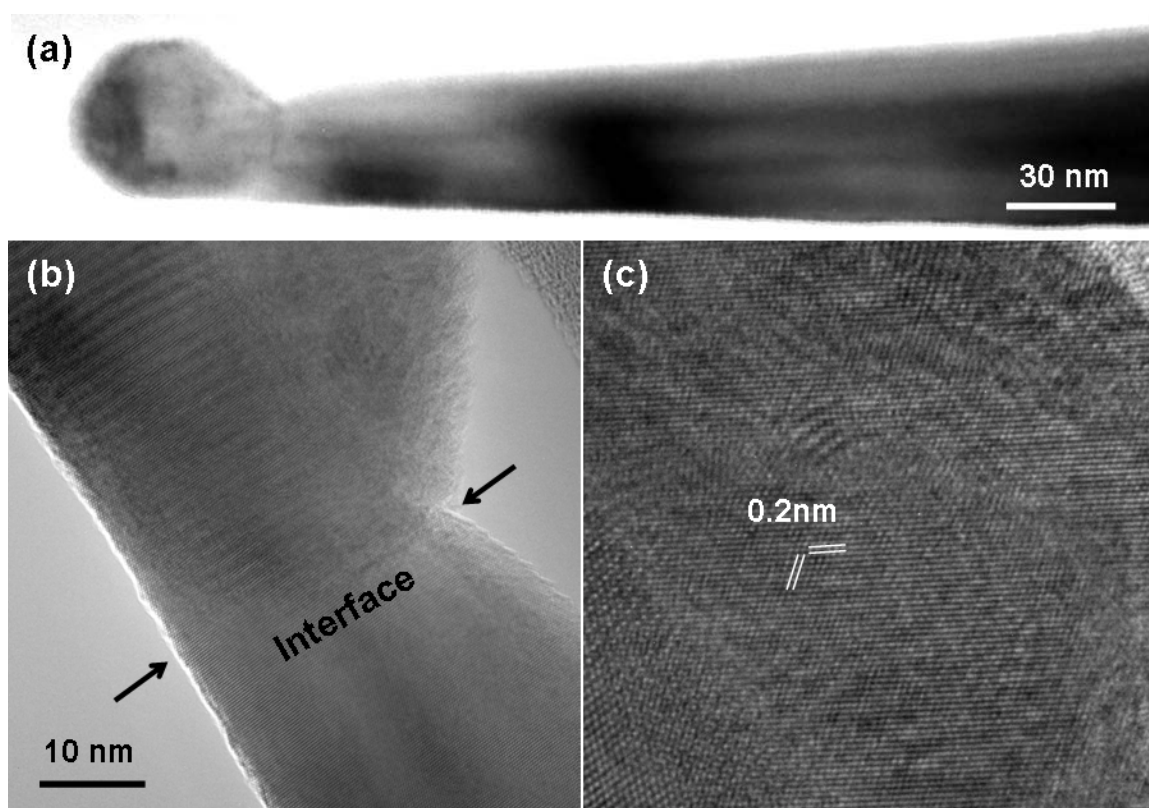


Figure 5.26: (a) Bright-field image of a GaN nanowire grown using Ni as the catalyst.. The image was collected along the GaN 0002 zone axis. (b) HRTEM image collected near the particle. Moiré fringes that resulted from the overlapping of the particle and the nanowire are evident in the left half of the particle. (c) Higher magnification image of the particle showing $\{111\}$ lattice fringes of Ni_3Ga . Growth conditions: 900°C ($T_s = 825^\circ\text{C}$), 100 Torr, 4 sccm TMG, 100 sccm NH_3 .

SAD and XEDS were also carried out on this sample. SAD (not shown) was collected from an area that consisted of just the nanowire as well as both the nanowire and seed particle. The growth direction was obtained for four nanowires. The growth direction was $[11\bar{2}0]$ for two of them and $[1\bar{1}00]$ for the other two nanowires. The particle was found to be single crystalline and was indexed to Ni_3Ga . The average lattice parameter for this sample was found to be larger than previous samples at a value of 0.3621 nm. A composition line profile was obtained through the nanoparticle, and the Ni/Ga peak intensity ratio decreased to 2.56 ± 0.14 . These observations correlate well with experimental data relating the lattice constant of Ni_3Ga to the Ga content (Figure 5.27). The lattice parameter is expected to increase as the Ga content within the catalyst increases. Increasing the TMG flowrate to 4 sccm leads to a higher incorporation of Ga within the seed particle, since more gallium is available for reaction. This is evidenced by the increase in average lattice parameter from 0.3584 nm at 3 sccm TMG to 0.3621 at 4 sccm TMG and the respective decrease in the Ni/Ga ratio from 2.79 ± 0.05 to 2.56 ± 0.14 .

Finally, TEM characterization was executed on a sample grown at a higher NH_3 flowrate. This sample is of particular interest based on the SEM findings when the NH_3 flowrate was varied (Figure 5.12). In those findings increasing the NH_3 flowrate, led to a dramatic increase in the length and diameter of the GaN nanowires. Possible conclusions as to why this occurred surrounded around an increase in the gas phase velocity, decrease in the thermal conductivity of the gas phase mixture, and an increase in the deposition rate due to higher NH_3 flowrates.

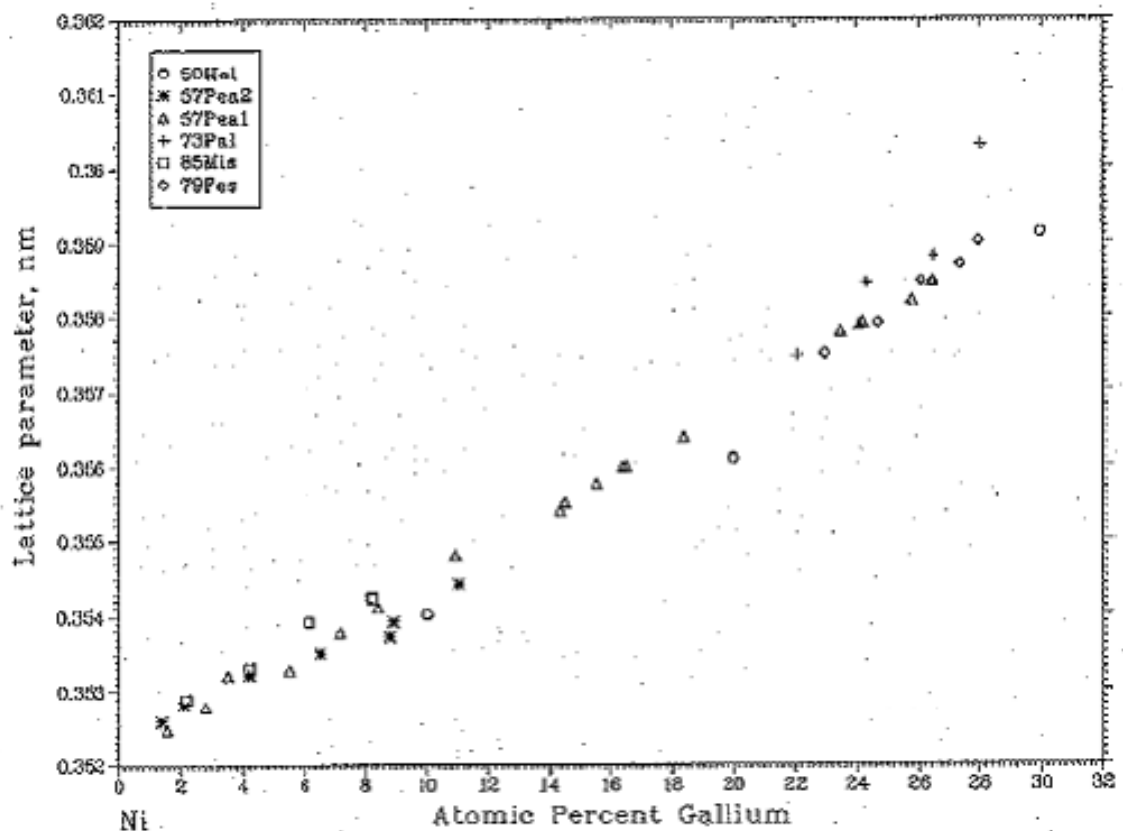


Figure 5.27: Lattice parameter of the (Ni) and α' (Ni_3Ga) phases as a function of Ga composition.⁵ Data is presented for the (Ni) phase from 0-23 at.% Ga. Data is presented for the α' (Ni_3Ga) phase from ~23-32 at.% Ga.

Another possible reason may be a change in the nanowire growth direction. The NH_3 flowrate has been observed to affect the growth orientation and morphology of GaN nanowires.^{40,41} If this were true, the axial (nanowire) growth rate would change, and it would also cause the sidewall facets to change which could lead to a change in the radial (thin film) growth rate.⁴² The GaN sidewall facets can either be terminated with Ga atoms or N atoms based on the growth direction of the nanowire. The Ga adatom diffusion length varies based on which species terminates the surface. When the surface is terminated with Ga atoms, Ga adsorbs on the surface and forms Ga dimers. These

dimers form a weak bond, therefore it is relatively easy to break the bond and allow the Ga atoms to diffuse further.⁴³ When the surface is terminated with N atoms, Ga impinges onto the surface and bonds to the N atoms. The bonding in this situation is significantly stronger, and it becomes difficult to break these bonds. As a result, the Ga is incorporated into the nanowire, which can lead to an increase in the thin film deposition rate.⁴⁴ If the facets happened to be N-terminated, it would explain the increase in the nanowire diameter when the NH₃ flowrate was increased.

TEM characterization was performed to further investigate this concept and determine if the nanowire growth direction changed. TEM images of three GaN nanowires grown at an NH₃ flowrate of 200 sccm are shown in Figure 5.28. One obvious difference between these samples and previous samples is the faceting of the catalyst. In previous samples, the shape of the seed particle was hexagonal. The particle in Figure 5.28 (a) has maintained the hexagonal shape to a degree, whereas the particle in Figure 5.28 (b) is clearly no longer hexagonal but rather rectangular in shape. An attempt was made to obtain HRTEM images of the catalyst for these samples, however the quality of the pictures was not up to par. Attempts were also made to collect SAD patterns of the catalysts but failed because of difficulty rotating the nanowire samples to a zone axis.

A fast Fourier transformation (FFT) was taken of the HRTEM image of the catalyst in Figure 5.28 (b) and is shown in Figure 5.29. The FFT was taken across a 35 x 35 nm field of the particle and the GaN nanowire. The spots that are due to the nanoparticle are circled on the image. Looking closely at those spots, there is a split which indicates that two phases are actually present. The lattice parameters of these two

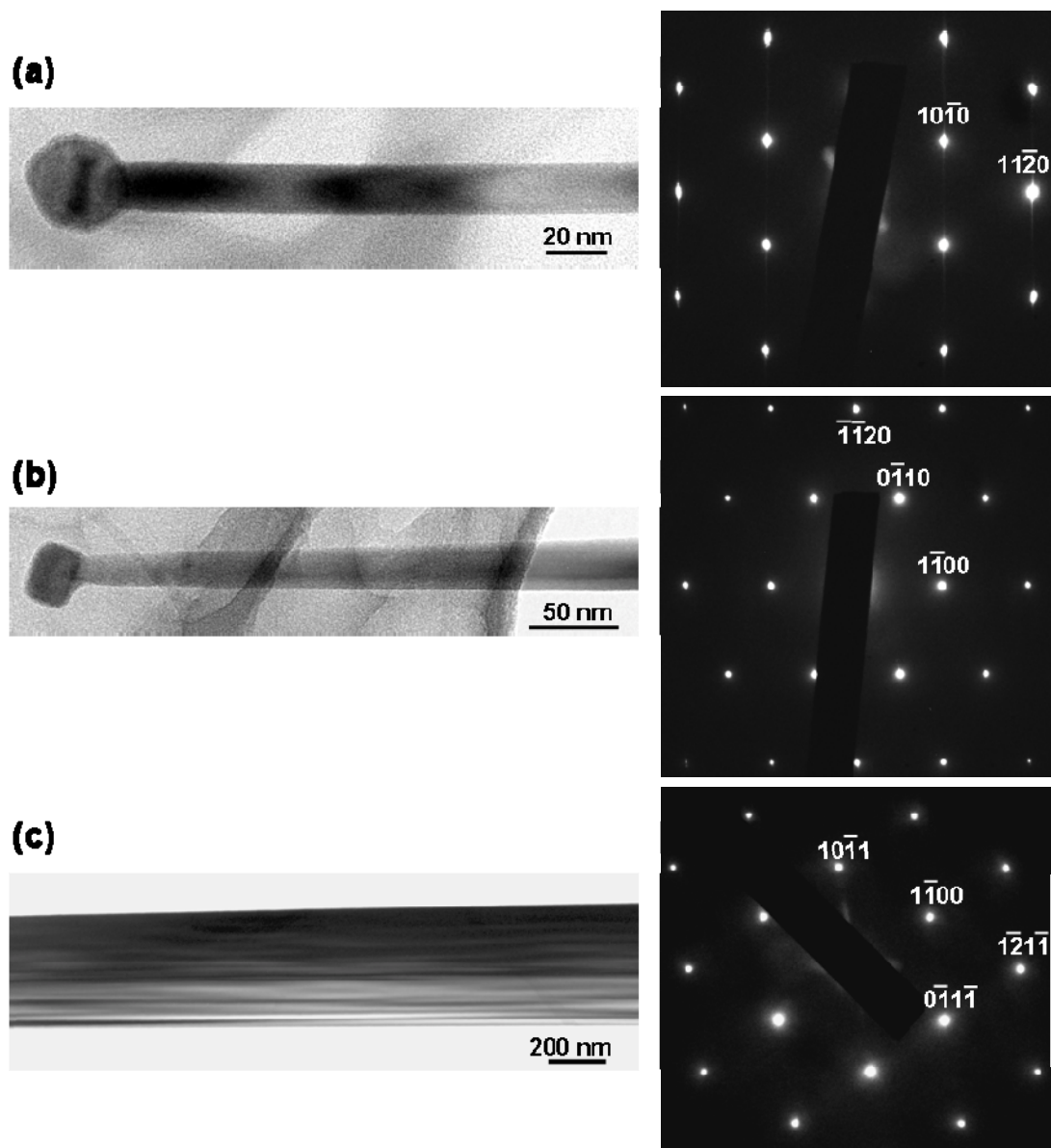


Figure 5.28: TEM images of various GaN nanowire samples grown at 200 sccm NH_3 . The nanowires were found to possess three growth directions: (a) $1\bar{1}\bar{2}0$ growth direction, (b) $1\bar{1}00$ growth direction, and (c) $\bar{1}2\bar{1}\bar{1}$ growth direction. Growth conditions: 900°C ($T_s = 825^\circ\text{C}$), 100 Torr, 3 sccm TMG, 200 sccm NH_3 .

phases were found to be approximately 0.361 nm and 0.348 nm. The lattice parameter of 0.361 nm matches well with the Ni_3Ga phase. The lattice parameter of 0.348 nm appears

to be closest to the (Ni) phase based on Table 5.1. The (Ni) phase is a Ga-soluble face-centered cubic Ni phase.³³

Looking back at the Ni-Ga phase diagram (Figure 5.21), (Ni) phase could be present if the Ga content in the catalyst decreased. This is plausible, since the samples were grown in a NH₃-rich environment. From a thermodynamic standpoint, increasing the NH₃ flowrate would result in a shift to the left in the Ni-Ga phase diagram in order to maintain an equilibrium state between the catalyst and nanowire. If this shift were significant enough, it would place the catalyst composition in the two-phase region of the Ni-Ga phase diagram which consists of the (Ni) phase and the Ni₃Ga phase.

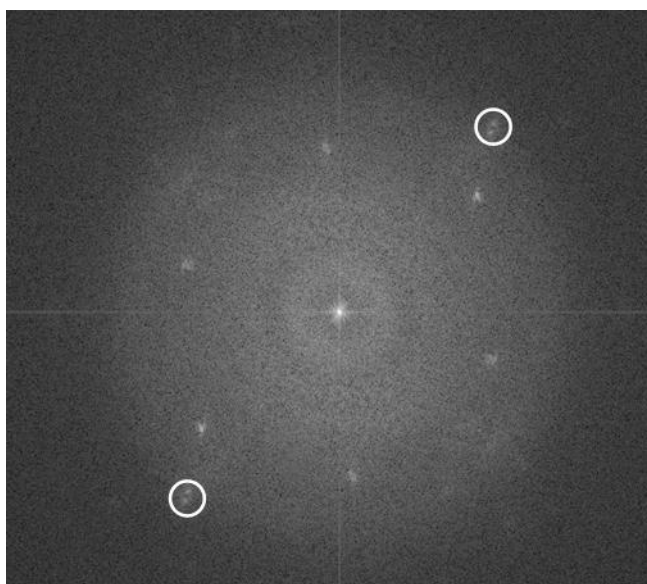


Figure 5.29: Fast Fourier Transformation (FFT) of 35 x 35 nm field of catalyst and nanowire in Figure 5.21 (b). The nanoparticle spots are circled on the image. Splitting of the spots indicates the presence of two phases.

Finally, SAD was collected for 12 nanowires to look at the growth direction and determine if a change in growth direction occurred at the higher NH₃ flowrate. Six of the nanowires ((Figure 5.21 (a)) were found to have a growth direction of $[11\bar{2}0]$, whereas

two of the nanowires (Figure 5.21 (b)) had a growth direction of $[1\bar{1}00]$. Four of the nanowires, however, had a growth direction of $[\bar{1}2\bar{1}\bar{1}]$, which has not been observed in any of the studies (Figure 5.21 (c)). Nanowires with this growth direction were all found to be significantly larger in diameter and length than the typical results. It appears as though these results may be, indeed, linked to a change in growth direction due to a higher NH_3 flowrate.

5.4.3 Photoluminescence

A great deal of effort has been invested in studying the optical properties of GaN. The room temperature band gap has been determined to be 3.4 eV, while a yellow luminescence peak has been observed to be centered at 2.2 eV.⁴⁵ A general consensus exists that the yellow luminescence is due to a radiative recombination between shallow donors and deep level traps.^{46,47} However, the chemical origin of these transitions is still uncertain. It has been proposed that native lattice defects such as gallium vacancies are partially responsible for the presence of the yellow luminescence.^{48,49} The uncertainty surrounds the belief that impurities contribute to the intensity of the yellow luminescence. Various studies have examined the effect of H, C, and O, among other impurities, on the optical properties of GaN.⁵⁰ In particular, carbon has gained support as a major contributor to the yellow luminescence peak.^{48,50,51} Carbon is of particular importance to this study as the GaN nanowires were grown by MOCVD. The decomposition of TMG in GaN growth acts as a source of carbon that can become incorporated within the material and must be accounted for when analyzing the photoluminescence data.

Photoluminescence (PL) measurements of GaN nanowires grown at a variety of conditions were taken to determine the effect of the growth conditions on the optical quality of GaN. The photoluminescence measurements were taken at room temperature, and the excitation wavelength of the laser was 266 nm. It should be noted that the PL was obtained from samples containing both thin film deposition and nanowires, therefore it is necessary to ascertain the contributions of each morphology to the photoluminescence spectrum. Studies carried out at the University of Bristol in England in which the GaN nanowires were mechanically removed from the substrate and transferred onto InP substrates for PL measurements⁵² gave very similar results to the PL studies reported here which were obtained with nanowires attached to the original substrate.

A typical photoluminescence spectrum of GaN nanowires still attached to the sapphire substrate is shown in Figure 5.30. The PL in Figure 5.30 was taken for samples grown at 850°C ($T_s = 775^\circ\text{C}$) and 900°C ($T_s = 825^\circ\text{C}$). The pressure was held constant at 100 Torr, whereas the TMG and NH_3 flowrates were 3 sccm and 100 sccm, respectively. A peak at 3.38 eV which corresponds to the GaN near band-edge emission was present in the spectra along with deep-level emission centered at about 2.25 eV. Due to the peaks and valleys present in the deep-level emission, it is believed that multiple peaks are present that overlap. These peaks appear to be centered at 2.38 eV, 2.27 eV, and 2.15 eV. For the sample grown at a 900°C furnace temperature ($T_s = 825^\circ\text{C}$), the ratio of band-edge to deep-level emission was 11. This value dropped to 0.42 at 850°C ($T_s = 775^\circ\text{C}$) and 0.06 at 800°C ($T_s = 725^\circ\text{C}$). PL of individual GaN nanowires grown at 900°C ($T_s = 825^\circ\text{C}$) yielded similar results, indicating that the PL contributions are predominantly

from the GaN nanowires rather than the underlying thin film.⁵² It should be noted that PL of individual nanowires was only carried out for the sample grown at 900°C ($T_s = 825^\circ\text{C}$).

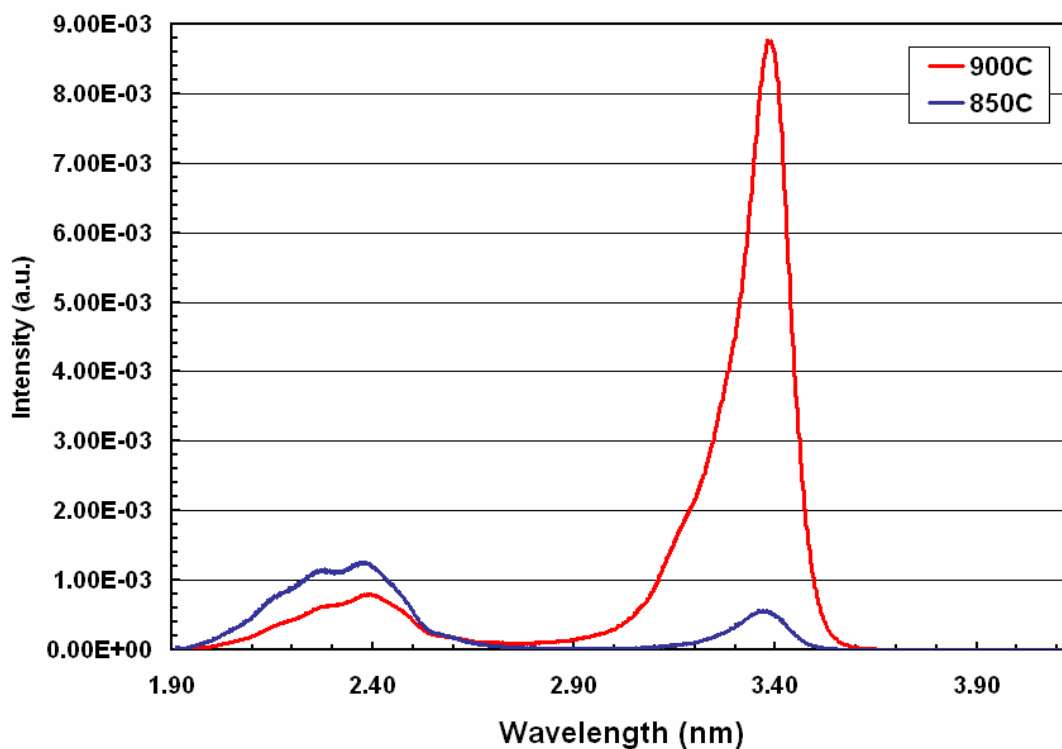


Figure 5.30: Effect of growth temperature on photoluminescence measurements. Growth conditions: 100 Torr, 3 sccm TMG, 100 sccm NH_3 , 250 sccm H_2 .

Similar results were reported by Wang et al. for GaN nanowires grown by MOCVD in a cold-wall reactor, and the degradation of the optical quality of the nanowires was attributed to increased carbon incorporation from the TMG source at lower growth temperatures.⁵³ Hydrocarbons will adsorb and either become incorporated into the growing material or desorb from the surface. At elevated temperatures, a higher degree of hydrocarbons will desorb from the surface, and as a result a lower concentration of carbon will be present in the GaN structure.¹⁸ Carbon has been found to

not only affect the yellow luminescence of GaN but also the band-edge emission,⁵⁰ therefore the PL results are not unusual.

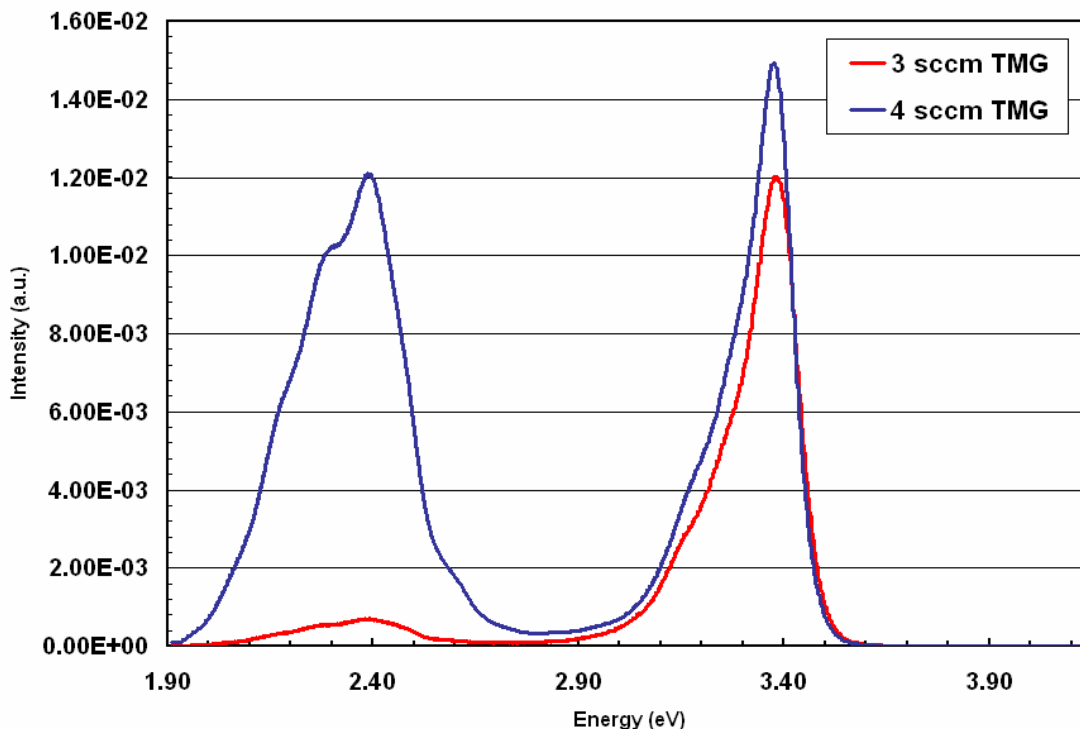


Figure 5.31: Effect of TMG flowrate on photoluminescence measurements. Growth conditions: 900°C ($T_s = 825^\circ\text{C}$), 100 Torr, 100 sccm NH_3 .

To investigate the effect of carbon incorporation further, a sample was grown at a furnace temperature of 900°C ($T_s = 825^\circ\text{C}$) but with an increased flow rate of TMG (4 sccm) which decreased the V/III ratio to 25. The band-edge to deep-level emission ratio decreased from 17.5 for the sample grown with a V/III ratio of 33 in this case to 1.2 for a V/III ratio of 25 (Figure 5.31). Increasing the TMG flowrate would introduce more hydrocarbons to the gas phase mixture with the potential for higher incorporation of carbon into the GaN structure. The PL results provide further support that carbon may be partially responsible for the yellow luminescence observed in GaN.

Photoluminescence measurements were also taken of samples grown at higher NH_3 flowrates. The TMG flowrate was held constant at 3 sccm, whereas the NH_3 flowrate was increased to 150 sccm ($\text{V/III}=50$) and 200 sccm ($\text{V/III}=67$). The band-edge to deep-level emission ratio was found to be 6.2 for a V/III ratio of 50 and decreased to 0.7 at a V/III ratio of 67 (Figure 5.32). Increasing the NH_3 flowrate led to a decrease in the intensity of the band-edge emission and an increase in the yellow luminescence peak even though the TMG flowrate remained constant. Increasing the NH_3 flowrate, however, could lead to an increase in the Ga vacancy concentration present in the GaN nanowires. As was previously noted, Ga vacancies are believed to be partially responsible for the yellow luminescence peak; therefore, an increase in the Ga vacancy concentration could be responsible for the degradation of the optical properties at elevated NH_3 flowrates. Another consideration would be incorporation of oxygen. Impurities associated with ammonia are water and oxygen, therefore increasing the NH_3 flowrate could lead to a higher incorporation of oxygen within the GaN nanowires. Oxygen has also been found in previous studies to enhance the intensity of the yellow luminescence in GaN.⁵⁰

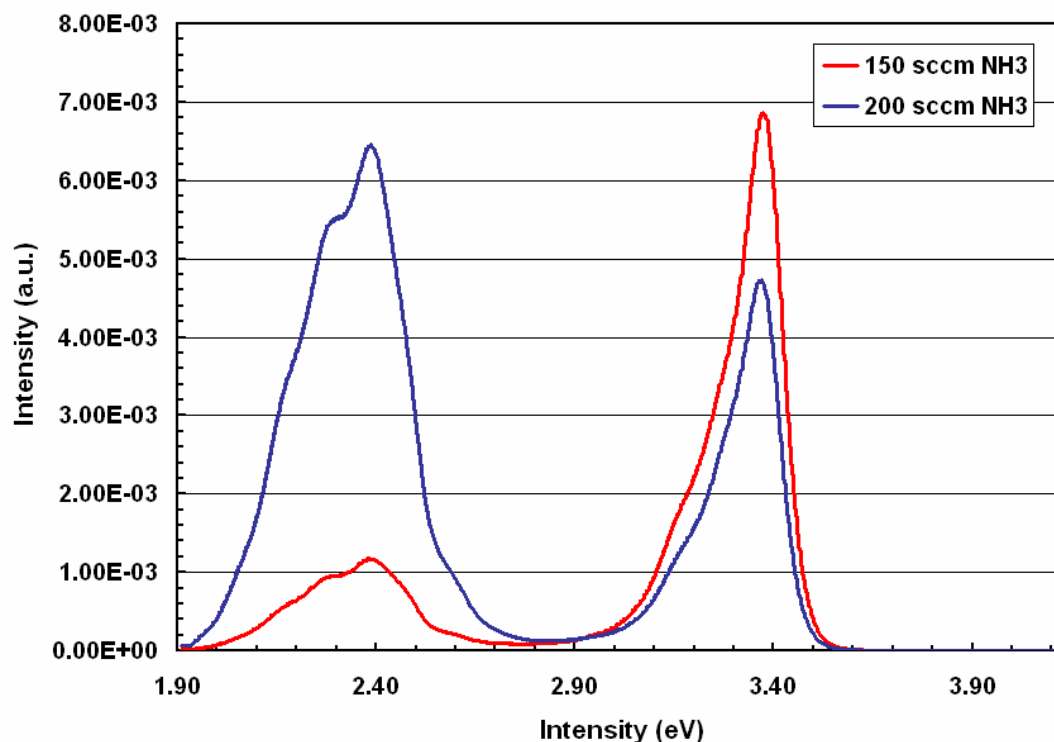
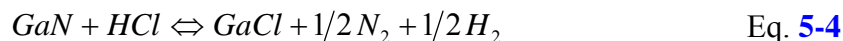


Figure 5.32: Effect of NH_3 flowrate on photoluminescence measurements. Growth conditions: 900°C ($T_s = 825^\circ\text{C}$), 100 Torr, 3 sccm TMG.

5.5 Growth of GaN Nanowires with the Addition of GeCl_4

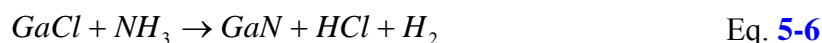
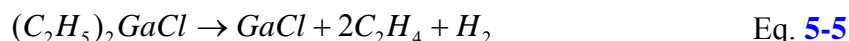
As was previously noted, tapering was found to be a significant issue with GaN nanowire growth using metalorganic precursors. The tapering was a byproduct of the competition between axial (vapor-solid-solid) growth and radial (vapor-solid) growth. A variety of growth conditions were explored in an attempt to overcome the tapering. The author was able to minimize the tapering but not eliminate the issue. One possible solution to resolve the tapering issue involved in the growth of GaN nanowires is the

addition of a Cl-based source. A typical byproduct of the gas phase reactions involved in this chemistry is HCl. HCl will interact with GaN via the following reaction:⁵⁴



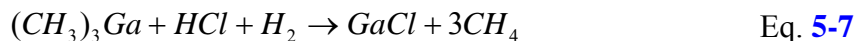
Based on this reaction, the presence of HCl creates a pathway to etch away GaN that deposits on the sidewalls of GaN nanowires by vapor-solid deposition.

A Cl-based precursor that has been investigated as an alternative to TMG is diethylgallium chloride (DEGaCl). Diethylgallium chloride (DEGaCl) has been employed for thin film growth and epitaxial lateral overgrowth (ELO) of GaN and GaAs.⁵⁴⁻⁵⁷ In ELO, GaN or GaAs is grown on a patterned substrate at conditions that promote a high lateral-to-vertical growth rate ratio. At these conditions, GaN and GaAs films preferentially deposit in openings of a mask that were patterned on the substrate. The main chemical reactions for ELO growth of GaN are as follows:⁵⁵



These reactions result in an HVPE-like (Hydride Vapor Phase Epitaxy) growth chemistry near the growth front in the MOCVD set-up but with the control of MOCVD. DEGaCl has shown the ability to improve the growth behavior for thin film growth and eliminate tapering issues concerning ELO growth. Chlorine atoms have been observed to passivate the side facets in ELO growth, inhibiting the thin film deposition on the side facets and improving the vertical ELO growth.⁵⁸ Cl is believed to lower the surface energy of the facets, increasing the adatom diffusion length for Ga before incorporation which reduces the tapering of the side facets.

HCl gas has also been examined for the growth of GaN films in a process known as metalorganic hydrogen chloride vapor phase epitaxy (MOHVPE).⁵⁹⁻⁶¹ TMG and HCl are mixed together upstream of the reactor in a mixing zone at 750°C in order to form gaseous GaCl via the following reaction:



GaCl is transported downstream to the substrate where it combines with NH₃ to grow GaN (Equation 5-6). Kumagai *et al.* have utilized this technique in an attempt to grow thick high-quality GaN films on GaAs (111)A substrates for freestanding GaN substrates.^{59,60} Kumagai *et al.* were successful in growing a 100 μm thick GaN film with high quality.⁶¹

HCl gas has also been used to address tapering issues present in Au- and Ti-catalyzed Si nanowires using SiH₄ as the source gas.⁶²⁻⁶⁴ The addition of HCl to the gas phase mixture was found to reduce the axial and radial growth rate, however a steeper reduction in the radial (uncatalyzed) growth of Si was observed. HCl has also been used successfully to grow GaN nanowires using a growth technique known as hydride vapor phase epitaxy (HVPE).⁶⁵⁻⁶⁷ HVPE involves the reaction of Ga metal with HCl in N₂ at temperatures of 750-850°C to form GaCl. The GaCl is transported to a substrate in another section of the reactor where it mixes with NH₃ to form GaN. GaN nanowires have been grown on sapphire and silicon substrates with and without the use of a catalyst and minimal tapering.

As a result of these studies, the decision was made to look at alternative precursors as a method to eliminate tapering of the GaN nanowires. Since DEGaCl and

and HCl were not readily available, initial studies were performed using germanium tetrachloride (GeCl_4) since this source was already set up on the nanowire CVD system. Based on the literature, GeCl_4 has been found to chemisorb dissociatively on Si (100) at a temperature of 300°C to form GeCl_2 and GeCl .⁶⁸ At 500°C , GeCl_2 breaks down into trace amounts of GeCl and Ge . The overall decomposition reaction for GeCl_4 is:⁶⁹



A byproduct of the decomposition of GeCl_4 is HCl which can be utilized for the GaN nanowire growth. HCl would potentially react with TMG to form GaCl, altering the gas phase chemistry in the reactor (Equation 5-7) and possibly the GaN nanowire growth.

5.5.1 Preliminary Results

A set of GaN nanowire experiments adding GeCl_4 to the gas phase mixture were performed in order to investigate its effect on the wire morphology. Initial experiments were performed using the standard conditions of 900°C , 100 Torr, 3 sccm TMG, and 100 sccm NH_3 for GaN nanowire growth. The quartz boat was placed 2 inches from the TMG inlet, and Ni-coated sapphire wafer pieces were placed along the length of the boat. The only change in the growth conditions was a reduction in the H_2 carrier gas flowrate to 150 sccm due to the addition of GeCl_4 . For the preliminary experiments, 0.15 sccm GeCl_4 ($\text{GeCl}_4/\text{TMG} = 0.05$) was introduced to the gas phase mixture through the group III inlet. The addition of a small amount of GeCl_4 led to a pronounced change in the GaN nanowire growth. By introducing GeCl_4 to the system, a high density of nanowire growth was achieved over a large region spanning from the front edge of the boat into the

constant temperature region. Figure 5.33 displays the dramatic change in the nanowire density compared to previous results (Figure 5.9 (d)). There is some variation in the nanowire diameter, however a significant portion of the nanowires have a diameter in the range of 50-90 nm with a length of 2-3 μm . A reduction in tapering can be seen as the nanowires appear to be more uniform in diameter. The inset in Figure 5.33 (c) shows the presence of a triangular cross-section, consistent with previous results for GaN nanowire growth.

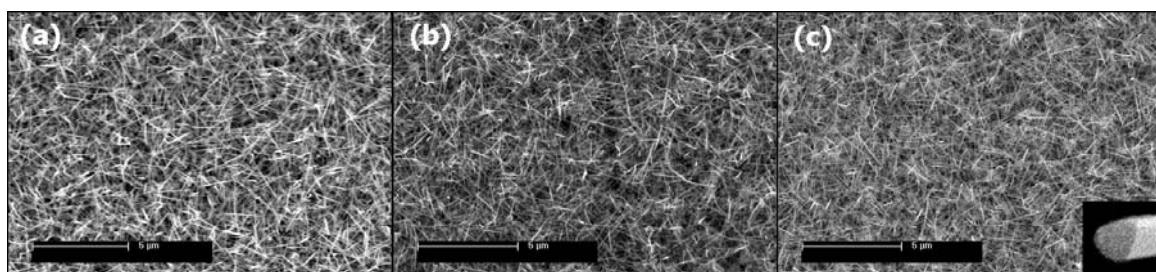


Figure 5.33: SEM images of GaN nanowire growth with GeCl_4 at a position (a) 2.75 inches (b) 4 inches, and (c) 4.75 inches from the TMG inlet. Inset of a triangular cross-section of a GaN nanowire. Growth conditions: 900°C, 100 Torr, 3 sccm TMG, 100 sccm NH_3 , 150 sccm H_2 , 0.15 sccm GeCl_4 , and 5 minute growth.

Preliminary characterization was done on these samples to determine if the nanowires were indeed GaN. While the sample was in the SEM, x-ray energy dispersive spectroscopy (EDS) was performed to determine what elements were present on the sample. The EDS scan illustrated the presence of Ga and N peaks corresponding to GaN, the presence of Al and O peaks corresponding to the sapphire substrate, and a Ge peak which overlaps with the Ga peak. X-ray diffraction (XRD) was utilized to investigate the structural properties of the GaN nanowire sample (Figure 5.34). The highest intensity peak corresponds to the sapphire substrate. The primary planes observed in the x-ray

diffraction scan for GaN were (100), (002), and (101). The (220) Ge peak was also observed indicating the presence of Ge within the sample, however its intensity was much lower than the GaN peaks.

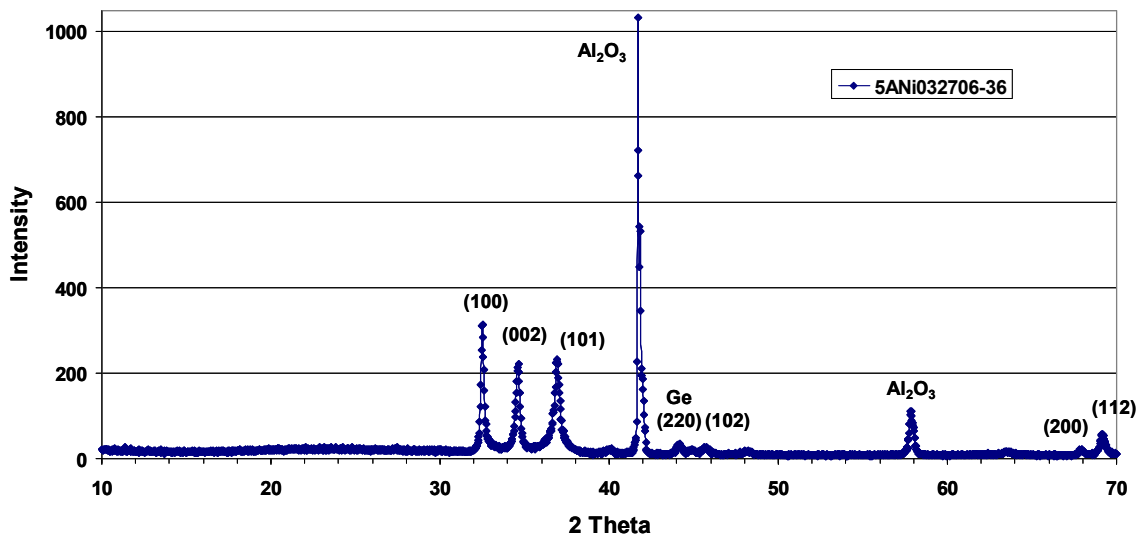


Figure 5.34: X-ray diffraction scan of GaN nanowire sample grown with the addition of GeCl_4 . Growth conditions: 900°C , 100 Torr, 3 sccm TMG, 100 sccm NH_3 , 150 sccm H_2 , 0.15 sccm GeCl_4 , and 10 minute growth.

After the initial success of the addition of GeCl_4 to the gas phase mixture, additional experiments were performed to examine the overall effect of GeCl_4 on GaN nanowire growth. The first series of experiments focused on the effect of the GeCl_4 concentration on GaN nanowire growth. The temperature set-point was held constant at 900°C at a pressure of 100 Torr. The TMG and NH_3 flowrates were maintained at 3 sccm and 100 sccm, respectively, while the H_2 carrier gas flowrate was held constant at 150 sccm. The GeCl_4 flowrate was varied from 0.15 sccm ($\text{GeCl}_4/\text{TMG} = 0.05$) to 0.40 sccm ($\text{GeCl}_4/\text{TMG} = 0.13$). The results of this series of experiments are shown in Figure 5.35. Based on the SEM images, a reduction in tapering was evident when the

GeCl₄ flowrate was increased from 0.15 sccm to 0.30 sccm. This was not the case when the flowrate was raised to 0.40 sccm where the increase led to the nanowires becoming rough on the surface either due to deposits or kinking. The nanowire diameter remained roughly the same for lower GeCl₄ flowrates spanning a range of 50-90 nm; however, the diameter increased to a range of 100-150 nm at 0.40 sccm.

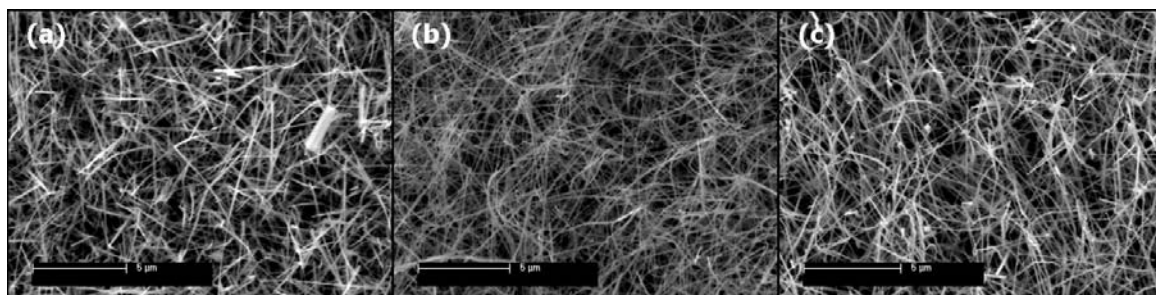


Figure 5.35: SEM images of GaN nanowire growth after introducing GeCl₄ flowrates of (a) 0.15 sccm, (b) 0.30 sccm, and (c) 0.40 sccm to the growth. Growth conditions: 900°C, 100 Torr, 3 sccm TMG, 100 sccm NH₃, 150 sccm H₂, and 10 minute growth.

To further observe the effect of the addition of GeCl₄ to the system, the temperature and V/III ratio (TMG and NH₃ flowrates) were varied and compared to previous results. When the temperature was raised to 1000°C, primarily thin film deposition occurred over the entire growth zone for a GeCl₄ flowrate of 0.15 sccm. However, increasing the GeCl₄ flowrate while operating at 1000°C, led to nanowire growth over the entire growth regime with diameters in the range of 60-150 nm. Small diameter nanowires (50-90 nm) were also achieved when the TMG and NH₃ flowrates were increased to 4 sccm and 200 sccm, respectively, at 900°C, although an underlying thin film deposition was present in this case. The decrease in diameter proved to be quite drastic compared to previous results without the addition of germanium tetrachloride (Figure 5.5). A high density of nanowire was even apparent when the TMG flowrate was

reduced to 2 sccm at 900°C. These results exemplify the effect that even a small amount of Cl can have on the growth chemistry and morphology of the nanowires.

Based on these results, it appears as though GeCl_4 does, indeed, alter the gas phase chemistry in the reactor. Due to the decomposition of GeCl_4 , HCl is produced which, in turn, reacts with the TMG to form GaCl. GaCl is known to be stable above 700°C due to its high binding energy (5.5 eV). It has been suggested that GaCl remains stable until it adsorbs onto the growth surface and reduces to form Ga for incorporation.⁷⁰ If this were the case, the typical Ga-based adducts would not form, and GaCl would be transported to the substrate for deposition. The GaCl would adsorb on the Ni catalyst, reduce to Ga, and form a Ni-Ga alloy. NH_3 would react with the Ga at the particle/nanowire interface, leading to the formation of a GaN nanowire. As a result, HCl would be a viable option to overcome the issues with gas phase depletion.

5.5.2 Transmission Electron Microscopy

Transmission electron microscopy was utilized to examine the structural properties of the GaN nanowires grown with GeCl_4 . The growth conditions for this sample were as follows: 900°C, 100 Torr, 3 sccm TMG, 100 sccm NH_3 , 150 sccm H_2 , and 0.15 sccm GeCl_4 . A low magnification TEM image of a collection of nanowires are shown in Figure 5.36. Two types of nanowires were observed for this sample. One set of nanowires (indicated with red arrow) were jagged on the surface and resembled nanosaws, whereas the other set of nanowires (indicated with blue arrow) were smooth

on the surface. HRTEM, SAD, and XEDS were utilized to examine the two types of nanowires and understand the similarities and differences that exist between them.

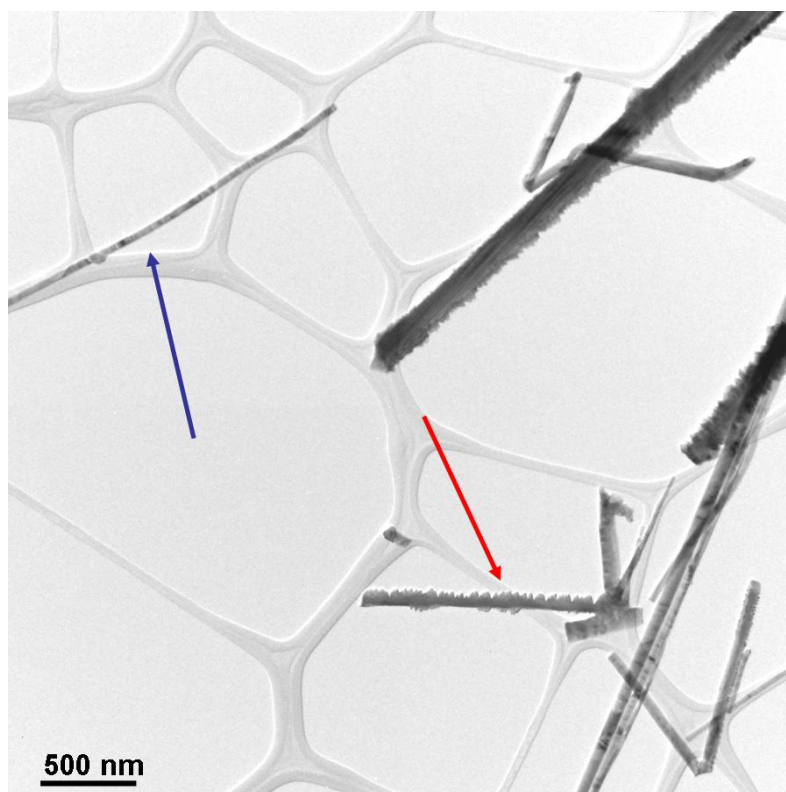


Figure 5.36: Low magnification TEM image. Two types of nanowires were observed: smooth surface (indicated by blue arrow) and rough surface (indicated by red arrow). Growth conditions: 900°C, 100 Torr, 3 sccm TMG, 100 sccm HN_3 , 150 sccm H_2 , 0.15 sccm GeCl_4 .

Figure 5.37 (a) is an example of a nanowire that was serrated on the surface. The bright-field TEM image displays a nanowire core with faceted islands protruding from the core. SAD was completed on the nanowire to determine its structure (Figure 5.37 (b)), and it was found to possess both the wurtzite and zinc blende phases of GaN. A high density of twins and stacking faults were found to exist in the serrated nanowires, and this can be viewed in the SAD pattern (Figure 5.37 (b)). The core of the nanowire was found to primarily consist of wurtzite GaN with a high degree of stacking faults,

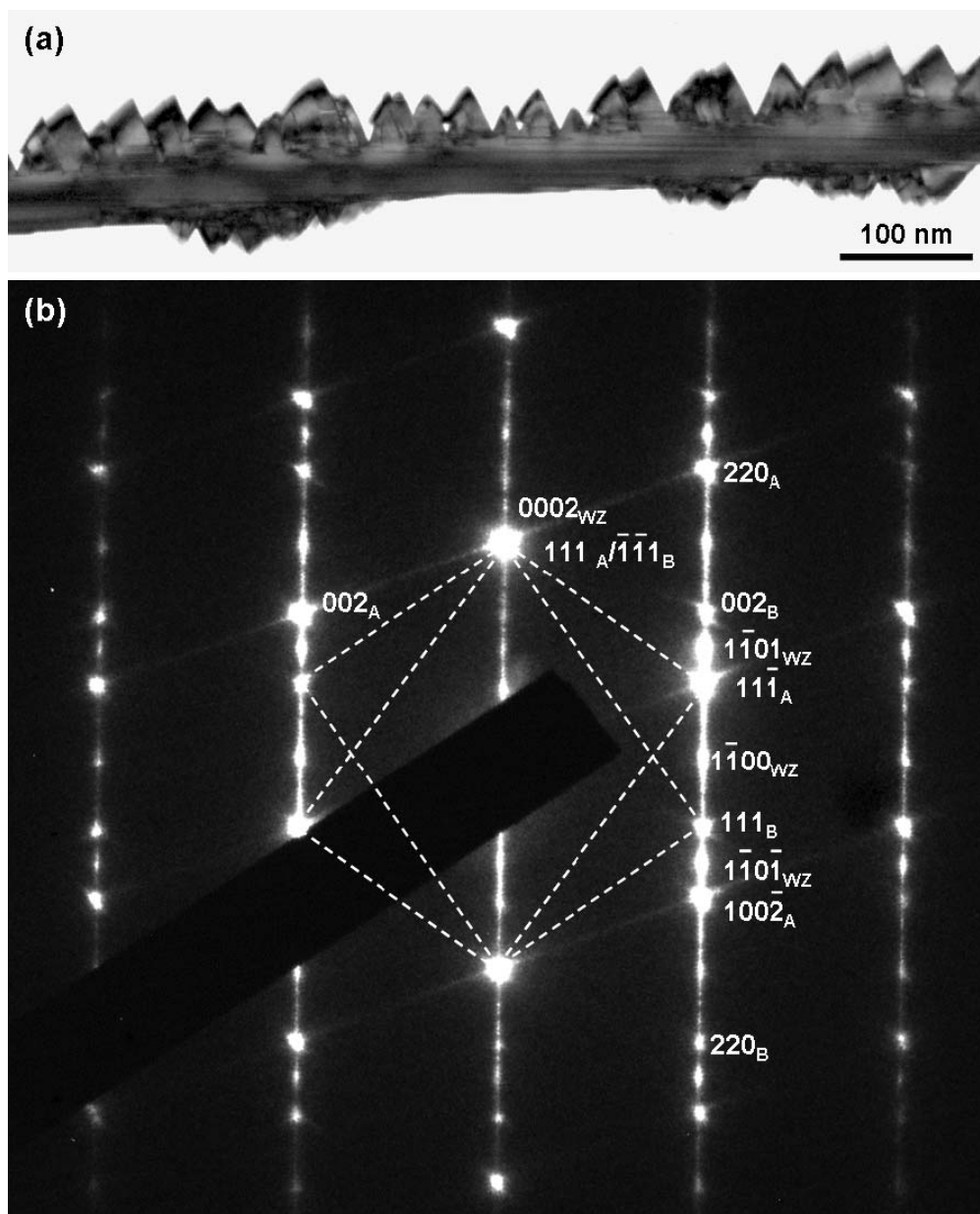


Figure 5.37: (a) Bright-field TEM image of a nanowire with faceted islands on the surface. (b) The corresponding SAD pattern. The wire contains both wurtzite (WZ) and zinc blende (ZB) GaN phases with a high density of twins and stacking faults. The crystallographic relationship between the WZ and ZB GaN is $\langle 1\bar{1}00 \rangle_{WZ} // \langle 112 \rangle_{ZB}$, $\langle 11\bar{2}0 \rangle_{WZ} // \langle 1\bar{1}0 \rangle_{ZB}$, and $\langle 0001 \rangle_{WZ} // \langle 111 \rangle_{ZB}$. The growth direction of the nanowire is $\sim 4^\circ$ away from $\langle 1\bar{1}00 \rangle_{WZ}$ and $\langle 112 \rangle_{ZB}$. Growth conditions: 900°C, 100 Torr, 3 sccm TMG, 100 sccm NH_3 , 150 sccm H_2 , 0.15 sccm GeCl_4 .

whereas the islands are zinc blende GaN (Figure 5.38). A zinc blende twin is present at the interface between the nanowire and the faceted island. Looking closely at the SAD pattern, the twin (A and B) can be observed. The diamond patterns overlaying the image adjoin the four $\{111\}$ reflections of A and B. The twin boundary is found to be parallel to the wurtzite 0002 plane. The vertical streaking that is evident in the SAD pattern is due to stacking faults in the wurtzite GaN and twin boundaries in the zinc blende GaN.

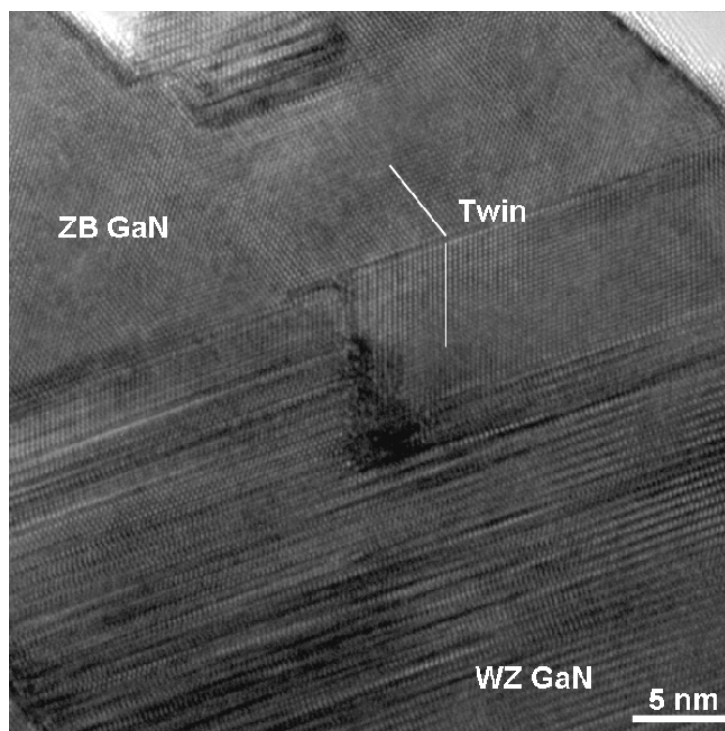


Figure 5.38: HRTEM image collected near the surface of the nanowire. The nanowire core is wurtzite GaN with stacking faults while the islands are twinned zinc blende GaN. The twinning occurs at the interface between the nanowire core and the faceted islands.

The streaking that is present roughly 30° from horizontal is a byproduct of the stacking faults in the zinc blende islands. The growth direction of the nanowire was determined to be approximately 4° away from $[1\bar{1}00]$ for wurtzite GaN and $[112]$ for zinc blende GaN. XEDS spectra were collected from both the wurtzite core of the nanowire and the faceted

zinc blende islands. Ga, N, and Ge peaks were present, therefore Ge has been incorporated into the nanowire even though there is no evidence of Ge deposition on the surface based on the HRTEM image.

HRTEM images were taken along the length of the nanowire in hopes of elucidating the growth mechanism for the zinc blende islands. Previously, GaN nanowires with a wurtzite core and a zinc blende shell have been grown by the direct reaction of Ga metal vapor with NH_3 without the use of a catalyst.⁷¹⁻⁷³ In that study, the author concluded that both phases grew together along the length of the wire. In this study, the goal was to determine if the faceted islands resulted directly from the nanowire growth or formed on the side facets after the formation of the nanowire segment. Figure 5.39 provides a low magnification image of a GaN nanowire along with high resolution images of different sections of the nanowire beginning at the tip. Simply looking at the low magnification image and scanning the length of it beginning at the seed particle, it is evident that the faceting becomes more pronounced further away from the nanoparticle. The increased faceting is simply magnified in the HRTEM images. This observation leads to the belief that the faceting occurs after the nanowire segment has been synthesized by vapor-solid deposition.

For MBE growth of GaN, Ga-rich conditions along with low substrate temperatures have been used successfully to grown zinc blende GaN.^{74,75} Gallium on the surface appears to reduce the surface energy and promote the growth of zinc blende GaN. This hypothesis was verified when zinc blende GaN was achieved only in Ga-rich conditions, whereas wurtzite GaN grew in N-rich conditions. For both MBE and MOCVD growth, zinc blende GaN has been found to grow on c-plane sapphire (0001)

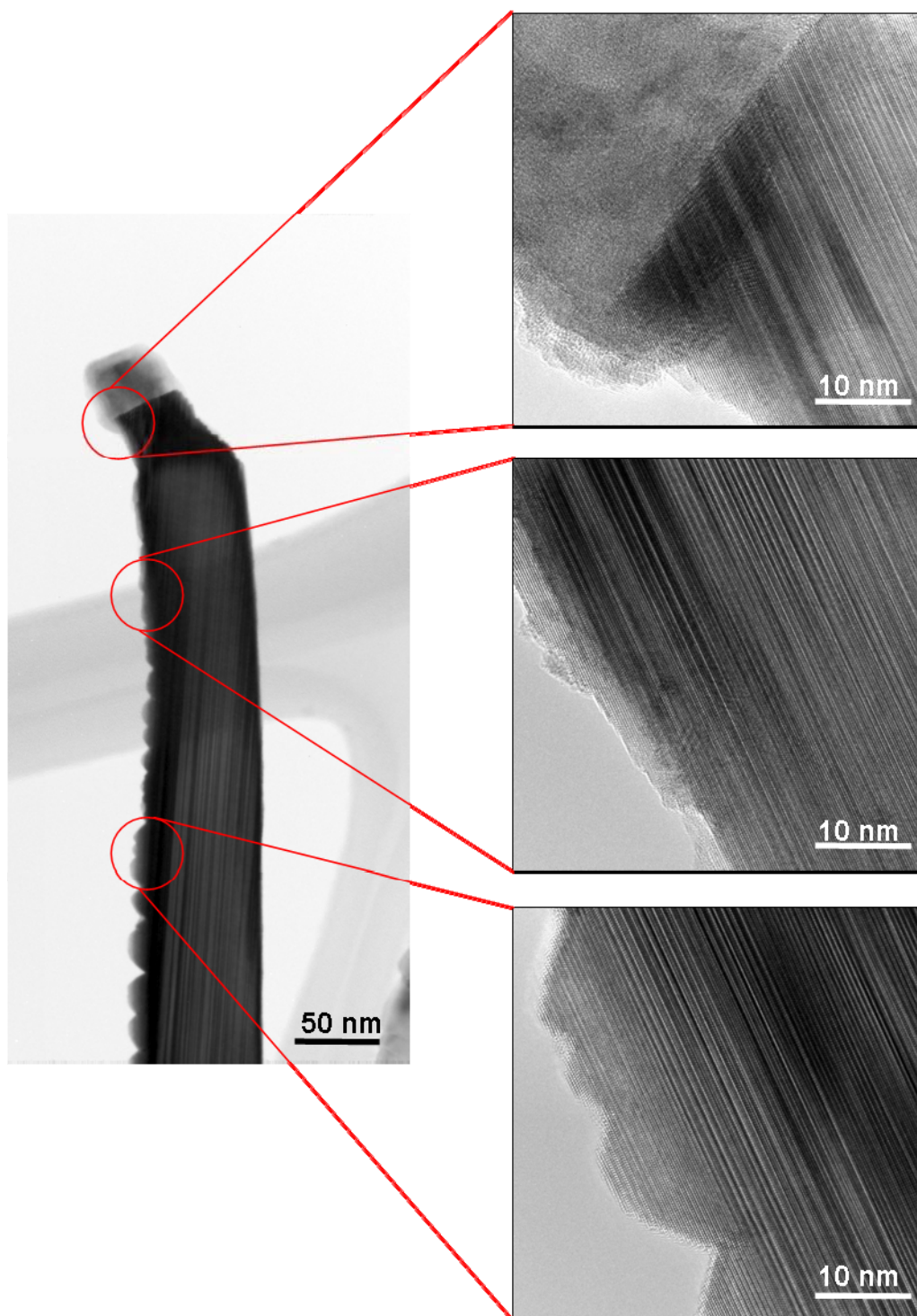


Figure 5.39: Low magnification image of a GaN nanowire growth with GeCl_4 (left) along with HRTEM images of different segments of the nanowire beginning at the tip and traveling towards the base of the nanowire (right).

which happens to be the same plane as the side facets of the nanowire.^{76,77} The triangular/trapezoidal nature of the zinc blende growth results due to the zinc blende growth consisting of (111) planes in contact with the nanowire surface. In the MOCVD study, the island edges were all found to be oriented along one of three $\langle 110 \rangle$ directions, and the facet contact angle was found to be approximately 55° or the contact angle between (111) and (100) planes.⁷⁷ Due to the change in the gas phase chemistry, excess Ga could be depositing on the sidewalls of the nanowire and leading to the formation of the islands. The role that Ge plays in the growth, if any, remains uncertain. It is possible that Ge could promote the island growth, therefore it is pertinent to perform a series of experiments with HCl to determine if the island growth is a byproduct of Ge deposition or excess Ga on the surface.

As was previously mentioned, a second type of nanowire was found that consisted of a smooth surface instead of a rough surface. An example of such a wire is shown in Figure 5.40 (a). Selected area diffraction was completed on the wire, and it was found to consist of pure wurtzite GaN with (0001) planar defects which are evident in the low magnification and high resolution images in Figure 5.40 (a) and (c). XEDS of the nanowire resulted in Ga, N, and Ge peaks, therefore Ge is present within the nanowire to some degree. The most interesting observation was the growth direction for the nanowires with smooth surfaces was determined to be [0002]. The growth direction for the nanowires with rough surfaces had been determined to be a few degrees away from $[1\bar{1}00]$. This observation supports the belief that the nanowire facets for the nanowires with rough surfaces promote zinc blende GaN growth, since the zinc blende islands are not present in the nanowires with smooth surfaces.

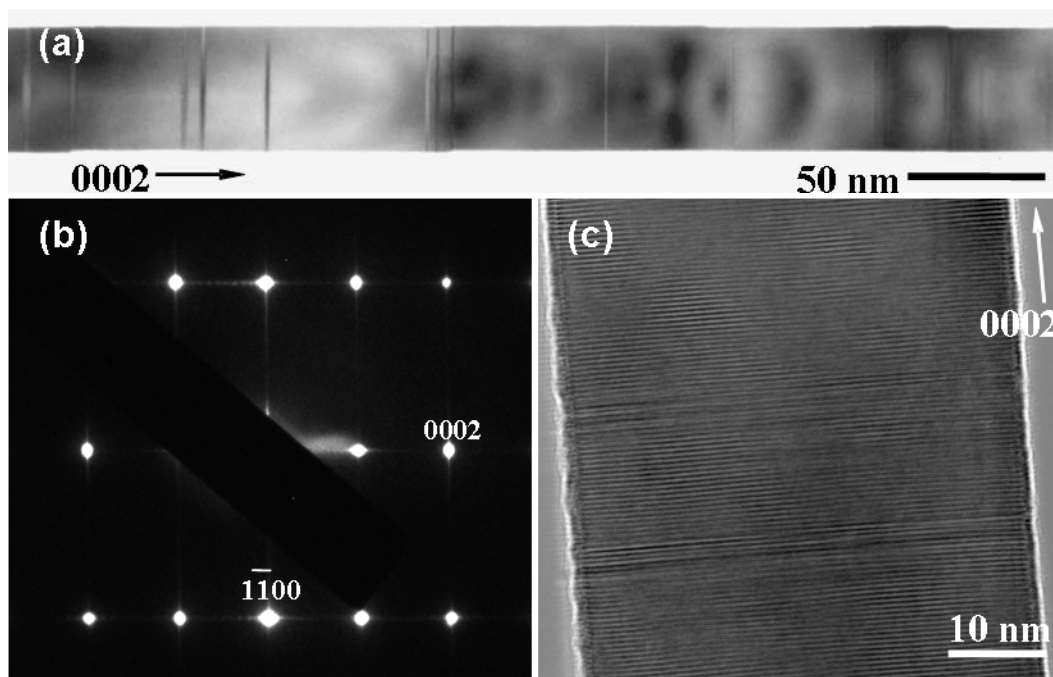


Figure 5.40: (a) Bright-field TEM image of a nanowire with smooth surface. (b) SAD pattern of nanowire indicating the presence of the wurtzite GaN structure with (0001) planar defects. (c) HRTEM image of GaN nanowire.

5.5.3 Photoluminescence

Photoluminescence measurements were also completed for this sample. Figure 5.41 shows photoluminescence for two samples grown for 5 minutes and 10 minutes using GeCl_4 . The intensity of the band-edge peak is much lower than the typical spectrum (Figure 5.30). The decrease in intensity may be due to Ge incorporation or the fact that the nanowires contain a significant amount of defects.⁷⁰ It also should be noted that the band-edge peak is shifted in each case compared to the typical spectrum. For the sample that was grown for 5 minutes, the band-edge peak is located at roughly 3.30 eV. For the sample that was grown for 10 minutes, the peak has shifted to 3.46 eV, whereas

the typical peak is located at 3.38 eV. The TEM analysis leads to the speculation that the PL shift may be due to the formation of the zinc blende structure for GaN as the band-edge emission for the sample grown for 5 minutes is similar to that of cubic-GaN.⁷⁸⁻⁸⁰ Another possibility may lie in the growth direction that is observed for both nanowire structures as previous reports have shown the band-edge emission can be influenced by growth direction.^{13,81,82} The PL shift observed between the 5 minute and 10 minute growth raises speculation as to the effect of Ge incorporation on the PL spectrum. It is possible that the Ge incorporation may cause the GaN nanowires to become strained which has been known to affect the PL.^{83,84}

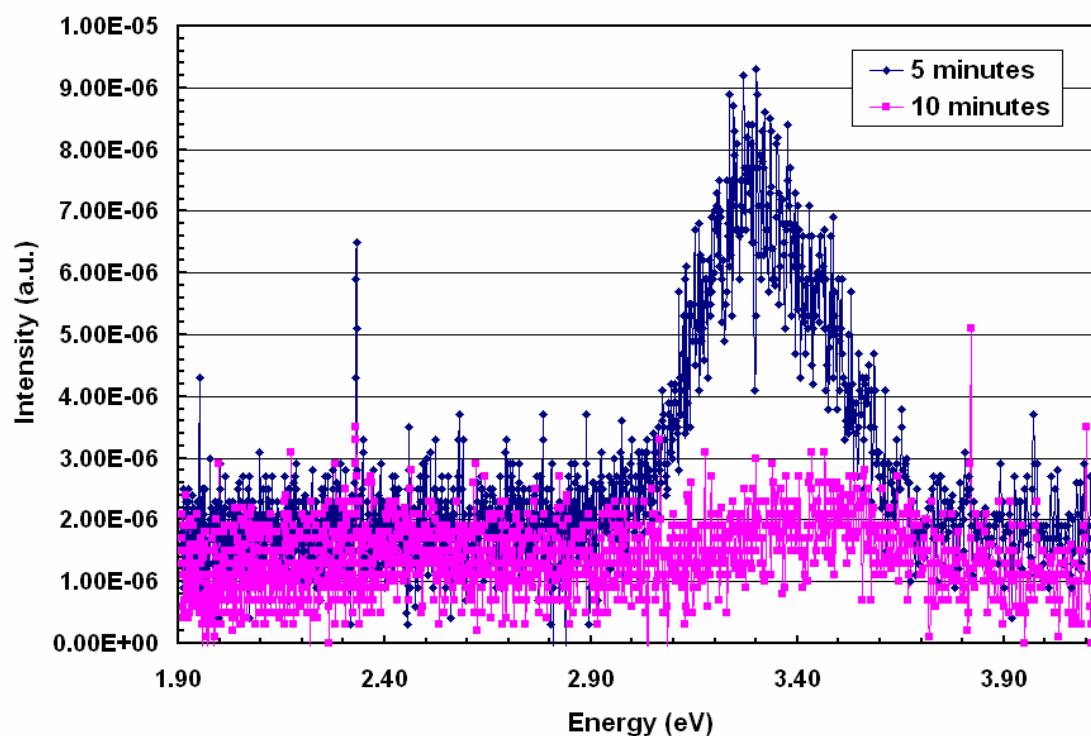


Figure 5.41: Photoluminescence spectra of GaN nanowire samples grown with addition of GeCl₄ for 5 min and 10 min. Growth conditions: 900°C, 100 Torr, 3 sccm TMG, 100 sccm NH₃, 150 sccm H₂, 0.15 sccm GeCl₄.

5.6 Conclusions

In conclusion, the growth conditions for the synthesis of GaN nanowires by MOCVD were investigated on sapphire substrates using Au and Ni as metal catalysts. Initial studies were completed with the quartz boat in the constant temperature region but with little success. The quartz boat was shifted 2 inches closer to the TMG inlet, and this resulted in the ability to grow GaN nanowires. CFD modeling found that the lack of success in the constant temperature region was due to issues with depletion of the precursors in the gas phase prior to the reaction front.

A series of experiments were completed with the boat in its new location, and a growth window was determined for GaN nanowire growth. GaN nanowire growth was achieved for a temperature range of 800-900°C, a TMG flowrate range of 2-4 sccm, and a NH₃ flowrate range of 100-200 sccm. At temperatures higher than 900°C and lower than 800°C, the modeling found vapor-solid deposition to dominate. When the NH₃ flowrate was increased, a dramatic increase in the diameter and length of the GaN nanowires resulted. The modeling demonstrated that increasing the NH₃ flowrate led to a shift of adducts further into the furnace and an increase in the thin film deposition rate as a result. H₂ and N₂ were both investigated as a carrier gas, and H₂ was determined to be the best choice as microworms resulted when N₂ was utilized due to the combination of an increase in thin film deposition rate and the lack of an etchant for the radial growth. The growth conditions were found to have a significant effect on the optical properties of the nanowires. In particular, photoluminescence results suggest that carbon incorporation at

lower temperatures is believed to be responsible for the decrease in the band edge emission relative to the deep level emission.

Based on the reduced temperature range observed for GaN nanowire growth, TEM characterization was completed to investigate the state of the seed particle. Reports in the literature have suggested that GaN nanowire growth occurs by the vapor-liquid-solid (VLS) mechanism even though growth is only possible in a temperature range of 800-1000°C. Based on the Ni-Ga phase diagram, the particle would either have to be extremely Ga-rich or the growth temperature would need to be roughly 1200°C for VLS growth to happen. TEM was performed on the seed particle for various growth conditions and was determined to consist of Ni₃Ga in all cases. As a result, the GaN nanowire growth was concluded to occur via a vapor-solid-solid (VSS) mechanism, since Ni₃Ga is located in the Ni-rich regime of the Ni-Ga phase diagram. Further evidence of the VSS mechanism was found when the seed particle was observed to overlap or sit on top of the nanowire.

Finally, a series of experiments were performed with GeCl₄ in an attempt to reduce the tapering observed in MOCVD growth of GaN nanowires. The issue surrounds the competition between nanowire growth and thin film deposition. GeCl₄ was utilized for preliminary studies to examine the effect of HCl on the nanowire growth. Introducing a small fraction of GeCl₄ to the gas phase mixture led to a reduction in the nanowire tapering and diameter. In addition, SEM results revealed the successful growth of GaN nanowires in the constant temperature region of the tube furnace. It is believed that GeCl₄ decomposes into HCl which then reacts with TMG to form GaCl. GaCl is thermally stable in the gas phase to elevated temperatures leading to a change in the gas

phase chemistry and GaN nanowire growth as a result. TEM was employed to investigate the structural properties of these nanowires, and two morphologies were found. One set of nanowires were observed to be smooth and consisted of wurtzite GaN with (0001) planar defects. The other set were jagged on the surface and consisted of primarily a wurtzite GaN core with zinc blende GaN islands protruding from the sidewalls of the nanowires. The islands were deemed to form after the axial growth of the nanowire. The main difference between the two structures was established to be the growth direction where the smooth wires had a [0002] growth direction, and the rough wires had a growth direction a few degrees away from $[1\bar{1}00]$.

5.7 References

- 1 S. A. Safvi, J. M. Redwing, M. A. Tischler, and T. F. Kuech, in *A Modeling Study of GaN Growth by MOVPE*, 1996 (Materials Research Society), p. 255-260.
- 2 C. Theodoropoulos, T. J. Mountziaris, H. K. Moffat, and J. Han, *Journal of Crystal Growth* **217**, 65-81 (2000).
- 3 J. X. Sun, J. M. Redwing, and T. F. Kuech, *Journal of Electronic Materials* **29**, 2-9 (2000).
- 4 T. Mihopoulos, Doctor of Philosophy Thesis, Massachusetts Institute of Technology, 1999.
- 5 *Phase Diagrams of Binary Nickel Alloys; Vol. 6*, edited by P. Nash (ASM International, Materials Park, 1991).
- 6 T. Kuykendall, P. Pauzauskie, S. K. Lee, Y. F. Zhang, J. Goldberger, and P. D. Yang, *Nano Letters* **3**, 1063-1066 (2003).
- 7 D. K. T. Ng, L. S. Tan, and M. H. Hong, *Current Applied Physics* **6**, 403-406 (2006).
- 8 C. K. Kuo, C. W. Hsu, C. T. Wu, Z. H. Lan, C. Y. Mou, C. C. Chen, Y. J. Yang, L. C. Chen, and K. H. Chen, *Nanotechnology* **17**, S332-S337 (2006).
- 9 J. Zhang and L. D. Zhang, *Journal of Vacuum Science & Technology B* **21**, 2415-2419 (2003).
- 10 C.-C. Chen and C.-C. Yeh, *Advanced Materials* **12**, 738-741 (2000).
- 11 O. Ambacher, H. Angerer, R. Dimitrov, W. Rieger, M. Stutzmann, G. Dollinger, and A. Bergmaier, *Physica Status Solidi a-Applied Research* **159**, 105-119 (1997).

- 12 S. A. Safvi, J. M. Redwing, M. A. Tischler, and T. F. Kuech, *Journal of the*
13 *Electrochemical Society* **144**, 1789-1796 (1997).
- 14 T. Kuykendall, P. J. Pauzauskie, Y. F. Zhang, J. Goldberger, D. Sirbuly, J.
15 Denlinger, and P. D. Yang, *Nature Materials* **3**, 524-528 (2004).
- 16 T. G. Mihopoulos, V. Gupta, and K. F. Jensen, *Journal of Crystal Growth* **195**,
17 733-739 (1998).
- 18 B.-J. Baek, S.-J. Kang, J.-T. Kim, B. Pak, and C.-R. Lee, *Journal of Crystal*
19 *Growth* **304**, 211-218 (2007).
- 20 B. E. Poling, J. M. Prausnitz, and J. P. O'Connell, *The Properties of Gases and*
21 *Liquids*, 5 ed. (McGraw-Hill, New York, 2000).
- 22 D. D. Koleske, A. E. Wickenden, R. L. Henry, J. C. Culbertson, and M. E. Twigg,
23 *Journal of Crystal Growth* **223**, 466-483 (2001).
- 24 O. Ambacher, H. Angerer, R. Dimitrov, W. Rieger, M. Stutzmann, G. Dollinger,
25 and A. Bergmaier, *Physica Status Solidi (a)* **159**, 105-119 (1997).
- 26 D. D. Koleske, A. E. Wickenden, R. L. Henry, J. C. Culbertson, and M. E. Twigg,
27 *Journal of Crystal Growth* **223**, 466-483 (2001).
- 28 S. H. Lee, Y. H. Mo, K. S. Nahm, E.-K. Suh, and K. Y. Lim, *Physica Status*
29 *Solidi (c)* **0**, 148-151 (2002).
- 30 Y. Inoue, A. Tajima, A. Ishida, and H. Mimura, *Physica Status Solidi (c)* **5**, 3001-
31 3003 (2008).
- 32 B. S. Simpkins, P. E. Pehrsson, M. L. Taheri, and R. M. Stroud, *Journal of*
33 *Applied Physics* **101**, - (2007).
- K. Dick, T. Dhanasekaran, Z. Zhang, and D. Meisel, *Journal of the American*
Chemical Society **124**, 2312-2317 (2002).
- P. Buffat and J. P. Borel, *Physical Review A* **13**, 2287-2298 (1976).
- A. I. Persson, M. W. Larsson, S. Stenstrom, B. J. Ohlsson, L. Samuelson, and L.
R. Wallenberg, *Nature Materials* **3**, 677-681 (2004).
- K. A. Dick, K. Deppert, T. Martensson, M. Bernhard, L. Samuelson, and W.
Seifert, *Nano Letters* **5**, 761-764 (2005).
- K. A. Dick, K. Deppert, L. S. Karlsson, L. R. Wallenberg, L. Samuelson, and W.
Seifert, *Advanced Functional Materials* **15**, 1603-1610 (2005).
- D. Aurongzeb, K. B. Ram, M. Holtz, M. Basavaraj, G. Kipshidze, B. Yavich, S.
A. Nikishin, and H. Temkin, *Journal of Applied Physics* **99**, - (2006).
- H. S. Venugopalan, S. E. Mohney, B. P. Luther, S. D. Wolter, and J. M. Redwing,
Journal of Applied Physics **82**, 650-654 (1997).
- T. Ikeda, Y. Nose, T. Korata, H. Numakura, and M. Koiwa, *Journal of Phase*
Equilibria **20**, 626-630 (1999).
- G. E. Murch and I. V. Belova, *Journal of Materials Processing Technology* **118**,
82-87 (2001).
- L. Lari, R. T. Murray, T. J. Bullough, P. R. Chalker, M. Gass, C. Cheze, L.
Geelhaar, and H. Riechert, *Physica E-Low-Dimensional Systems &*
Nanostructures **40**, 2457-2461 (2008).
- W. X. Yuan, Z. Y. Qiao, H. Ipsen, and G. Eriksson, *Journal of Phase Equilibria*
and Diffusion **25**, 68-74 (2004).

- 34 J. Johansson, B. A. Wacaser, K. A. Dick, and W. Seifert, *Nanotechnology* **17**, S355-S361 (2006).
- 35 J. Han, K. Kim, J. Su, M. Gherasimova, A. V. Nurmikko, S. F. Chichibu, and C. Broadbridge, in *MOCVD Growth and Characterization of AlGaInN Nanowires and Nanostructures*, Boston, MA, 2006 (Materials Research Society), p. 0892-FF31-01.1-10.
- 36 F. Qian, Y. Li, S. Gradecak, D. L. Wang, C. J. Barrelet, and C. M. Lieber, *Nano Letters* **4**, 1975-1979 (2004).
- 37 M. Tchernycheva, C. Sartel, G. Cirlin, L. Travers, G. Patriarche, L. Largeau, O. Mauguin, J.-C. Harmand, L. S. Dang, J. Renard, B. Gayral, L. Nevou, and F. Julien, *Physica Status Solidi (c)* **5**, 1556-1558 (2008).
- 38 Y. Inoue, A. Tajima, S. Takeda, A. Ishida, H. Mimura, and S. Sakakibara, *Physica Status Solidi (c)* **4**, 2366-2370 (2007).
- 39 X. M. Cai, A. B. Djuricic, M. H. Xie, C. S. Chiu, and S. Gwo, *Applied Physics Letters* **87**, - (2005).
- 40 X. M. Cai, A. B. Djuricic, M. H. Xie, C. S. Chiu, and S. Gwo, *Applied Physics Letters* **87**, 183103 (2005).
- 41 C. Y. Nam, D. Tham, and J. E. Fischer, *Applied Physics Letters* **85**, 5676-5678 (2004).
- 42 M. Nagahara, S. Miyoshi, H. Yaguchi, K. Onabe, Y. Shiraki, and R. Ito, *Journal of Crystal Growth* **145**, 197-202 (1994).
- 43 T. Zywietz, J. Neugebauer, and M. Scheffler, *Applied Physics Letters* **73**, 487-489 (1998).
- 44 J. Neugebauer, T. Zywietz, and M. Scheffler, *Physical Review Letters* **90**, 056101 (2003).
- 45 S. C. Jain, M. Willander, J. Narayan, and R. Van Overstraeten, *Journal of Applied Physics* **87**, 965-1006 (2000).
- 46 A. Y. Polyakov, M. Shin, J. A. Freitas, M. Skowronski, D. W. Greve, and R. G. Wilson, *Journal of Applied Physics* **80**, 6349-6354 (1996).
- 47 D. M. Hofmann, D. Kovalev, G. Steude, B. K. Meyer, A. Hoffman, L. Eckey, R. Heitz, T. Detchprom, H. Amano, and I. Akasaki, *Physical Review B* **52**, 16702-16706 (1995).
- 48 R. Armitage, W. Hong, Q. Yang, H. Feick, J. Gebauer, E. R. Weber, S. Hautakangas, and K. Saarinen, *Applied Physics Letters* **82**, 3457-3459 (2003).
- 49 J. Neugebauer and C. G. Van de Walle, *Applied Physics Letters* **69**, 503-505 (1996).
- 50 S. O. Kucheyev, M. Toth, M. R. Phillips, J. S. Williams, C. Jagadish, and G. Li, *Journal of Applied Physics* **91**, 5867-5874 (2002).
- 51 C. H. Seager, A. F. Wright, J. Yu, and W. Gotz, *Journal of Applied Physics* **92**, 6553-6560 (2002).
- 52 H. F. Ji, M. Kuball, R. A. Burke, and J. M. Redwing, *Nanotechnology* **18**, - (2007).
- 53 G. T. Wang, A. A. Talin, D. J. Werder, J. R. Creighton, E. Lai, R. J. Anderson, and I. Arslan, *Nanotechnology* **17**, 5773-5780 (2006).

- 54 L. Zhang, S. L. Gu, T. F. Kuech, and M. P. Boleslawski, *Journal of Crystal Growth* **213**, 1-9 (2000).
- 55 L. Zhang, S. L. Gu, R. Zhang, D. M. Hansen, M. P. Boleslawski, and T. F. Kuech, *Journal of Crystal Growth* **235**, 115-123 (2002).
- 56 K. Okamoto, O. Ito, and K. Yamaguchi, *Japanese Journal of Applied Physics* **31**, L820-L822 (1992).
- 57 T. F. Kuech, M. A. Tischler, and R. Poternski, *Applied Physics Letters* **54**, 910-912 (1989).
- 58 T. F. Kuech, *Semiconductor Science and Technology* **8**, 967-978 (1993).
- 59 Y. Kumagai, H. Murakami, H. Seki, and A. Koukitu, *Journal of Crystal Growth* **246**, 215-222 (2002).
- 60 Y. Matsuo, N. Kawaguchi, M. Fujino, Y. Kangawa, Y. Kumagai, T. Irisawa, and A. Koukitu, *Journal of Crystal Growth* **275**, e1631-e1636 (2005).
- 61 Y. Kumagai, H. Murakami, Y. Kangawa, and A. Koukitu, *Physica Status Solidi (c)* **2**, 2058-2061 (2005).
- 62 S. Sharma, T. I. Kamins, and R. S. Williams, *Journal of Crystal Growth* **267**, 613-618 (2004).
- 63 S. Sharma, T. I. Kamins, and R. S. Williams, *Applied Physics A* **80**, 1225-1229 (2005).
- 64 M. S. Islam, S. Sharma, T. I. Kamins, and R. S. Williams, *Nanotechnology* **15**, L5-L8 (2004).
- 65 H. M. Kim, Y. H. Cho, and T. W. Kang, *Advanced Materials* **15**, 232-+ (2003).
- 66 H. M. Kim, D. S. Kim, Y. S. Park, D. Y. Kim, T. W. Kang, and K. S. Chung, *Advanced Materials* **14**, 991-+ (2002).
- 67 G. Seryogin, I. Shalish, W. Moberlychan, and V. Narayanamurti, *Nanotechnology* **16**, 2342-2345 (2005).
- 68 D. A. Lapiano-Smith and F. R. McFeely, *Thin Solid Films* **225**, 187-190 (1993).
- 69 R. Soman, A. Reisman, D. Temple, and R. Alberti, *Journal of the Electrochemical Society* **147**, 1847-1853 (2000).
- 70 J. E. Huffman and N. L. Casey, *Journal of Crystal Growth* **129**, 525-531 (1993).
- 71 M. He, A. Motayed, and S. N. Mohammad, *The Journal of Chemical Physics* **126**, 064704-1-5 (2007).
- 72 B. W. Jacobs, V. M. Ayres, M. P. Petkov, J. B. Halpern, M. He, A. D. Baczewski, K. McElroy, M. A. Crimp, J. Zhang, and H. C. Shaw, *Nano Letters* **7**, 1435-1438 (2007).
- 73 B. W. Jacobs, V. M. Ayres, M. A. Crimp, and K. McElroy, *Nanotechnology* **19**, 1-6 (2008).
- 74 J. Suda, T. Kurobe, and H. Matsunami, *Journal of Crystal Growth* **201/202**, 437-440 (1999).
- 75 B. M. Shi, M. H. Xie, H. S. Wu, N. wang, and S. Y. Tong, *Applied Physics Letters* **89**, 151921-1-3 (2006).
- 76 L. X. Zheng, H. Yang, D. P. Xu, X. J. Wang, X. F. Li, J. B. Li, Y. T. Wang, L. H. Duan, and X. W. Hu, *Thin Solid Films* **326**, 251-255 (1998).

- 77 X. H. Wu, D. Kapolnek, E. J. Tarsa, B. Heying, S. Keller, B. P. Keller, U. K. Mishra, S. P. DenBaars, and J. S. Speck, *Applied Physics Letters* **68**, 1371-1373 (1996).
- 78 S. J. Xu, L. X. Zheng, S. H. Cheung, M. H. Xie, and S. Y. Tong, *Applied Physics Letters* **81**, 4389-4391 (2002).
- 79 J. H. Kim and P. H. Holloway, *Applied Physics Letters* **84**, 711-713 (2004).
- 80 H. Okumura, K. Ohta, K. Ando, W. W. Ruhle, T. Nagatomo, and S. Yoshida, *Solid-State Electronics* **41**, 201-204 (1997).
- 81 A. H. Chin, T. S. Ahn, H. Li, S. Vaddiraju, C. J. Bardeen, C.-Z. Ning, and M. K. Sunkara, *Nano Letters* **7**, 626-631 (2007).
- 82 M. K. Sunkara, H. Li, and A. H. Chin, in *Direction Dependent Homoepitaxial Growth and Bandgap of GaN Nanowires*, 2006 (SPIE), p. 612110I-1-11.
- 83 L. H. Robins, K. A. Bertness, J. M. Barker, N. A. Sanford, and J. B. Schlager, *Journal of Applied Physics* **101**, 113505 (2007).
- 84 H. W. Seo, S. Y. Bae, J. Park, H. Yang, P. K.S., and S. Kim, *Journal of Chemical Physics* **116**, 9492-9499 (2002).

Chapter 6

Synthesis of GaSb Nanowires

6.1 Introduction

To date, only a handful of studies have been performed concerning the growth of GaSb nanowires. As was discussed in Chapter 3, the different growth techniques that have been utilized for the growth of GaSb nanowires include: 1) the focused ion beam approach,^{1,2} 2) direct antimonidization/reactive vapor transport,³ and 3) conventional (cold-wall) MOCVD.⁴⁻⁷ There is limited information on the synthesis and properties of GaSb nanowires, therefore it was essential to perform a systematic study of the effect of the growth conditions on the structural and optical properties.

This chapter begins by focusing on obtaining a better understanding of the conditions that are necessary for the growth of GaSb nanowires. In this study, a hot-wall tube furnace reactor with metalorganic precursors was employed rather than the conventional cold-wall reactor due to its availability. Sapphire and Si (111) substrates were utilized for the experiments and were coated with 2 nm Au thin films and 50 nm Au colloid solutions. Due to limited information on GaSb nanowire growth, an initial set of growth conditions was explored based on the thin film literature. Preliminary experiments in this study were performed at the lower range of growth temperatures for GaSb thin film deposition (450-550°C) in order to minimize competition between thin film deposition and nanowire growth. GaSb thin films were successfully grown using

low pressure and atmospheric pressure MOCVD, therefore a pressure range of 13-600 Torr was investigated for nanowire growth. Finally, the V/III ratio was varied over a narrow range of 0.5-2. Typically, GaSb thin films are grown at a V/III ratio near unity due to the low equilibrium vapor pressure of TMSb. A V/III ratio less than unity usually leads to the formation of Ga droplets on the surface, whereas a V/III ratio greater than unity tends to produce Sb hillocks on the thin film surface.⁸ At the same time, samples grown with a V/III ratio near unity were found to possess the best electrical and optical properties.⁹

After completing the experiments, SEM was employed to investigate the effect of the growth conditions on the morphologies of the final products. Based on the initial findings utilizing the SEM, TEM was carried out on a selected set of samples in order to investigate the structural properties of the nanowires. In particular, the characterization focused on analysis of the diameter, growth direction, and composition of the seed particle. Photoluminescence (PL) measurements were also carried out in order to compare the optical properties of the nanowires to published reports in the thin film literature. PL data was collected from a variety of samples including samples grown on both sapphire and silicon. PL measurements were also obtained on a set of samples where the V/III ratio was altered, which has been shown in the past to be a critical factor in the optical properties of GaSb.

The author would like to acknowledge individuals who contributed to this work. The growth studies were performed solely by the author, while the TEM analysis was carried out by Dr. Xiaojun Weng. The photoluminescence work was completed at the University of Canterbury in New Zealand by Professor Roger Reeve's group in the

Department of Physics and Astronomy. All post-PL analysis was completed by the author.

6.2 Growth of GaSb Nanowires on Sapphire Substrates

In the following studies, the precursor pyrolysis studies discussed in Chapter 3 were utilized to gain a better understanding of the growth conditions necessary for the synthesis of GaSb nanowires. Comparisons were also made to the GaSb thin film literature. The following sections summarize the effects of the main process parameters (temperature, pressure, and V/III ratio) that were investigated.

6.2.1 Effect of Temperature

The effect of temperature on the growth of GaSb nanowires was initially investigated. The furnace temperature set-point was varied over a range of 450-550°C, while the pressure was held constant at 100 Torr with a H₂ flowrate of 100 sccm. For the temperature study, the V/III ratio was maintained at a value of 1 by introducing a flowrate of 1 sccm for both TMG and TMSb to the gas phase mixture. Samples for this study consisted of 5 nm Ni thin films on sapphire, 2.5 nm Au thin films on sapphire, and sapphire substrates coated with a 5% solution of 50 nm Au nanoparticles. The samples were loaded into a quartz boat which was placed in the center of a 12 inch hot zone (Figure 4.6 (b)). It should also be noted that a concentric tube inlet was not used for these

studies. The results concerning the Au thin films will be reported later in this chapter as some differences were observed between the use of nanoparticles and thin films.

The nickel results, however, are not reported here due to limited success with this catalyst. This observation was expected, since Ga and Sb would not be expected to form a liquid alloy with Ni over this temperature range. Assessing the Ni-Sb phase diagram, VLS growth would not be possible as the catalyst would remain a solid at all concentrations of Sb.¹⁰ Looking back at the Ni-Ga phase diagram (Figure 5.17), the seed particle would have to consist of approximately 95 at.% Ga, making it highly unlikely that a liquid alloy would form.

On the other hand, GaSb nanowire growth would be expected when using Au as the catalyst. Figure 6.1 displays the binary phase diagrams for Au-Ga and Au-Sb. For the Au-Ga phase diagram, the eutectic point is at 339°C for a composition of 36.6 at.% Ga. For the Au-Sb phase diagram, a liquid alloy could possibly form at a temperature of 360°C and a composition of 35.5 at.% Sb. These values are well within the range of temperatures utilized in these studies. A line has been drawn at a temperature of 500°C in order to exemplify this point. At 500°C, a liquid alloy would form at roughly 22 at.% Ga for the Au-Ga phase diagram and 27 at.% Sb for the Au-Sb phase diagram. Unless specified, this chapter will focus on the results concerning the use of 50 nm Au nanoparticles.

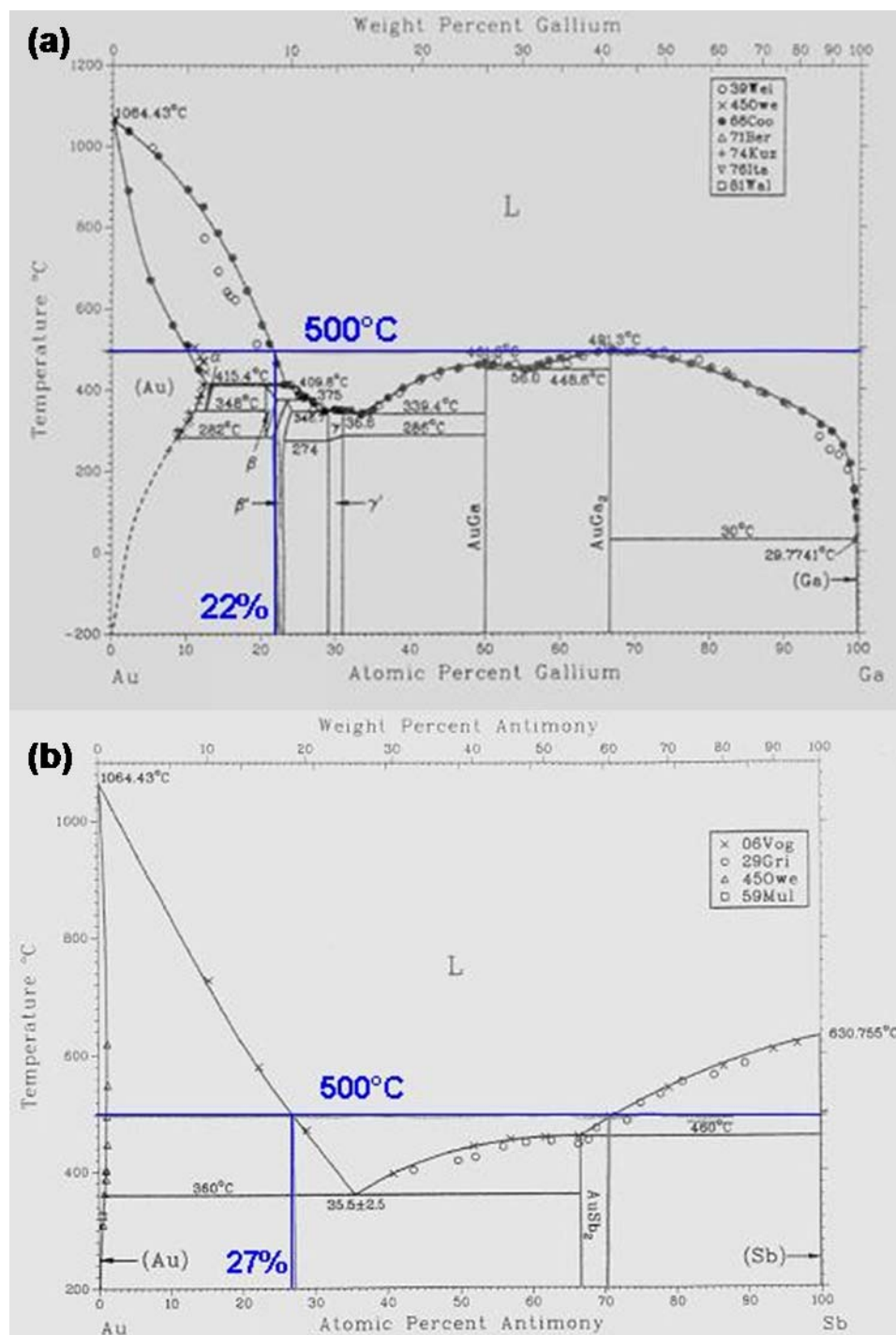


Figure 6.1: Binary phase diagrams for (a) Au-Ga and (b) Au-Sb. A line is drawn at 500 °C to indicate the temperature at which GaSb nanowire growth resulted.¹¹

In general, a small growth window was found with respect to temperature under these conditions. Nanowire growth was not achieved at temperatures below 475°C or above 525°C (Figure 6.2). In Figure 6.2 (a), the sapphire substrate does not appear to have any GaSb deposits. The particles that are present on the surface are 50 nm Au nanoparticles. Based on the pyrolysis studies, it does not appear to be possible to grow GaSb nanowires at temperatures below 475°C and low reactor pressures due to insufficient decomposition of TMG and TMSb. Further evidence of this was seen by recording the location of the tube wall deposits with respect to the quartz boat. At 450°C, the wall deposits were located downstream of the quartz boat, indicating a low rate of precursor pyrolysis at the location of the substrate.

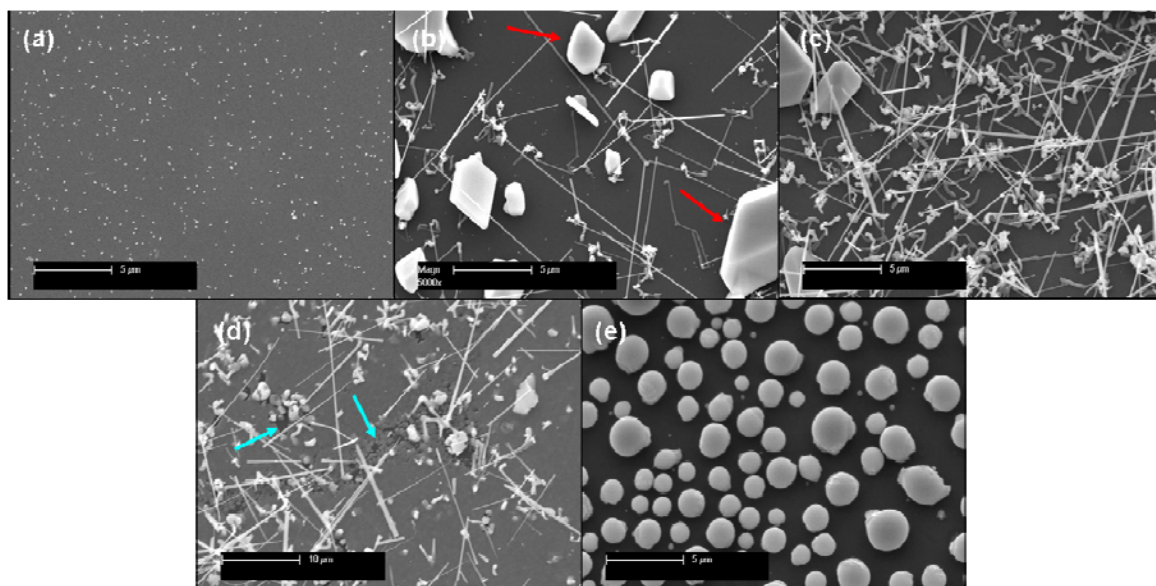


Figure 6.2: SEM images of GaSb growth at temperatures of (a) 450°C, (b) 475°C, (c) 500°C, (d) 525°C, and (e) 550°C. Growth conditions: 100 Torr, 1 sccm TMG, 1 sccm TMSb, 100 sccm H₂, and 5 minutes.

Over the temperature range of 475-525°C, GaSb nanowires were successfully synthesized (Figure 6.2 (b)-(d)). Over this temperature range, the quartz tube wall deposits were found to span the entire hot zone of the furnace. GaSb crystallites were present, which are indicated with red arrows in Figure 6.2 (b). The nanowires grown at 475°C were roughly uniform in diameter, although they became more tapered with an increase in temperature. This is likely due to thin film deposition on the surface of the nanowires during growth. The presence of a competing thin film deposition is evident at 525°C. The thin film growth can be seen in the background of Figure 6.2 (d) and discontinuities in the growth are marked with blue arrows.

At 550°C, nanowire growth was not observed and was replaced with large particle deposits (Figure 6.2 (e)). In order to determine the composition of these particles, EDS was employed. EDS confirmed the presence of Ga and Sb within this sample. In another experiment at a growth temperature of 550°C, the total metalorganic flowrate was doubled to 4 sccm, which led to the sapphire surface being entirely coated with a thin film. The temperature, in this case, appears to be too high for nanowire growth, as an operating temperature of 550°C is commonly used for thin film deposition of GaSb.

There may also be an issue with depletion of the gas phase precursors prior to the growth front as the wall deposits were located upstream of the quartz boat. Temperature has been observed in previous III-V nanowire studies to impact the precursor decomposition which in turn alters the local V/III ratio.^{12,13} In the case of the growth of InAs nanowires, higher temperatures led to a depletion of In at the growth front, leading to a reduction in the growth rate and eventually termination of nanowire growth.¹² A thin film was still present on the surface though. However, the cessation temperature was

found to increase when the TMI_n flowrate was increased (decreasing the V/III ratio) to overcome the problem of depletion of In. This can become a factor for GaSb nanowire growth at higher temperatures if one precursor were to become depleted prior to the growth front, which in essence would alter the V/III ratio. Instead, Ga or Sb droplets could form on the surface at low metalorganic flowrates or a thin film could develop at higher flowrates. It may still be possible to grow GaSb nanowires at higher temperatures if the quartz boat was either shifted towards the front edge of the hot zone or the V/III ratio was altered to account for the loss of the gas phase precursors.

In order to acquire a rough estimate of the nanowire diameter and length for the temperature studies, high magnification SEM images were obtained. TEM characterization of the nanowires was also utilized to determine the average diameter, and those results will be discussed later in this chapter. For the SEM analysis, Image J software was utilized to measure the diameters and lengths of a sampling of nanowires over the temperature range of 475-525°C. The average diameter of the GaSb nanowires for a sample grown at 500°C was determined to be approximately 94 nm with a standard deviation of 31 nm. The nanowire diameter was found to be significantly larger than the 50 nm Au nanoparticles which were utilized as the seed particle. The diameter change can be attributed to the volume increase that is necessary to incorporate Ga and Sb into the catalyst. Based on the VLS growth mechanism, Ga and Sb will absorb on the Au surface and diffuse into the seed particle. A liquid alloy will form when the seed particle consists of the appropriate amount of Ga and Sb. The volume of the alloy will grow until the particle becomes supersaturated, and GaSb will precipitate out of the catalyst in a crystalline form. The diameter of the nanowire will be dependent on the size of the

alloyed particle prior to precipitation. As a result, the GaSb nanowires possess an average diameter that is significantly larger than the initial Au catalyst.

Unlike the diameter, the average length of the nanowires was found to have a strong dependence on temperature. The nanowire samples were grown at a pressure of 100 Torr with a V/III ratio of 1 (1 sccm of TMG and TMSb) for 5 minutes. The average length as a function of temperature is shown in Figure 6.3. In order to determine a rough estimate of the growth rate, the average length was divided by the growth time. The growth rate was found to be 1.09 ± 0.24 $\mu\text{m}/\text{min}$ at 475°C and increased to 4.58 ± 0.77 $\mu\text{m}/\text{min}$ at 525°C . Additional studies will be necessary in order to obtain more precise measurements of the growth rates for various temperatures.

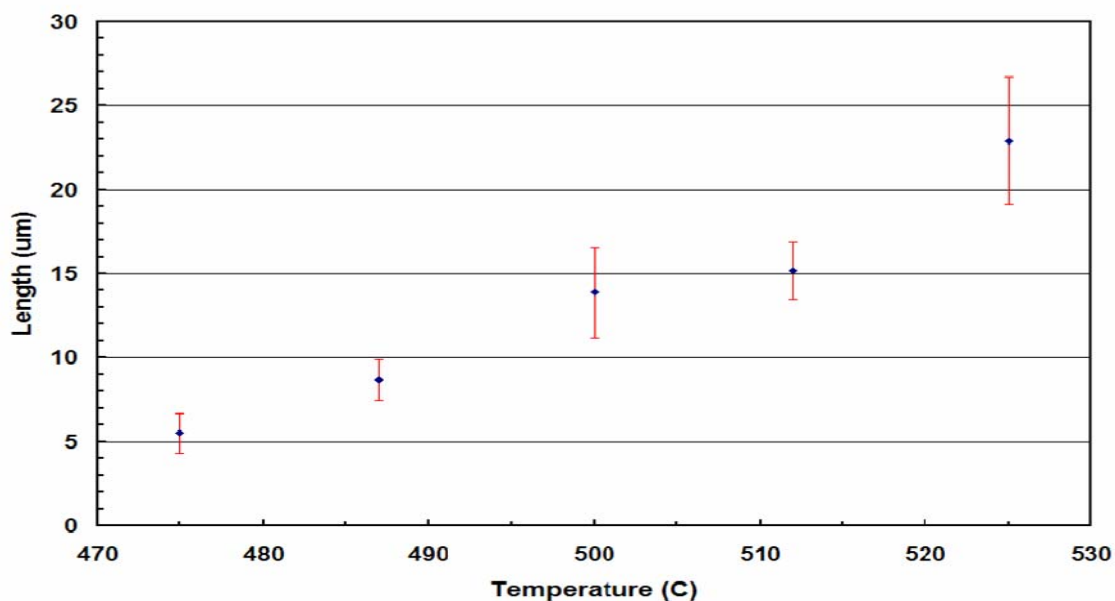


Figure 6.3: Graph of temperature vs. length for GaSb nanowires grown at 475°C , 487°C , 500°C , 512°C , and 525°C . Growth conditions: 100 Torr, 1 sccm TMG, 1 sccm TMSb, 100 sccm H_2 , and 5 minutes.

The growth rate information obtained in this study was subsequently graphed as a function of temperature to determine if an Arrhenius dependence exists. Figure 6.4 is a graph of the natural log of the growth rate vs. the reciprocal of temperature in Kelvin. The data was determined to fit reasonably well with a linear fit ($R^2 = 0.9698$). Based on the results, GaSb nanowire growth proceeds in the kinetically-limited regime over the nanowire growth temperature range. This is also typically observed for thin film growth of GaSb as the growth temperatures necessary lead to incomplete pyrolysis of TMG and TMSb. (Ref) The activation energy for GaSb was calculated based on the slope of the linear fit, and it was determined to be 30.5 ± 5.1 kcal/mol. The activation energy fits well with analysis of GaSb/GaAs nanowire heterostructures completed by Jeppsson *et al.* where the activation energy was determined to be 32.7 kcal/mol (127 kJ/mol) at a V/III

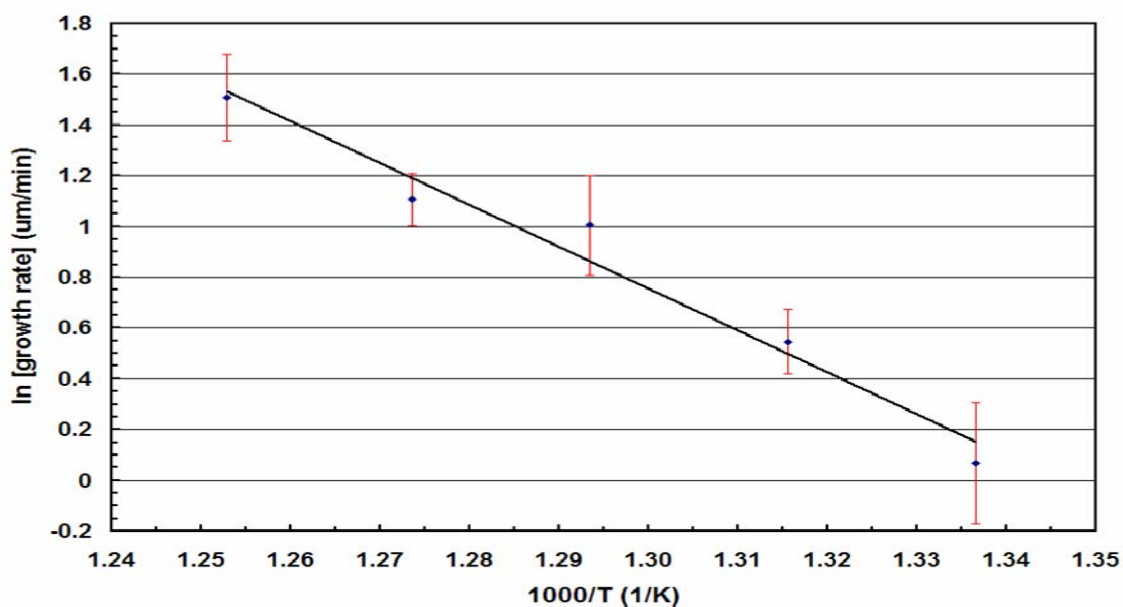


Figure 6.4: Arrhenius plot of GaSb nanowire growth at temperatures ranging from 475°C to 525°C. Growth conditions: 100 Torr, 1 sccm TMG, 1 sccm TMSb, and 5 minute growth.

ratio of 1.2.⁷ For the GaSb thin film literature, the activation energy varied between 19.3 kcal/mol and 54 kcal/mol depending on the study.^{8,14-16}

A growth rate study, however, was completed at a temperature of 500°C using the same conditions as above. GaSb nanowire samples were grown for 1, 3, 5, 10, and 15 minutes. Length measurements were taken from SEM images for each growth time using the Image J software, and the average length was graphed as a function of time (Figure 6.5). The data was found to fit well with a linear fit ($R^2 = 0.992$). The nanowire growth rate was determined by the slope of the line. The growth rate was calculated as 2.24 ± 0.23 $\mu\text{m}/\text{min}$ for a growth temperature of 500°C. In Figure 6.3, the nanowire growth rate was calculated as 2.78 ± 0.54 $\mu\text{m}/\text{min}$ for a growth temperature of 500°C.

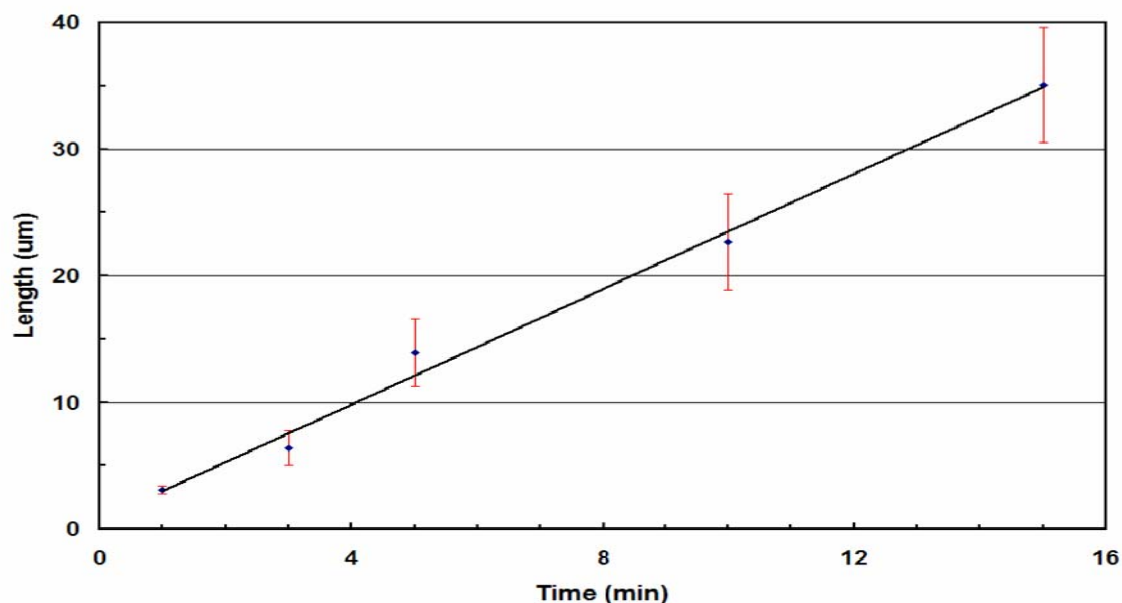


Figure 6.5: Plot of length vs. time for various GaSb nanowire samples grown at 500°C. The growth rate was calculated from the slope of the line as 2.24 ± 0.23 $\mu\text{m}/\text{min}$. Growth conditions: 100 Torr, 1 sccm TMG, 1 sccm TMSb, and 100 sccm H_2 .

It should be noted that the growth rate observed for this study is significantly higher than published reports for MOCVD growth of GaSb nanowires.^{5,7} In both published reports, GaSb/GaAs heterostructures were synthesized using conventional cold-wall reactors. Initially, GaAs nanowire segments were grown on GaAs (111)B substrates using Au as the catalyst. After this growth was complete, GaSb nanowire segments were grown. The growth rates for these studies were determined to be ~ 1.67 nm/min and ~ 17.9 nm/min for samples grown at 425°C and 470°C , respectively. It is possible the significant difference in growth rates could be attributed to the use of a cold-wall reactor versus a hot-wall reactor for the studies. In the 2nd study at 470°C , the author attributed the slow growth rate to incomplete pyrolysis of the gas phase precursors.⁷ At the same time, the typical flowrates in a cold-wall reactor are significantly higher than a hot-wall reactor. For example, in the 2nd study the total gas flowrate was on the order of 13 L/min, while the total gas flowrate for this study is only 0.14 L/min or roughly 100 times lower. As a result, this would lead an appreciably higher molar fraction of TMG and TMSb in the gas phase compared to the cold-wall studies, which can affect the nanowire growth rate. Based on calculations, the metalorganic molar fraction for the cold-wall study was $\sim 8 \times 10^{-5}$, while the molar fraction for this study was ~ 0.014 or roughly 175 higher than the cold wall study.

A byproduct of this study was the ability to look at the nucleation properties of GaSb nanowire growth. Nanowires were found to nucleate from the sapphire surface, although there appeared to be a tendency for GaSb nanowires to nucleate from the base of other nanowires or crystallites on the surface. An example of this concept is displayed in the SEM image in Figure 6.6. The red dotted circles in this image indicate locations

where GaSb nanowire growth appears to have nucleated from other nanowires or growths on the surface. Sapphire is not an ideal substrate choice for the growth of GaSb due to its large lattice mismatch (~22%). Ideally, GaAs (111) would be a much better fit, however the nanowire CVD system is not equipped with an arsine source to prevent the evaporation of As from the GaAs substrate. The nucleation issue was observed in other samples and will be reintroduced in the Au thin film studies to explain some of the observations.

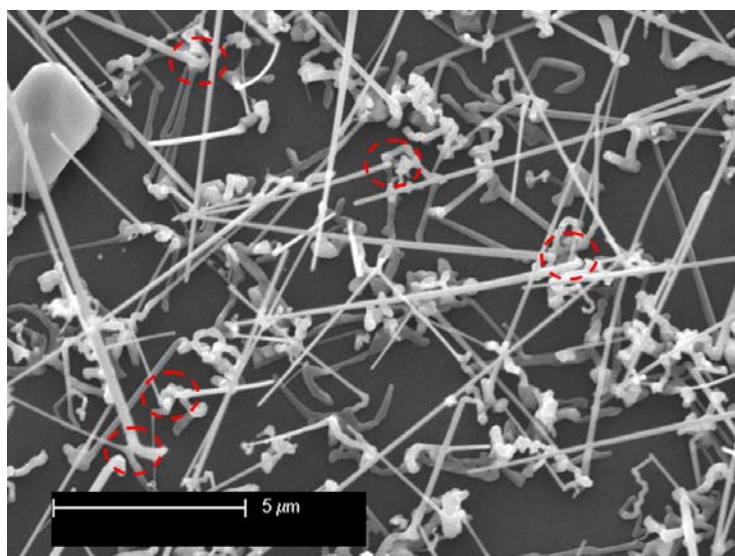


Figure 6.6: SEM image of GaSb nanowire growth at 500°C, 100 Torr, 1 sccm TMG, 1 sccm TMSb, and 100 sccm H₂. The sample was grown for 5 minutes. The red dotted circles indicate locations where GaSb nanowire growth nucleated from other wires or growths on the surface.

6.2.2 Effect of Pressure

Once a temperature range was established for the synthesis of GaSb nanowires, the focus shifted to examining the effect of pressure on the growth of GaSb nanowires.

For this study, the temperature was held constant at 500°C, and the V/III ratio was maintained at a value of 1. For these conditions, nanowire growth was achieved over a pressure range of 100-300 Torr (Figure 6.7 (b)-(d)). At 13 Torr (Figure 6.7 (a)), there appears to be no evidence of GaSb nanowire growth. At this pressure, the residence time appears to be too short for sufficient decomposition of the precursors for nanowire growth. Over a pressure range of 100-250 Torr, the nanowire length and density increase, although the nanowires also become more tapered (Figure 6.7 (b)-(c)). In this range, increasing the pressure leads to an increase in the nanowire growth rate, however higher pressures are also more common for thin film deposition, which explains the increase in tapering.⁹ This is also evident in the presence of a higher density of GaSb crystals in the background at higher pressures.

At a pressure of 200 Torr (Figure 6.7 (c)), a higher degree of nanowires appear to grow with a preferred orientation when compared to samples grown at lower pressures. The observation of a preferred orientation along with a general increase in density with pressure is believed to be a byproduct of a change in the gas phase chemistry.¹⁷ Due to the higher pressures, the pyrolysis of TMG and TMSb proceed further to completion. It is believed that an increase in the partial pressure of Ga on the surface of the nanoparticles leads to a change in the catalyst composition, an increase in the nanowire nucleation density, and a higher degree of wires growing with a preferred orientation. This concept will be discussed further in the next section which concentrates on the effect of the V/III ratio.

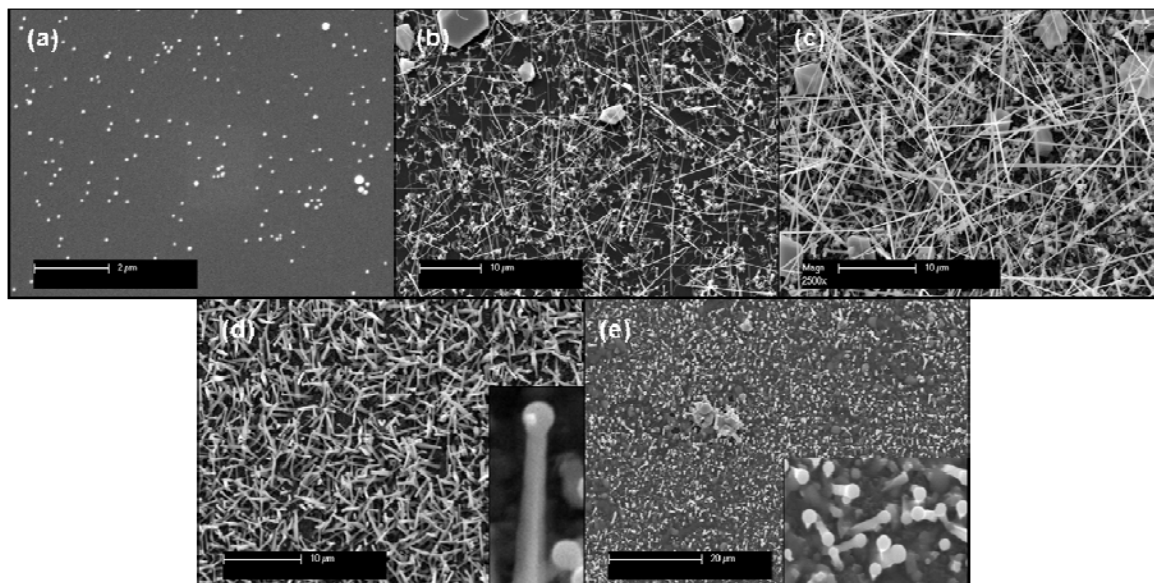


Figure 6.7: SEM images of GaSb growth at pressures of (a) 13 Torr, (b) 100 Torr, (c) 200 Torr, (d) 300 Torr, and (e) 400 Torr. Inset in (d) is a high magnification image of a GaSb nanowire. Inset in (e) shows the thin film/nanowire matrix that forms at 400 Torr. Growth conditions: 500°C, 1 sccm TMG, 1 sccm TMSb, 100 sccm H₂, and 5 minute growth time.

At 300 Torr, a transition results where the nanowires are significantly shorter and much larger in diameter (Figure 6.7 (d)). A high magnification image of such a wire is shown as an inset in Figure 6.7 (d). The nanowire diameter and length at various pressures were determined from SEM images and are provided in Table 6.1. There is no diameter change between 100 Torr and 200 Torr, however at 300 Torr, the diameter increases from ~93 nm to ~229 nm. At the same time, the nanowire length decreases from 20.6 μm to 3.2 μm. As the pressure is increased further to 400 Torr, the morphology consists of a thin film/nanowire matrix. The nanowires are very short and appear to protrude from the thin film. Increasing the pressure to 600 Torr leads to the

surface being coated with large droplets similar to those seen at 550°C in the previous study (Figure 6.2 (e)).

Table 6.1: Diameter and length measurements of GaSb nanowires at various reactor pressures.

Pressure (Torr)	Diameter (nm)	Std. Dev. (nm)	Length (μm)	Std. Dev. (μm)
100	94	31	13.9	2.7
200	93	25	20.6	4.2
300	229	18	3.2	1.0

The location of the wall deposits were recorded for this series of experiments. The wall deposits were observed to span the entire hot zone at 100 Torr. At 200 Torr, the wall deposits were heaviest at the location of the quartz boat. As the pressure increased, the wall deposits continued to shift upstream as they were located prior to the boat by 400 Torr. As was noted in Chapter 3, pressure can have a significant effect on the pyrolysis of the precursors. As the pressure increases, the gas velocity decreases which increases the residence time in the reactor and therefore the extent of precursor decomposition. H_2 also becomes more of a factor in the decomposition of TMG and TMSb due to an increase in the frequency of collisions between H radicals and the precursors. Consequently, this leads to an increase in the decomposition rate of the precursors and shifts the growth front upstream. Based on the wall deposit observations, eventually this results in the primary gas phase reactions occurring prior to the location of the samples.

6.2.3 Effect of the V/III Ratio

The V/III ratio tends to be critical to the deposition of high quality GaSb thin films. Typically, a V/III ratio near unity has been found to be ideal for growth of GaSb, however this value can change depending on the reactor design and growth conditions.⁹ In the thin film literature, deviating to a V/III ratio less than unity (Ga-rich) tends to lead to the formation of Ga droplets on the surface, whereas an Sb-rich condition ($V/III > 1$) leads to the formation of Sb hillocks on the surface.⁸

In this set of experiments, the V/III ratio was varied between 0.5 and 2. This was done by adjusting the TMG and TMSb flowrates while maintaining a total metalorganic flowrate of 2 sccm. The furnace set-point was maintained at a temperature of 500°C, while the pressure was held constant at 100 Torr. The results of this study are shown in Figure 6.8. As the V/III ratio was decreased to 0.5 (Ga-rich), a slight decrease in the nanowire length (growth rate) was observed (Figure 6.8 (a)). At the same time, an increase in the nanowire density was observed along with a higher density of GaSb crystals. There also appears to be a higher degree of nanowires growing with a preferred orientation in this case. It is believed that increasing the TMG partial pressure in the gas phase mixture leads to a change in the composition of the alloyed particles. As a result, this leads to a change in the surface energy and nucleation barrier and promotes a preferred orientation for GaSb nanowire growth.^{17,18} These results coincide well with those obtained at higher pressures in the previous study.

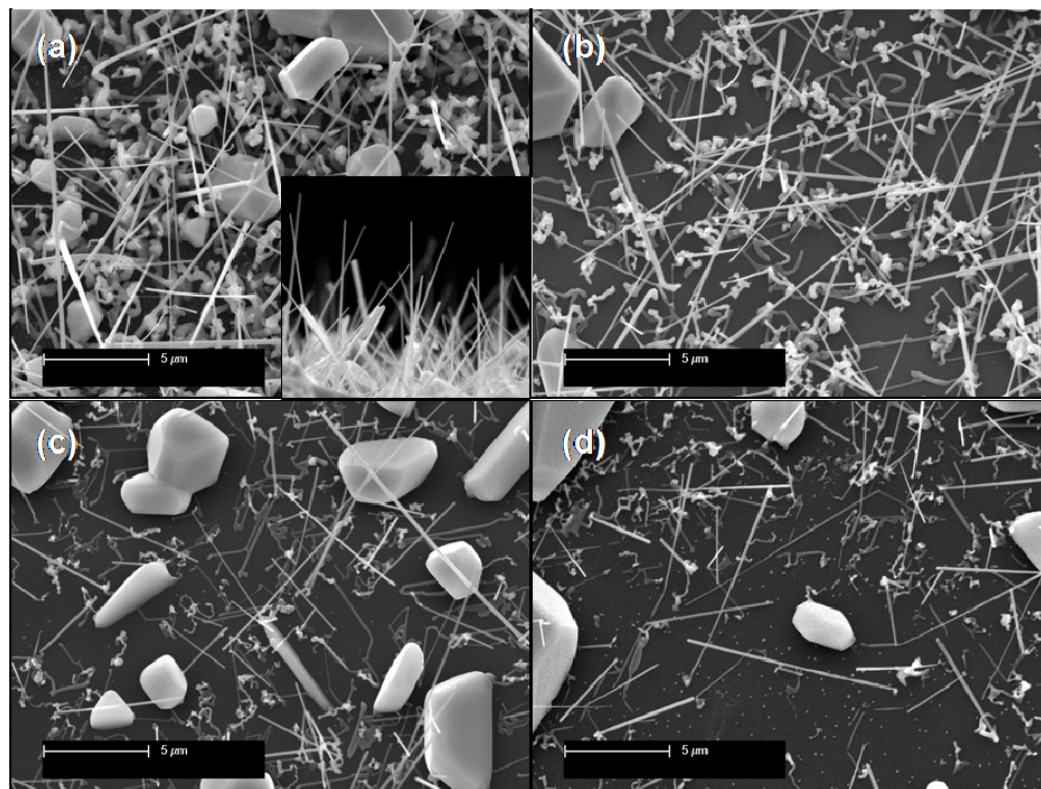


Figure 6.8: SEM images of GaSb nanowire growth at V/III ratios of (a) 0.5, (b) 1, (c) 1.5, and (d) 2. Inset in (a) shows higher degree of nanowires growing with a preferred orientation. Growth conditions: 500°C, 100 Torr, 100 sccm H₂, and 5 minute growth.

A negative effect to decreasing the V/III ratio was the presence of a significant tapering of the nanowires. The wires were approximately 100 nm at the tip, however they were 300 nm at the base. According to the thin film literature, the synthesis of GaSb in Ga-rich conditions typically leads to Ga droplet formation on the surface.⁸ In this case, the excess Ga deposits are believed to promote thin film deposition on the sidewalls of the nanowires. There also appears to be an increase in the density of kinked nanowires for Ga-rich conditions compared to Sb-rich conditions. For Si nanowire growth, kinking has been attributed to instabilities in the seed particle.^{19,20} It is possible this may be the case for GaSb nanowire growth too.

The effect of the V/III ratio was more noticeable when the TMSb flowrate was increased. Increasing the V/III ratio (Sb-rich) resulted in a noticeable decrease in the nanowire density (Figure 6.8 (c) and (d)). The GaSb nanowires were also found to be relatively shorter in length compared to a V/III ratio of 1. At a V/III ratio of 1.5, the nanowires were found to be uniform in diameter. Interestingly enough, when the V/III ratio was increased to 2, some nanowires were observed to actually increase in diameter as they grew, otherwise known as a “reverse tapering.”²¹⁻²³

This effect was magnified when the overall metalorganic (MO) flowrate was increased to 3 sccm. In this case, the TMG flowrate was maintained at 1 sccm, while the TMSb flowrate was increased to 2 sccm. For comparison, a sample was grown at a Ga-rich condition (V/III=0.5) where the TMSb flowrate was maintained at 1 sccm, and the TMG flowrate was increased to 2 sccm. The results of these experiments can be seen in Figure 6.9 (a) and (b). The blue arrows in Figure 6.9 (a) identify the location of the tip for the sample grown at a V/III ratio of 0.5. In this sample, it is obvious that the nanowires are tapered due to a competing thin film deposition. On the other hand, the red arrows in Figure 6.9 (b) demonstrate how the nanowires increase in diameter as they grow for a V/III ratio of 2. Higher magnification images of the “reverse tapering” were obtained for nanowires grown with a total MO flowrate of 2 sccm (Figure 6.9 (c)) and 3 sccm (Figure 6.9 (d)). The nanowire tips have once again been labeled with red arrows. Diameter measurements were taken of both the base and tip for each case. The nanowires were found to possess a tip and base diameter of 105 ± 25 nm and 61 ± 11 nm, respectively, for a total MO flowrate of 2 sccm. Nanowires that were grown at a total

MO flowrate of 3 sccm were determined to have a tip and base diameter of 99 ± 18 nm and 61 ± 14 nm, respectively.

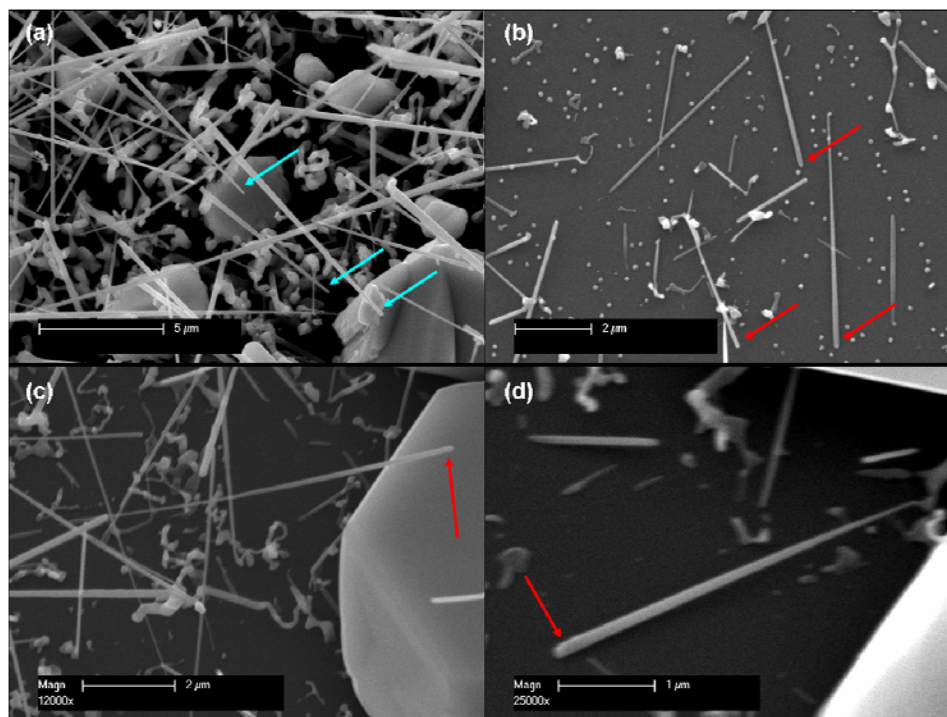


Figure 6.9: SEM images of GaSb nanowires grown at V/III ratios of (a) 0.5 and (b) 2. The total MO flowrate for these experiments was increased to 3 sccm. (c) and (d) are higher magnification images of GaSb nanowires grown at a V/III ratio of 2 with a total metalorganic flowrate of 2 sccm and 3 sccm respectively. The blue and red arrows in the images are located near the seed particle.

The average nanowire length for each V/III ratio was also determined from SEM images, and the results are displayed in Table 6.2. The average length was measured for samples grown with a total metalorganic flowrate of 2 sccm and 3 sccm. There is one exception to this case. A total metalorganic flowrate of 4 sccm was employed for the sample grown at a V/III ratio of 1. As can be seen, the nanowire length for Sb-rich conditions is approximately half the length that was measured for nanowires grown at a V/III ratio of 1. The nanowire length decreases when a Ga-rich condition is employed,

however the difference is not as prominent. When the total metalorganic flowrate was increased for a $V/III \leq 1$, an increase in the nanowire growth rate was observed. Consequently, the opposite effect was observed when the V/III ratio was 2. At a V/III ratio of 2, the growth rate was found to decrease. This trend has been previously observed for the growth of GaSb thin films.²⁴

Table 6.2: Length measurements of GaSb nanowires at various V/III ratios. For certain growths, the total metalorganic flowrate was increased and is noted in the table.

V/III Ratio	Total MO Flowrate (sccm)	Length (μm)	Std. Dev. (μm)
0.5	2	11.4	1.7
0.5	3	13.7	3.9
1	2	13.9	2.7
1	4	17.1	2.4
1.5	2	7.7	2.8
2	2	8.4	1.7
2	3	5.2	1.3

Based on these results, a hypothesis has been suggested concerning the effect of the V/III ratio on GaSb nanowire growth. It is believed that the nucleation and growth rate are dependent on the supply of Ga (TMG) to the substrate. This belief is supported by various observations from the V/III ratio study. First off, the nanowire density was observed to increase substantially in a Ga-rich environment, while a significant decrease in the nanowire density was observed in a Sb-rich environment. At the same time, the growth rate was found to be a maximum at a V/III ratio of 1 and decreased slightly at a V/III ratio of 0.5. The reduction in the growth rate became more prominent when the V/III ratio was increased to 1.5 and 2. When the V/III ratio is less than unity, it is believed that Ga droplets deposit on the side facets of the nanowires, promoting thin film deposition. As a result, the nanowire growth rate is hindered slightly, while the radial

growth rate increases. When the V/III ratio is raised, an excess of Sb is present compared to the concentration of the Ga in the gas phase. As a result, the nanowire growth rate is retarded, since the transport of Ga to the seed particle appears to be the rate-limiting step for GaSb nanowire growth. This effect is exemplified when the total metalorganic (MO) flowrate is increased. By increasing the total MO flowrate, the overall Ga and Sb concentrations in the gas phase mixture increase which leads to an increase in the growth rate at a V/III ratio of 0.5 and a reduction in the growth rate at a V/III ratio greater than 1.

The dependence of the nucleation and the growth rate on the V/III ratio has been observed before for other III-V systems.^{12,25,26} In particular, this trend has been observed for the synthesis of InAs nanowires using TMIIn and AsH₃. The nucleation density and growth rate were found to be dependent on both the V/III ratio and the growth temperature.¹² At a V/III ratio of 60, the nanowire cessation temperature was determined to be 525°C; however, when the V/III ratio was lowered to 7.5, nanowire growth was achieved at temperatures as high as 560°C. At higher temperatures, issues arose concerning the depletion of In at the Au nanoparticle interface, which were overcome by decreasing the V/III ratio. When the temperature was held constant and the V/III ratio was decreased, the density and length of InAs nanowires increased. Both the TMIIn and AsH₃ flowrates were varied to change the V/III ratio, and the nanowire growth rate was found to possess a higher dependence on the TMIIn flowrate. At the same time, increasing the TMIIn flowrate also led to a significant tapering of the InAs nanowires as the radial deposition increased.¹² A similar growth rate dependence was observed for the growth of GaAs nanowires by MOCVD.²⁵ As the TMG flowrate was increased, the GaAs nanowire growth increased. At the same time, lower temperatures led to a decrease

in the growth rate, and this observation was attributed to incomplete pyrolysis of TMG. These studies support the belief that the nucleation density and growth rate are dependent on the TMG (group III) flowrate for the synthesis of GaSb nanowires.

The importance of the supply of Ga to the substrate was only reinforced when looking at the results of the GaSb nanowires grown in a Sb-rich environment ($V/III=2$). Under these conditions, a selection of nanowires was found to possess a “reverse tapering” where the diameter of the nanowires initially increased as they grew before the diameter of the nanowires stabilized. It is believed that this effect is due to a deficiency of Ga to the seed particle in the Sb-rich growth conditions. This resulted in the precipitation of the GaSb nanowire before the seed particle was able to stabilize in its final state, which has been observed in other nanowire systems.^{19,22} For a nanoparticle consisting of Au and Ga, the time necessary for the nanoparticle to reach equilibrium composition has been calculated to be around one minute.²⁷ This value, however, is found to depend on the conditions utilized for growth.

Therefore, the time required for the Au-Ga nanoparticle to reach equilibrium would be expected to be higher at a V/III of 2 than a V/III ratio of 0.5, since there is a lower concentration of Ga reaching the seed particle. As a result, it is believed that the nanowire precipitates from the Au-Ga nanoparticle prior to the particle reaching its final state of equilibrium. The nanowire will continue to increase in diameter until this equilibrium state is reached. When the final composition is achieved, the nanowire diameter appears to stabilize (Figure 6.9 (c) and (d)).²¹ A schematic of this concept is found in Figure 6.910. This concept is further illustrated in the diameter calculations from these studies. In those calculations, the diameter of the base was found to be

approximately 60 nm for both a total metalorganic flowrate of 2 and 3 sccm. This value is slightly larger than the original Au nanoparticle, which can be attributed to incorporation of Ga and Sb to precipitate the nanowire. The diameter of the tip, however, was found to be around 100 nm which is similar to the typical diameter observed for samples grown at a V/III ratio of 1 (94 ± 31 nm). It is also possible the diameter increase could be due to the incorporation of excess Sb into the nanoparticle, which would cause the diameter of the nanowire to increase with time. This concept could be tested by increasing the V/III ratio or growth time. If the original hypothesis is correct, then the diameter of the tip should remain the same independent of V/III ratio or growth time.

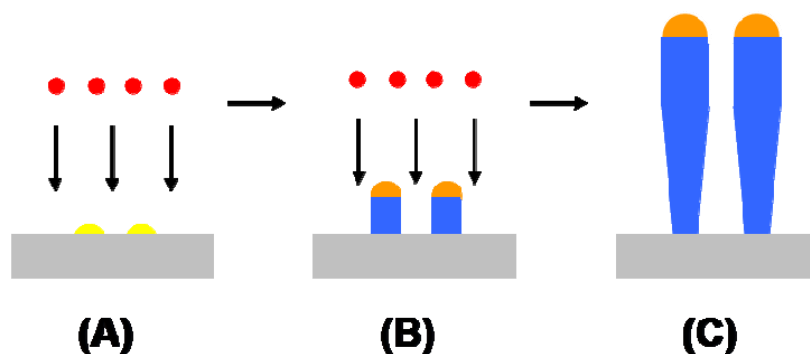


Figure 6.10: Schematic of “reverse tapering.” (a) Gas precursors flown to reaction site and react with nanoparticles. (b) Precipitation of GaSb crystal from catalyst. (c) Catalyst continues to grow in size as the nanowire grows until it reaches equilibrium and then levels out.

Under Ga-rich conditions, this instability is not an issue as the particle appears to reach equilibrium before the nanowire growth begins (Figure 6.11). The higher concentration of Ga reaching the seed particle leads to a decrease in the time necessary for the particle to reach equilibrium. It should be reiterated that this effect is also not observed at a V/III ratio of 1.5. It appears as though the nanowire growth goes through a

transition at some point between a V/III ratio of 1.5 and 2. In order to confirm these observations, the nanowire diameter was calculated for samples grown at a V/III ratio of 0.5 and 1.5. The average diameter of the tip was found to be 102 ± 17 nm for a V/III ratio of 0.5 and 104 ± 20 nm for a V/III ratio of 1.5, which are similar to results obtained at V/III ratios of 1 and 2.

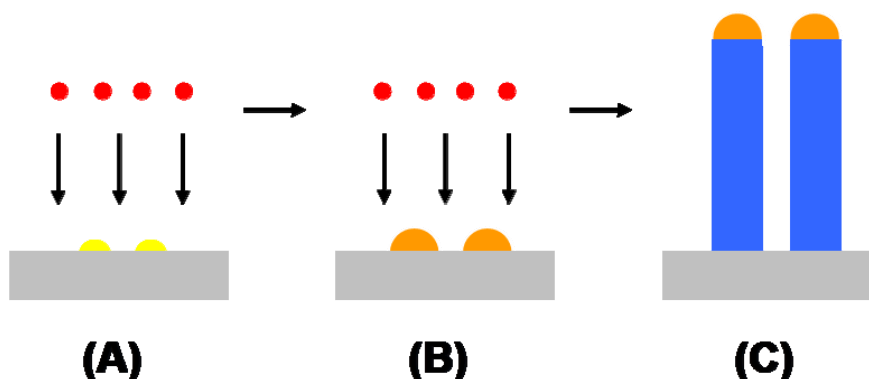


Figure 6.11: Schematic of growth in Ga-rich condition. (a) Gas precursors flown to reaction site and react with nanoparticles. (b) Particle continues to grow until they reach their supersaturation point. (c) Precipitation of GaSb crystal from catalyst leading to nanowire growth.

In summary, the Ga-species appears to be responsible for the nucleation and growth rate of the GaSb nanowires. Growing in Ga-rich conditions leads to an increase in the nucleation density due to a sufficient supply of Ga to form the alloyed particle. A slight decrease in the growth rate was observed and is believed to be due to deposition of Ga droplets on the facets of the nanowire which promotes radial thin film growth. The nanowire growth rate was found to be a maximum at a V/III ratio of 1, and a significant decrease in the growth rate was observed at a V/III ratio of 1.5 and 2. The decrease is believed to be due to the fact that the TMG precursor appears to be the rate-limiting step. This effect was exemplified when the total metalorganic flowrate was increased. At the

same time, a V/III ratio of 2 led to the presence of a “reverse tapering” for a collection of the nanowires. Since there is a deficiency of Ga, the seed particle has not reached equilibrium prior to precipitation of the GaSb nanowire. As a result, the nanowire appears to increase in diameter until the seed particle reaches its final composition. At this point, the nanowire appears to become uniform in diameter. This concept was reinforced as diameter measurements of the tip and base of the nanowires exhibited a base diameter similar to the original Au nanoparticle, whereas the tip diameter was similar to measurements taken from samples grown at a V/III ratio of 1.

6.2.4 Effect of Position

In Chapter 5, the position of the substrate in the reactor tube was found to be an important factor in successfully growing GaN nanowires. It proved to be impossible to achieve nanowire growth in the constant temperature region when TMG and NH_3 were utilized as the precursors. Eventually, the quartz boat was shifted 2 inches closer to the TMG inlet resulting in GaN nanowire growth. CFD modeling was employed to investigate the nature of this issue, and it was determined that the lack of success in the constant temperature region was due to the depletion of gas phase precursors prior to the growth front. This issue was due, in part, to the reactivity of TMG and NH_3 at room temperature.

TMG and TMSb do not react with one another at room temperatures, however the decomposition kinetics of these precursors prove to be a problem. As was discussed in Chapter 3, the pyrolysis kinetics can be quite complex depending on the growth

conditions and reactor configurations. Physical proof of this concept was displayed in the shift of the tube wall deposits as the temperature and pressure were varied. Increasing the temperature and pressure led to a shift of the wall deposits further upstream in the reactor. In particular, raising the pressure led to an increase in the frequency of collisions between H radicals and the gas phase precursors due to a decrease in the gas velocity.

As a result, it was necessary to examine the effect of the placement of the substrates for these variables. Experiments were completed to look at the effect that placement posed at various temperatures and pressures. In each case, sapphire substrates coated with 50 nm Au nanoparticles were placed at multiple positions on the quartz boat. In terms of temperature, minimal variation was found with respect to position, especially over a range of 475-500°C. In the case of pressure, however, a significant difference in the morphology of the GaSb nanowire growth was observed at elevated pressures based on the location of the sapphire substrate. An example of the results obtained from this study is shown in Figure 6.12. These samples were grown at a temperature of 500°C, a V/III ratio of 1, and a pressure of 300 Torr. The sample in Figure 6.12 (a) was placed at the front of the quartz boat which is approximately 1.5 inches upstream of the center of the heated zone. The sample in Figure 6.12 (b) was placed approximately 1 inch further back or about 0.5 inches upstream of the center of the hot zone. As is evident from the SEM images, the morphology in each case is quite different. The nanowires in Figure 6.12 (a) were found to be approximately 42 μm long with a standard deviation of 5.7 μm . It should be also noted that these nanowires are quite tapered, which would be expected at an elevated pressure due to the presence of a competing thin film (radial) deposition. On the other hand, when the sample was placed 1 inch further back, a thin

film/nanowire matrix results which resembles the morphology obtained at 400 Torr in the pressure series (Figure 6.7 (e)).

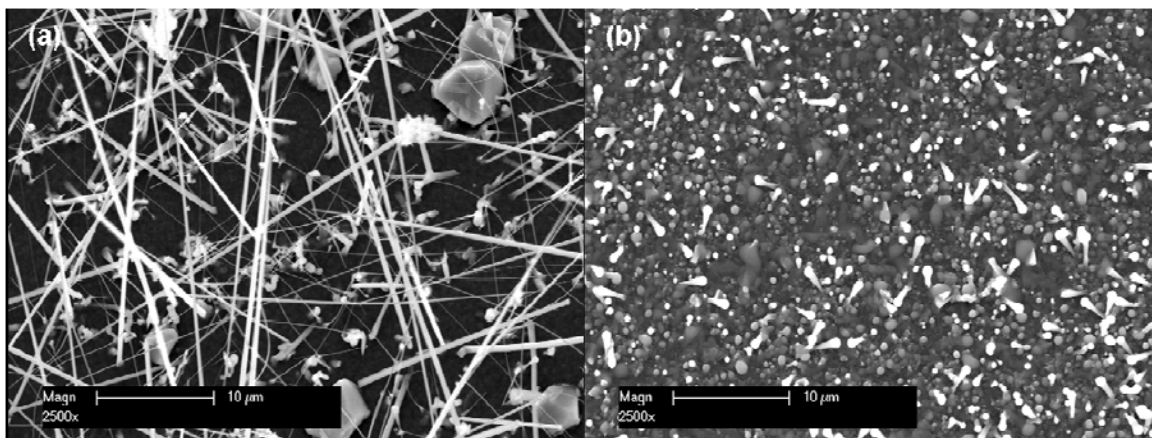


Figure 6.12: SEM images of GaSb nanowire growth with 5% 50 nm Au nanoparticles. The boat is located in the center of the hot zone. (a) is located ~ 1.5 inches upstream from the center of the hot zone. (b) is located ~ 0.5 inches upstream of the center of the hot zone (~ 1 inch further back than (a)). Growth conditions: 500°C , 300 Torr, 1 sccm TMG, 1 sccm TMSb, 100 sccm H_2 , and 5 minute growth time.

To further illustrate the importance of position at higher pressures, the sample in Figure 6.12 (a) can be compared to the GaSb nanowires obtained at 300 Torr in the pressure series experiments (Figure 6.7 (d)). The sample that was grown at 300 Torr in the previous study was placed approximately $\frac{1}{4}$ of an inch further back. In the previous sample, the nanowire diameter dramatically increased to an average diameter of 229 nm, and the length was determined to be $\sim 3.2 \mu\text{m}$. The significant difference in length exemplifies the importance of position at higher pressures. Increasing the pressure appears to have a significant effect on the frequency of collisions between the carrier gas and the precursors, causing a shift in the gas phase reactions. The shift led to a maximum in the nanowire growth rate at the location of the first sample and a dramatic drop-off in

the growth rate at a sample placed $\frac{1}{4}$ of an inch further back. As was previously noted, TEM characterization was performed on the sample from the previous study to determine the cause of the dramatic increase in diameter and decrease in length, and the results will be reported later in this chapter.

6.3 Growth of GaSb Nanowires with Au Thin Films

A separate section on the synthesis of GaSb nanowires using Au thin films has been included due to some variation in the results compared to the use of 50 nm Au nanoparticles. When performing the experiments examining the effect of temperature, pressure, and V/III ratio involving the use of Au nanoparticles, sapphire substrates coated with 2-2.5 nm Au thin films were also included as a comparison. This was also done, in part, due to prior experiments involving the synthesis of Si nanowires using Au nanoparticles. In these studies, Pramod Nimmatoori, a graduate student in Dr. Joan Redwing's group, observed the nanowire growth to be sensitive to the growth environment. In some cases, nanowire growth would occur on Au thin films but would not be observed when Au nanoparticles were utilized. Therefore, it was pertinent to include Au thin film samples in order to clarify if certain growth conditions did not lead to nanowire growth or if the sensitivity of the Au nanoparticles was actually responsible for unsuccessful nanowire growth.

In performing these experiments, the Au thin film results were consistent with the nanoparticle results when varying the furnace temperature and V/III ratio. However, there was a variation in the results when investigating the effect of pressure. Nanowire

growth was achieved over a pressure range of 100-300 Torr, which is consistent with the results obtained for growth with Au nanoparticles. At 100 Torr, a mixture of straight and kinked nanowires was observed (Figure 6.13 (a)). Based on SEM, the nanowires were determined to vary in diameter from 80 nm to 160 nm with an average diameter of 125 nm. The length was found to span 6 to 9 μm . At a pressure of 400 Torr, a thin film/nanowire matrix was present which resembles the previous results (Figure 6.7 (e)).

The disparity in the results was found to exist over a pressure range of 200-300 Torr. In this pressure range, the nanowire growth transitioned to a vertically oriented nature as can be seen in Figure 6.13 (b) and (c). Looking closely at the surface of the sample grown at a pressure of 200 Torr, the nanowires appear to be growing with a preferred orientation from GaSb platelets that formed during growth (Figure 6.13 (b)). In Figure 6.13 (c), the vertically oriented nature of the growth is evident in the inset. It also appears as though an underlying thin film has resulted as a byproduct of the growth. In the process of loading the samples for this experiment, they were accidentally scratched by the tweezers, removing portions of the Au thin film as a result. This accounts for areas on the samples where nanowire growth did not occur. The nanowires that were grown at a pressure of 200 Torr were found to possess an average diameter of 153 nm (range of 70-270 nm) and a length of 7-15 μm . A noticeable difference in tapering and length was observed at 300 Torr, which is comparable to the previous results. The nanowire tip was determined to vary from 90-230 nm, while the base was measured between 230-390 nm. The nanowires, in this case, were much shorter in length with a range of 2-3 μm . In general, the increase in diameter and distribution of the diameter for these experiments is due to the use of Au thin films. The thin films anneal into particles

as the furnace temperature increases to its set-point. The particle size, however, is dependent on how the film breaks up, leading to a large variation in nanoparticle diameter.

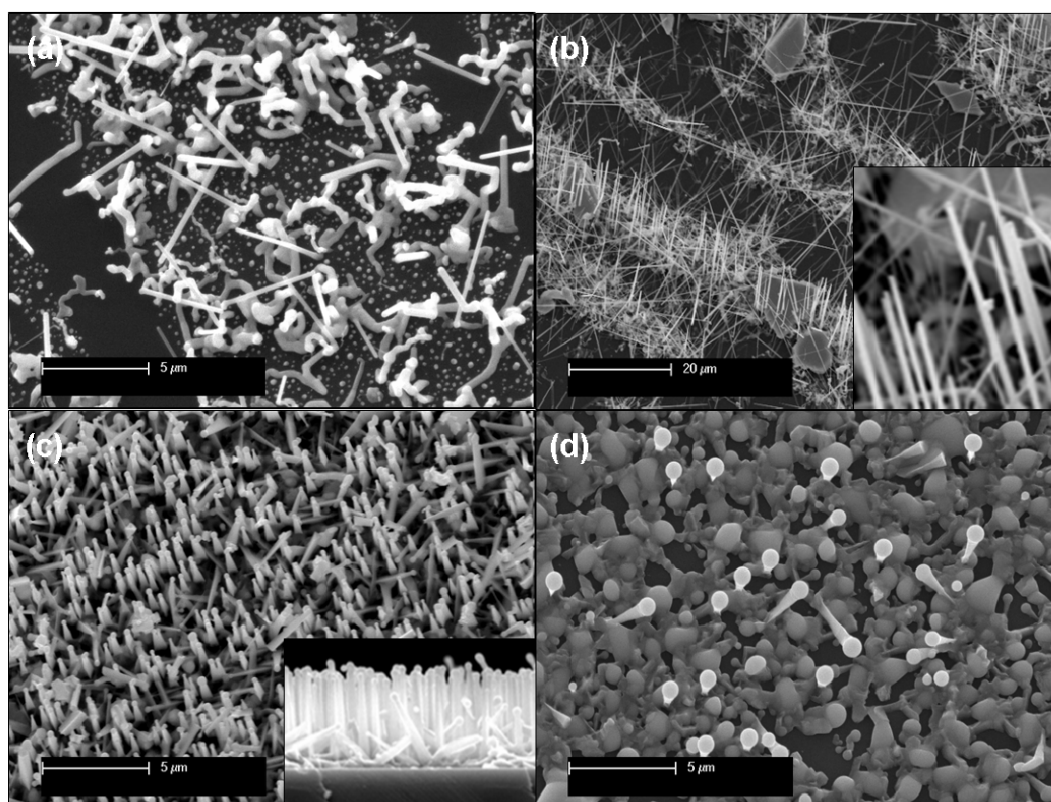


Figure 6.13: SEM images of GaSb nanowire growth using 2.5 nm Au thin films at pressures of (a) 100 Torr, (b) 200 Torr, (c) 300 Torr, and (d) 400 Torr. Inset in (b) is a higher magnification image of the nanowire growth. Inset in (c) shows the epitaxial nature of the GaSb nanowire growth. Growth conditions: 500°C, 1 sccm TMG, 1 sccm TMSb, 100 sccm H₂, and 5 minute growth.

As was previously noted, Au thin film samples were included in the experiments due to a previously observed sensitivity of Au nanoparticles to the growth environment. Interestingly enough, growth with Au nanoparticles was not an issue, however reproducibility of the results concerning Au thin films was a problem. In particular, it became difficult to synthesize nanowires at a pressure of 100 Torr. Eventually, the issue

extended to pressures as high as 200 Torr. The reason for this change isn't known, however a few hypotheses were proposed and examined.

The first concern surrounded the source of the Au-coated sapphire substrates. For the preliminary set of experiments, the Au thin film was deposited by Chad Eichfeld, a graduate student in Dr. Suzanne Mohny's group, using a sputtering tool that belonged to their group. Unfortunately, the sputtering tool became non-functional, therefore the Au-coated sapphire substrates were obtained from another source. The sputtering tool, in this case, was utilized by multiple users, and the possibility of cross-contamination had to be taken into account. From thickness measurements, it was also determined that the tool needed to be recalibrated, since attempting to deposit a 2 nm thin film resulted in a 4 nm thin film.

Consequently, a series of experiments were carried out using thin films from both sources. The goal was to determine if nanowire growth could be achieved with either set of Au-coated sapphire samples. Figure 6.14 is an example of SEM images from an experiment carried out at a pressure of 200 Torr. These samples were grown at a temperature of 500°C and with a V/III ratio of 1. Au-coated sapphire pieces from both sources were placed at various positions along the length of the quartz boat in order to look at the effect of position. The results are shown for one set of thin film samples, since similar results were obtained in both cases. In this experiment, nanowire growth was not observed on the sample placed closest to the metalorganic inlet (Figure 6.14 (a)). It appears as though Au and the precursors formed an alloy, however it did not lead to nanowire growth. The alloying effect can be seen in the inset in Figure 6.14 (a) as there is some phase contrast within the particle indicating the presence of two different phases.

This effect has been seen previously in samples grown at a pressure of 100 Torr. The lack of growth contradicts previous results where nanowire growth was observed on the sample placed closest to the metalorganic inlet (Figure 6.13 (b)). Nanowire growth, however, was achieved on samples placed further away from the metalorganic inlet. The 2nd sample was placed 1.5 inches away from the first sample, and the 3rd sample was placed 2.75 inches away from the first sample. The wires in the 2nd sample are heavily imbedded in a thin film matrix, whereas the wires in the 3rd sample are short, tapered, and resemble nanowires typically grown at 300 Torr.

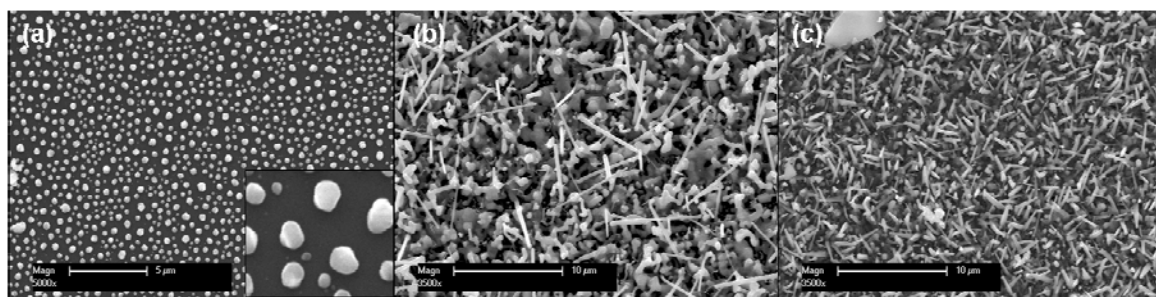


Figure 6.14: SEM images of GaSb growth on 2 nm Au thin films at multiple positions on the quartz boat. (a) was placed at the front of the boat or 1.25 inches upstream of the center of the hot zone. (b) was placed 1.5 inches away from (a). (c) was placed 2.75 inches away from (a). Growth conditions: 500°C, 200 Torr, 1 sccm TMG, 1 sccm TMSb, 100 sccm H₂, and 5 minute growth time.

It should also be noted that the heaviest wall deposits were located over the 2nd half of the quartz in this experiment. In previous experiments at 200 Torr, the wall deposits were observed to be heaviest over the entire length of the quartz boat. It appears as though the reaction zone for the gas phase precursors has shifted. This may be due to modifications that were made to the system, or the fact that the nanowire CVD system is also utilized for the growth of Si and Ge nanowires. The modifications could have

resulted in a change in the reactor flow patterns, and the Si and Ge precursors could have caused some cross-contamination that is altering the gas phase reactions.

Another hypothesis addressed the diameter distribution of the particles after they were annealed. Due to the annealing process, there is very little control over the nanoparticle diameter. On the other hand, when commercially-produced Au colloids are employed, the diameter distribution is quite small. When the Au thin films are annealed, the particles are typically much larger than 50 nm which may pose a problem. In previously published reports, a critical nanowire diameter has been observed for growth of III-V nanowires on lattice-mismatched substrates.²⁸ For certain systems, nanowire growth terminated above a certain diameter. When InAs nanowires were grown on (111) Si, the largest diameter nanowire was found to be 26 nm. The critical diameter for InP nanowires grown on (111) Si and (111)B GaAs was found to be 36 nm and 96 nm, respectively.

Based on this study, it may be possible that a critical diameter exists for the growth of GaSb nanowires on sapphire. In order to examine this potential effect, samples were prepared with gold colloids varying in diameter between 10 nm and 100 nm. The concentration of the Au solutions was adjusted based on the nanoparticle density of the original colloid in order to achieve the same surface coverage at each diameter. The experiment was completed at a temperature set-point of 500°C while maintaining a pressure of 100 Torr and a V/III ratio of 1. The results from this experiment are displayed in Figure 6.15.

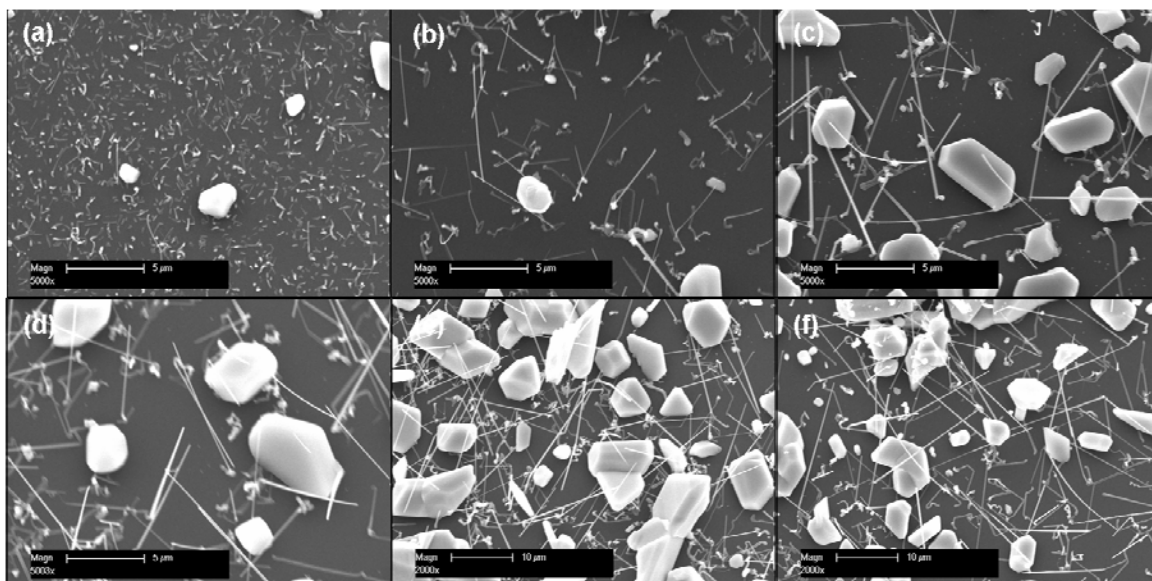


Figure 6.15: SEM images of GaSb nanowire growth using (a) 10 nm, (b) 20 nm, (c) 40 nm, (d) 50 nm, (e) 80 nm, and (f) 100 nm Au nanoparticles. Growth conditions: 500°C, 100 Torr, 1 sccm TMG, 1 sccm TMSb, 100 sccm H₂, and 5 minute growth time.

SEM was utilized to determine nanowire length and diameter ranges at each of the conditions, and these values are provided in Table 6.3. For each case, the wire diameter was found to be at least 20-40 nm larger than the original Au nanoparticle diameter. The significant increase in nanowire diameter was expected due to the volume change that occurs as the particle becomes supersaturated with Ga and Sb prior to precipitation of crystalline GaSb. The nanowire growth rate was also determined to increase with Au nanoparticle diameter, which has been observed in previous studies involving the growth of III-V nanowires.^{29,30} Based on these results, there does not appear to be a critical diameter for the growth of GaSb nanowires over the Au nanoparticle range that was studied. Although there does not appear to be a critical diameter for GaSb nanowire growth on c-plane sapphire, it still would be worthwhile to

complete an experiment involving larger Au nanoparticle diameters in order to confirm this observation.

Table 6.3: GaSb nanowire diameter and length ranges for various Au nanoparticle diameters.

Au Nanoparticles (nm)	Nanowire Diameter (nm)	Length (μm)
10	30-50	1-3
20	50-70	3-8
40	70-90	10-15
50	80-100	10-15
80	120-140	15-20
100	140-170	15-20

The final hypothesis which will be considered involves the density of the Au seed particles created by the annealing of the thin films. As was previously observed in the Au colloid studies, GaSb nanowires were found to grow from the sapphire surface, the base of other nanowires, and GaSb crystals that form on the surface. When utilizing the Au colloids, the spacing between Au nanoparticles is roughly 500 nm to 1 μm . For the case of the thin films, the particles are typically only 150-300 nm apart. The presence of a higher nanoparticle density may impede the diffusion of the gas phase precursors on the surface and also inhibit the growth of GaSb nanowires from other nanowire bases and GaSb crystals. It may be possible to test this hypothesis by creating a patterned sample containing quadrants of Au nanoparticles with various spacings.

6.4 Transmission Electron Microscopy

6.4.1 Structural Properties and Catalyst Composition Analysis

As was discussed in the Chapter 5, there still remains some uncertainty as to the mechanism responsible for the growth of III-V nanowires. Until recently, the vapor-liquid-solid (VLS) mechanism was believed to be responsible for the synthesis of III-V nanowires. However a few years ago, a new nanowire growth mode known as vapor-solid-solid (VSS) growth was suggested as an alternative to the well-known VLS growth mechanism to explain experimental observations.³¹ Although the Au seed particle was found to contain the constituents necessary for VLS growth, an analysis of the composition of the catalyst had not been performed. Dick *et al.*^{27,32} investigated this point for various III-V nanowires by carrying out EDS point-scan measurements. The results were then compared to the binary-phase diagram formed between the group III element and the metal catalyst to determine if the composition places the alloy in the liquid or solid region of the phase diagram for the nanowire growth temperature. For the GaP and GaAs systems, the evidence suggested only a solid Au-Ga solution would form through most of the growth temperature range.²⁷ The maximum concentration of Ga within the seed particle was found to be 10 at.% which placed the alloy in the solid region of the Au-Ga phase diagram. For the growth of InAs nanowires, it was possible to form a liquid alloy between Au and In, however nanowire growth terminated when the temperature and In content caused the alloy to form a liquid.³² In this case, nanowire growth only proceeded when the alloy was in a solid state.

Recently, the same author completed a TEM study of MOCVD-grown GaSb/GaAs nanowire heterostructures.⁷ When the GaSb nanowires were grown at a high V/III ratio of 2, the seed particle consisted of 46 at.% Ga and 52 at.% Au. When the GaSb nanowires were grown at a lower V/III ratio of 0.8, the seed particle contained 64 at.% Ga and 35 at.% Au. In both cases, only trace amounts (2 at.%) of Sb were found. Based on the ternary phase diagram for Au-Ga-Sb, the seed particle was determined to be AuGa or AuGa₂. The author, however, did not state if the nanowire growth proceeded via the VLS or VSS mechanism.

Based on these studies, it was pertinent not only to utilize TEM to look at the structural properties of the nanowires but also examine the composition of the seed particle to determine if nanowire growth proceeded by the VLS or VSS mechanism. Initial TEM analysis was performed on a sample grown at 500°C while maintaining a reactor pressure of 100 Torr and a V/III ratio of 1. These conditions were defined as the standard conditions for GaSb nanowire growth, and samples grown with different conditions will be compared to this sample. A low magnification image of a GaSb nanowire grown at these conditions is displayed in Figure 6.16 (a), whereas a HRTEM image of an additional nanowire is shown in Figure 6.16 (b). The majority of the nanowires which were inspected were found to possess a slight tapering. This is not unexpected as MOCVD growth of nanowires typically leads to a competition between thin film and nanowire growth. From selected area diffraction (inset in Figure 6.16 (a)), the wires were found to consist of the single crystalline zinc blende structure, and a portion of the wires were observed to have twin boundaries along the length of the nanowire. A sharp interface between the GaSb nanowire and the Au catalyst is evident in

Figure 6.16 (b), and the catalyst is approximately the same size as the nanowire. There also appears to be a thin oxide layer (Sb_2O_3 , Ga_2O_3) on the order of 3-4 nm surrounding the nanowires.

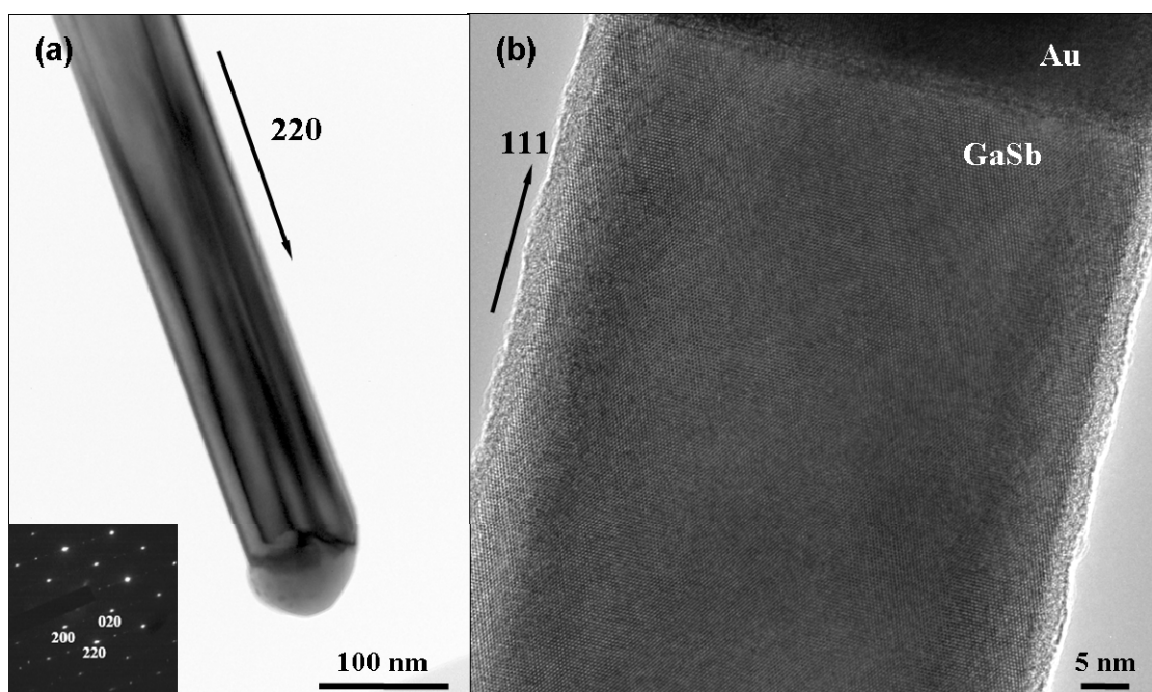


Figure 6.16: (a) Low magnification and (b) high resolution TEM images of GaSb nanowires. Inset in (a) is an electron diffraction pattern. The sharp interface between the nanowire and seed particle can be seen in (b). Growth conditions: 500C, 100 Torr, 1 sccm TMG, and 1 sccm TMSb.

An extensive analysis of this sample was performed to determine the average diameter and growth direction of the nanowires. The study was carried out on 58 nanowires for the diameter analysis and 40 nanowires for the growth direction analysis. The nanowire diameter was found to be approximately 91 ± 31 nm. The predominant growth direction ($\sim 68\%$ of the nanowires) was found to be [111]. [220] was also found to be a common growth direction ($\sim 23\%$ of wires). Other growth directions observed were [331], [221], [112], and [104].

X-ray energy-dispersive spectroscopy (XEDS) was utilized to examine the constituents present in the seed particle and the homogeneity of the nanowire. An EDS point-scan was taken of the body of the nanowire to determine the elements that were present (Figure 6.17 (b)). The Ga and Sb peaks correspond to the GaSb nanowire, whereas the Cu peak is a byproduct of the carbon lacy grid. Composition line profiles were taken along the axis (A-A') and cross section (B-B') of the nanowire (Figure 6.17 (a)). Looking at the line scan through the cross section, the intensity of the Ga and Sb peaks increase as the scan approaches the midpoint of the nanowire and then decrease once again (Figure 6.17 (c)). This is due to a change in thickness of the nanowire due to

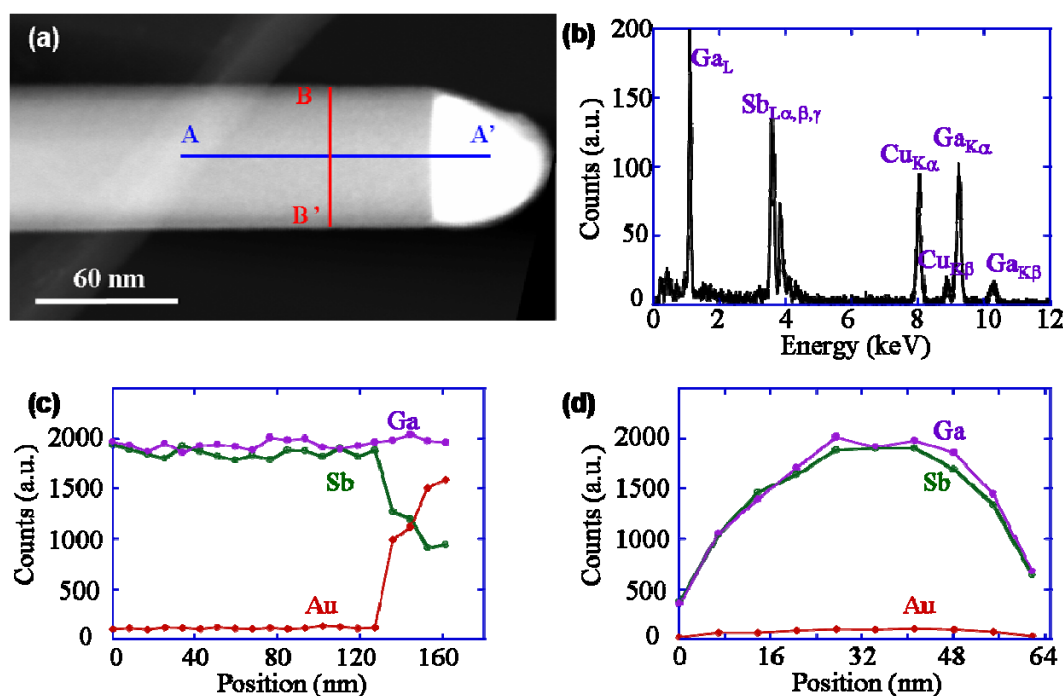


Figure 6.17: (a) High-angle annular dark-field (HAADF) STEM image of a GaSb nanowire. (b) Typical EDS spectrum of the body of the GaSb nanowire. The Cu peak is due to the lacy carbon grid. (c) and (d) are XEDS line profiles along the axis and cross section of the nanowire.

its circular cross section. The uniformity of the scan indicates that the nanowire is indeed homogenous. An abrupt change in the Au intensity was observed at the interface between the seed particle and the nanowire in the axial composition line scan (Figure 6.17 (d)). As the line scan continues into the catalyst, the Ga peak intensity does not change, whereas a decrease in the Sb intensity is observed. The presence of Au, Ga, and Sb in the catalyst suggests that the VLS growth mechanism is responsible.

In order to further investigate the growth mode, the composition of the particle seed was estimated. As was the case for the catalyst analysis for the GaN nanowires, the ES Vision Standardless Quantification method was used to determine the composition ratio of each element present in the particle. The composition ratio of the catalyst is determined by multiplying the intensity ratio by a k-factor which is theoretically determined for each constituent. The k-factor for the alloy is determined by the following equation:

$$k(AB) = \frac{k(B)}{k(A)} \quad \text{Eq. 6-1}$$

where k(A) and k(B) are the k-factors for elements A and B. The theoretical k-factors for Au, Ga, and Sb are 5.950, 2.832, and 3.209, respectively. Once the k-factor for the alloy has been calculated, the composition ratio of the alloy is determined by the following equation:

$$\frac{C(A)}{C(B)} = k(AB) \times \frac{I(A)}{I(B)} \quad \text{Eq. 6-2}$$

where C(A) and C(B) are the compositions of element A and B, and I(A) and I(B) are the intensity values for element A and B which are obtained from the XEDS line scans.

The concentration of each element present was calculated by the ES Vision software, and the values for the four points located in the catalyst are provided in Table 6.4. The first two points are relatively close to the interface between the catalyst and the nanowire, therefore points 3 and 4 are more representative of the actual concentration within the catalyst. The Au-Sb phase diagram could not be used to determine the state of the particle as Sb would be expected to precipitate out of the Au catalyst when cooling the nanowires to room temperature, since the solid solubility of Sb in Au is considered to be approximately 1%.¹¹ As a result, the Au-Ga phase diagram was utilized to determine if the alloyed particle would be located in the solid or liquid region of the phase diagram at the nanowire growth temperature. Based on the Au-Ga phase diagram (Figure 6.1 (a)), a liquid alloy would be expected to form between Au and Ga, confirming the presence of the VLS growth mechanism. It should also be noted that the Sb content in the MOCVD-grown GaSb nanowires is significantly higher than the 1% solid solubility of Sb in Au. This observation will be addressed later in this section.

Table 6.4: Composition of GaSb nanowire seed particle.

Point Scan #	% Ga	% Sb	% Au
1	50.0	23.6	26.4
2	45.3	25.6	29.1
3	43.2	16.5	40.3
4	44.6	13.8	41.6

As was previously noted, the average diameter of the GaSb nanowires was 91 nm. This amounts to a significant increase in the nanowire diameter with respect to the original 50 nm Au nanoparticles. Through the ES Vision software, it was determined that a large concentration of the particle consists of Ga and Sb. Based on these findings, the

nanowire diameter would be expected to increase in order to incorporate the high concentration of Ga and Sb atoms diffusing into the gold nanoparticles. In a previous study of MOCVD-grown GaSb nanowires, the seed particles were determined to transform from an Au-Ga solid solution into either AuGa or AuGa₂.⁷ The diameter of seed particles consisting of these phases was estimated and was found to fit well with the diameters observed for the MOCVD-grown GaSb nanowires.

SAD was utilized in an attempt to identify the phase(s) present in the seed particle for nanowires grown at 500°C, however the quality of the images was poor. Based on the Au-Ga phase diagram (Figure 6.1 (a)), a two phase mixture of γ' (Au₂Ga) and AuGa would be expected to form based on the concentration of Ga found in the catalyst. For the Sb concentration in the catalyst, the value is located between the Au-Sb solid solution and AuSb₂ line compound based on the Au-Sb phase diagram (Figure 6.1 (b)). If multiple phases were present in the catalyst, it would have made obtaining good quality SAD patterns difficult.

Interestingly enough, nanowires grown at a temperature of 475°C were actually found to be bicrystalline with a seed particle consisting of two grains. An example of such a nanowire is shown in Figure 6.18. The two grains in the particle have been labeled A and B, and the phase contrast in the lower half of the wire indicates the boundary of the bicrystalline nanowire and coincides well with the interface between the two grains in the catalyst. The growth direction of the top half of the nanowire was determined to be [220], a commonly observed growth direction for the nanowires grown at a temperature of 500°C.

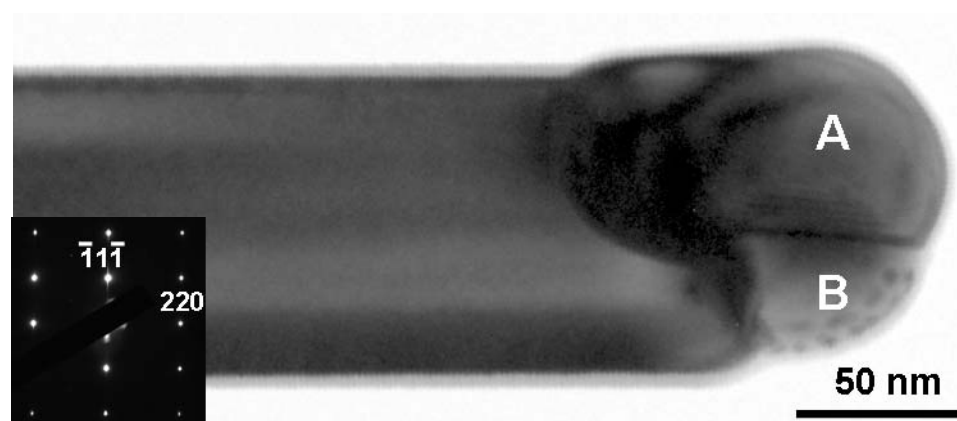


Figure 6.18: High magnification image of a bicrystalline GaSb nanowire with a catalyst particle containing two grains. Inset is a selected area diffraction pattern displaying a growth direction of $[220]$ for the top part of the nanowire. Growth conditions: 475°C , 100 Torr, and V/III ratio of 1. The image was collected along the $\bar{1}12$ zone axis.

XEDS was utilized to examine the composition of the catalyst and determine the constituents responsible for the multiphase particle. An annular dark-field STEM image of the nanowire is shown in Figure 6.19 (a). Composition line scans were carried out along the x-axis and y-axis of the particle. The line scan proceeding along the x-axis and through grain A (A-A') exhibited a sharp increase in the Au peak, while the Ga peak climbed slightly (Figure 6.19 (b)). However, a significant decrease in the Sb intensity was observed. The line scan proceeding along the x-axis and through grain B (B-B') displayed the opposite effect. As the interface was approached, the Sb intensity actually increased and a significant decrease in the Ga intensity was observed (Figure 6.19 (c)). Composition line scans along the y-axis and through grains A and B confirmed the effects observed in the axial line scans (C-C' and D-D'). In each case, as the beam approached the interface between the two grains, the intensity of the Sb peak dropped, whereas the intensity of the Ga peak rose.

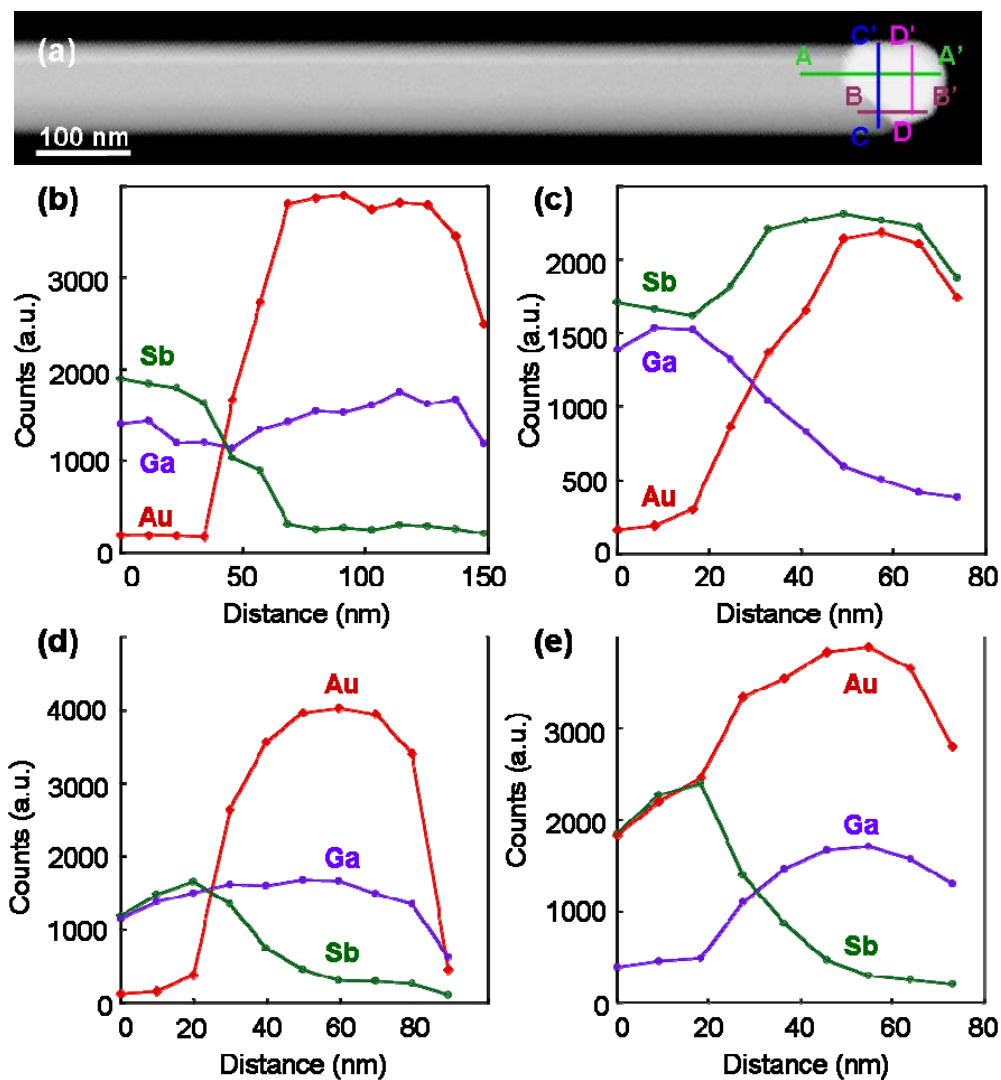


Figure 6.19: (a) High-angle annular dark-field (HAADF) STEM image of a GaSb nanowire. Compositional line profiles of (b) A-A', (c) B-B', (d) C-C', and (e) D-D'. The image was collected along the $1\bar{1}0$ zone axis.

Figure 6.20 (a) is an example of another nanowire grown at a temperature of 475°C. Once again, it is evident that the nanowire appears to be bicrystalline, but it is difficult to tell if the particle contains multiple grains based on the low magnification image. HRTEM images were obtained of the interface between the catalyst (Figure 6.20 (b)) and nanowire, the top of the catalyst (Figure 6.20 (c)), and the boundary of the

bicrystalline nanowire (Figure 6.20 (d)). The locations where these images were obtained from are identified by the red, blue, and orange boxes in Figure 6.20 (a). Looking at the HRTEM image of the catalyst (Figure 6.20 (c)), it is apparent that the seed particle consists of two grains A and B. Based on the image of the nanowire/catalyst interface (Figure 6.20 (b)), the 2nd grain is not present on the left side of the particle, but it appears

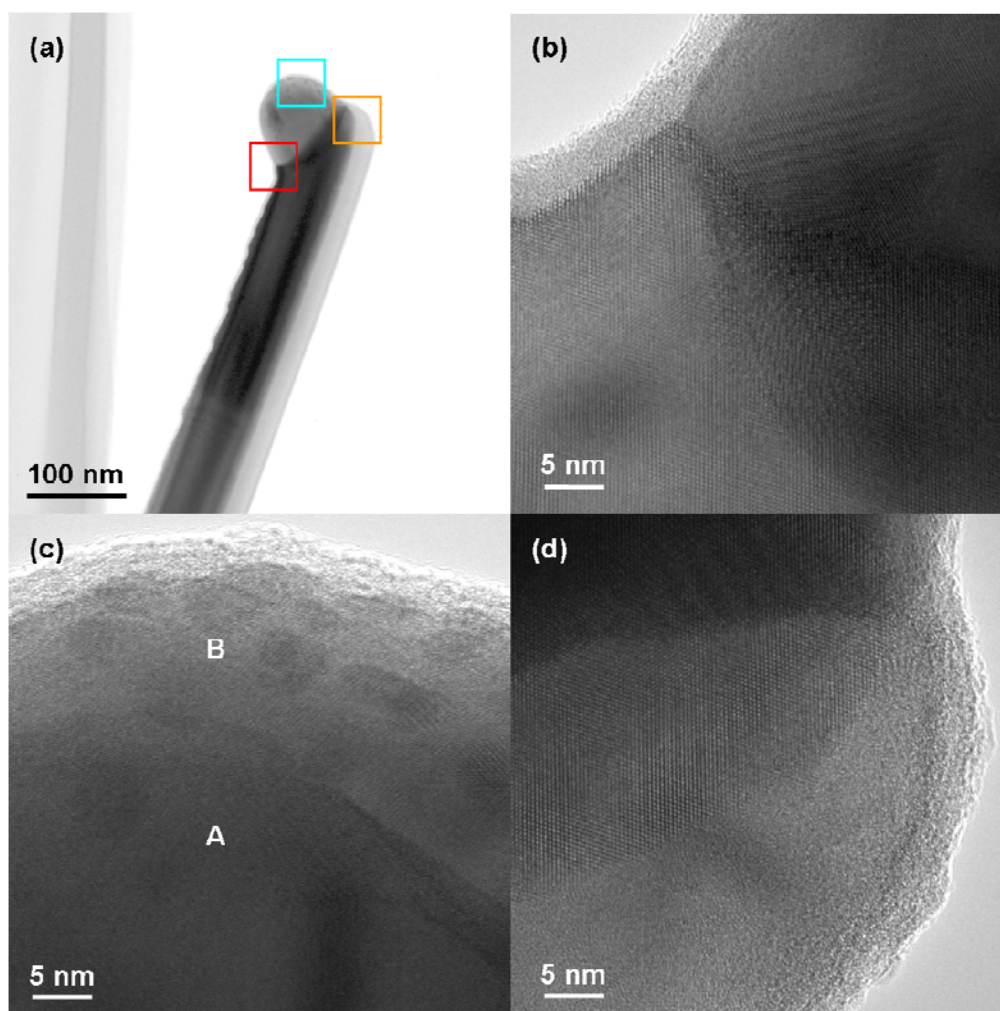


Figure 6.20: (a) Low magnification TEM image of GaSb nanowire grown at 475°C. High resolution images of (b) interface between left side of nanowire and particle, c) top of seed particle exhibiting grains A and B, and (d) right side of nanowire. The nanowire appears to be bicrystalline. The left side of the nanowire is a few degrees away from the [111] growth direction. The image was taken along the $1\bar{1}0$ zone axis.

to begin towards the top of the particle and continue on the right side of the particle leading to the bicrystalline boundary.

Composition line scans were completed to investigate the nature of the catalyst. Figure 6.21 (a) is an annular dark-field STEM image displaying the location of the scans that were completed. The initial scan was carried out along the axis of the nanowire spanning from a portion of the nanowire through the catalyst. As the interface is approached, the Au peak spikes, whereas there is a slight increase in the Ga peak. The Sb intensity drops significantly throughout most of the catalyst, however at a distance of approximately 150 nm, there is a spike in the Sb peak, which appears to correspond with

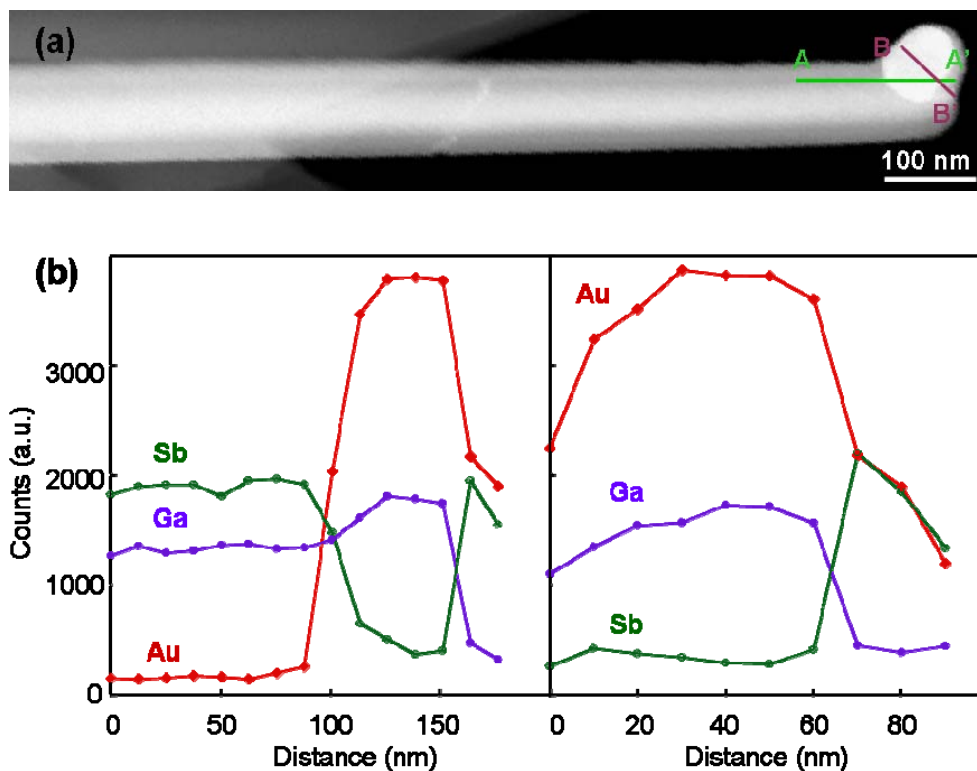


Figure 6.21: (a) High-angle annular dark-field (HAADF) STEM image of a GaSb nanowire. Compositional line profiles of (b) A-A' and B-B'. The image was collected along the $1\bar{1}0$ zone axis.

the location of grain A on the right side of the particle. At the same point, the intensity of the Au and Ga peaks drop dramatically. XEDS was also employed to perform a line scan that traveled through the particle beginning at the left side. Once again as the beam approaches the interface between grain A and B, a spike in the Sb intensity is observed, whereas the Au and Ga peaks decrease noticeably.

The XEDS data which has been provided only measures the intensity of the elements present in the catalyst but does not account for the characteristics of the individual species. Therefore, it is difficult to determine the concentration of each species simply based on the intensities. As was discussed earlier, the ES Vision Standardless Quantification method can be used to determine the content of each element in the seed particle by multiplying the intensity values by the k-factors for each constituent. This method was utilized to calculate values for the composition of both particles and was graphed as a function of distance in Figure 6.22. Based on the results, grain A appears to be Ga-rich, whereas grain B is Sb-rich. Grain A for the first particle (Figure 6.19) was found to contain ~40 at.% Ga, 55-60 at.% Au, and 0-5 at.% Sb, while Grain A for the second particle (Figure 6.21) consisted of 30-35 at.% Ga, 60-65 at.% Au, and 0-4 at.% Sb. Grain B, on the other hand, for both catalysts was found to consist of 55 at.% Sb, 43 at.% Au, and 2 at.% Ga.

With this knowledge, the binary phase diagrams can be used to determine potential compounds responsible for each grain in the seed particle. Looking at the Au-Ga phase diagram (Figure 6.1 (a)), the γ' (Au_2Ga) phase is found to exist between 29-31 at.% Ga, while AuGa is a line compound at 50 at.% Ga. The Ga concentration in grain A in the first particle is located in the Au_2Ga -AuGa two phase region. As a result, both

phases would be expected to be present. It is uncertain if this is the case though, since the author was unable to obtain SAD patterns for this catalyst. The Ga concentration in grain A in the second particle, however, appears to fit well with the Au_2Ga compound. In general, it is difficult to decipher the Au-Ga phase diagram due to the large number of Au-Ga alloys that can form.

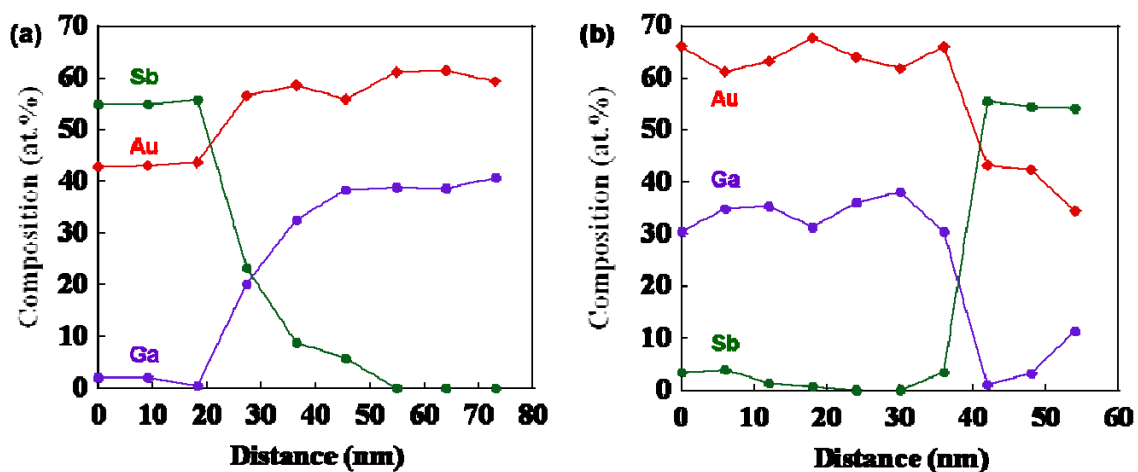


Figure 6.22: Composition (at.%) line profiles of D-D' in Figure 6.19 and B-B' in Figure 6.21.

The Au-Sb phase diagram (Figure 6.1 (b)), on the other hand, is quite simple to interpret since only two compounds exist: the Au-Sb solid solution and the AuSb_2 line compound. AuSb_2 would only be expected to form if the Sb concentration approached ~67%. Otherwise, Sb would be expected to precipitate out of the alloy, since the solid solubility of Sb in Au is roughly 1%. However, this does not happen for the seed particles that have been examined.

The deviation from the norm can actually be explained by a new Au-Sb phase diagram that was developed from TEM studies of nanometer-sized Au-Sb alloy systems

(Figure 6.23).^{33,34} In this study, Au and Sb were evaporated onto an amorphous carbon film and annealed at 510K before cooling to allow the atoms to diffuse in the particles until they reached phase equilibrium. Depending on the sample, the particle was found to consist of the Au-Sb solid solution, the AuSb₂ compound, or in some cases a two-phase particle consisting of both the Au-Sb solid solution and the AuSb₂ compound was found to exist. Defects were not observed, because it was believed that the size of the particles allowed the lattice to become elastically soft and accommodate lattice distortion induced by the diffusion of the Au and Sb atoms.³⁵ In this study, the Au-Sb solid solution was found to extend to roughly 15 at.% Sb, while the AuSb₂ compound was observed over a range of 52-77 at.% Sb.³³ In general, the solid solubility of Sb was found to increase significantly in nm-sized Au particles compared to GaSb bulk materials. The solid solubility was enhanced even more as the diameter of the alloyed particles decreased.

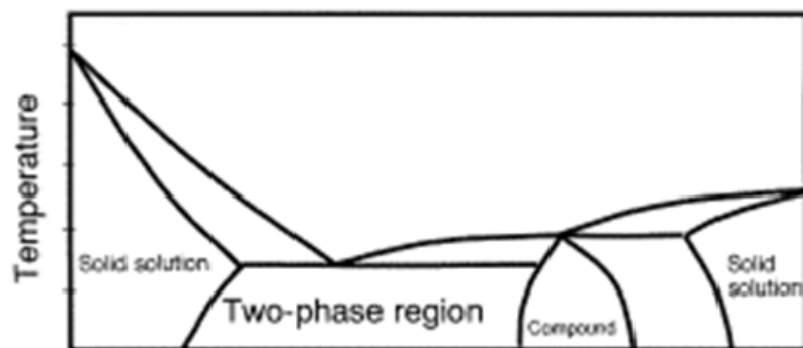


Figure 6.23: Schematic representation of Au-Sb phase diagram for Au-Sb alloys on the nanometer scale.³³

With these new findings, it is possible to determine the compound responsible for grain B. The Sb concentration was found to be 55 at.% in both cases, which fits well into the range observed for AuSb₂ at the nanoscale. This new knowledge can also be used to

explain the observation of 14-17 at.% Sb in the seed particle of the GaSb nanowire grown at a temperature of 500°C (Figure 6.17). This range coincides with the increase in the solubility of Sb in the Au-Sb solid solution at the nanoscale. For samples grown at 475°C, the Sb and Ga atoms appear to diffuse within the catalyst to form a two-grained structure. One grain is observed to be Ga-rich and primarily consists of a two-phase Au₂Ga-AuGa alloy. The author was unable to find a revised Au-Ga phase diagram that accounted for nanoscale systems, but it may be possible that only Au₂Ga or AuGa is present in this structure. In the TEM study of the nanoscale Au-Sb particles, the Au-Sb solid solution and the AuSb₂ phase were found to coexist in a disordered state.³⁴ If the Au-Ga system were to follow a similar trend, it may be possible for the Au₂Ga and AuGa phases to coexist. Error associated with the XEDS measurements or discrepancies in the theoretical k-factors could also lead to a shift in the reported Ga concentration. A small concentration of Sb is also present due to the solubility of Sb in the Au-Sb solid solution. The other grain is observed to be Sb-rich and primarily consists of AuSb₂, however a small concentration of Ga was found due to the solubility of Ga in the Au-Ga solid solution. For the sample grown at a temperature of 500°C, the Ga content coincides with the Au₂Ga-AuGa two phase alloy, while the Sb content exemplifies the increased solubility of Sb in the Au-Sb solid solution.

Further evidence of these findings was illustrated in a GaSb nanowire sample grown at a V/III ratio of 0.5. The temperature set-point for this sample was 500°C, while the reactor pressure was maintained at 100 Torr. Upon close inspection of the nanowire, the nanowire/catalyst interface appears to be sharp, and a planar defect that is parallel to the growth direction is observed within the seed particle (Figure 6.24 (a)). The location

of the defect is designated by the red arrow. However, after exposure to the electron beam, the planar defect is no longer present (Figure 6.24 (b)). The constituents from the catalyst are also found to diffuse into the nanowire. The original interface is indicated by the blue arrows in the TEM images. The diffusion process caused a phase transformation in the nanowire near the interface. This new secondary phase is designated by the red arrow in Figure 6.25 (a). The darker contrast is most likely due to moire fringes that result due to the overlap between the nanowire and the new phase.

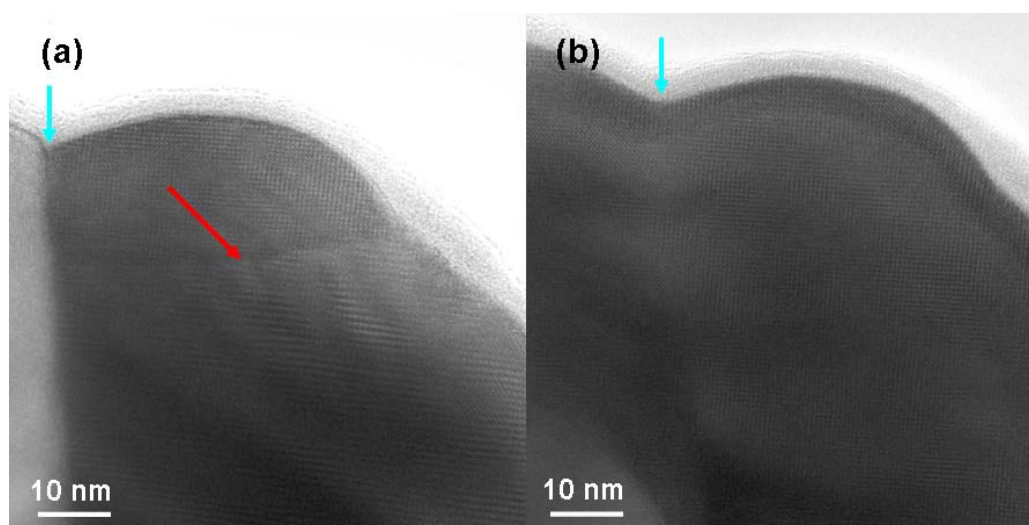


Figure 6.24: HRTEM images of catalyst/nanowire interface (a) before and (b) after exposure to electron beam. Blue arrows indicate the location of the original interface. Red arrow indicates the location of the planar defect present before exposure to the electron beam. Growth conditions: 500C, 100 Torr, 1.33 sccm TMG, and 0.67 sccm TMSb.

XEDS was performed to investigate the nature of this defect. Axial line scans were completed through a section of the nanowire that includes the phase transformation (A-A') and also a section that does not contain the phase transformation (B-B'). In both scans, the intensity of the Sb peak dropped dramatically, however for the line scan

through the phase transformation, a slight increase in the Sb peak was observed (Figure 6.25 (c)). At the same time, a significant decrease in the Ga intensity was observed. Based on these results, it appears as though Sb was responsible for the defect. It is believed that the defect was formed as a result of the Sb atoms diffusing in the catalyst in an attempt to form a two phase particle. The lattice distortion caused by the dissolution of the Sb atoms led to the formation of a planar defect.

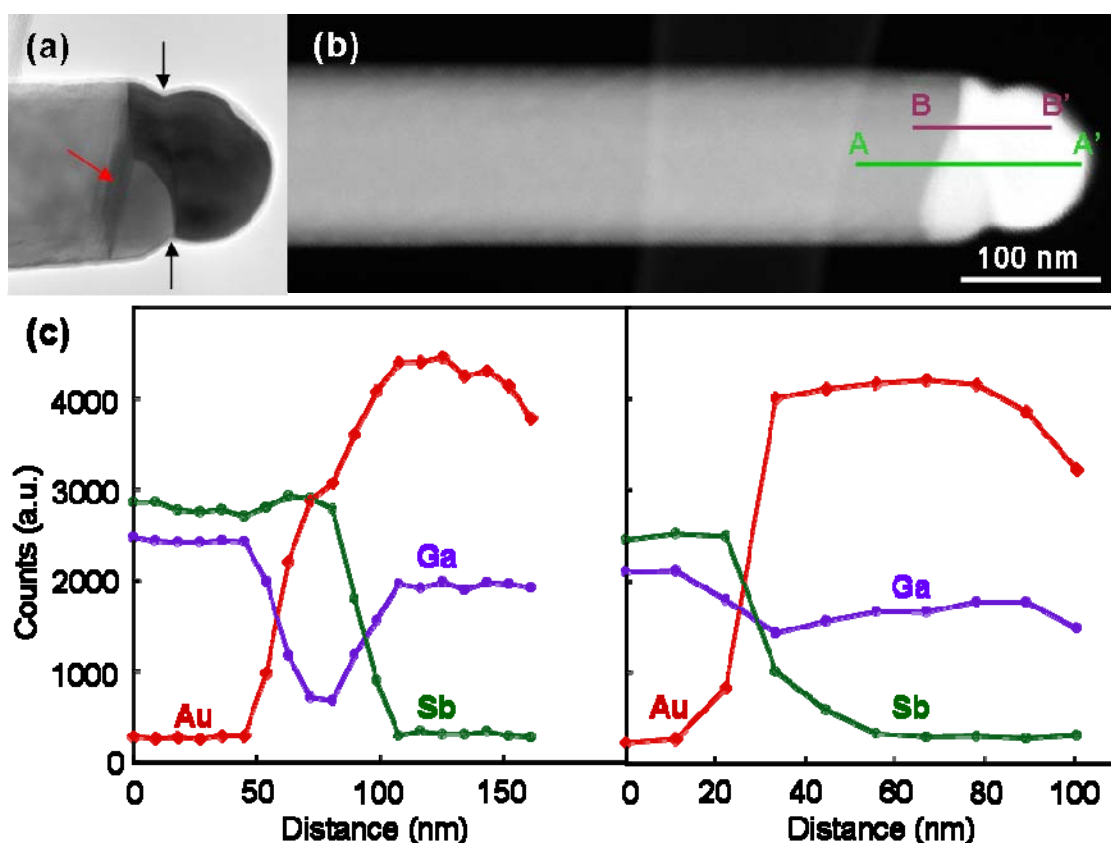


Figure 6.25: (a) TEM image of GaSb nanowire after exposure to an electron beam. The arrows indicate the original interface between the nanowire and the particle. A secondary phase is present in the nanowire (red arrow). (b) High-angle annular dark-field STEM image of the GaSb nanowire. The image was collected along the $1\bar{1}0$ zone axis. (c) Composition line profiles of A-A' and B-B'. Growth direction of the nanowire was determined to be $[111]$.

Upon further TEM analysis, a third type of seed particle has been found to exist. Figure 6.26 (a) is a dark-field STEM image of a GaSb nanowire that was found to have a pronounced neck below the seed particle. This nanowire sample was grown at a temperature of 500°C while maintaining a pressure of 100 Torr and a V/III ratio of 2. A necking region has been observed before for growth of III-V nanowires.³¹ In one study, GaAs nanowires were grown by chemical beam epitaxy (CBE), and TEM was utilized to look at the effects of cooling a nanowire sample after growth with and without an arsine overpressure present. In the case where an arsine overpressure was not used, the nanowires exhibited a high degree of stacking faults. When an arsine overpressure was used, a necking region was present. The necking region was determined to be a byproduct of Ga within the catalyst reacting with the arsine as the sample cooled down. The diameter of the nanowire decreased due to a volume change in the catalyst as it was depleted of Ga.

XEDS was employed to look at the catalyst and determine if a similar situation may be responsible for the pronounced necking of the nanowire below the seed particle. Line scans were carried out along the axis and cross section of the nanowire (Figure 6.26 (b) and (c)). As the line scan approached the interface, a slight decrease was observed in the Ga peak, while a significant decrease in the intensity was found for Sb. The composition (at.%) was determined for each element in the particle using the ES Vision Standardless Quantification method, and the seed particle was found to consist of 26.0±2.2 at.% Ga, 0.8±0.9 at.% Sb, and 73.1±2.0 at.% Au. Not only was there a decrease in the concentration of Sb from previous studies (4-17 at.% and 55 at.% Sb), but there was also a decrease in the typical concentration found for Ga (35-45 at.% Ga). The low

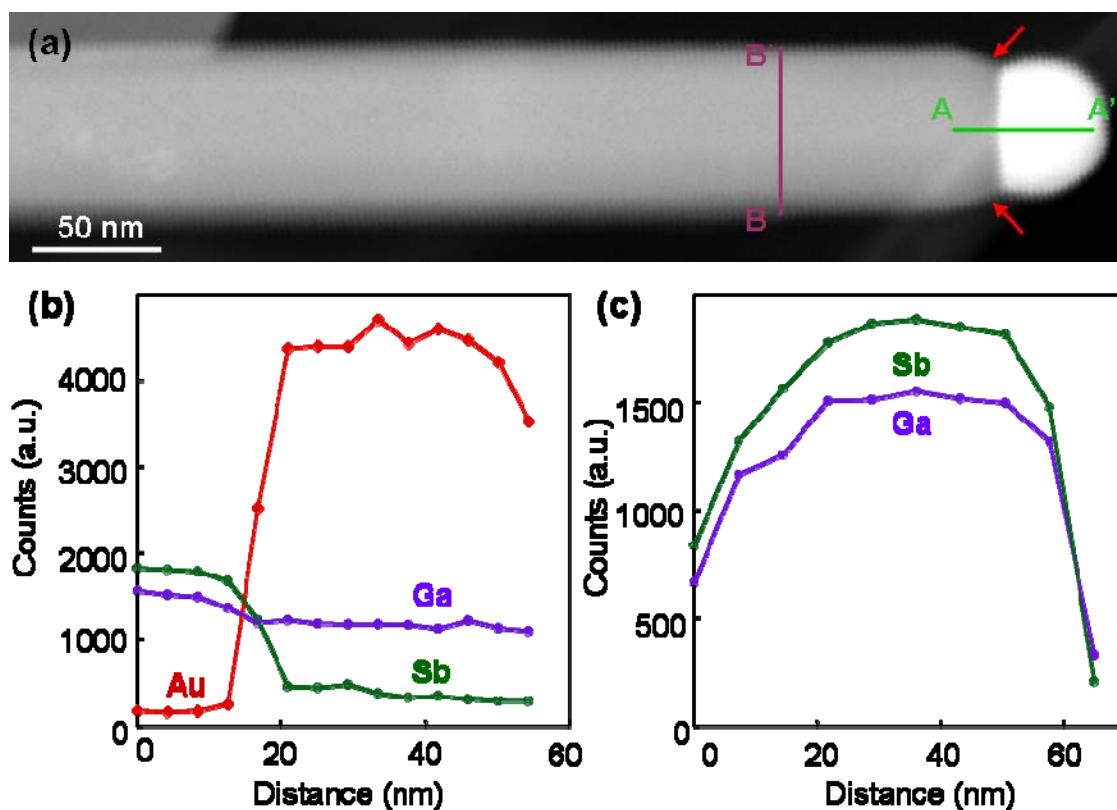


Figure 6.26: (a) High-angle annular dark-field STEM image of a GaSb nanowire. The image was collected along the $1\bar{1}0$ zone axis. Red arrows indicate the necking region of the nanowire. (c) Composition line profiles of A-A' and B-B'. Growth direction of the nanowire was determined to be $[111]$. Growth conditions: 500°C, 100 Torr, and V/III ratio of 2.

concentration of Sb may be a byproduct of background noise from the XEDS line scan, but the value of around 1% also coincides with the anticipated solid solubility of Sb in Au. It is believed that the necking region is actually due to the diffusion of Sb out of the catalyst during cool down to reduce the Sb content to the reported value of solid solubility. In order for this to occur, Ga atoms also diffuse out of the catalyst in order to precipitate out crystalline GaSb, reducing the concentration of Ga in the catalyst. The

necking region results due to a volume change of the seed particle as the precipitation reaction takes place.

6.4.2 Analysis of GaSb Nanowires Grown At Various Pressures

As was previously reported, a significant change in the nanowire morphology was observed in the pressure study. Increasing the pressure up to 300 Torr led to an increase in the nanowire growth rate, and the nanowires appeared to become oriented. At 300 Torr, however, a transition resulted where the nanowires were found to be significantly shorter and much larger in diameter. As a result, TEM analysis of these samples was completed with the hope of determining a cause for this transition. The analysis of the sample grown at a pressure of 100 Torr was discussed in the previous section.

Figure 6.27 is an example of a GaSb nanowire grown at a pressure of 200 Torr. The nanowires, in general, were found to possess a higher degree of tapering than the nanowires grown at a pressure of 100 Torr. The increase in tapering is expected due to an increase in the thin film deposition rate at elevated pressures.⁹ Based on the sampling that was examined, no twin boundaries were observed. The growth direction of this wire was found to be [111], which is the predominant growth direction observed in the previous studies. A thin oxide on the order of 4-5 nm can be found to surround the nanowire and catalyst (Figure 6.27 (b)).

Low magnification and high-resolution TEM images of a typical nanowire grown at a reactor pressure of 300 Torr are displayed in Figure 6.28. The significant increase in diameter of the nanowire and seed particle is evident in the low magnification image.

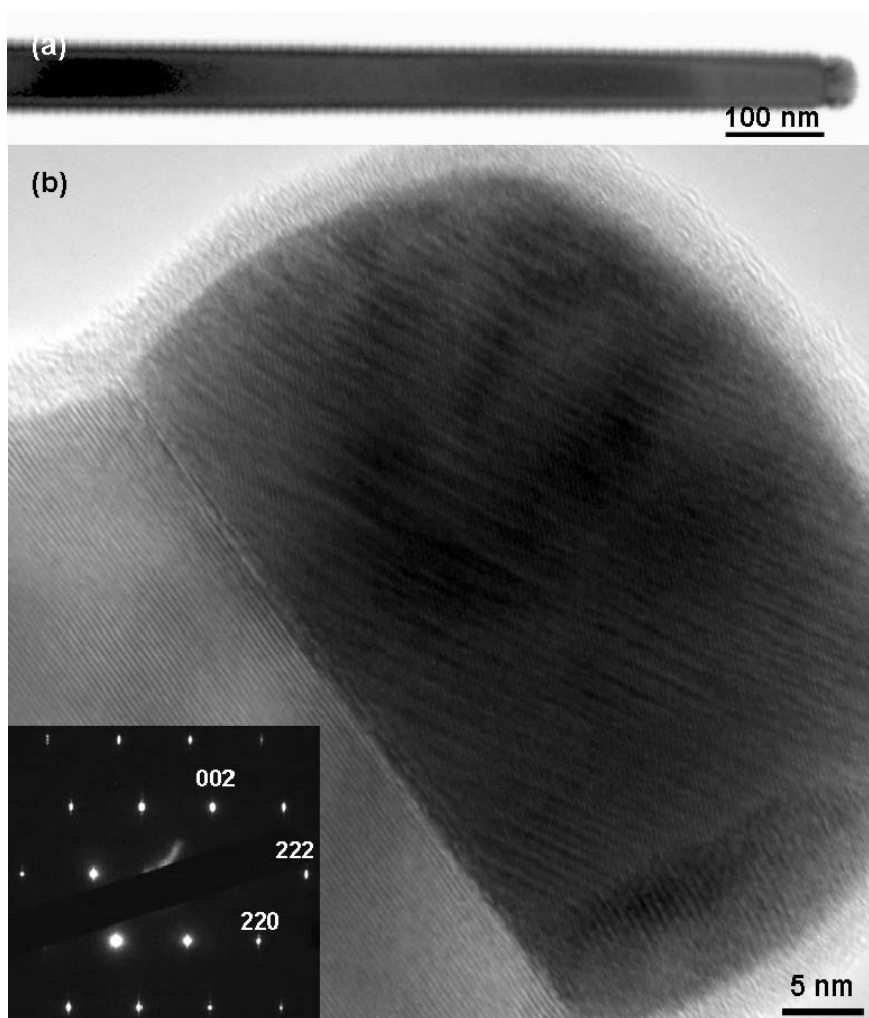


Figure 6.27: (a) Low magnification and (b) HRTEM images of GaSb nanowire grown at 200 Torr with Au catalyst. Inset is an selected area diffraction pattern. The growth direction was determined to be $[111]$. The image was collected along the $1\bar{1}0$ zone axis. Growth conditions: 500°C, 200 Torr, 1 sccm TMG, and 1 sccm TMSb.

Looking at the HRTEM image (Figure 6.28 (b)), there appears to be a secondary phase present on the surface. The secondary phase is found over the entire surface of the nanowire as spots due to the phase contrast. This observation has also been seen for nanowires grown at a Ga-rich condition. According to the thin film literature, growth of GaSb at Ga-rich conditions leads to Ga droplets forming on the surface of the thin film.³⁶

Therefore, it is believed that the secondary phase present on the surface of the nanowire is actually excess Ga. A thin oxide on the order of 3-4 nm was present on the surface, and the growth direction for this nanowire was determined to be $[111]$. Analysis of the catalyst found the particle to be amorphous, and twins were observed to span the cross section of the nanowire near the seed particle.

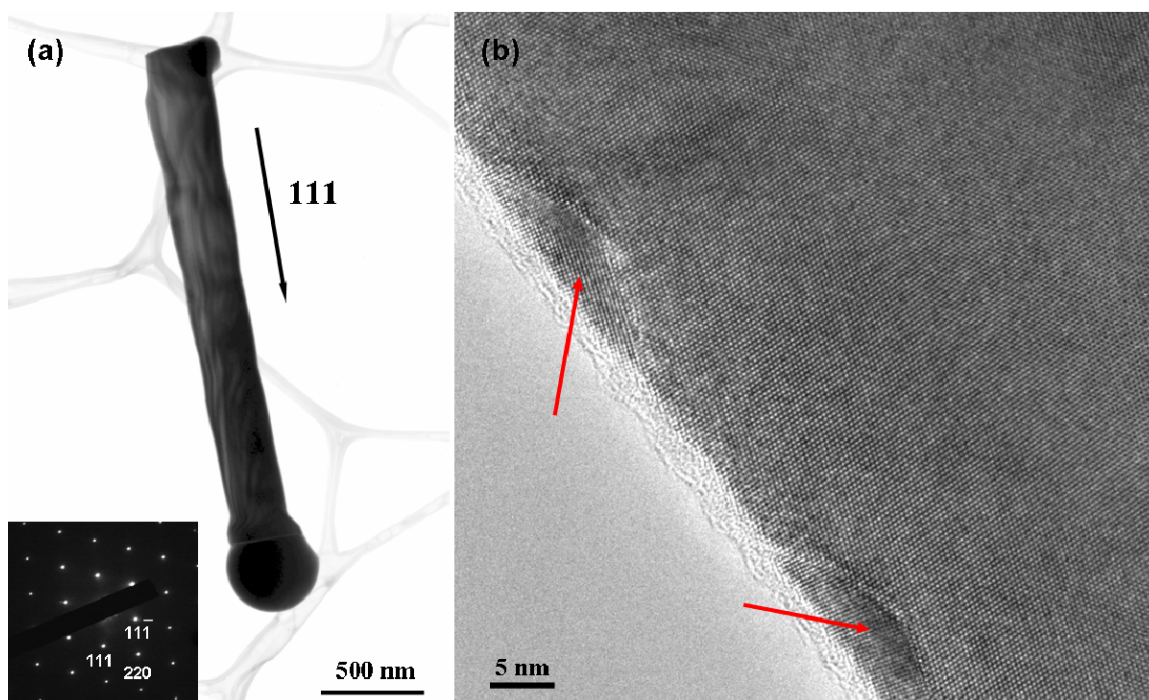


Figure 6.28: (a) Low magnification and (b) high-resolution TEM images of a GaSb nanowire grown at a pressure of 300 Torr. Inset is a SAD pattern showing the $[111]$ growth direction. Red arrows indicate a secondary phase present on the surface of the nanowire. The image was collected along the $1\bar{1}0$ zone axis. Growth conditions: 500°C , 300 Torr, 1 sccm TMG, and 1 sccm TMSb.

XEDS of each sample was employed to investigate the composition of the catalyst, and the results are compared to those obtained for the TEM analysis of the GaSb nanowire sample grown at 100 Torr. The results from this analysis are shown in Figure 6.29. As was previously reported, the GaSb nanowire grown at a pressure of 100

Torr possessed a seed particle that contained approximately 43.9 ± 1.0 at.% Ga, 15.2 ± 1.9 at.% Sb, and 41.0 ± 0.9 at.% Au. For the GaSb nanowire sample grown at a pressure of 200 Torr, the Ga peak dipped slightly as the line scan approached the nanowire/particle interface, while a significant drop was observed in the Sb intensity. The ES Vision software was utilized to determine the content of each constituent, and the seed particle was found to contain 28.9 ± 2.8 at.% Ga, 0.7 ± 0.8 at.% Sb, and 70.5 ± 2.6 at.% Au. Looking at the dark-field STEM and HRTEM images of the sample grown at a pressure of 200 Torr (Figure 6.27 (b) and Figure 6.29 (b)), a noticeable necking region of the nanowire near the catalyst is present. This observation along with the calculated values for the composition of the catalyst coincide well with the data obtained for the GaSb nanowire grown at a V/III ratio of 2 (Figure 6.26). It appears that Sb diffuses out of the catalyst in order to reduce the Sb content to approximately 1%. As a result, the Ga concentration also decreases in order to form the necking region. This was not the only type of seed particle that was observed for the 200 Torr nanowire sample. In another nanowire, the catalyst was found to contain approximately 36.1 ± 3.6 at.% Ga, 13.4 ± 1.9 at.% Sb, and 50.6 ± 3.2 at.% Au. These values are consistent with seed particles that were observed to have an increased solubility of Sb in the Au-Sb solid solution on the nanoscale (Figure 6.17).

Unlike nanowire samples grown at 100 and 200 Torr, the seed particles for GaSb nanowires grown at a reactor pressure of 300 Torr were found to consist of pure gallium. Looking at the composition line scan for the sample at 300 Torr, Au was not found to exist in the nanowire or catalyst, while the Sb intensity dropped off significantly as the nanowire/particle interface was reached. The Ga peak, on the other hand, increased

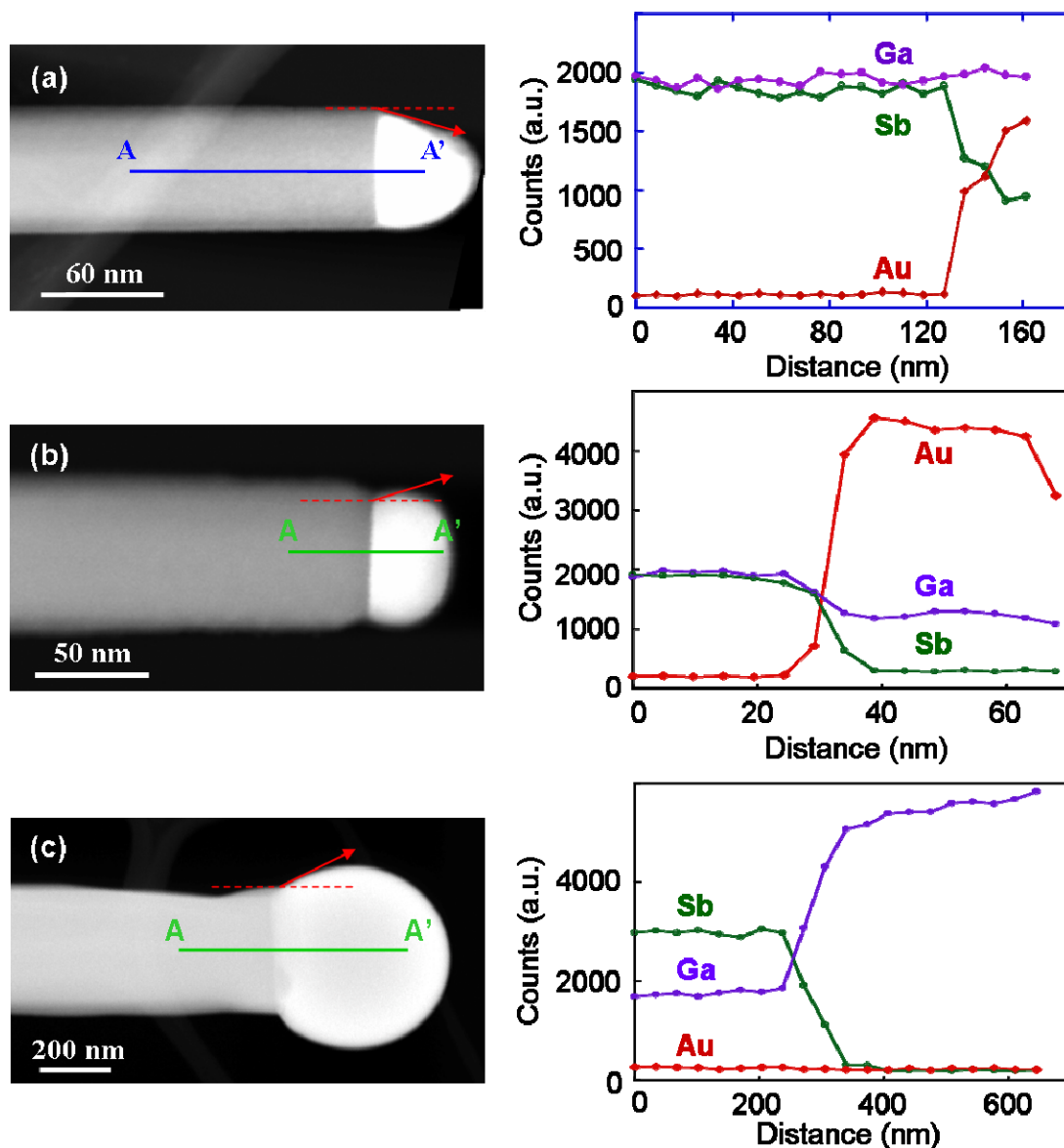


Figure 6.29: High-angle annular dark-field STEM images and XEDS axial line scans for GaSb nanowires samples grown at pressures of (a) 100 Torr, (b) 200 Torr, and (c) 300 Torr. The red arrows demonstrate the contact angle observed in each case.

significantly as the interface was approached. The disparity in the Ga and Sb intensities in the nanowire body was attributed to the large diameter observed for GaSb nanowires grown at a pressure of 300 Torr, which resulted in an increased absorption of x-rays from Ga by Sb. In order to test this hypothesis, XEDS data was collected at various

thicknesses of a TEM specimen prepared from a GaSb wafer. The Sb intensity was observed to increase faster than the Ga intensity as the sample became thicker, resulting in a large disparity in intensities in the thick regions.

Looking at the Ga-Sb phase diagram (Figure 6.30), it is quite possible that GaSb nanowire growth actually proceeded from a Ga-based seed particle. At 500°C, a liquid alloy will immediately form between Ga and Sb. Once the composition of the catalyst reaches 4 at.% Sb, the catalyst will enter the two phase region of the liquid and α -GaSb line compound. Self-catalytic growth of III-V nanowires have been observed before in multiple reports.^{23,37-39} In one such study, GaN nanowires were grown using Ga(NO₃)₃-derived catalysts, however Ga droplets were not observed at the tip of the nanowire.³⁷ In another study, InP nanowires were found to grown from In droplets that deposited on the surface of a InP (111)B substrate.²³ In this case, a surface reconstruction was believed to be responsible for the deposition of In droplets on the surface.

In this study, it is believed that the elevated pressure leads to the deposition of Ga droplets on the surface. Once this occurs, Sb reacts with the catalyst, and the growth of a GaSb nanowire results. The growth is believed to proceed via self-catalytic growth, since the catalyst consists of pure Ga. If this were true, it would also account for the significant decrease in the growth rate as self-catalytic growth is typically slower than VLS growth of nanowires.^{23,38} If growth proceeds via a self-catalytic mechanism, the increased diameter of the catalyst contributes to the decrease in the growth rate, since an increase in Sb would be required for growth.^{23,40} The significant degree of tapering could be due to two aspects of the nanowire growth. One contributing factor is the fact that Ga not only acts as the seed particle but also is the source of Ga for reaction with Sb to form the GaSb

nanowire. If the flux necessary for GaSb nanowire growth is higher than the flux of Ga to the particle, then the Ga seed particle will become depleted of Ga, leading to a reduction in size and the tapered structure.³⁸ Another possibility involves the diffusion of Ga and Sb atoms on the surface of the substrate and sidewalls of the nanowire. If the diffusion length of Ga and Sb atoms along the surface of the wire were smaller than the length of the nanowire, the Ga and Sb atoms would become incorporated within the wire and lead to a tapered structure.⁴¹ It is highly possible that this did occur as a GaSb thin film was found on the surface of the Au-coated sapphire substrate (Figure 6.13 (c)).

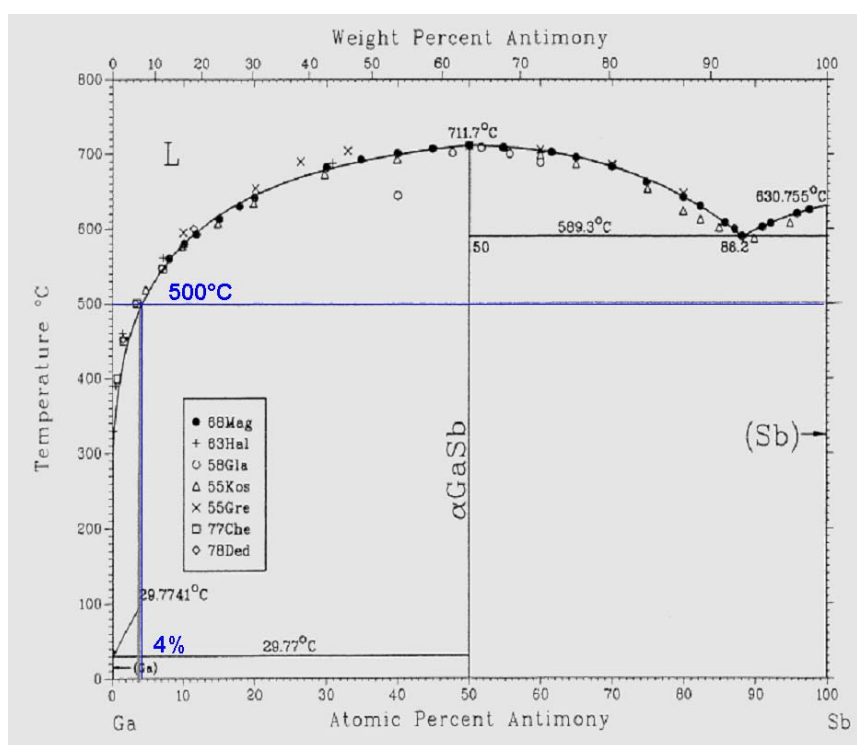


Figure 6.30: Binary phase diagram for Ga-Sb system. The blue line indicates the point at which GaSb would precipitate out of the catalyst at a growth temperature of 500°C.⁴²

Looking at the dark-field STEM images closely (Figure 6.29), it becomes apparent that the composition of the catalyst has an effect on the contact angle between the seed particle and the nanowire interface. Nebol'sin *et al.*⁴³ investigated the effect of the catalyst composition on the contact angle and stability of Si nanowire growth. In general, a few correlations were made between the surface energies of the liquid-vapor, solid-vapor, and liquid-solid interfaces. If the growth is in a state of equilibrium, a few assumptions can be made. If the cross section of the nanowire can be viewed as a rectangle, then the interfacial energy vector of the liquid-solid interface runs parallel to the nanowire/particle interface, while the interfacial energy vector of the solid-vapor runs perpendicular to the nanowire/particle interface (Figure 6.31). As a result, the vector for the liquid-vapor interfacial energy can be broken into x- and y-components where the y-component is equivalent to the surface energy for the solid-vapor interface and the x-component is equivalent to the surface energy of the solid-liquid interface. These concepts can be expressed in the following equations:

$$\gamma_{SV} = \gamma_{LV} \cos \Phi \quad \text{Eq. 6-3}$$

$$\gamma_{SL} = \gamma_{LV} \sin \Phi \quad \text{Eq. 6-4}$$

where Φ is equal to $\Theta - 90^\circ$. Θ is the angle formed between the liquid-vapor vector and the nanowire/particle interface. Unlike the catalyst, the solid-vapor interfacial energy will remain constant, since a GaSb crystal is precipitated out of the seed particle. The liquid-vapor and liquid-solid interface energies will change based on the composition of the catalyst.

Based on the dark-field STEM images (Figure 6.29), it appears as though the determining factor between the contact angle being greater than 90° or less than 90° is the presence of a high concentration of Sb. This observation can be tested by creating a model where one seed particle is found to contain a high concentration of Sb, while another particle only consists of Au and Ga. This simple model is displayed in Figure 6.31. Values can be obtained from the literature for liquid surface tensions for each of the elements/compounds and used as values for the liquid-vapor interfacial energy. The liquid surface tensions of Au, Ga, Sb, and GaSb are 1.140 J/m^2 , 0.677 J/m^2 , 0.355 J/m^2 , and 0.520 J/m^2 , respectively.⁴⁴⁻⁴⁶ These values can be utilized in conjunction with the vector for the solid-vapor interface to determine a rough estimate of the contact angle between the nanowire and the catalyst. The equation relating the solid-vapor interfacial energy to the liquid-vapor interfacial energy can be adjusted so the contact angle is proportional to the ratio of the solid-vapor interfacial energy to the liquid-vapor interfacial energy:

$$\cos \Phi = \frac{\gamma_{SV}}{\gamma_{LV}} \quad \text{Eq. 6-5}$$

The contact angle is equal to $90^\circ + \Phi$. If the ratio is greater than 1, then Φ will be negative, and the contact angle will be less than 90° . If the ratio is less than 1, then Φ will be positive, and the contact angle will be greater than 90° .

Based on the liquid surface tensions, a catalyst consisting of Sb would lead to a contact angle less than 90° . For all other cases, the contact angle would be observed to be larger than 90° . This observation fits well with the contact angles observed for particles in the dark-field STEM images (Figure 6.29). The contact angle is only an

estimate, because ideally a value for the solid surface tension of GaSb would be used and the contact angle could change upon solidification. An assumption is being made that the surface tension values would change proportionally for all elements/compounds. Beyond this, the true effect of the Sb incorporation within the catalyst is unknown. Sb has been found to have a significant effect in reducing the surface tension of molten Si, therefore this holds well for the observations seen in this study.

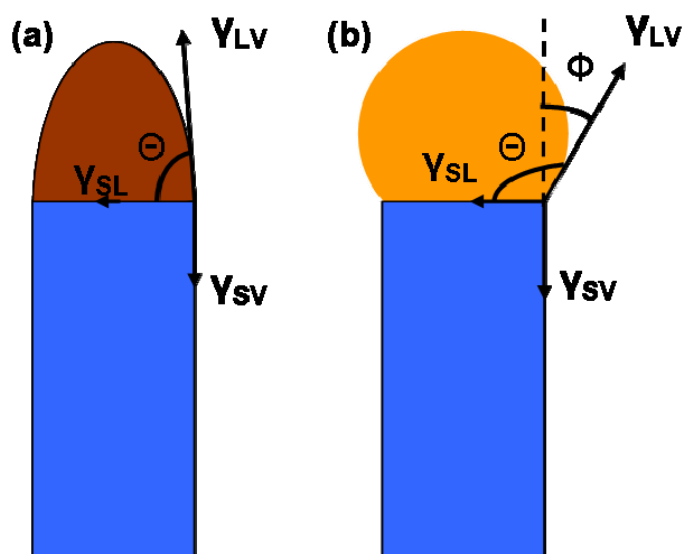


Figure 6.31: Diagram of a nanowire demonstrating the contact angle, Θ , for a catalyst consisting of (a) Au, Ga, and Sb versus a catalyst consisting of (b) Au and Ga. γ_{SL} , γ_{LV} , and γ_{SV} are representative of the surface energies for the solid-liquid, liquid-vapor, and solid-vapor interfaces, respectively. Adapted from Nebol'sin *et al.*⁴³

Further evidence of the effect of Sb on the contact angle between the catalyst and the nanowire can be seen in Figure 6.32. The GaSb nanowire was grown at a temperature of 500°C, while maintaining a pressure of 100 Torr, and a V/III ratio of 2. Looking at the low magnification image, the seed particle appears to consist of two phases based on the phase contrast (Figure 6.32 (a)). This observation is similar to previous studies where

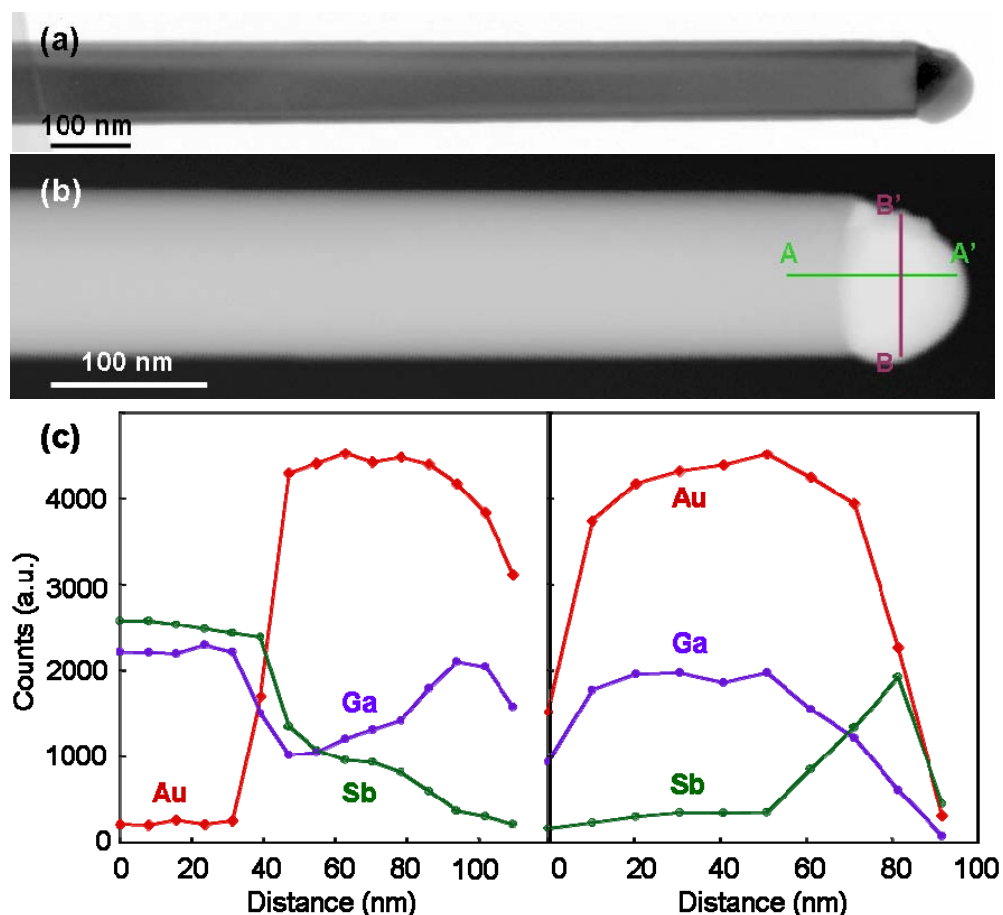


Figure 6.32: (a) Low magnification image of GaSb nanowire. (b) High-angle annular dark-field STEM image of the GaSb nanowire. (c) Composition line scans through the catalyst along the x-axis (A-A') and y-axis (B-B') of the particle. The growth direction was determined to be $[111]$. The images were collected along the $1\bar{1}0$ zone axis.

one grain was found to be Ga-rich, while the other grain was found to be Sb-rich. XEDS was employed to confirm if this is the case for this sample. In the axial line scan, the Ga and Sb peaks were observed to drop as the nanowire interface was approached, however the Ga intensity increased further into the particle. In the line scan through the cross section of the seed particle, the Sb intensity was found to spike near the top side of the nanowire. Interestingly enough, the spike in the Sb peak also coincides with a decrease in the contact angle to less than 90° . In the region where Sb is not present (B point in line

scan), the contact angle was found to be greater than 90° . These results further support the belief that the Sb concentration is responsible for the change in the contact angle between the particle and the nanowire.

6.5 Growth of GaSb Nanowires on Si (111) Substrates

From the TEM analysis, the GaSb nanowires were found to possess a predominant growth direction of [111], while the [220] was the secondary growth direction. The next logical step for the growth of GaSb nanowires was attempting to grow the nanowires epitaxially. GaAs (111)B substrates would be ideal for this process, however the nanowire CVD system is not equipped with an arsine source to provide an arsine overpressure during the ramping of the temperature. This is necessary to prevent evaporation of As from the GaAs substrate. Therefore as an alternative, Si (111) substrates were utilized for the experiments, since Si (111) substrates has been used in the past for epitaxial growth of other III-V nanowires.^{30,47-49} The substrates were coated with 50 nm Au colloids and 2 nm Au thin films, and a BOE etch was performed immediately preceding the experiment. The BOE etch was necessary to remove the native oxide present on the Si surface. This step proved to be extremely important as nanowire growth was not achieved on substrates where the native oxide remained. A series of experiments similar to those completed with sapphire substrates were carried out, and some of the results will be discussed in this section.

In general, similar results were obtained for growth on Si (111) compared to sapphire. The growth conditions that led to growth of GaSb nanowires on sapphire also

led to nanowire growth on Si (111) as long as a BOE etch was completed prior to the growth. A growth rate study was completed for GaSb nanowire samples grown on silicon, and the results were compared to those obtained with sapphire. The GaSb nanowires were grown at a temperature of 500°C, a pressure of 100 Torr, and a V/III ratio of 1. These samples were grown for lengths of 1, 3, 5, 10, and 15 minutes. An example of the resulting GaSb nanowire growth is shown in Figure 6.33. As was previously observed in the sapphire studies, GaSb crystals are evident in the background and appear to enlarge with growth time. Overall, the density of the nanowire growth appeared to increase with time. It is believed that this observation is due to variability in the nucleation time of the Au particles with the precursors. In general, a higher propensity of growth was observed on Si (111) compared to sapphire substrates.

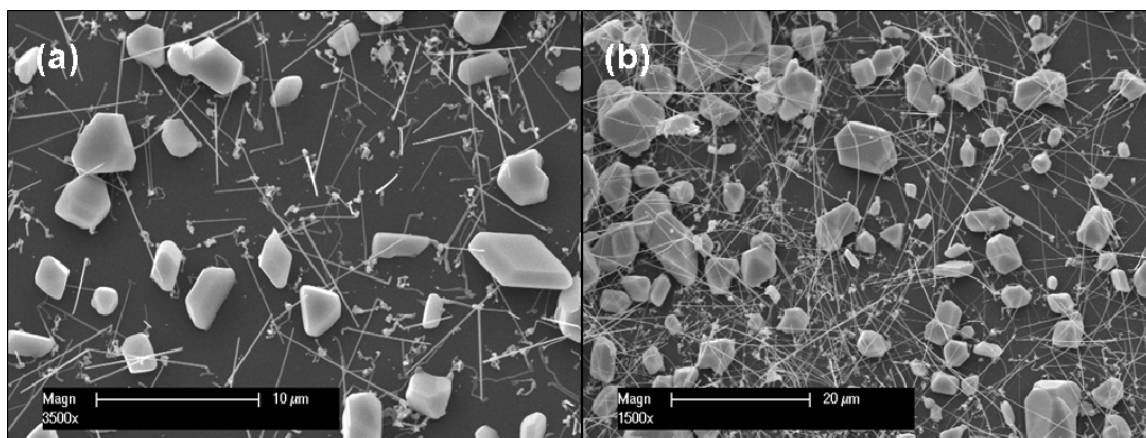


Figure 6.33: SEM images of GaSb nanowire grown on Si (111) coated with 50 nm Au. The samples were grown for (a) 3 minutes and (b) 10 minutes. Scale bars are 10 μm and 20 μm , respectively. Growth conditions: 500°C, 100 Torr, 1 sccm TMG, 1 sccm TMSb, and 100 sccm H_2 .

Length measurements were taken from SEM images for each growth time using the Image J software, and the average length was graphed as a function of time (Figure 6.34). The data was found to fit well with a linear fit ($R^2 = 0.9883$). The nanowire growth rate was determined by the slope of the line and was calculated as $2.39 \pm 0.29 \mu\text{m}/\text{min}$ for a growth temperature of 500°C . As was previously reported, the nanowire growth rate on sapphire was determined to be $2.24 \pm 0.23 \mu\text{m}/\text{min}$, which is quite similar to the results obtained here. The standard deviation for the length measurements increased with growth time, and this fact is believed to be due to variability in the nucleation time of the Au nanoparticles and human error. In particular,

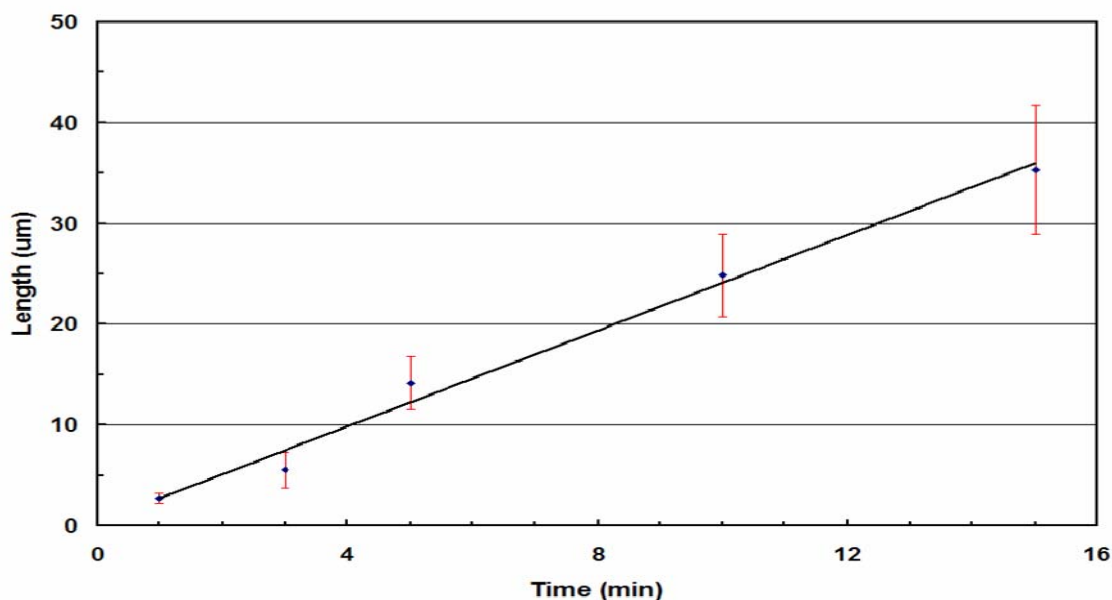


Figure 6.34: Plot of length vs. time for various GaSb nanowire samples grown at 500°C . The growth rate was calculated from the slope of the line as $2.38 \mu\text{m}/\text{min}$. Growth conditions: 100 Torr, 1 sccm TMG, 1 sccm TMSb, and 100 sccm H_2 .

it became more difficult to measure the nanowire lengths for longer growth times as the nanowires were on the order of 35 μm in length and spanned the entire viewing area for the SEM window.

Since the goal of these studies was to successfully grow epitaxial nanowires on Si (111), the following results will focus on conditions that led to epitaxial growth on sapphire. In the series of experiments using sapphire as a substrate, a small fraction of wires appear to be growing vertically at elevated pressures. Similar results were observed for growth on silicon with Au nanoparticles while varying the pressure, and SEM images of these results are shown in Figure 6.35. As was the case for growth on sapphire, not only is there a higher degree of oriented nanowires at elevated pressure, but there is also a dramatic increase in the density of nanowire growth. It was previously hypothesized that this is due to a change in the gas phase mixture at elevated pressures. Due to the increased pressures, an increase in collisions between H radicals and the group III precursors would result, leading to the pyrolysis of TMG and TMSb going further to completion. It is also believed the increase in the TMG partial pressure leads to a higher nucleation rate of the Au nanoparticles due to an increase in the supply of Ga to the nanoparticle interface. The Ga supply was found to be the primary factor leading to nucleation of the particles in the V/III ratio study on sapphire. At the same time, it is believed that the composition of the Au nanoparticles changes which alters the interfacial energy between the particle and the substrate, leading to a higher degree of vertically oriented growth. The vertically oriented nature of the growth can clearly be seen in the insets in Figure 6.35 (c) and (d). These images correspond to pressures of 200 and 250 Torr.

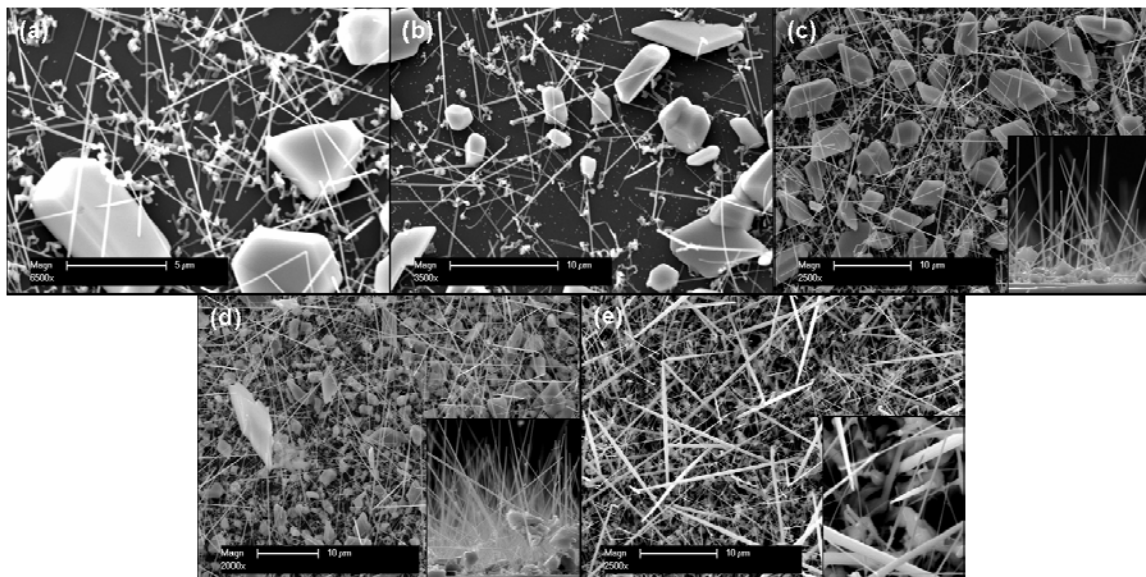


Figure 6.35: SEM images of GaSb nanowire growth on Si (111) using 50 nm Au nanoparticles. Samples were grown at pressures of (a) 100 Torr, (b) 150 Torr, (c) 200 Torr, (d) 250 Torr, and (e) 300 Torr. Insets in (c) and (d) show presence of epitaxial growth. Inset in (e) shows disparity in nanowire diameter. These samples were located 1.5 inches upstream of the center of the hot zone. Growth conditions: 500°C, 1 sccm TMG, 1 sccm TMSb, and 100 sccm H₂.

It can also be seen that the nanowire growth is not exclusively perpendicular to the silicon surface. The nanowires can also grow along other directions of the $\langle 111 \rangle$ family due to etching of the silicon substrate. It has been determined in prior studies that Au has a tendency to etch the silicon substrate by forming a Si-Au alloy prior to growth which exposes the other $\{111\}$ facets.⁴⁷ It has also been noted that the wires can kink upon the initial precipitation reaction.²⁰ The nanowires may also grow along other directions such as the secondary direction $[220]$, and the lattice mismatch between Si (111) and GaSb can also play a factor. It should also be noted that thin film growth is also evident at higher pressures based on the increased density of GaSb crystals and also tapering of the GaSb nanowires at elevated pressures. This can be clearly seen in the

inset in Figure 6.35 (e). Not only are the wires quite tapered, but there is also a distribution of small diameter and larger diameter nanowires.

Similar results were obtained when using Au thin films instead of nanoparticles. When growing with Au thin films, vertically oriented growth was observed at pressures of 150 and 200 Torr (Figure 6.36 (a) and (b)). It should be noted that the samples in this study were located approximately 1.5 inches further back than the Au nanoparticle samples. This may have contributed to the shift in pressures at which vertically oriented growth was obtained. The preferred orientation effects are displayed in Figure 6.36 (a) and (b), and the vertically oriented nature of the growth can clearly be seen in Figure 6.36 (c) and (d) which are cross-section SEM images of the growth. Once again, the nanowire growth is not exclusively perpendicular to the silicon surface. The nanowire growth rate increased from 150 Torr to 200 Torr, however it is also apparent that the thin film growth rate also rose. The nanowires at 200 Torr are significantly larger in diameter (Figure 6.36 (d)). The competing thin film growth is present in the form of GaSb crystals in the cross-section view of the sample grown at a pressure of 150 Torr (Figure 6.36 (c)). During the growth rate study, it was also apparent that a thin film coated the surface of the silicon substrate, and the nanowires were protruding from the thin film. As a result, the thin film could also contribute to the epitaxial nature of the nanowires. It should also be noted that position proved to be an important factor for these studies as samples that were placed further back in the quartz boat displayed a different morphology just as was the case for nanowires grown on sapphire.

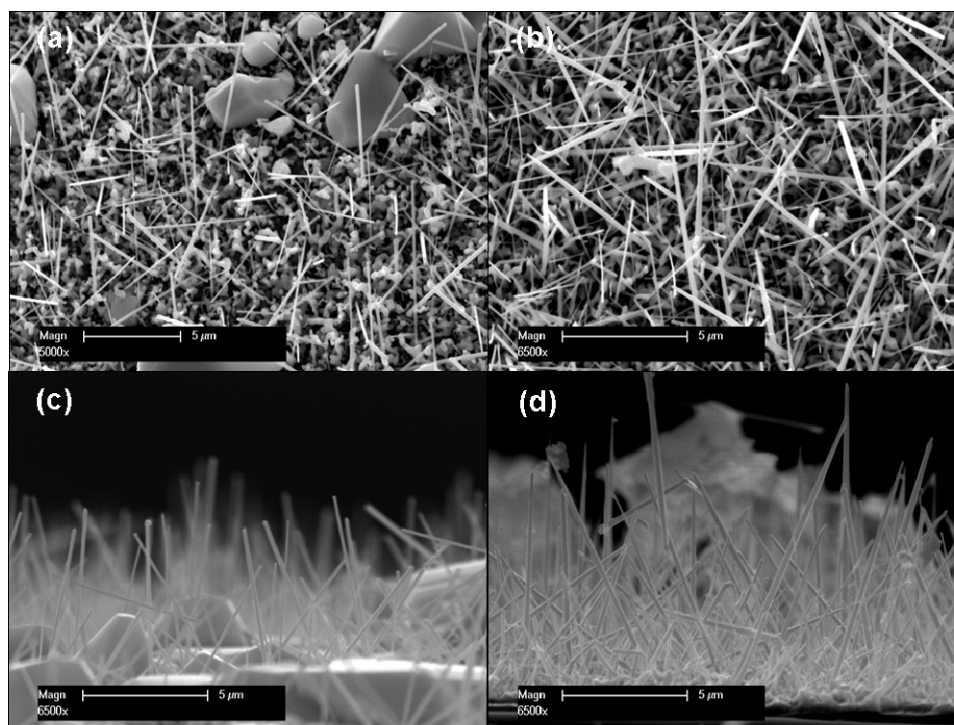


Figure 6.36: SEM images (tilted 15°) of GaSb nanowire growth on Si (111) using 2 nm Au thin film. Samples were grown at pressures of (a) 150 Torr and (b) 200 Torr. (c) and (d) show cross sections of (a) and (b). These samples were located in the center of the hot zone. Growth conditions: 500°C, 1 sccm TMG, 1 sccm TMSb, and 100 sccm H₂.

6.6 Photoluminescence Measurements

Independent of the growth technique, undoped GaSb has always been observed to be p-type in nature.⁹ Extensive work was performed to investigate the nature of the unintentional doping, and a native defect has been linked to this characteristic.^{50,51} The native defect acts as a residual acceptor affecting the electrical and optical properties of the material. A series of defect centres were investigated in order to determine the cause of the unintentional p-type doping. Through studies involving melt-grown GaSb single crystals, the residual acceptor was found to decrease in concentration when the GaSb

crystals were grown under Sb-rich conditions.⁵² As a result of these studies, it was deduced that the residual acceptor was due to excess Ga or a deficiency of Sb in the GaSb single crystal. The complex was identified as a $V_{\text{Ga}}\text{Ga}_{\text{Sb}}$ centre where a Ga atom occupies a Sb site due to a Sb vacancy and leaves a Ga vacancy behind. The acceptor was also determined to be doubly ionizable when the hole concentration was reduced by two orders of magnitude when ion-paired with Li.⁵³

Due to the presence of this native defect and the small band gap of GaSb, the low temperature photoluminescence spectrum is quite complicated. Over 20 transitions have been located over an energy range of 680-830 eV for GaSb. A chart which summarizes the various transitions has been provided in Table 6.5. The band gap has been determined to be approximately 812 meV at 4K and 720 meV at room temperature.^{54,55} The variation in the band gap at cryogenic temperatures versus room temperature is attributed to the relaxation of the GaSb lattice with increasing temperature.⁵⁶ For the low temperature photoluminescence, there are three series of peaks which are typically observed in GaSb. The dominant peak is located at 777 meV and is known as the A peak. This transition is normally between a donor located 2-3 meV below the conduction band and the native acceptor or a transition between the conduction band and the native acceptor. This peak has been observed to vary between 772-779 meV depending on the study and growth technique.⁵⁷⁻⁶⁰ The shift is normally due to strain produced by the lattice mismatch between the substrate and GaSb, the native acceptor concentration, or competing donor-acceptor pair and conduction band-acceptor transitions.⁶⁰ A longitudinal-optical (LO) phonon replica of this peak has been observed at 746 meV. A

peak is also observed at 710 meV which is linked to a transition between the conduction band and the first ionized state of the doubly ionizable acceptor.⁶¹

Table 6.5: Photoluminescence transitions for bulk GaSb at 4.2K. Adapted from Dutta *et al.*⁵⁴

Energy (meV)	Transition	Energy (meV)	Transition
830 (77K)	(e,h) Recombination	792	Exciton bound to $(V_{Ga}Ga_{Sb})^0$
812	Band gap	781	$C-(V_{Ga}Ga_{Sb})^0$
810	Free exciton	777	$D^+-(V_{Ga}Ga_{Sb})^0$
808	Excitonic transition	775	C-Zn acceptor
807	Excitonic transition	765	LO phonon replica of the 796 meV transition
805	Exciton bound to $(V_{Ga}Ga_{Sb})^0$	758	Acceptor B
803	Exciton bound to $(V_{Ga}Ga_{Sb})^0$	746	LO phonon replica of 777 meV transition
801	D^+ -Si-acceptor	740	$C-(V_{Ga}Ga_{Sb}Te_{Sb})^0$
800	Exciton bound to $(V_{Ga}Ga_{Sb})^0$	728	LO phonon replica of 758 meV transition
797	Excitonic transition	717	Exciton bound to $(V_{Ga}Ga_{Sb})^+$
796	Exciton bound to $(V_{Ga}Ga_{Sb})^0$	710	$C-(V_{Ga}Ga_{Sb})^+$
795	Excitonic transition	682	LO phonon replica of the 710 meV transition

Another major series of peaks are the bound exciton peaks, BE1-BE4, which are located between 796 meV and 805 meV.^{59,62,63} The peaks are attributed to excitons bound to the native acceptor. The ratio of the BE peaks to the A peak is normally an indication of the optical and electrical quality of a sample.^{64,65} The third peak which is usually observed in low temperature photoluminescence measurements of GaSb is the B peak, otherwise known as acceptor B. This peak is located at a value of 758 meV. The true nature of the acceptor in this case is not known, however it has been hypothesized that it is a $V_{Ga}Ga_{Sb}V_{Ga}$ complex based on Te-doping studies.^{66,67} This transition has a LO phonon replica at 728 meV.

Unlike the GaSb thin film literature, only two photoluminescence studies have been completed involving GaSb nanowires.^{3,6} The first study was carried out on nanowires grown using either direct antimodization of Ga metal droplets or reactive vapor transport of Ga metals with the presence of Sb in the vapor phase.³

Photoluminescence measurements were taken at room temperature, and a peak was observed at 0.72 eV (~1720 nm) which is attributed to the band gap. Temperature-dependent photoluminescence measurements were also carried out, and the spectrum was observed to blue-shift with decreasing temperature. At 20K, a peak was observed at 0.78 eV (~1580 nm). The second study involved GaSb/GaAs nanowire heterostructures grown by cold-wall MOCVD.⁶ In this study, photoluminescence measurements were taken on individual nanowires. A single dominant peak was normally obtained between 0.785 eV and 0.805 eV. The origin of the peak was not determined, since the peak position was found to vary from wire to wire.

In this study, photoluminescence (PL) measurements were obtained for GaSb nanowire samples grown at various conditions. The analysis for a series of three samples will be included in this section. The first two samples which will be discussed were grown at a pressure of 300 Torr. The growth temperature in each case was 500°C, and the V/III ratio was maintained at 1. The first sample was grown on silicon (Figure 6.37 (a)), and the second sample was grown on sapphire (Figure 6.37 (b)). In both cases, Au thin films were employed as the catalyst. Photoluminescence was performed on these two samples, in part, due to concerns that the low nanowire density on samples grown with Au nanoparticles would affect the intensity of the PL spectrum. The third set which will be discussed involved a series of samples grown at various V/III ratios using Au nanoparticles. These samples were grown at a temperature of 500°C and a pressure of 100 Torr (Figure 6.8). In the thin film literature, the V/III ratio has been found to be critical to the optical properties of GaSb, therefore it proved prudent to investigate the effect of the V/III ratio on the optical properties of the nanowires. The analysis for these

samples was completed using the 488 nm line of an argon laser with an output power of 30-150 mW. It should also be noted that the PL measurements were taken with the nanowires still attached to the underlying substrate. As a result, the GaSb nanowires, crystals, and any thin film deposition could potentially contribute to the PL spectrum.

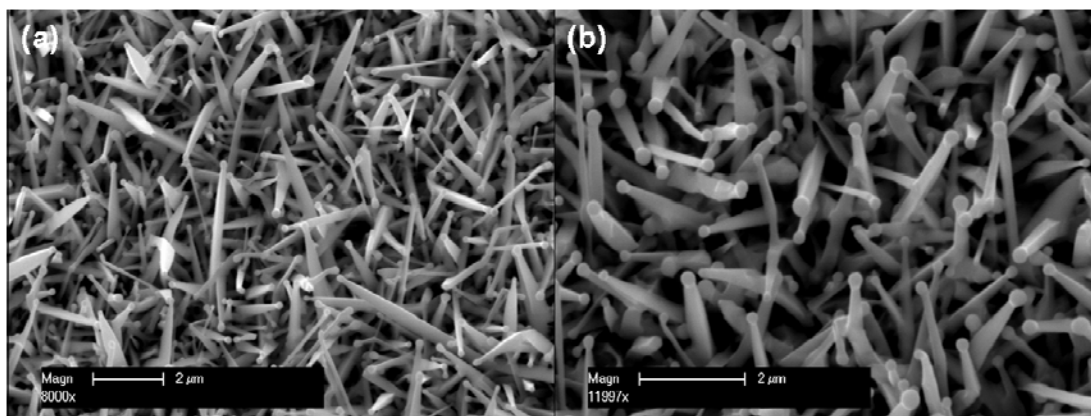


Figure 6.37: SEM images of GaSb nanowires grown at 300 Torr on (a) Si (111) and (b) sapphire using Au thin films. The silicon sample was placed directly in front of the sapphire sample on the quartz boat. Growth conditions: 500°C, 1 sccm TMG, 1 sccm TMSb, and 5 minute growth time.

The sample which was grown on Si (111) at a pressure of 300 Torr is discussed first, since the resulting PL spectrum is representative of a typical spectrum obtained for a GaSb thin film. Temperature-dependent PL measurements were obtained for this sample with a laser output power of 30 mW. The results for this experiment are shown in Figure 6.38. The spectra were taken over a temperature range of 4-280K. Graphing and analysis software called IGOR Pro was utilized in an attempt to resolve the locations of the peaks for each temperature-dependent spectrum. IGOR Pro has a built-in macro which is capable of fitting the curves to Gaussian, Lorentzian, and Voigt functions among others. The software is programmed to automatically locate the peaks based on smoothing and noise factors. At the same time, the user is capable of manually inserting

additional peaks if it is believed that the software omitted peaks. This proves to be extremely useful in cases where peaks are believed to be overlapped. The χ^2 factor is also provided when fitting the curves in order to gain an idea of how good the fit actually is. It should be noted, however, that potential human and program errors do exist. In some cases, the software attempted to fit a peak that extended into the negative intensity regime. It is also possible for the user to omit a peak due to overlapping peaks, which in turn affects the position of the existing peaks.

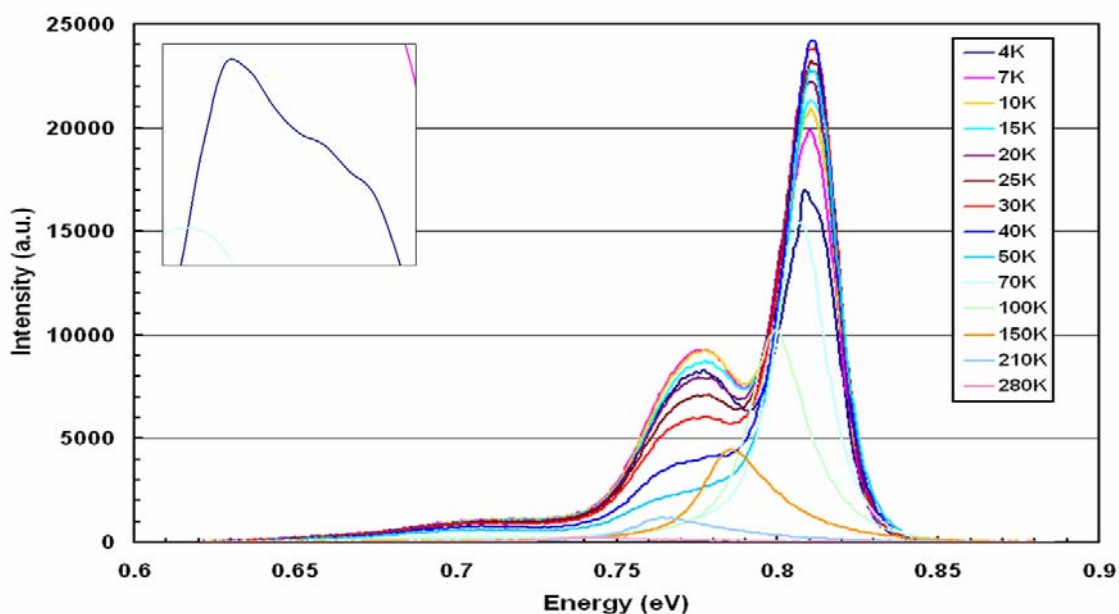


Figure 6.38: Temperature-dependent photoluminescence spectrums of a GaSb nanowire sample grown on Si (111) at a pressure of 300 Torr. Inset shows shoulder on high energy side of peak at 4K.

An example of the peak-fitting capabilities of IGOR Pro is shown in Figure 6.39 for the sample grown on Si (111) at a pressure of 300 Torr. Using the peak-fitting macro, four transitions were observed for the PL spectrum. The first peak was located at approximately 812 meV at 4K and is associated with the band gap for GaSb at low

temperatures.⁵⁴ This peak red-shifted as the temperature increased as expected due to the relaxation of the lattice. At 280K, the peak location was determined to be approximately 738 meV. A scan was not obtained at room temperature, therefore no conclusions can be drawn as to the room temperature band gap. At low temperatures (4-7K), a shoulder is observed on the high energy side of this peak (Figure 6.38). The shoulder is actually due to competing free exciton (FE) and band gap transitions. As the temperature increases, the shoulder disappears and the intensity of the peak increases until 40K. The binding energy of the free excitons is extremely small, therefore it is relatively easy to excite them into the conduction band leading to an increase in band gap transitions. Above 40K, the intensity and the overall area underneath the curve decrease because of non-radiative recombinations.

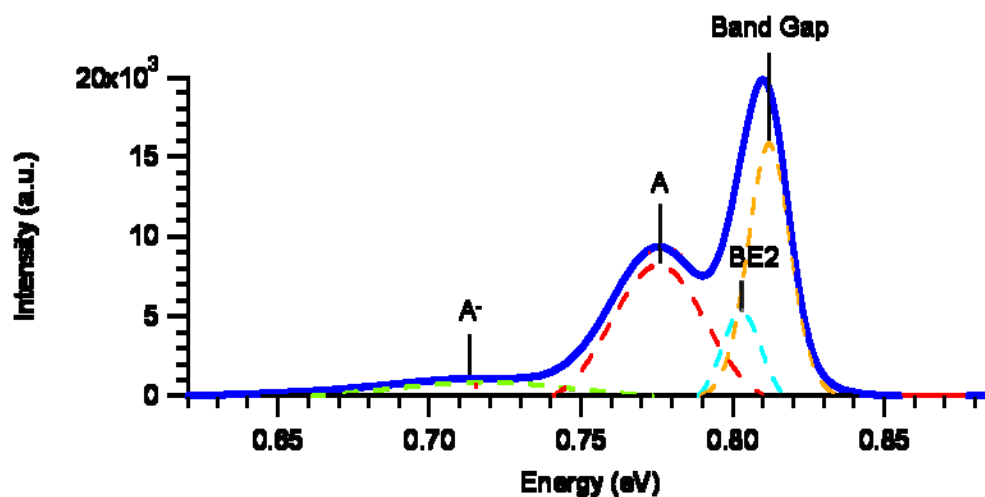


Figure 6.39: Photoluminescence spectrum of GaSb nanowire sample grown on silicon at 7K. The dotted peaks are peak fits for the various transitions and are offset from the axis. The blue peak is the overall fit for the spectrum. The red underlying spectrum is the original curve based on the PL data.

A second peak was resolved at approximately 803 meV (Figure 6.39). Based on the transition table, this peak is attributed an exciton bound to the native acceptor (BE2). It is also possible that the other bound excitation peaks (BE1, BE3, and BE4) contribute to the intensity of the overall peak, however the author was unable to resolve these peaks. In the thin film literature, BE1 and BE2 have primarily been observed in samples grown under stoichiometric or Ga-rich conditions, whereas BE3 has been observed in samples grown under Sb-rich conditions.⁶⁸ There is also differing opinions as to the origin of the BE4 transition. In some studies, this transition has been linked to an exciton bound to the native acceptor, while in other studies it is believed to be bound to the first ionization level of the native acceptor.^{68,69}

A third peak was found to be centered around 775 meV. This transition is known as the A-line and is the dominant emission peak for the native defect. At low temperatures, this peak is found to be a donor-acceptor pair (DAP) transition. Power-dependent PL can be employed to verify the presence of the DAP transition. The power-dependence study was carried out using optical density (OD) filters in order to vary the incident power of the argon beam. The A-line was observed to shift 2-3 meV per decade increase in the power intensity which is expected for a DAP transition.⁷⁰ The intensity with respect to % power was also graphed, and the intensity saturates as the power output nears 30 mW, which is also indicative of a donor-acceptor pair (Figure 6.40).⁵⁹

The binding energy for the donors and acceptors for this transition can be determined by looking at the shift in the location of the peak as the temperature is increased (Figure 6.38). The donor level is located approximately 2-3 meV below the conduction band; therefore as the temperature increases, the electrons bound to the donor

are excited into the conduction band.^{59,70} As a result, the 775 meV peak will shift to higher energies until it becomes a conduction band-acceptor (CB-A) transition. Based on the PL data, the A-line was found to shift to 777.5 meV, which would correspond to a donor binding energy of 2.5 meV. Based on the donor binding energy and the location of the band gap, the acceptor binding energy would be approximately 34 meV. This value corresponds well with acceptor binding energies of 33-36 meV that were calculated in previous studies.^{59,70,71}

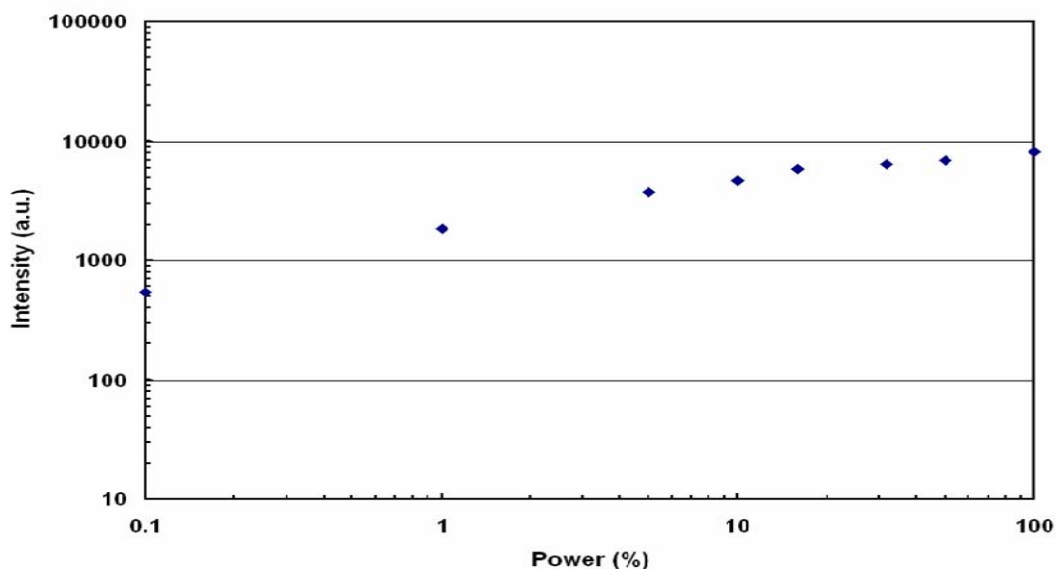


Figure 6.40: Graph of intensity of 777 meV (A) transition with respect to % Power. The intensity saturates at high power output indicating a donor-acceptor pair transition.

The final peak was resolved to be centered at 713 meV. This places the peak in between the 710 meV transition and the 717 meV transition. A peak at 710 meV corresponds to a transition from a donor or the conduction band to the first ionization level of the doubly ionizable native acceptor.⁶¹ The 717 meV peak, on the other hand, has been attributed to an exciton bound to the doubly ionized native acceptor.⁵⁹ In this

sample, the peak is believed to be the 710 meV transition rather than the 717 meV transition based on the trend it follows as the temperature is increased. It may be possible that both peaks are present, however the author was only able to resolve one peak in this energy range. The maximum intensity of this peak was found to only be about 1100 compared to 9300 for the 777 meV (A) transition.

The 710 meV transition and its correlation to the 777 meV (A) transition can be explained by looking at a graph of the intensity of these transitions with respect to temperature along with a band energy diagram of these transitions (Figure 6.41). At 5K, the dominant transition occurs between the donor and the native acceptor. At about 15K, the donor is ionized, and the PL transition proceeds from the conduction band to the native acceptor. As the temperature is increased above 15K, the 777 meV transition starts to be quenched and the intensity of this transition begins to drop. The Fermi level crosses the neutral state of the native acceptor at about 25K, and the intensity begins to drop at a faster rate.⁷⁰ The native acceptor is doubly ionizable, because it is able to bind two holes. As a result, the native acceptor becomes ionized, and the 710 meV peak begins to dominate as transitions occur between the conduction band and the first ionized state of the neutral acceptor. At about 35K, both peaks are being quenched, and their intensities begin to decrease. Between PL temperatures of 50-60K, the Fermi level crosses the ionized state of the neutral acceptor, and the intensity begins to drop at a faster rate.⁵⁹ The native acceptor is now doubly ionized, and the 710 meV and 777 meV transitions disappear. Non-radiative recombinations and band gap transitions continue to dominate the PL spectrum up to room temperature.

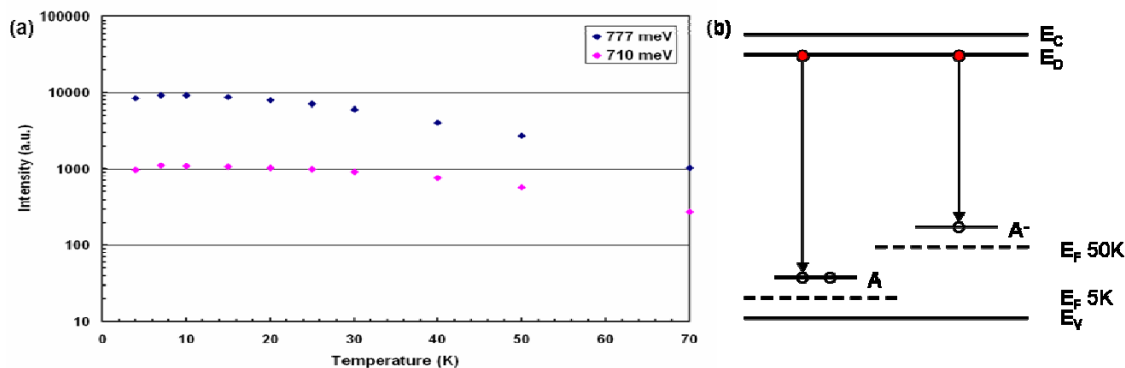


Figure 6.41: (a) Graph of intensities of 710 meV (first ionized state of native acceptor) and 777 meV (native acceptor) with respect to temperature. (b) Energy band diagram of native acceptor (A) and its first ionized state (A^-). E_C , E_D , E_F , and E_V stand for the conduction band, donor level, Fermi level, and valence band, respectively. Adapted from Nicholas *et al.*⁵⁹

Overall, the sample grown on a Si (111) substrate at a pressure of 300 Torr fits well with previous studies concerning GaSb thin films and bulk. The sample was found to possess strong BE and band-edge transitions compared to the native defect transitions, signifying that the sample was of good optical quality. The ratio of the high energy peak to the A-line peak was approximately 2 at low PL temperatures. Further analysis of the sample clearly indicated that the peak at 775 meV at 4K was attributed to the A-line, whereas the peak at 713 meV was associated with the first ionization level of the native acceptor. As the temperature of the PL measurements increased, the 775 meV transition shifted to higher energies as would be expected for a donor-acceptor pair transition. The 713 meV transition was, in turn, linked to the 775 meV transitions by comparing its trend with increasing PL temperature to previous studies in the GaSb literature.

Photoluminescence spectra from the sample grown on sapphire at a pressure of 300 Torr, however, do not resemble those obtained for the GaSb nanowires grown on Si

(111). Temperature-dependent PL was obtained on this sample over a temperature range of 3.6-200K. The power output of the argon laser in this case was 150 mW, however optical density filters were used to regulate the power. For this sample, the lowest optical density filter used for this experiment had a rating of 1.3 which corresponds to a power output of approximately 7.5 mW. It should be noted that this value is significantly smaller than the 30 mW used in the temperature-dependent PL for the Si sample. The results from this experiment are shown in Figure 6.42. The resulting spectrum in this case is a single, broad peak. From the thin film literature, a broad peak is normally indicative of strain caused by the lattice mismatch between the GaSb and the substrate.^{58,59} Lattice mismatch may be a contributing factor to the broadness of the peak, since the previous results on this sample showed an underlying GaSb thin film (Figure 6.13 (c)). The PL spectrum from this sample at 3.6K and a power output of 4.74

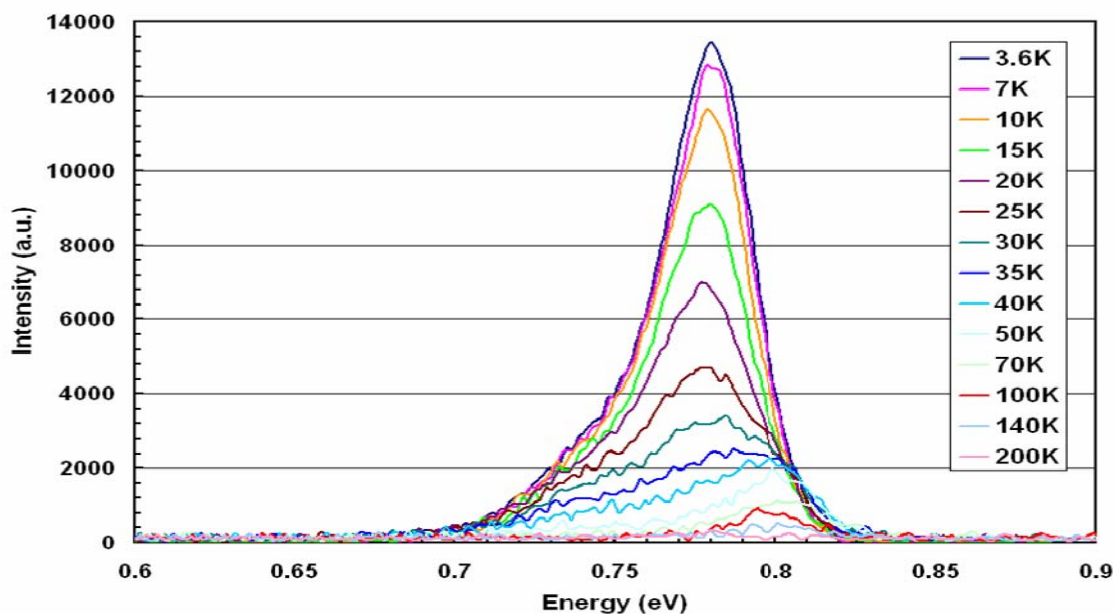


Figure 6.42: Temperature-dependent photoluminescence spectrums of a GaSb nanowire sample grown on sapphire at a pressure of 300 Torr.

mW was compared to a spectrum from the silicon sample at 4K and a power output of 4.75 mW. The spectrum from the Si sample was found to fit within the width of the single peak observed for the sample grown on sapphire.

The IGOR Pro software was employed in an attempt to find the best fit for the broad peak. Due to the lack of distinctive features, it was difficult to determine the proper number of transitions; however, the best fit appeared to consist of four peaks. An example of the peak-fitting for the PL data at 3.6K is provided in Figure 6.43. The four peaks were found to be centered at 729.8, 747.5, 796.8, and 780.6 meV. The dominant transition was determined to be at 780.6 meV. Based on the transitions table (Table 6.5), it is believed that the peaks are blue-shifted and are all associated with either the native acceptor or acceptor B. The peaks may be blue-shifted due to the apparent high concentration of the native defect, however this can't be confirmed without further analysis. It is also possible that a higher energy peak is missing from the peak-fit which would shift the location of additional peaks to lower energies. For example, BE and band-edge transitions were not resolved in IGOR Pro for this sample. It should also be noted that the overall peak is not shifted compared to the spectrum obtained from the sample grown on silicon. This observation in combination with the fact that the samples are p-type eliminates the Burstein-Moss effect as a possible reason for the blue-shift. The Burstein-Moss effect has been observed in Te-doped GaSb thin films⁷² and n-type InN thin films.⁷³ In these cases, a blue-shift in the spectrums is observed at low PL temperatures because of band-filling of the conduction band due to the high electron concentrations in the samples.⁷⁴ As a result, transitions occur at higher states within the

conduction band. Since the native defect increases the hole concentration, the Burstein-Moss effect can't be applied to this situation.

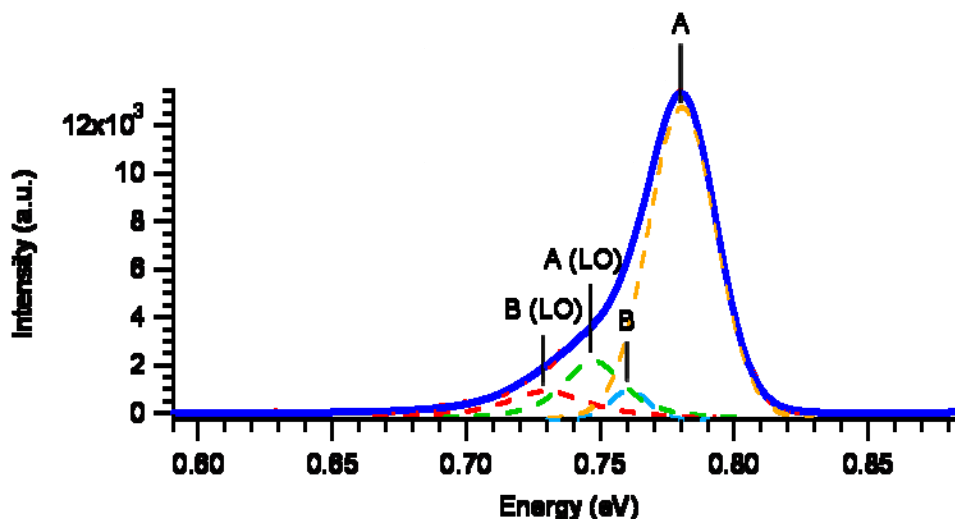


Figure 6.43: Photoluminescence spectrum of GaSb nanowire sample at 3.6K. The dotted peaks are peak fits for the various transitions and are offset from the axis. The blue peak is the overall fit for the spectrum. The red underlying spectrum is the original curve based on the PL data.

If the spectrum is indeed blue-shifted and the peaks are associated with the native defect and acceptor B, it would explain the broadness of the peak. In general, the native acceptor peaks have been observed to be broad in nature and lack distinctive features.⁷⁵ This can also be seen for the 710 meV and 777 meV transitions in the Si sample as the peak-fits for IGOR Pro are broad compared to the BE and band gap transitions (Figure 6.39). The peak centered at 780.6 meV would coincide with the 777 meV peak or the A-line. The peak located at 747.5 meV would correspond to the 746 meV transition which is the LO phonon replica of the 777 meV transition. The peak centered at 760.8 meV would be the 758 meV transition which is also known as acceptor B. As was previously stated, the nature of the acceptor at this transition is unknown, however it

has been hypothesized to be linked to a $V_{\text{Ga}}\text{GaSb}V_{\text{Ga}}$ centre. Finally, the peak located at 729.8 meV would coincide with the LO phonon replica of the 758 meV transition.

Power-dependent PL studies also concur with these results as the overall peak was observed to shift to higher energies as the power intensity was increased. Looking further at the temperature-dependent studies, it appears as though the peak shifts to higher energies as the temperature increases, however this is not the case. As the temperature increases, the native acceptor ionizes and non-radiative recombinations dominate leading to the decrease in the intensity of the spectrum. The peak that remains is believed to be the band gap transition. Since the native acceptor dominates at low temperatures, the author was unable to resolve this peak, however this is not an issue as the temperature increases. If this peak is attributed to the band gap transition, then the peak actually shifts to lower energies at elevated temperatures. Using IGOR Pro, the peak was resolved at 777.6 meV at a temperature of 200K.

An explanation as to why the 777 meV transition is the dominant peak can be found by looking back at the TEM analysis for this sample. For this sample, the catalyst was found to consist of exclusively Ga rather than a Ga-Au alloy. It was believed that at higher pressures, Ga droplets deposited on the surface of the substrate, resulting in the synthesis of GaSb nanowires. The Ga-Sb phase diagram confirmed the possibility of this formation. From the HRTEM images, secondary phases were found on the surface of the nanowires and were believed to be excess Ga depositing on the facets of the nanowires. From the thin film literature, growth under Ga-rich conditions typically leads to the formation of Ga droplets on the surface. The combination of Ga-rich conditions and the Ga seed particle could potentially lead to a significant increase in the concentration of Sb

vacancies within the nanowires. This would, in turn, lead to an increase in the concentration of native acceptors, $V_{\text{Ga}}\text{GaSb}$ centres. As a result, the 777 meV peak would be the dominant transition.

The only inconsistency with this explanation is the fact that the same trend is not observed for the GaSb nanowire sample grown on silicon. It should be noted that the Si sample was placed directly in front of the sapphire sample. TEM analysis was not completed on this sample, therefore the state of the seed particle can't be confirmed. However, based on the SEM results (Figure 6.37 (a)), it appears as though the catalyst may be Ga-based for this sample. As was previously stated, the nanowires were not separated from the substrate prior to taking the PL measurements. As a result, it is not clear what contributions of the PL come from the nanowires versus the thin film present on the substrates. Strain caused by lattice mismatch between the GaSb and the substrate can play a factor in the PL results, therefore the author must be cautious in the analysis of the results. For future work, it would be necessary to separate the contributions to the PL by the nanowires and the thin film deposition. This can be done by sonicating the nanowires from the surface, placing them on a clean substrate and performing the PL analysis or obtaining PL of the Si and sapphire samples before and after sonication.

Another explanation for the differing photoluminescence spectrums could be linked to the substrate choice. When using Si (111) coated with an Au thin film, the Au will form nanoparticles upon heating, but a Au-Si alloy will also result.⁴⁷ The silicon present within the catalyst must be taken into account if growth occurs from the gold. It is possible that the Si can become incorporated within the nanowire. Si has been used as a p-type dopant for GaSb thin film growth.⁷⁶ In the thin film studies, Si has been found

to reduce the intensity of the 777 meV peak. Si can substitute for Sb in the GaSb lattice, thereby occupying Sb vacancies present in the nanowire. If this were the case, then this would reduce the concentration of $V_{\text{Ga}}\text{Ga}_{\text{Sb}}$ complexes. On that note, more analysis needs to be completed to determine why a difference in the PL results is evident at a pressure of 300 Torr if sapphire is used as the substrate instead of silicon.

The final series of samples that will be discussed here involved varying the V/III ratio. As was previously noted, the V/III ratio is critical to the quality of the optical and electrical properties of GaSb. In general, a V/III ratio around unity is found to be ideal for the optical properties of GaSb. As a result, it would be useful to investigate how the V/III ratio affects the PL data for the GaSb nanowires. Photoluminescence measurements were carried out on four samples grown on sapphire with 50 nm Au nanoparticles. The samples were grown at V/III ratios of 0.5, 1, 1.5, and 2. Power-dependent PL studies (12, 38, and 120 mW) were completed for samples with V/III ratios of 0.5, 1.5, and 2, while only one laser power (15 mW) was utilized for the sample grown at a V/III ratio of 1. A power-dependent PL study was not completed for the GaSb nanowires grown at a V/III ratio of 1, because this sample had been analyzed with the first set of samples by one individual, while the samples grown at V/III ratios of 0.5, 1.5, and 2 were completed with a second set of samples by another individual. The results for this study at low laser powers are shown in Figure 6.44. PL measurements for the sample grown at a V/III ratio of 1 were carried out a laser power of 15 mW and a temperature of 3.5K. The rest of the samples were analyzed at a laser power of 12 mW and a temperature of 5K. The intensities of the PL at V/III ratios of 1, 1.5, and 2 were multiplied by a factor of 8 for comparison purposes. It is believed that the high intensity

observed at a V/III ratio of 0.5 is due to the higher nanowire density on this sample. In general, the overall intensity is found to decrease with increasing V/III ratio which also coincides with a decrease in the nanowire density. A quick look at the graph indicates that high energy transitions dominate at a V/III ratio of 1, while lower energy transitions dominate above and below a V/III ratio of 1.

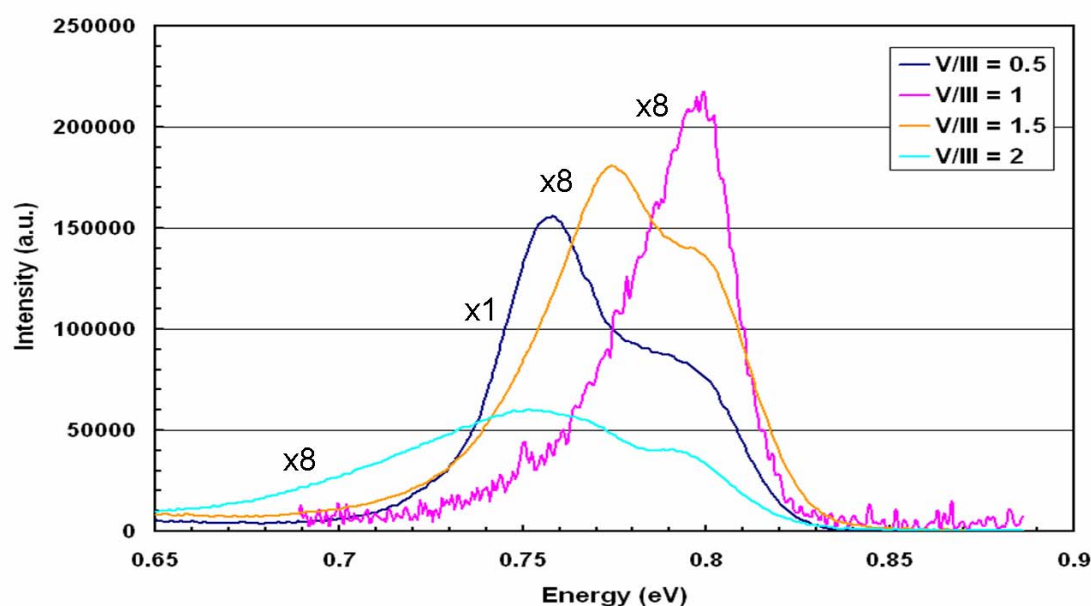


Figure 6.44: Photoluminescence measurements of GaSb nanowire samples grown on sapphire using 50 nm Au nanoparticles at V/III ratios of 0.5, 1, 1.5, and 2. The sample grown at a V/III ratio of 1 was completed with a laser power of 15 mW and a temperature of 3.5K. The other samples were analyzed at a laser power of 12 mW and a temperature of 5K. The intensities of the photoluminescence for samples grown at V/III ratios of 1, 1.5, and 2 were multiplied by 8 for comparison purposes. Growth conditions: 500°C, 100 Torr, and 5 minute growth time.

IGOR Pro software was employed once again for peak-fitting purposes for each of the samples in an attempt to understand how the V/III ratio affects the transitions observed in the PL measurements. For the samples grown at V/III ratio of 0.5, 1.5, and 2, PL data was collected at lower energies which produced an additional peak between 0.65

and 0.67 eV. This peak has been ignored for this analysis, since the author was not able to find information for any transitions below 682 meV. The first sample that was analyzed with the software was grown at a V/III ratio of 0.5. In this case, three peaks were observed at energies of 756.9, 783.4, and 801.5 meV. The peak at 756.9 meV is believed to be the acceptor B located at 758 meV, whereas the peak at 801.5 meV is believed to be BE2 peak at 803 meV. At higher energies the transition at 801.5 meV was found to shift to about 804 meV based on the peak-fitting software. This transition corresponds to an exciton bound to the native acceptor.

There is less certainty as to the source of the transition at 783.4 meV. Based on the transition table, it is located between transitions at 781 and 792 meV. In an attempt to resolve this peak, an additional peak was added to the spectrum, however IGOR Pro resolved it as being centered at 768.5 meV and lowered the intensity of the BE2 transition. Since the sample is grown in Ga-rich conditions, the A peak would be expected to be present as the conditions would promote Sb vacancies. A 5th peak was added to the peak-fitting macro, and this time the peak was resolved at about 779.7 meV. As a result, the peak at 783.4 meV will be attributed to the transition observed at 781 meV, and a peak will be added at 779.7 meV which corresponds to the donor-acceptor pair transition typically observed at 777 meV. The peak at 781 meV is attributed to a transition between the conduction band and the native acceptor. Based on the power-dependent PL studies, the acceptor B line is found to dominate at low power intensities, while the BE2 line is observed to dominate at high power intensities which is expected since the BE2 line is an excitonic transition. These results correlate well with previous results involving MOCVD-grown GaSb thin films.^{58,68} In the thin film studies, the BE2

line was found to be stronger in samples grown at Ga-rich conditions, and the acceptor B line was found to increase as the V/III ratio decreased. As a result, it is believed that acceptor B is related to the native defect.

The next sample which will be discussed was grown at a V/III ratio of 1. For this sample, four peaks were resolved. These peaks were located at energies of 760.4, 782.8, 796.7, and 804.2 meV. The peak at 760.4 meV is believed to coincide with acceptor B at 758 meV. The peak at 782.8 meV is once again between the transitions at 781 and 792 meV. An additional peak was added to the peak-fitting macro which shifted the peak at 782.8 meV to 783.7 meV and resolved a peak at 769.4 meV. Once again, it is believed that a peak should be present at 777 meV, and the peak at 782.8 meV is actually the 781 meV transition. These issues exemplify the concerns with the peak-fitting. It is possible that a higher energy peak is missing which would shift the other peaks to lower energies, however this is just an assumption at this point. The transition observed at 796.7 meV, however, fits well with the BE4 line located at 796 meV. This transition is attributed either to an excitation bound to the native acceptor or the first ionization level of the native acceptor. A final peak was resolved at 804.2 meV, and it appears to coincide with the BE2 line at 803 meV. At a laser power of 15 mW, the peaks at 781 meV, BE2, and BE4 were all found to have roughly the same intensity.

The third sample for analysis was grown at a V/III ratio of 1.5. Three peaks were found to present at this condition. These peaks were centered at 762.7, 775.4, and 800.1 meV. The peak at 762.7 meV is attributed to the acceptor B transition at 758 meV. At higher laser powers, the peak at 762.7 meV red-shifted to 758.2 meV. The peak at 775.4 meV is believed to be the A line transition at 777 meV, whereas the peak at 800.1 meV

coincides with the BE3 transition at 800 meV. At low power intensities, all three peaks were found to be roughly the same in intensity. At high laser powers, the BE3 line at 800 meV was observed to dominate. This corresponds well with the literature where the BE3 peak typically was stronger in Sb-rich conditions.⁶⁸

The final sample for PL analysis was grown at a V/III ratio of 2. An example of the peak fits for this sample at a laser power of 12 mW is shown in Figure 6.45. There is a peak centered at 650 meV, however it is going to be ignored for this study as previous stated. As a result, there were four peaks resolved for this sample at energies of 729.3, 756.1, 770.3, and 794.9 meV. The peak at 756.1 meV is the acceptor B line at 758 meV, whereas the peak at 729.3 meV would correspond to the LO phonon replica of acceptor B at 728 meV. The transition at 794.9 meV is believed to be the BE4 line at 796 meV. This peak is associated with an exciton bound to the native acceptor or its first ionization level. It is found to increase to 796.7 meV at a laser power of 38 mW and 797 meV at a power output of 120 mW. The peak observed at 770.3 meV is located in between transitions at 765 and 777 meV. Since the BE4 line is present, this transition appears to be linked to the 765 meV transition which is the LO phonon replica of the BE4 line. At low power intensities, acceptor B and its LO phonon replica were found to dominate. At higher power intensities, the BE4 line was found to dominate. It should also be noted that the A-line is not observed for this study. This result is expected as growth in Sb-rich conditions should reduce the native acceptor concentration with the GaSb nanowires. The dominance of the BE4 line at high laser powers and the absence of the A-line correspond well with results obtained in the thin film literature.^{60,68,76}

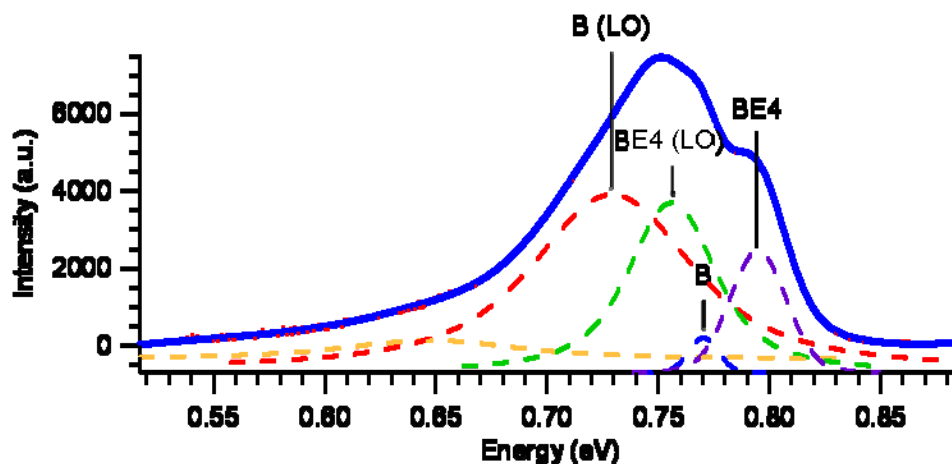


Figure 6.45: Photoluminescence spectrum at 5K of GaSb nanowire sample with a V/III ratio of 2. The dotted peaks are peak fits for the various transitions and are offset from the axis. The blue peak is the overall fit for the spectrum. The red underlying spectrum is the original curve based on the PL data.

In review, the V/III ratio had a significant effect on the resulting photoluminescence measurements. The photoluminescence supported previous studies of GaSb in the thin film literature. At a V/III ratio of 0.5, transitions associated with the native acceptor and acceptor B were found to dominate, while the A-line was observed to decrease and disappear when growth occurred in Sb-rich conditions. Acceptor B was still present in these conditions, and its true nature is still not known. A V/III ratio near unity appeared to possess the best optical properties as higher energy transitions were found to dominate even at low laser powers.

6.7 Conclusions

In conclusion, the growth conditions for the synthesis of GaSb using TMG and TMSb as the precursors were investigated in order to determine a growth window for

GaSb nanowire growth. These studies were completed on sapphire substrates utilizing both Au and Ni thin films and Au nanoparticles and Si (111) substrates using Au nanoparticles and thin films. Limited success was realized when growing with Ni thin films which was expected based on the Ni-Ga and Ni-Sb phase diagrams. Nanowire growth was achieved with both Au thin films and nanoparticles over a temperature range of 475-525°C, a pressure range of 100-300 Torr, and a V/III ratio of 0.5-2. At temperatures below 475°C, no deposition was observed and was attributed to insufficient decomposition of the gas phase precursors. As the temperature was increased, the nanowires became more tapered, indicating an increase in the thin film deposition. Eventually at temperatures above 525°C, nanowire growth no longer resulted and was replaced by either thin film deposition or large GaSb particles.

Upon examination of the pressure studies, vertically oriented growth was found to result on the Au thin film sapphire samples over a pressure range of 200-300 Torr. At a pressure of 300 Torr, the nanowires were found to be significantly larger in diameter with a high degree of tapering. Vertically oriented growth was realized on Si (111) over a pressure range of 150-250 Torr, however this was expected since the predominant growth direction was found to be [111]. An explanation as to the cause of the vertically oriented growth on sapphire is not clear, but it is believed to be due to a combination of an underlying GaSb thin film and a change in the composition of the seed particle which promote the vertically oriented growth. Similar results were obtained when varying the V/III ratio. When growing under Ga-rich conditions, orientation effects were observed along with an increase in the nanowire density. As a result, Ga is believed to play a significant role in the nucleation of the GaSb nanowires. This fact was exemplified when

the samples were grown in Sb-rich conditions as the nanowire density decreased dramatically. At the same time, the growth rate was found to decrease by a factor of 2, and a “reverse tapering” was observed for a selection of nanowires. The reverse tapering is believed to be due to an instability of the catalyst at the onset of growth, since it has not reached its final composition.

Upon completion of the experiments and SEM analysis, TEM characterization was carried out to examine the state of the catalyst and determine a cause for the orientation effects and change in morphology at higher pressures. By utilizing XEDS, the composition of the catalyst was determined. The seed particle was found to consist of ~25-40 at.% Ga and ~40-75 at.% Au. Based on the Au-Ga phase diagram, it is evident that nanowire growth proceeded via the VLS mechanism as a liquid alloy formed. An interesting note from this study was the Sb content in the catalyst. The Sb concentration was determined to be either 1, 15, or 55 at.%, which corresponded to three nanowire structures. When the Sb concentration was only 1 at.%, a necking region was observed and was attributed to diffusion of Sb and Ga out of the catalyst when the sample was cooled. A concentration of 15 at.% Sb led to the formation of a Au-Sb solid solution within the catalyst. Typically, the solid solubility of Sb in Au is only around 1 at.%, however at the nanoscale level it has been observed as high as 15 at.%. At the same time, the AuSb₂ line compound at ~67 at.% Sb has been found to expand to a region of ~52-77 at.% Sb at the nanoscale. This range corresponds to the third Sb concentration of 55 at.%. When the seed particle consisted of 55 at.% Sb, the nanowires were observed to be bicrystalline as a phase separation of the particle was observed. The particle consisted of an AuSb₂ grain and a AuGa or Au₂Ga grain.

Differences in the particle composition were also realized when looking at samples grown at various pressures. Based on the initial TEM analysis, GaSb nanowires grown at a pressure of 300 Torr were observed to have an amorphous catalyst. Upon further inspection utilizing XEDS, the catalyst was found to consist of exclusively Ga. It appears as though Ga droplets deposited on the surface of the substrate and acted as a catalyst for GaSb nanowire growth. Based on the Ga-Sb phase diagram, it was shown this was highly possible. If this were the case, it would explain the reduction in the nanowire growth rate and the significant tapering of the nanowire, since the particle would also be the source of Ga and the growth would proceed via a self-catalytic mode. During this study, it was also observed that the contact angle between the seed particle and the nanowire varied from sample to sample. By looking at the composition of the catalyst and surface tensions for the different elements and compounds, it was deduced that Sb played a critical role in the final contact angle. In situations where the seed particle consisted of 1 at.% Sb, the contact angle was observed to be greater than 90° . When the seed particle was composed of 15 at.% Sb, the contact angle was less than 90° . For the cases where the particle consisted of two grains, the Sb-rich component had a contact angle less than 90° , while the Ga-rich component had a contact angle greater than 90° .

Finally, photoluminescence measurements were carried out for a collection of GaSb nanowire samples. PL from the sample grown on silicon at a pressure of 300 Torr was similar to that of a typical GaSb thin film with good optical properties. Band-edge transitions were found to dominate the photoluminescence, however peaks associated with the native acceptor at 777 meV and 710 meV were also present. The PL from the

sapphire sample at 300 Torr, on the other hand, corresponded to a GaSb thin film with poor optical properties. For this sample, transitions associated with the native acceptor and acceptor B dominated the PL spectrum. The final series of GaSb nanowire samples that were analyzed exemplified the critical nature of the V/III ratio on the optical properties. A V/III ratio around unity produced nanowires with the best optical properties as higher energy transitions dominated the luminescence. When the nanowires were grown under Ga-rich conditions, transitions associated with the native acceptor and acceptor B dominated the luminescence. This observation was expected since Ga-rich conditions promote the formation of Sb vacancies and $V_{\text{Ga}}\text{Ga}_{\text{Sb}}$ centres which are linked to the native acceptor. When the GaSb nanowires were grown in Sb-rich conditions, the A-line, coinciding with the major native acceptor transitions, was no longer present.

6.8 References

- ¹ A. Lugstein, J. Bernardi, C. Tomastik, and E. Bertagnolli, *Applied Physics Letters* **88**, 163114 (2006).
- ² A. Lugstein, C. Schoendorfer, M. Weil, C. Tomastik, A. Jauss, and E. Bertagnolli, *Nuclear Instruments and Methods in Physics Research B* **255**, 309-313 (2007).
- ³ S. Vaddiraju, M. K. Sunkara, A. H. Chin, C. Z. Ning, G. R. Dholakia, and M. Meyyappan, *Journal of Physical Chemistry C* **111**, 7339-7347 (2007).
- ⁴ Y. Kim, Q. Gao, H. J. Joyce, H. H. Tan, C. Jagadish, M. Paladugu, and J. Zou, in *III-V nanowires for optoelectronics*, 2006 (SPIE), p. 635226.
- ⁵ Y. N. Guo, J. Zou, M. Paladugu, H. Wang, Q. Gao, H. H. Tan, and C. Jagadish, *Applied Physics Letters* **89**, 231917 (2006).
- ⁶ M. Jeppsson, K. Dick, H. Nilsson, N. Skold, J. Wagner, P. Caroff, and L.-E. Wernersson, *Journal of Crystal Growth* (2008).
- ⁷ M. Jeppsson, K. Dick, J. Wagner, P. Caroff, K. Deppert, L. Samuelson, and L.-E. Wernersson, *Journal of Crystal Growth* (2008).
- ⁸ A. Subekti, E. M. Goldys, and T. L. Tansley, in *Growth of Gallium Antimonide (GaSb) by Metalorganic Chemical Vapour Deposition*, 1997 (IEEE), p. 426-429.
- ⁹ R. M. Biefeld, *Materials Science & Engineering R-Reports* **36**, 105-142 (2002).

- 10 *Phase Diagrams of Binary Nickel Alloys; Vol. 6*, edited by P. Nash (ASM
International, Materials Park, 1991).
- 11 *Phase Diagrams of Binary Gold Alloys; Vol.*, edited by H. O. a. T. B. Massalski
(ASM International, Metals Park, Ohio, 1987).
- 12 S. A. Dayeh, E. T. Yu, and D. Wang, *Nano Letters* **7**, 2486-2490 (2007).
- 13 S. A. Dayeh, E. T. Yu, and D. Wang, *Small* **3**, 1683-1687 (2007).
- 14 M. K. Rathi, B. E. Hawkins, and T. F. Kuech, *Journal of Crystal Growth* **296**,
117-128 (2006).
- 15 A. Subekti, E. M. Goldys, M. J. Paterson, K. Drozdowicz-Tomsia, and T. L.
Tansley, *Journal of Materials Research* **14**, 1238-1245 (1999).
- 16 F. Pascal, F. Delannoy, J. Bougnot, L. Gousskov, G. Bougnot, P. Grosse, and J.
Kaoukab, *Journal of Electronic Materials* **19**, 187-195 (1990).
- 17 X. N. Zhang, C. R. Li, and Z. Zhang, *Applied Physics A* **82**, 33-37 (2006).
- 18 A. Lugstein, M. Steinmair, Y. J. Hyun, E. Bertagnolli, and P. Pongratz, *Applied
Physics Letters* **90**, 023109 (2007).
- 19 E. I. Givargizov, *Journal of Crystal Growth* **20**, 217-226 (1973).
- 20 H. Schmid, M. T. Bjork, J. Knoch, H. Reil, and W. Riess, *Journal of Applied
Physics* **103**, 024304 (2008).
- 21 S. N. Mohammad, *Nano Letters* **8**, 1532-1538 (2008).
- 22 J. B. Hannon, S. Kodambaka, F. M. Ross, and R. M. Tromp, *Nature* **440**, 69-71
(2006).
- 23 C. J. Novotny and P. K. L. Yu, *Applied Physics Letters* **87**, 203111 (2005).
- 24 W. Guang-Yu and P. Rui-Wu, *Journal of Electronic Materials* **23**, 217-220
(1994).
- 25 M. Borgstrom, K. Deppert, L. Samuelson, and W. Seifert, *Journal of Crystal
Growth* **260**, 18-22 (2004).
- 26 L. C. Chuang, M. Moewe, S. Crankshaw, and C. Chang-Hasnain, *Applied Physics
Letters* **92**, 013121 (2008).
- 27 K. A. Dick, K. Deppert, L. S. Karlsson, L. R. Wallenberg, L. Samuelson, and W.
Seifert, *Advanced Functional Materials* **15**, 1603-1610 (2005).
- 28 L. C. Chuang, M. Moewe, C. Chase, N. P. Kobayashi, and C. Chang-Hasnain,
Applied Physics Letters **90**, 043115 (2007).
- 29 J. Bauer, V. Gottschalch, H. Paetzelt, G. Wagner, B. Fuhrmann, and H. S.
Leipner, *Journal of Crystal Growth* **298**, 625-630 (2007).
- 30 J. Johansson, B. A. Wacaser, K. A. Dick, and W. Seifert, *Nanotechnology* **17**,
S355-S361 (2006).
- 31 A. I. Persson, M. W. Larsson, S. Stenstrom, B. J. Ohlsson, L. Samuelson, and L.
R. Wallenberg, *Nature Materials* **3**, 677-681 (2004).
- 32 K. A. Dick, K. Deppert, T. Martensson, B. Mandl, L. Samuelson, and W. Seifert,
Nano Letters **5**, 761-764 (2005).
- 33 H. Yasuda and H. Mori, *Journal of Crystal Growth* **237-239**, 234-238 (2002).
- 34 H. Yasuda, M. Takeguchi, K. Mitsuishi, M. Tanaka, M. Song, K. Furuya, and H.
Mori, *Journal of Electron Microscopy* **51**, S215-S218 (2002).
- 35 H. Mori and H. Yasuda, *materials Science & Engineering A* **217/218**, 244-248
(1996).

- 36 C. A. Wang, S. Salim, K. F. Jensen, and A. C. Jones, *Journal of Crystal Growth* **170**, 55-60 (1997).
- 37 B. S. Simpkins, L. M. Ericson, R. M. Stroud, K. A. Pettigrew, and P. E. Pehrsson, *Journal of Crystal Growth* **290**, 115-120 (2006).
- 38 M. He and S. N. Mohammad, *Journal of Vacuum Science and Technology B* **25**, 1909-1915 (2007).
- 39 M. Sacilotti, P. Cheyssac, G. Patriarche, J. Decobert, T. Chiaramonte, L. P. Cardoso, M. F. Phillis, M. J. Brasil, F. Iikawa, M. Nakaema, Y. Lacroute, J. C. Vial, and F. Donatini, *Surface & Coatings Technology* **201**, 9104-9108 (2007).
- 40 J. Johansson, C. Svensson, T. Martensson, L. Samuelson, and W. Seifert, *Journal of Physical Chemistry B* **109**, 13567-13571 (2005).
- 41 V. G. Dubrovskii, G. E. Cirlin, I. P. Soshnikov, A. A. Tonkikh, N. V. Sibirev, Y. B. Samsonenko, and V. M. Ustinov, *Physical Review B* **71**, 205325 (2005).
- 42 T. L. Ngai, R. C. Sharma, and Y. A. Chang, *Bulletin of Alloy Phase Diagrams* **9**, 586-589 (1988).
- 43 V. A. Nebol'sin and A. A. Shchetinin, *Inorganic Materials* **39**, 899-903 (2003).
- 44 V. K. Kumikov and K. B. Khokonov, *Journal of Applied Physics* **54**, 1346-1350 (1983).
- 45 S. C. Hardy, *Journal of Crystal Growth* **71**, 602-606 (1985).
- 46 A. Tegetmeier, A. Croll, A. Danilewsky, and K. W. Benz, *Journal of Crystal Growth* **166**, 651-656 (1996).
- 47 E. Bakkers, M. Borgstrom, and M. A. Verheijen, *MRS Bulletin* **32**, 117-122 (2007).
- 48 A. L. Roest, M. A. Verheijen, O. Wunnicke, S. Serafin, H. Wondergem, and E. Bakkers, *Nanotechnology* **17**, S271-S275 (2006).
- 49 T. Martensson, C. Svensson, B. A. Wacaser, M. W. Larsson, W. Seifert, K. Deppert, A. Gustafsson, L. R. Wallenberg, and L. Samuelson, *Nano Letters* **4**, 1987-1990 (2004).
- 50 Y. J. Van Der Meulen, *Journal of Physics and Chemistry of Solids* **28**, 25-32 (1967).
- 51 W. G. Hu, Z. Wang, B. F. Su, Y. Q. Dai, S. J. Wang, and Y. W. Zhao, *Physics Letters A* **332**, 286-290 (2004).
- 52 D. Effer and P. J. Etter, *Journal of Physics and Chemistry of Solids* **25**, 451-460 (1964).
- 53 R. D. Baxter, R. T. Bate, and F. J. Reid, *Journal of Physics and Chemistry of Solids* **26**, 41-48 (1965).
- 54 P. S. Dutta, H. L. Bhat, and V. Kumar, *Journal of Applied Physics* **81**, 5821-5870 (1997).
- 55 A. G. Milnes and A. Y. Polyakov, *Solid-State Electronics* **36**, 803-818 (1993).
- 56 Y.-W. Song, Masters Thesis, University of Canterbury, 2008.
- 57 S. C. Chen and Y. K. Su, *Journal of Applied Physics* **66**, 350-353 (1989).
- 58 Y. K. Su and S. M. Chen, *Journal of Applied Physics* **73**, 8349-8352 (1993).
- 59 D. J. Nicholas, M. Lee, B. Hamilton, and K. E. Singer, *Journal of Crystal Growth* **81**, 298-303 (1987).

- 60 M. Lee, D. J. Nicholas, K. E. Singer, and B. Hamilton, *Journal of Applied Physics* **59**, 2895-2900 (1986).
- 61 P. S. Dutta, K. S. Sangunni, and H. L. Bhat, *Physical Review B* **51**, 2153-2158 (1995).
- 62 W. Ruhle, D. Bimberg, W. Jakowetz, and R. Linnebach, *Journal of Luminescence* **12/13**, 501-506 (1976).
- 63 S. M. Chen and Y. K. Su, *Journal of Applied Physics* **74**, 2892-2895 (1993).
- 64 T. Koljonen, M. Sopanen, H. Lipsanen, and T. Tuomi, *Journal of Electronic Materials* **24**, 1691-1696 (1995).
- 65 F. Royo, A. Giani, F. Pascal-Delannoy, L. Gousskov, J. P. Malzac, and J. Camassel, *Materials Science & Engineering B* **28**, 169-173 (1994).
- 66 R. Vargas-Sanabria, E. Rosendo, J. Martinez, T. Diaz, H. Juarez, G. Garcia, P. Rosendo-Francisco, M. Rubin, and F. De Anda, *Physica Status Solidi C* **4**, 1406-1410 (2007).
- 67 W.-J. Jiang, Y.-M. Sun, and M.-C. Wu, *Journal of Applied Physics* **77**, 1725-1728 (1995).
- 68 E. Chidley, S. K. Haywood, A. B. Henriques, N. J. Mason, R. J. Nicholas, and P. J. Walker, *Semiconductor Science and Technology* **6**, 45-53 (1991).
- 69 A. Subekti, E. M. Goldys, and T. L. Tansley, *Journal of Physics and Chemistry of Solids* **61**, 537-544 (2000).
- 70 P. S. Dutta, K. S. R. Rao, H. L. Bhat, and V. Kumar, *Applied Physics A* **61**, 149-152 (1995).
- 71 S. Basu, U. N. Roy, B. M. Arora, and A. K. Srivastava, *Applied Surface Science* **59**, 159-162 (1992).
- 72 C. Ghezzi, R. Magnanini, A. Parisini, B. Rotelli, L. Tarricone, A. Bosacchi, and S. Franchi, *Semiconductor Science and Technology* **12**, 858-866 (1997).
- 73 W. Walukiewicz, S. X. Li, J. Wu, K. M. Yu, J. W. Ager III, E. E. Haller, H. Lu, and W. J. Schaff, *Journal of Crystal Growth* **269**, 119-127 (2004).
- 74 W. M. Becker, A. K. Ramdas, and H. Y. Fan, *Journal of Applied Physics* **32**, 2094-2102 (1961).
- 75 R. D. Wiersma, J. A. H. Stotz, O. J. Pitts, C. X. Wang, M. L. W. Thewalt, and S. P. Watkins, *Physical Review B* **67**, 165202 (2003).
- 76 C. Agert, P. S. Gladkov, and A. W. Bett, *Semiconductor Science and Technology* **17**, 39-46 (2002).

Chapter 7

Thesis Summary and Future Work

7.1 Summary

GaN and GaSb are direct-gap semiconductors with band gap energies of 3.4 eV and 0.72 eV, respectively at room temperature. GaN can be alloyed with InN and AlN to tune the band gaps and emission wavelengths from the infrared to the ultraviolet with a particular interest in the blue-green region of the visible spectrum for LED applications. GaSb, on the other hand, can be alloyed with InSb and AlSb to fabricate optoelectronic devices in the near- to mid-infrared region of the electromagnetic spectrum. As electronic devices have become smaller in size, the need for thin film features smaller than the limits of lithography has been realized. Due to this fact and unique properties that have been observed on the nanoscale, the interest in nanowires has grown immensely.

GaN and GaSb nanowires have been synthesized using various techniques such as vapor transport and MBE, however MOCVD is of particular interest since it is the technique of choice in the commercial market. Advantages of MOCVD over other techniques include its high throughput and switching capabilities that allow a high degree of control over doping and heterostructure growth. A significant amount of work has been carried out in the GaN nanowire field, however the primary focus has involved the vapor transport technique. Over the last few years, MOCVD growth of GaN nanowires

has gained interest, yet there still remains a lack of data concerning the effect of the growth conditions on the nanowire properties or a resolution to the issue of tapering that has been observed throughout the studies. On the other hand, only a limited number of studies have been carried out in the area of GaSb nanowire growth. As a result, very little is known about GaSb nanowire growth and their properties. With this motivation, the goal of this research project was to study the effect of the growth conditions on the structural and optical properties of GaN and GaSb nanowires. At the same time, there is uncertainty as to the mechanism (VLS vs. VSS) responsible for nanowire growth in each case. As a result, an additional focus of this project was to determine the nature of the seed particle for GaN and GaSb nanowire growth, thereby providing insight into the growth mechanism.

In the first study, growth conditions for the synthesis of GaN nanowires by MOCVD were investigated on sapphire substrates using Au and Ni as metal catalysts. Position of the substrate within the reactor tube was found to play a critical role in the success of this technique. Minimal success was realized when the quartz boat was placed in the constant temperature region of the furnace; however, when the quartz boat was moved closer to the TMG inlet, GaN nanowire growth was achieved. Nanowire growth was obtained over a furnace temperature range of 800-900°C, a TMG flowrate range of 2-4 sccm, and a NH₃ flowrate range of 100-200 sccm using Ni as the catalyst. CFD modeling was utilized in conjunction with the experimental results to determine the reason for these findings. The nanowire diameter and length were observed to increase with increasing precursor flowrate, although increasing the NH₃ flowrate led to a more dramatic increase in the diameter and length. At the same time, the growth conditions

were found to have a significant effect on the optical properties of the nanowires with an increase in the near-band-edge photoluminescence observed with increasing growth temperature compared to the deep-level emission. This behavior was attributed to a reduction of carbon in the nanowires.

Once the growths were complete, TEM was employed to examine the structure and composition of the seed particle. Based on the temperature range observed for GaN nanowire growth, it was believed that the VSS mechanism rather than the VLS mechanism was responsible for nanowire growth. Looking at the Ni-Ga phase diagram, the particle would only form a liquid alloy at extremely Ga-rich conditions or if the growth temperature was at least 1200°C. Upon further inspection with TEM, the seed particle was found to be faceted, indicating the formation of an intermetallic phase. XEDS measurements verified this observation as the particle was found to possess a Ga concentration of ~24-30 at. %. SAD patterns of the catalyst revealed a cubic structure with a lattice parameter ranging from 3.578 to 3.597 Å. These findings indicate that the seed particle is composed of Ni₃Ga which is located in the Ni-rich regime of the Ni-Ga phase diagram and is strongly suggestive of VSS growth.

The final series of experiments in this study involved the addition of GeCl₄ to the gas phase chemistry in an effort to modify the growth chemistry and reduce the tapering effect observed. The addition of a small fraction of GeCl₄ to the gas phase chemistry not only resulted in a reduction in the nanowire diameter and tapering, but also led to the ability to grow GaN nanowires over a large area including the constant temperature region of the furnace. It is believed that GeCl₄ decomposes into Ge and HCl, and the

HCl reacts with TMG to form GaCl. GaCl is stable at higher temperatures and may not decompose until coming into contact with the Ni catalyst.

TEM analysis and PL measurements were carried out on a select few samples in order to investigate the effect of GeCl₄ on the structural and optical properties of nanowires. Two types of nanowires were observed. One set of nanowires were found to consist of smooth surfaces and the wurtzite crystal structure with (0001) planar defects, while the other set of nanowires were jagged with wurzite cores and zinc blende islands protruding from the surface. It is hypothesized that the zinc blende islands form on the side facets of the nanowires after the nanowire has been formed due to excess Ga or Ge deposits on the surface. It is also noted that the smooth wires possessed a growth direction of [0002], while the serrated nanowires had a growth direction a few degrees away from $[1\bar{1}00]$.

The second study investigated the synthesis of GaSb nanowires on sapphire and Si (111) substrates using Au nanoparticles and thin films. Initial experiments were carried out using sapphire substrates, and nanowire growth was achieved over a temperature range of 475-525°C, a pressure range of 100-300 Torr, and a V/III ratio of 0.5-2. The nanowires were found to become more tapered with increasing temperature and pressure and decreasing V/III ratio, since these conditions promoted thin film growth on the side facets of the nanowires. During the pressure studies, nanowire growth was found to proceed with a preferred orientation on Au-coated sapphire and Si (111) samples over pressure ranges of 200-300 Torr and 150-250 Torr, respectively. Si (111) substrates were used in a secondary study, since TEM results showed that the predominant growth direction of the nanowires was [111]. The nature of the oriented growth over these

pressure ranges is uncertain. It is proposed that the effect is due to a combination of the formation of an underlying GaSb thin film and a change in the composition of the seed particle at elevated pressures which correspond to Ga-rich conditions. At the same time, nanowires grown at a pressure of 300 Torr were found to be significantly larger in diameter and possess a higher degree of tapering than samples grown at other pressures.

TEM was employed to investigate the nature of the seed particle and elucidate an explanation for the variation in nanowire morphology based on the reactor pressure. XEDS was utilized to determine the composition of the catalyst and the values were compared to the Au-Ga phase diagram to determine the mechanism responsible for GaSb nanowire growth. The catalyst was found to consist of Au, Ga, and Sb for most of the samples. Depending on the sample, the seed particle was found to consist of ~25-40 at.% Ga and ~40-75 at.% Au. These values placed the composition in the liquid region of the binary phase diagram, indicating VLS growth. An interesting byproduct of this analysis was the fact that the Sb concentration in the catalyst for the nanowire samples was found to be one of three values: 1 at.%, 15 at.%, or 55 at.% Sb. Nanowires that possessed a particle concentration of 1 at.% Sb were observed to contain a necking region due to the diffusion of Sb and Ga out of the catalyst during the cooling process. Typically, the solid solubility of Sb in Au (Au-Sb solid solution) is only 1 at.%, however the concentration of Sb in Au was observed to be as high as 15 at.% on the nanoscale. As a result, a seed particle that consisted of 15 at.% Sb was also associated with the formation of the Au-Sb solid solution. When the particle was found to consist of 55 at.% Sb, the nanowires were observed to be bicrystalline due to a phase separation of the particle. One grain was believed to be either AuGa or Au₂Ga, while the other one was the AuSb₂ line compound.

The AuSb₂ line compound is typically located at ~67 at.% Sb, however it has been found to expand to a range of ~52-77 at.% Sb at the nanoscale.

TEM characterization was also carried out on samples grown at various pressures to determine a cause for the variation in morphology with respect to reactor pressure. Based on the characterization, nanowires grown at 300 Torr consisted of amorphous Ga catalysts. Growth at this pressure is believed to proceed via a self-catalytic process after the formation of Ga droplets on the substrate. This would explain the dramatic increase in diameter and tapering of the nanowires as the catalyst would also serve as the group-III source. During this study, it was also noted that the contact angle varied depending on the growth conditions. A relationship was ascertained between the contact angle and the seed particle composition. Based on surface tension values, a high concentration of Sb (≥ 15 at.% Sb) in the catalyst led to a contact angle less than 90°, while a low concentration (~1 at.% Sb) led to a contact angle greater than 90°. The exception was the case where the seed particle was composed of two grains. If the grain consisted of the AuSb₂ compound, the contact angle was less than 90°, whereas the contact angle was greater than 90° when the grain consisted primarily of AuGa or Au₂Ga (~1 at.% Sb).

The final segment of this study examined the optical properties of the nanowires using PL. The sample grown on Si (111) at a pressure of 300 Torr was found to possess good optical properties. The PL spectra were dominated by band-edge transitions with weaker transitions at 777 meV and 710 meV which correspond to the native acceptor. The PL spectra for a sample grown on sapphire at 300 Torr, however, were dominated by transitions associated with the native acceptor and acceptor B. In this series of experiments, the effect of the V/III ratio was also investigated, since it is a critical factor

in the optical quality of GaSb growth. For nanowires grown under Ga-rich conditions, native acceptor and acceptor B transitions dominated the PL spectra, since Ga-rich conditions favor the formation of Sb vacancies and $V_{\text{Ga}}\text{Ga}_{\text{Sb}}$ centres linked to the native acceptor. In contrast, nanowires that were grown under Sb-rich conditions did not exhibit the native acceptor transition. Nanowires grown with a V/III ratio of 1 possessed the best optical properties similar to that reported for GaSb thin films.

7.2 Future Work

7.2.1 GaN Nanowires

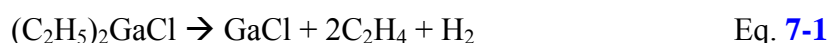
A consistent observation throughout the GaN nanowire studies was the competition between thin film (vapor-solid) growth and nanowire (vapor-solid-solid) growth. The thin film growth resulted in tapering of the GaN nanowire diameter and affected the density of nanowire growth on the sapphire substrate. It also proved to be difficult to synthesize GaN nanowires in the constant temperature zone of the reactor due to the depletion of the gas phase precursors prior to the growth front. Attempts were made to overcome this issue by increasing the TMG and NH_3 flowrates, however this led to an overall increase in the nanowire diameter. At the same time, higher precursor flowrates also led to degradation in the optical quality of the GaN nanowires, which may be attributed to carbon incorporation, Ga vacancies, or O impurities depending on the precursor.

The introduction of GeCl_4 provides optimism that high density nanowire growth in the constant temperature region can be realized using Cl-based precursors. The addition of Cl is believed to alter the chemistry in MOCVD growth of GaN and may be responsible for the improved nanowire growth regime. Cl was also effective at reducing the tapering of GaN nanowires due to the formation of HCl, which is believed to etch GaN deposited on the nanowire sidewalls.¹ In the preliminary studies, not only did the addition of GeCl_4 lead to growth in the constant temperature region, but it also led to growth of dense, small diameter nanowires at elevated temperature and V/III ratios (TMG and NH_3 flowrates). The addition of GeCl_4 , however, also led to degradation in the optical properties of the nanowires. Upon further inspection using TEM, smooth and serrated nanowires were found. The serrated nanowires consisted of wurtzite GaN cores with a high density of stacking faults and faceted zinc blende islands, while the smooth nanowires only possessed a wurtzite structure with (0001) planar defects. The reason for the serrated nanowires is not known, however it is believed to be either due to excess Ga or Ge from the GeCl_4 source.

In order to determine the effect of Ge on the growth process, the next step should involve replacing GeCl_4 with HCl. HCl has been previously used to eliminate tapering of Au- and Ti-catalyzed Si nanowires^{2,3} and for HVPE growth of GaN nanowires.⁴⁻⁶ HCl gas has also been utilized for MOCVD growth of GaN thin films in a process known as MOHVPE.⁷⁻⁹ As was discussed in Chapter 4, TMG and HCl mix together and form GaCl. GaCl is believed to remain stable until it adsorbs onto the growth surface and reduces to form Ga for incorporation, eliminating the formation of adduct reactions between TMG and NH_3 .¹⁰ At the same time, Cl could potentially passivate the nanowire

facets reducing the radial growth rate.¹¹ By eliminating the presence of Ge, it can be determined if HCl or Ge is responsible for the nanowire morphology found in the GeCl₄ studies. Also, PL studies can be completed and compared to the GeCl₄ results and typical PL spectrum from samples grown without the addition of GeCl₄ in order to determine the cause for the degradation of the optical properties of the nanowires. In order to complete these studies, either an additional line and gas panel will need to be fabricated for the use of the HCl on the nanowire CVD system in 220 EE West or a line will have to be designated on the system which is being brought online in 10 Steidle. In either case, Fomblin SV oil would need to be used in the pump due to the corrosive nature of HCl.

Another precursor which can be investigated is diethylgallium chloride (DEGaCl). DEGaCl has been previously applied to the thin film growth technology to improve lateral epitaxy overgrowth (LEO) growth of GaN by producing high quality films with vertical, smooth side facets.^{1,12} DEGaCl could be utilized as an alternative to TMG, since it decomposes in the gas phase to GaCl via the reaction:



This results in HVPE-like growth chemistry near the growth front in the MOCVD set-up. An advantage over HVPE, however, is the switching capabilities in MOCVD growth and the ability to grow heterostructures using Cl-based Al and In sources. There are a couple of disadvantages that must be taken into consideration. DEGaCl has a low vapor pressure at room temperature, therefore it is necessary to heat the bubbler and run lines to approximately 60°C ($P_{\text{DEGaCl}} = 2$ Torr) in order to obtain an appreciable vapor pressure for growth.¹³ DEGaCl is not commercially available, therefore the availability and

quality of the source may be issues. One advantage of using HCl over DEGaCl is the individual control over the TMG/HCl and TMG/NH₃ ratios. Once again, TEM and PL analysis can be carried out and compared to previous results in order to determine the optimal set of precursors for GaN nanowire growth.

With the ultimate goal of device fabrication in mind, another area of interest for GaN nanowires would involve controlled incorporation of n-type and p-type dopants. A reasonable amount of research has been carried out in this area involving growth techniques such as vapor transport¹⁴⁻¹⁸ and HVPE⁶; however, to the author's knowledge, only two reports by one group exist concerning doping of GaN nanowires using MOCVD.^{19,20} In these studies, silane (SiH₄) and bis(cyclopentadienyl)magnesium (Cp₂Mg) were employed for n-type and p-type doping, respectively, of the GaN nanowires. One of the main advantages of MOCVD is the high degree of control over doping and heterostructure growth. Based on the GaN thin film²¹⁻²³ and nanowire reports, typical n-type and p-type dopants are Si and Mg, respectively. Therefore, initial n-type doping studies could be carried out on the reactor in 220 EE West using SiH₄, and p-type doping studies could be completed by acquiring an Cp₂Mg source and placing it on one of the metalorganic lines. This study will not only prove useful for device applications, but it should provide some insight into the mechanism responsible for dopant incorporation in the nanowire CVD reactor.

The final potential area of future work which will be discussed here involves epitaxial growth of GaN nanowires. Throughout the studies, the predominant growth direction was determined to be $[1\bar{1}20]$, however other growth directions exist. For the purposes of electrical measurements and device fabrication, it becomes difficult to

ascertain the accuracy of the measurements when uncertainty exists in terms of the growth direction of the nanowires being used in the fabrication process. In order to eliminate error in the measurements associated with variation in the growth direction, epitaxial growth of GaN nanowires is necessary. As was learned in Chapter 2, various substrates such as (100) γ -LiAlO₂, (111) MgO, and r-plane sapphire have been used to successfully grow epitaxial GaN nanowires.^{24,25} Based on the primary growth direction involved in the author's studies, initial experiments have been carried out using r-plane sapphire (Figure 7.1). Growths were carried out at 900°C, 100 Torr, and a V/III ratio of

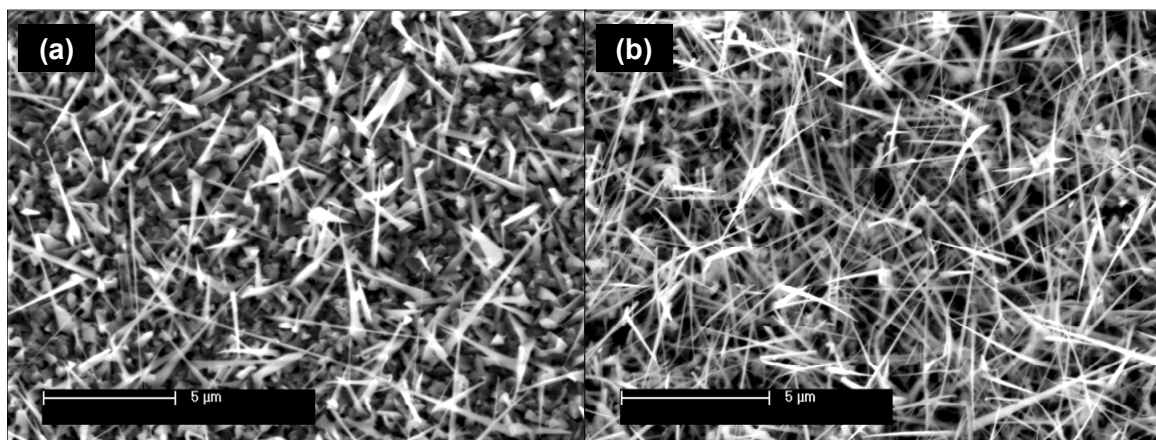


Figure 7.1: SEM images of GaN growth on r-plane sapphire (a) without and (b) with the addition of GeCl₄ to the gas phase mixture. Growth conditions: 900°C, 100 Torr, 3 sccm TMG, 100 sccm NH₃, and 10 minute growth time. For the growth with GeCl₄, the GeCl₄ flowrate was 0.15 sccm.

33 with and without the addition of GeCl₄ to the gas phase mixture. TEM and XRD analysis were not carried out on these samples; however, based on initial SEM observations, it appears as though epitaxial growth was not a success. In the GeCl₄ studies reported in Chapter 5, the growth direction was found to change and may contribute to the results seen below. Once the studies are completed with HCl, TEM can

be employed to investigate the growth direction and choose a proper substrate for epitaxial growth.

7.2.2 GaSb Nanowires

Based on the preliminary studies concerning the growth of GaSb by MOCVD, the predominant growth direction was observed to be [111], while a secondary growth direction was found to be [220]. As was discussed in the GaN nanowire future work, the presence of multiple growth directions can lead to errors in electrical measurements as the electrical properties can vary depending on the growth direction. In order to minimize this error, the substrate can be utilized as a template to promote epitaxial growth. At the same time, epitaxial growth of nanowires can simplify the fabrication process as was shown for a Si nanowire-based thermoelectric device in Chapter 1 (Figure 1.3 (b)).

In order to obtain epitaxial growth, it is necessary to choose a substrate that possesses the growth orientation observed for GaSb nanowire growth. It is also important to choose a substrate that can be utilized as a base for device applications. Due to the prominence and maturity of Si in the semiconductor industry, it has been investigated as a potential substrate for III-V nanowire growth.²⁶⁻²⁹ Studies that have already been completed in this dissertation using Si (111) substrates show promise that epitaxial growth of GaSb nanowires can be realized. It would be useful to continue these experiments in an effort to refine the growth process and produce high quality vertically oriented nanowires. Another substrate that can also be utilized for these studies is GaAs

(111)B. Ideally, GaAs (111)B substrates would have already been utilized for these studies, however the nanowire CVD system lacks an arsine source to provide an arsine overpressure when heating the reactor or cooling it down. This is necessary to prevent evaporation of As from the GaAs substrate.

As a result, the initial studies of GaSb nanowire growth were carried out using sapphire and silicon substrates. The system which is currently being constructed in 10 Steidle, however, will be capable of growing GaAs nanowires. Therefore, it would be possible to attempt to grow epitaxial GaSb nanowires on GaAs substrates. The only success to date, to the author's knowledge, is the synthesis of GaSb/GaAs nanowire heterostructures in a cold-wall MOCVD reactor.^{30,31} There are no published reports of GaSb nanowire growth direction on GaAs (111)B substrates. A third substrate that can be investigated for this study is GaSb (111). The GaSb substrate would be ideal for a thermoelectric device similar to Si nanowire-based one discussed in Chapter 1. For this device, n-type or p-type Si nanowires were grown epitaxially on a complementary substrate. A polymer filler was added to the device along with a top contact. This device could also be applicable for GaSb, since GaSb is being examined as a potential thermoelectric material.

Once epitaxial growth is achieved, the next area of interest would be p-type and n-type doping of GaSb. MOCVD-grown GaSb is unintentionally doped p-type due to the presence of native defects. As a result, it is significantly more difficult to dope the nanowires n-type than p-type. Based on the GaSb thin film literature,³²⁻³⁷ typical p-type dopants are Si and C, whereas a typical n-type dopant is Te. Possible sources for Si- and C-doping would be silane (SiH_4) and carbon tetrachloride (CCl_4), whereas the typical

sources examined for Te-doping are diethyltellurium (DETe) or dimethyltellurium (DMTe). I-V measurements can be carried out on these samples to examine the electrical properties. It should be noted that initial 4 point resistivity and back-gated IV measurements were performed on unintentionally-doped GaSb nanowires by Professor Mayer's group in Electrical Engineering at Penn State. The nanowires were found to be p-type with a resistivity of $0.23 \pm 0.18 \Omega \cdot \text{cm}$.

7.3 References

- ¹ L. Zhang, S. L. Gu, T. F. Kuech, and M. P. Boleslawski, *Journal of Crystal Growth* **213**, 1-9 (2000).
- ² S. Sharma, T. I. Kamins, and R. S. Williams, *Journal of Crystal Growth* **267**, 613-618 (2004).
- ³ S. Sharma, T. I. Kamins, and R. S. Williams, *Applied Physics A* **80**, 1225-1229 (2005).
- ⁴ G. Seryogin, I. Shalish, W. Moberlychan, and V. Narayanamurti, *Nanotechnology* **16**, 2342-2345 (2005).
- ⁵ H. M. Kim, D. S. Kim, Y. S. Park, D. Y. Kim, T. W. Kang, and K. S. Chung, *Advanced Materials* **14**, 991-+ (2002).
- ⁶ H. M. Kim, Y. H. Cho, and T. W. Kang, *Advanced Materials* **15**, 232-+ (2003).
- ⁷ Y. Kumagai, H. Murakami, H. Seki, and A. Koukitu, *Journal of Crystal Growth* **246**, 215-222 (2002).
- ⁸ Y. Kumagai, H. Murakami, Y. Kangawa, and A. Koukitu, *Physica Status Solidi (c)* **2**, 2058-2061 (2005).
- ⁹ Y. Matsuo, N. Kawaguchi, M. Fujino, Y. Kangawa, Y. Kumagai, T. Irisawa, and A. Koukitu, *Journal of Crystal Growth* **275**, e1631-e1636 (2005).
- ¹⁰ J. E. Huffman and N. L. Casey, *Journal of Crystal Growth* **129**, 525-531 (1993).
- ¹¹ T. F. Kuech, *Semiconductor Science and Technology* **8**, 967-978 (1993).
- ¹² L. Zhang, S. L. Gu, R. Zhang, D. M. Hansen, M. P. Boleslawski, and T. F. Kuech, *Journal of Crystal Growth* **235**, 115-123 (2002).
- ¹³ K. Mori, M. Yoshida, A. Usui, and H. Terao, *Applied Physics Letters* **52**, 27-29 (1988).
- ¹⁴ X. Chen, S. J. Lee, and M. Moskovits, *Applied Physics Letters* **91**, 082109-1-3 (2007).
- ¹⁵ J. Liu, X.-M. Meng, C.-S. Lee, I. Bello, and S.-T. Lee, *Applied Physics Letters* **83**, 4241-4243 (2003).

- 16 P. V. Radovanovic, C. J. Barrelet, S. Gradecak, F. Qian, and C. M. Lieber, *Nano Letters* **5**, 1407-1411 (2005).
- 17 E. Cimpoiasu, E. Stern, R. Klie, R. A. Munden, G. Cheng, and M. A. Reed, *Nanotechnology* **17**, 5735-5739 (2006).
- 18 Z. H. Zhong, F. Qian, D. L. Wang, and C. M. Lieber, *Nano Letters* **3**, 343-346 (2003).
- 19 F. Qian, Y. Li, S. Gradecak, D. L. Wang, C. J. Barrelet, and C. M. Lieber, *Nano Letters* **4**, 1975-1979 (2004).
- 20 F. Qian, S. Gradecak, Y. Li, C. Y. Wen, and C. M. Lieber, *Nano Letters* **5**, 2287-2291 (2005).
- 21 K. S. Ramaiah, Y. K. Su, S. J. Chang, F. S. Juang, and C. H. Chen, *Journal of Crystal Growth* **220**, 405-412 (2000).
- 22 S. Li, C. Mo, L. Wang, C. Xiong, X. Peng, F. Jiang, Z. Deng, and D. Gong, *Journal of Luminescence* **93**, 321-326 (2001).
- 23 P. R. Hageman, M. A. C. Devillers, A. R. A. Zauner, V. Kirilyuk, W. S. Bouwens, R. C. M. Crane, and P. K. Larsen, *Physica Status Solidi B* **216** (1999).
- 24 G. T. Wang, A. A. Talin, D. J. Werder, J. R. Creighton, E. Lai, R. J. Anderson, and I. Arslan, *Nanotechnology* **17**, 5773-5780 (2006).
- 25 T. Kuykendall, P. J. Pauzauskie, Y. F. Zhang, J. Goldberger, D. Sirbuly, J. Denlinger, and P. D. Yang, *Nature Materials* **3**, 524-528 (2004).
- 26 E. Bakkers, M. Borgstrom, and M. A. Verheijen, *MRS Bulletin* **32**, 117-122 (2007).
- 27 T. Martensson, C. Svensson, B. A. Wacaser, M. W. Larsson, W. Seifert, K. Deppert, A. Gustafsson, L. R. Wallenberg, and L. Samuelson, *Nano Letters* **4**, 1987-1990 (2004).
- 28 A. L. Roest, M. A. Verheijen, O. Wunnicke, S. Serafin, H. Wondergem, and E. Bakkers, *Nanotechnology* **17**, S271-S275 (2006).
- 29 J. Johansson, B. A. Wacaser, K. A. Dick, and W. Seifert, *Nanotechnology* **17**, S355-S361 (2006).
- 30 M. Jeppsson, K. Dick, J. Wagner, P. Caroff, K. Deppert, L. Samuelson, and L.-E. Wernersson, *Journal of Crystal Growth* (2008).
- 31 Y. N. Guo, J. Zou, M. Paladugu, H. Wang, Q. Gao, H. H. Tan, and C. Jagadish, *Applied Physics Letters* **89**, 231917 (2006).
- 32 F. Pascal, F. Delannoy, J. Bougnot, L. Gousskov, G. Bougnot, P. Grosse, and J. Kaoukab, *Journal of Electronic Materials* **19**, 187-195 (1990).
- 33 R. D. Wiersma, J. A. H. Stotz, O. J. Pitts, C. X. Wang, M. L. W. Thewalt, and S. P. Watkins, *Physical Review B* **67**, 165202 (2003).
- 34 R. D. Wiersma, J. A. H. Stotz, O. J. Pitts, C. X. Wang, M. L. W. Thewalt, and S. P. Watkins, *Journal of Electronic Materials* **30**, 1429-1432 (2001).
- 35 C. Agert, P. S. Gladkov, and A. W. Bett, *Semiconductor Science and Technology* **17**, 39-46 (2002).
- 36 J. G. Cederberg and R. M. Biefeld, *Semiconductor Science and Technology* **19**, 953-958 (2004).
- 37 F. Nakamura, K. Taira, K. Funato, and H. Kawai, *Journal of Crystal Growth* **115**, 474-478 (1991).

Appendix

Nanowire Chemical Vapor Deposition System

Appendix A covers the aspects of the nanowire CVD system that are part of the original system. These include: 1) the system gas manifold, 2) the exhaust set-up, and 3) the control panel. For other aspects of the nanowire chemical vapor deposition system, please refer back to Chapter 4.

G.1 System Gas Manifold

The system gas manifold is the main feedthrough for the gas delivery system and the metalorganic delivery system. The nanowire chemical vapor deposition system is capable of growing Si, SiGe, Ge, GaN, and GaSb nanowires. Phosphine, TMB, and diborane gases are utilized to dope the Si nanowires n-type and p-type allowing for the synthesis of various heterostructures. The system gas manifold consists of pneumatic valves, mass flow controllers (MFCs), VCR fittings, and ¼ inch stainless steel tubing. The pneumatic valves and MFCs are controlled by a computer program called LabView (National Instruments Corp.). A schematic of the LabView display is shown in Figure 7.1. This schematic is also representative of the system gas manifold layout. The LabView software was designed to allow the user to turn the pneumatic valves on and off by simply clicking the valve on the display with the mouse. The pneumatic valves are

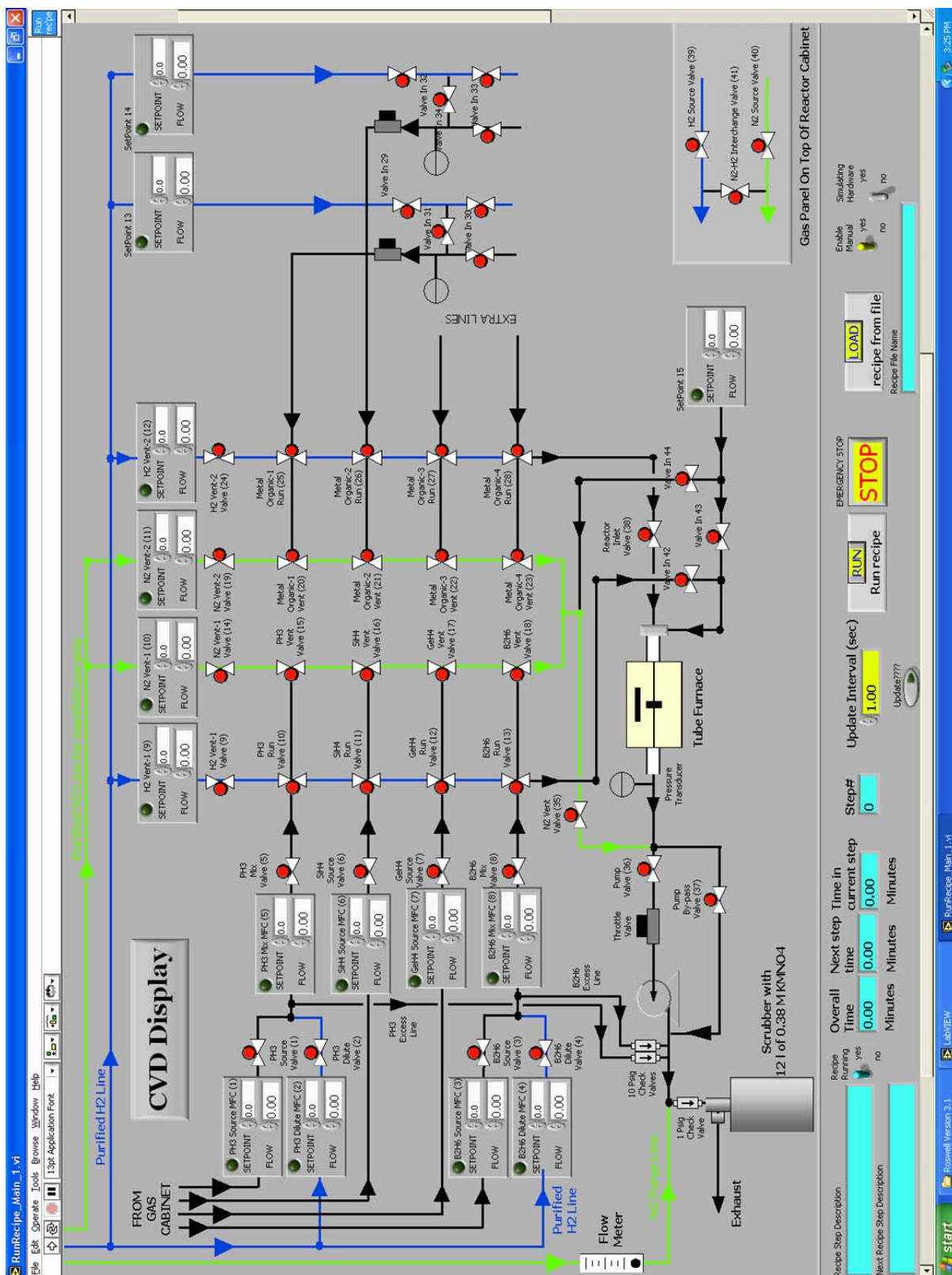


Figure 7.1: LabView set-up for controlling the mass flow controllers and pneumatic valves on the system gas manifold.

represented by red circles with two white triangle extensions. When the pneumatic valve is closed, the circle is red. When the pneumatic valve has been opened, the color of the circle becomes green. The mass flow controller is represented by the gray rectangular box with two smaller white inputs with numerical values. The top input box is labeled “Setpoint.” When the user wants to set the flowrate for the MFC, they enter the value here. The bottom input box is labeled “Flow.” The value present in the “Flow” input box is the actual flowrate being transmitted back to the LabView software program by the MFC. This is important so that the user is aware if the MFC is functioning properly or not.

The LabView software interface can be divided into three components: the gas delivery system, metalorganic delivery system, and system gas manifolds. Looking at Figure 7.1 after rotating it 90 degrees, the left section of the image is representative of the gas delivery system where the group-V precursors enter the system gas manifold. The right section of the image is representative of the metalorganic delivery system, and the center section is representative of the system gas manifold. The MFC located towards the bottom right of the image is the NH_3 MFC (Setpoint 15). It was plumbed directly to the furnace, because TMG and NH_3 are highly reactive at room temperature. At the bottom of the LabView schematic, there are options present to run growth recipes. Growth recipes can be utilized to automate the growth process for heterostructures. There is an alternative LabView program which is used to create these recipes. The system gas manifold consists of run (blue outer line on each side) and vent lines (inner green lines). The run lines are plumbed to the reactor for growth, whereas the vent lines bypass the reactor and run to the pump. Typically, hydrogen gas is flown through the run

lines, and nitrogen gas is flown through the vent lines; however, it is possible to flow nitrogen through the run lines via an interchange panel located in the bottom right corner of the LabView image and upper left portion of the reactor. If the H₂ source valve (39) is closed and the N₂-H₂ interchange valve (41) is opened, nitrogen gas will flow through the run lines. Hydrogen gas can also be run through the vent lines by closing the N₂ source valve (40) and opening the N₂-H₂ interchange valve (41). N₂ gas is commonly run through the run lines before and after growth to flush the reactor of any toxic gases or air that may have entered the reactor when loading a sample. The precursors for III-V and group-IV nanowire growth are flown into the reactor via four-way pneumatic valves located on the run lines. When the four-way valve is turned on (green circle), the precursors are directed into the run lines. When the four-way valve is turned off (red circle), the precursor gases bypass the run line and flow to the vent line. The pneumatic valves located on the vent lines are three-way valves. By switching these valves on when the four-way valves are off, it is possible to flow the precursor gases to the vent lines. This process is utilized before growth in order to allow the reactor to stabilize at the growth pressure. The same process is utilized after growth in order to stop growth while at the same time allowing the precursor lines to be drained while cooling the system down.

G.2 Exhaust Set-Up

The exhaust for the reactor consists of a vacuum pump, filters, valves, and a scrubber. An overview of the exhaust is displayed in Figure 7.2. Once the gases exit the

reactor, they are directed to the pump through a pneumatic valve labeled pump valve (36). If for some reason there is a need to bypass the pump, pump valve (36) can be closed and a pneumatic valve labeled pump bypass valve (37) is opened (Figure 7.1). This combination would be used if operating the system at atmospheric pressure and also when shutting down the system to equilibrate upstream and downstream of the pump. If the system is operated below atmospheric pressure, a throttle valve is utilized to control the pressure. A trap is attached to the entrance of the pump in order to prevent debris from breaking the pump, whereas an oil mist eliminator is attached to the exit of the pump. The pump, itself, is a D16B Leybold Trivac rotary vane pump with a pumping speed of 16 m³/hr. Nitrogen and precursor gases flowing to the vent lines enter the exhaust set-up after the pump. Additional non-purified nitrogen (~12-13 slm) enters into the exhaust post-pump in order to dilute the precursor gases and dilute hydrogen gases below their explosive limits. All of the gases flow through a scrubber (Model GSS-1250, Tek-Vac, Inc.) which contains twelve liters of 0.38M potassium permanganate (KMNO₄) before being expelled into the exhaust for the building. The scrubber is primarily used for the purpose of oxidizing the dopant gases for Si nanowire growth into a non-toxic form before expelling them into the exhaust for the building.

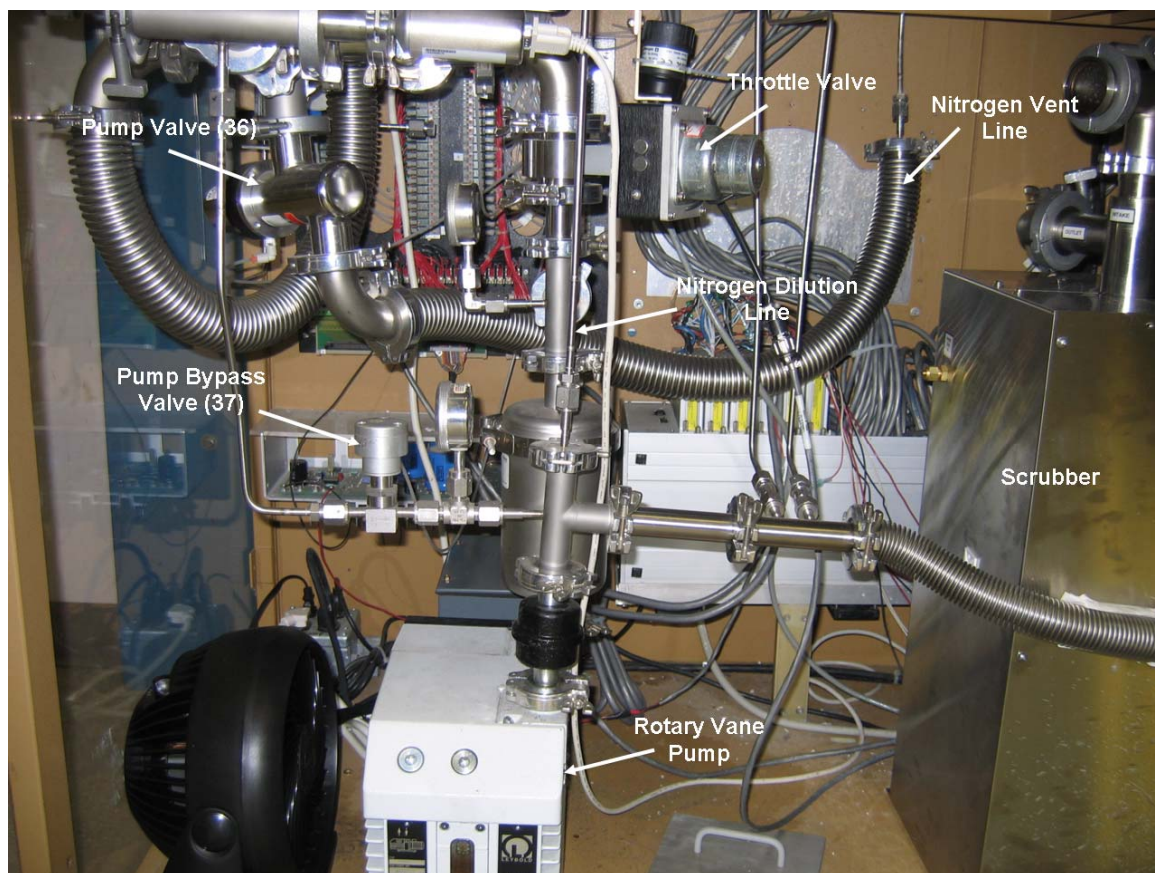


Figure 7.2: Exhaust set-up for nanowire CVD system including throttle valve, nitrogen vent line, nitrogen dilution line, scrubber, pump bypass valve (37), and pump valve (36).

G.3 Control Panel

The control panel consists of most of the electronics for operating the equipment on the nanowire CVD system (Figure 7.3). This includes power for the safety interlock, mass flow controllers, and the pressure controllers for the MOCVD set-up. The button located next to the safety interlock power button is a reset button. When the power is originally turned on, the alarm will sound until the reset button is depressed. The alarm will also sound if any of the safety features built into the system are triggered. When the

alarm sounds, the system automatically shuts down until the reset button is pushed and/or the problem has been resolved. When the system shuts down, power is cut off to the MFCs and pneumatic valves. The user is also capable of shutting down the system if an issue arises by hitting the emergency stop button on the panel. There is also an emergency button located on the LabView display at the bottom which serves the same function (Figure 7.1).

Below these buttons on the control panel are three LifeLine II toxic gas monitors (Honeywell International, Inc.) which are utilized in particular for detection of a PH_3 leak. These monitors are connected to detectors that are located on the exhaust for the gas cabinets, the exhaust for the reactor, and the bottom half of the system cabinet near the exhaust set-up. If for some reason any of these detectors were to be triggered, then the alarm would sound and the system would automatically shut down.

The throttle valve pressure controller is located below the LifeLine II units. This MKS 600 throttle valve controller is utilized to regulate the reactor pressure for growth purposes. The pressure controller possesses “open” and “close” buttons along with five pressure value presets. The pressure controller also has a built-in safety feature which is a pressure limit feature. When the system is off, the pressure limit is set for 850 Torr; however, when the system is under vacuum for growth or leak checking, the pressure limit is set to 650 Torr. If the pressure were to increase above 650 Torr due to a leak or a cracked/broken quartz tube, then the system alarm would be triggered, and the system would shut down until the issue was resolved.

The next two units below the throttle valve pressure controller are the power supply and controllers for the pressure transducers and solenoid valves used in the

MOCVD set-up. The pressure transducers (Type 122A, MKS Instruments, Inc.) and solenoid valves (MKS Instruments, Inc.) are connected to Type 260 pressure controllers (MKS Instruments, Inc.) and a Type 261 display. The operating pressure is set via a knob located on the pressure controller. The pressure transducer and solenoid valve work in conjunction with one another in order to maintain the required pressure. Finally, below these units is the power supply for the MFCs and a MKS 945 pirani pressure gauge display which is utilized for leak checking purposes.



Figure 7.3: Photo of the control panel for the nanowire CVD system which includes: 1) safety interlock power switch, 2) alarm reset, 3) alarm speaker, 4) emergency stop, 5) LifeLine II toxic gas monitors, 6) throttle valve pressure controller, 7) MOCVD pressure controller power supply, 8) MOCVD pressure controllers, and 9) MFC power supply. The pirani pressure gauge display is located below the MFC power supply.

VITA

Robert Alan Burke

Education

The Pennsylvania State University

Doctor of Philosophy in Materials Science and Engineering, 2008

Dissertation: *MOCVD Growth and Characterization of Gallium Nitride and Gallium Antimonide Nanowires*

Rensselaer Polytechnic Institute

Bachelor of Science in Materials Science and Engineering, 2003

Publications

Hangfeng, Ji, M. Kuball, R.A. Burke, and J.M. Redwing, "Vibrational and optical properties of GaN nanowires synthesized by Ni-assisted catalytic growth." *Nanotechnology* **12** (2007) 445704.

Burke, R.A., D.R. Lamborn, X. Weng, and J.M. Redwing, "Experimental and Computational Modeling Studies of GaN Nanowires Grown by the VSS Mechanism." Submitted to *Journal of Crystal Growth*.

X. Weng, R.A. Burke, J.M. Redwing, "'Nature of Catalyst Particles and Growth Mechanisms of GaN Nanowires Grown by Ni-Assisted Metalorganic Chemical Deposition.'" Submitted to *Nanotechnology*.

Burke, R.A., X. Weng, M.W. Kuo, A.M. Itsuno, T.S. Mayer, and J.M. Redwing, "Growth and Characterization of Unintentionally-Doped GaSb Nanowires." In Progress.